Development, Optimization and Implementation of the Design for a Centrifugal Reverse-Osmosis Desalination System

by

Peter Martin Wild

B.A.Sc University of British Columbia, 1983

A Dissertation Submitted in Partial Fulfillment of the Requirements for the Degree of

DOCTOR OF PHILOSOPHY

in the Department of Mechanical Engineering

We accept this dissertation as conforming to the required standard.

Dr. G. W. Vickers, Co-supervisor (Mechanical Engineering)

Dr. N. Djilali, Co-supervisor (Mechanical Engineering)

Dr. B. Tabarrok, Member (Mechanical Engineering)

Dr. A. Doige, Member (Mechanical Engineering)

Dr. A. Zielinski, Member (Electrical Engineering)

Dr. R. Venter, External Examiner (University of Toronto)

University of Victoria

Abstract

A new method of sea water desalination, Centrifugal Reverse-Osmosis (CRO), is developed from concept to patented design and functional prototype of capacity 11,355 litres of fresh water per day. CRO is shown to have significant benefits relative to the leading existing desalination technology, conventional reverse-osmosis. These benefits include: lower energy consumption, reduced initial and replacement membrane costs, lower noise levels and improved reliability. CRO is projected to show increasing cost efficiency as plant capacity increases. For a relatively large CRO plant, $651 m^3$ fresh water per day, the total cost of desalinated water is projected to be 25.9% lower than the total cost of water produced by a conventional RO plant of equivalent capacity. The current patented design requires further development in order to realize this potential. Toward this end, a computational and experimental study of rotor windage losses and an experimental study of fluid flow losses through the rotor are conducted. In addition a new method for the analysis of stresses in a filament wound rotor shell under combined centrifugal and pressure loading is developed.

Examiners:

Dr. G. W. Vickers, Co-supervisor (Mechanical Engineering)

Dr. N. Djilali, Co-supervisor (Mechanical Engineering)

Dr. B. Tabarrok, Member (Mechanical Engineering)

Dr. A. Doige, Member (Mechanical Engineering)

Dr. A. Zielinski, Member (Electrical Engineering)

Dr. R. Venter, External Examiner (University of Toronto)

Table Of Contents

Chapter 3

Development and Testing of First and Second Prototype CRO Systems

Chapter 4

An Experimental and Computational Investigation of Windage Losses Associated with a Rotating, Enclosed and Immersed Cylinder

Chapter 5

An Experimental Analysis of the Dependence of Flow Losses Through a CRO Rotor on the Speed of Rotor Rotation

Chapter 6

A New Method of Analysis of the Stresses and Strains in a Filament-Wound Cylindrical Shell Under Combined Loading

Chapter 7

Projected Economics of CRO

Chapter 8

Summary of Conclusions

List of Tables

List of Figures

Nomenclature Table

A_r	cross-sectional area of flow passages (normal to radial direction)
$C_{IJ}^{(m)}$	components of stiffness tensor of a single lamina in cylinder coordinates
$\overline{C}_{ij}$	components of stiffness tensor of complete laminate in cylinder coordinates
C_L	loss coefficient for flow through centrifuge $\left(= \dfrac{P_d}{\frac{1}{2}\rho V_R^2}\right)$
C_M	moment coefficient due to entire rotor
$C_{M_{CYL}}$	moment coefficient due to cylindrical surface of rotor
$C_{M_{DISC}}$	moment coefficient due to a disc (or rotor ends)
C_{cart}	center spacing of membrane cartridges in gattling gun design
D_{cart}	diameter of membrane cartridges
$D_{ij}^{(m)}$	components of stiffness tensor of a single lamina in cylinder coordinates
DF	degradation factor used in Last Ply Failure criteria
F_A	axial force applied to shell
F_h, F_p	homogeneous and particular solutions of Airy stress function, F
F_{ij}	quadratic failure criteria strength parameters
G_{Ii}	rotational strain transformation tensor

H_{turbo}	turbomachine (pump or turbine) "head"
$H_{li}^{(m)}$	rotational stress transformation tensor
L	rotor length
L_{mem}	membrane life
M_{CYL}	windage moment on cylindrical surface of rotor
M_{DISC}	windage moment on end surfaces of rotor
N_{cart}	number of cartridges
P_{outlet}	pressure at pump outlet
$P_{C_{max}}$	maximum pressure developed in a centrifuge
P_{diff}	pressure differential across membrane
P_d	pressure drop through centrifuge rotor $\left(= P_{in} - P_{out}\right)$
$P_d\big\vert_{incr}$	incremental pressure drop $\left(= P_d\big\vert_{\omega} - P_d\big\vert_{\omega=0}\right)$
P_{encl}	air pressure inside rotor enclosure
P_{ext}	external pressure loading on cylindrical shell
P_{int}	internal pressure loading on cylindrical shell
P_p	desalination process pressure
P_s	stagnation pressure
P_f	pressure developed within feed fluid passages in centrifuge
P_{in}	pressure of feed fluid at inlet to centrifuge
P_{out}	pressure of feed fluid at outlet from centrifuge

P_{sw}	pressure in sea water passages in centrifuge . Note that for CRO, $\left(P_{sw} = P_f\right)$
P_{fw}	pressure in fresh water passages in centrifuge
Q_{turbo}	turbomachine (pump or turbine) flow rate
Q_f	flow of feed fluid into centrifuge rotor
Q_{fw}	flow of fresh water from CRO rotor
Q_{sw}	flow of sea water into CRO rotor. Note that for CRO, $\left(Q_{sw} = Q_f\right)$
R	radial body force
R_{exit}	radius at which fluid leaves a centrifuge rotor
R_i	outer radius of rotor
R_{imp}	pump or turbine impeller radius
R_o	inner radius of rotor enclosure
R_{max}	maximum radius of feed flow path through centrifuge
Re	Couette Reynolds Number $\left(= \dfrac{\rho \omega R_i g_r}{\mu}\right)$
$\hat{R}e$	Tip Reynolds Number $\left(= \dfrac{\rho \omega R_i^2}{\mu}\right)$
RR	recovery ratio $\left(= \dfrac{Q_{fw}}{Q_{sw}}\right)$
S_{fw}	fresh water salinity

S_ϕ	source terms in momentum conservation equations
$S^{(k)}$	strength ratio of k-th layer
Ta	Taylor number $\left(= Re\sqrt{\dfrac{g_r}{R_i}} = \dfrac{\rho_{encl}\omega\sqrt{R_i}\, g_r^{3/2}}{\mu_{encl}} \right)$
Ta_c	critical Taylor number
$\overline{U}(r) = \overline{U}$	potential defining radial body force
$\left.\begin{array}{l} U(r,\theta) = U \\ V(r,\theta) = V \\ W(r,\theta) = W \end{array}\right\}$	functions arising as "constants of integration" in Appendix II
V_{accel}	measured voltage corresponding to rms-acceleration
V_{cart}	volume of a standard cylindrical membrane cartridge
V_{amc}	volume of annular membrane configuration
V_R	radial flow velocity
V_T	tangential flow velocity
X	fraction of feed flow release from rotor at R_{exit}
Z	constant calculated to determine Ta_c
$\overline{\boldsymbol{E}}_w$	specific energy consumption due to windage
$\overline{\boldsymbol{E}}$	total specific energy consumption
$\boldsymbol{F}, \boldsymbol{\psi}$	Airy stress functions

P_D	power to main drive motor of a CRO unit
P_w	power to windage
P_{conv}	power to a conventional RO unit
R	radial body force
a_{ij}	components of compliance tensor in cylinder coordinates
$a_{ij}^{(k)}$	components of compliance tensor of k-th layer in cylinder coordinates
b_k	radius of k-th layer interface
c	radius ratio for single layer shell $\left(=\frac{r_{int}}{r_{ext}}\right)$
c_k	radius ratio for multi layer shell $\left(=\frac{b_{k-1}}{b_k}\right)$
g	ratio of elastic properties for single layer shell $\left(=\left(\frac{\beta_{11}}{\beta_{22}}\right)^{\frac{1}{2}}\right)$
$\hat{g}$	acceleration due to gravity
g_a	axial gap width
g_k	ratio of elastic properties for multi layer shell $\left(=\left(\frac{\beta_{11}^{(k)}}{\beta_{22}^{(k)}}\right)^{\frac{1}{2}}\right)$

g_r	radial gap width $\left(= R_o - R_i\right)$
h	thickness of a single lamina
h_o	stagnation enthalpy
k	turbulent kinetic energy
q_k	interface pressure at k-th interface
r	radius
r_{int}	internal radius of cylindrical shell
r_{ext}	external radius of cylindrical shell
r_{mc}^{in}	inner radius of membrane configuration
r_{mc}^{out}	outer radius of membrane configuration
t	width of flow passages in impeller
u_r, u_θ, u_z	displacements in r, θ, z directions respectively in a single layer shell
u, v, w	fluid velocities in x, r, θ directions respectively
$u_r^{(k)}, u_\theta^{(k)}, u_z^{(k)}$	displacements in r, θ, z directions respectively in k-th layer of a multi layer shell
u_τ	wall-friction velocity $\left(= \left(\frac{\tau_w}{\rho}\right)^{1/2}\right)$
y^+	wall coordinate $\left(= \frac{y u_\tau}{\nu}\right)$

$\boldsymbol{\psi}, \boldsymbol{F}$	Airy stress functions
$\boldsymbol{\Delta}$	intermediate calculation variable
$\boldsymbol{\Gamma}_D$	centrifuge drive motor torque
$\boldsymbol{\Omega}$	general turbomachinery head coefficient
$\boldsymbol{\Omega}_c$	centrifuge velocity coefficient
$\boldsymbol{\Psi}$	general turbomachinery flow coefficient
$\boldsymbol{\Psi}_c$	centrifuge pressure coefficient
$\alpha_{(k)}$	wind angle of k-th layer of a filament wound shell
α_{opt}	constant wind angle for maximum loading at failure
$\varepsilon_r, \varepsilon_\theta, \varepsilon_z$	strains in r, θ, z directions in a single layer shell
$\varepsilon_r^{(k)}, \varepsilon_\theta^{(k)}, \varepsilon_z^{(k)}$	strains in r, θ, z directions in k-th layer of a multi layer shell
ε_z^0	constant axial strain
β_{ij}	reduced strain coefficients for a single layer shell
$\beta_{ij}^{(k)}$	reduced strain coefficients for k-th layer of a multi layer shell
$\nu_{\theta r}$	equivalent Poisson ratio for a single layer shell $\left(= -\dfrac{\beta_{12}}{\beta_{22}}\right)$
$\nu_{r\theta}^{(k)}$	equivalent Poisson ratio for a multi layer shell $\left(= -\dfrac{\beta_{12}^{(k)}}{\beta_{22}^{(k)}}\right)$

$\nu_{z\theta}$	Poisson ratio for a single layer shell $\left(=-\frac{a_{23}}{a_{33}}\right)$
$\nu_{z\theta}^{(k)}$	Poisson ratio for a multi layer shell $\left(=-\frac{a_{23}^{(k)}}{a_{33}^{(k)}}\right)$
$\left.\begin{matrix}\sigma_r, \sigma_\theta, \sigma_z \\ \tau_{r\theta}, \tau_{rz}, \tau_{\theta z}\end{matrix}\right\}$	stresses in a single layer shell in cylinder coordinates
$\sigma_r^{(k)}, \sigma_\theta^{(k)}, \sigma_z^{(k)}$	stresses in a multi layer shell in cylinder coordinates
$\overline{\sigma}_\theta, \overline{\sigma}_z$	"thin-wall" average stresses
ρ_{sw}	density of sea water
ρ_{fw}	density of fresh water
ρ_f	density of fluid
ρ_c	density of composite
ρ_k	density of k-th layer of multi-layer shell
ρ_{encl}	density of fluid (air) in rotor enclosure
κ	semi-empirical exponent
ω	rotational speed
ω_c	critical rotational speed corresponding to Ta_c
η_{mc}	volumetric efficiency of membrane configuration
μ	dynamic viscosity
μ_{encl}	dynamic viscosity of fluid (air) in rotor enclosure
ν	kinematic viscosity

μ_{eff}	effective viscosity
τ	shear stress at rotor surface

Acknowledgements

This work has been supported by the Canadian Department of National Defence, the Natural Sciences and Engineering Research Council and the Advanced Systems Institute of British Columbia.

Chapter 1

Introduction - Existing Desalination Technologies and the Potential of Centrifugal Reverse-Osmosis

1.0 The Growing Demand for Desalination

"Civilisation cannot survive without fresh water. Consequently, in the long struggle for survival, some of man's most creative ventures for human advancement have been directed toward the development of water resources. Today, one of the greatest challenges is the assurance of adequate fresh water for the future as the world's population rapidly expands" [1]. Although these words were spoken 25 years ago, the message is even more urgent today. In addition to expanding populations, the supply of fresh water is threatened by the exhaustion or contamination of traditional supplies and the possibility of climatic change under the uncertain influence of global warming. In a recent survey, it was found that "nearly half of all nations on Earth are now feeling or will experience water shortage, or crisis, within the next 25 years" [2]. Some analysts feel that water will replace oil as the commodity over which wars will be fought. In the Middle East, "political struggles over scarce water supplies could rip apart the fragile ties that exist between states [resulting in] great turmoil" [2]. The increasing importance of fresh water is reflected in the dramatic growth of the desalination industry as shown in the Figure 1.1.

The major processes which are competing for a share of the growing desalination market are multistage flash (MSF) distillation and reverse osmosis (RO). MSF is an evaporation process which employs a series of evaporation chambers at successively lower pressures and successively lower temperatures. RO is a membrane separation process in which a feed sea water stream is separated, under high pressure, into a fresh water stream and an exhaust sea water stream of higher concentration than the original feed sea water. Other desalination processes include multiple effect distillation, vapour compression distillation, electrodialysis and solar distillation. A qualitative comparison of the characteristics of MSF and RO is presented in Table 1.1.

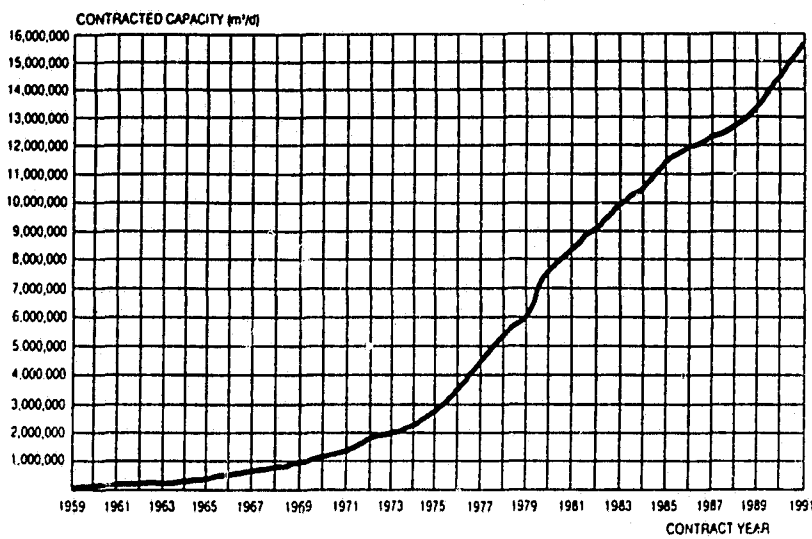

Figure 1.1 - Cumulative Installed Desalination Capacity Since 1959 [3]

	MSF	RO
ENERGY CONSUMPTION	*high* *(thermal energy)*	*low* *(mechanical energy)*
PHYSICAL SIZE	*large*	*compact*
MAINTENANCE COSTS	*high*	*moderate*
SEA WATER PRETREATMENT COSTS	*high*	*moderate*
POTENTIAL FOR FUTURE IMPROVEMENT	*limited*	*excellent*

Table 1.1 - A Comparison Of RO, MSF

Although RO appears to be superior to MSF in every category, MSF has, until recently, dominated the desalination market. MSF gained dominance during the 1960's and 1970's when RO was still an experimental technology. As RO has matured, however, it has gained an increasing share of the world market for desalination at the expense of MSF, as shown in the Figure 1.2. The share of worldwide installed desalination capacity held by RO has grown from approximately 20.0% in 1980 to approximately 70.0% in 1989. MSF remains the dominant technology for applications in which cheap thermal energy is readily available, such as in the Middle East where MSF is often installed in tandem with a power generation plant. In the absence of a cheap source of thermal energy, however, RO is the most economical source of desalinated water [4].

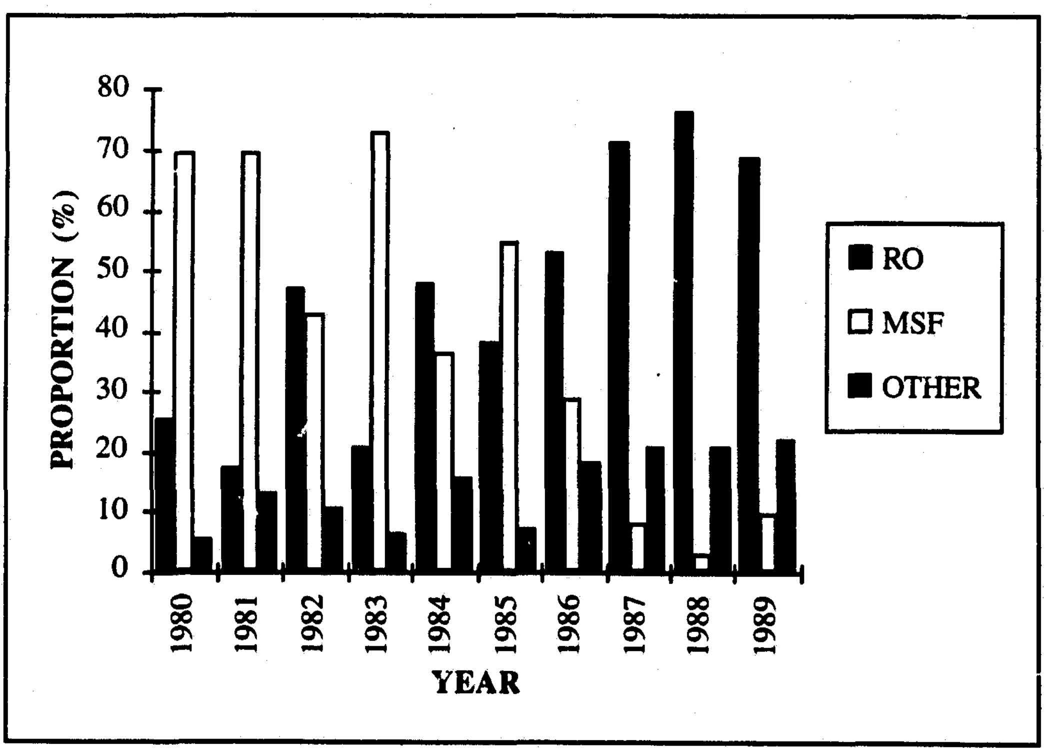

Figure 1.2 - The Worldwide Market Shares of RO, MSF and Other Desalination Technologies [5]

1.1 Conventional Reverse-Osmosis Desalination

1.1.1 Cross-Flow Filtration

Over the last two decades, membrane processes have gained a dominant position in a wide range of concentration, fractionation, purification and recycling applications in many industries, including: desalination, chemical processing, dairy processing, electronics manufacturing, food processing, pharmaceuticals, photographic, printing, petroleum processing, textiles, beverage manufacturing, sewage treatment, and pulp and paper. All of these membrane processes are "cross-flow" rather than "incident-flow" filtration processes.

In incident-flow filtration, as shown in Figure 1.3, the feed flow is perpendicular to the filter media and suspended or dissolved particles which are too large to pass through the pores in the filter media are retained in the filter media. In cross-flow filtration, also shown in Figure 1.3, the feed flow is parallel to the membrane and is separated into two streams: the "permeate", which contains only those dissolved or suspended particles which are small enough to pass through the pores in the membrane and the "concentrate" which retains those dissolved or suspended particles which are too large to pass through the pores in the membrane. The principal advantage of cross-flow filtration is that the dissolved and suspended solids do not clog the membrane but are swept away with the concentrate flow. This minimizes the frequency of filter replacement and cleaning.

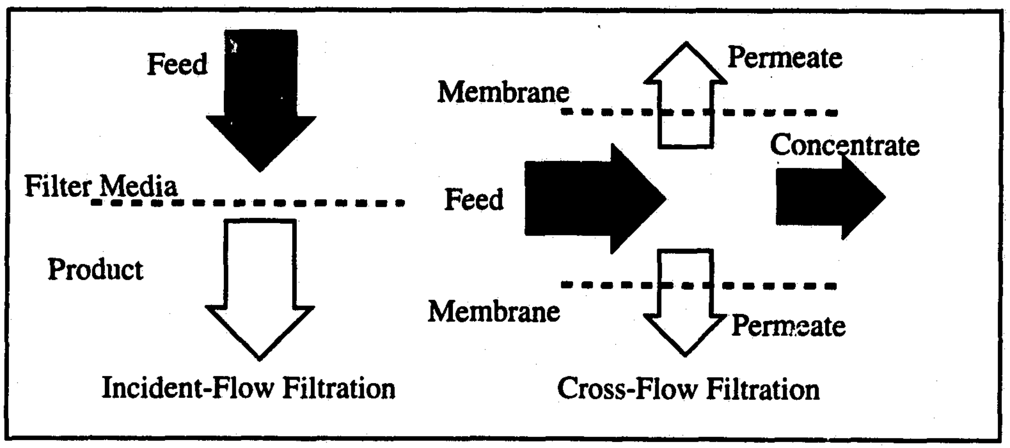

Figure 1.3 - Types of Filtration

1.1.2 Membrane Types

There is a broad spectrum of membrane types, each with its characteristic pore-size, chemical compatibility and transport characteristics, as shown in Figure 1.4.

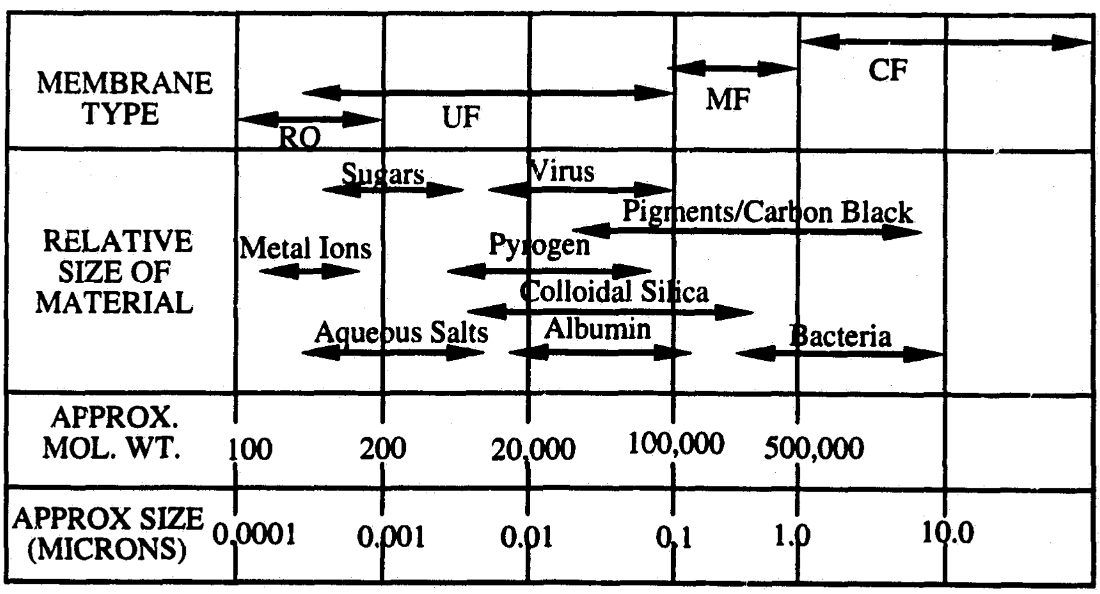

Figure 1.4 - Membrane Selection Chart [6]

For a given application, an appropriate membrane is selected based upon the size and chemical characteristics of the dissolved and/or suspended particles of concern. The three major categories of membrane filtration are, in descending order of pore size, "micro filtration" (MF), "ultra filtration" (UF) and "hyper filtration" (reverse-osmosis or RO). For desalination, the particles of concern are dissolved salts and metal ions and the appropriate membrane process is, therefore, RO.

1.1.3 Reverse-Osmosis

A reverse-osmosis membrane is designed to be relatively permeable to the solvent molecules of a given feed solution and relatively impermeable to the solute ions. In the case of sea water, the membrane is relatively permeable to water molecules and relatively impermeable to the ions of the dissolved salts and metals. Consider such a membrane separating sea water from fresh water, as shown in the left of Figure 1.5. Osmosis is the natural tendency for fresh water to dissolve into sea water. The pressure which drives this process is called the osmotic pressure and, for a sea water solution, it is equal to 2.58 MPa (374 psi). That is, a differential pressure of 2.58 Mpa must be applied to the sea water side of the membrane to establish an equilibrium in which there is no net transfer of water molecules across the membrane. If, however, the pressure applied to the sea water side of the membrane exceeds this osmotic pressure, as shown in the right of Figure 1.5, fresh water will flow from the sea water side to the fresh water side of the membrane. Since the natural process of osmosis has been reversed the resulting process has been called "reverse-osmosis".

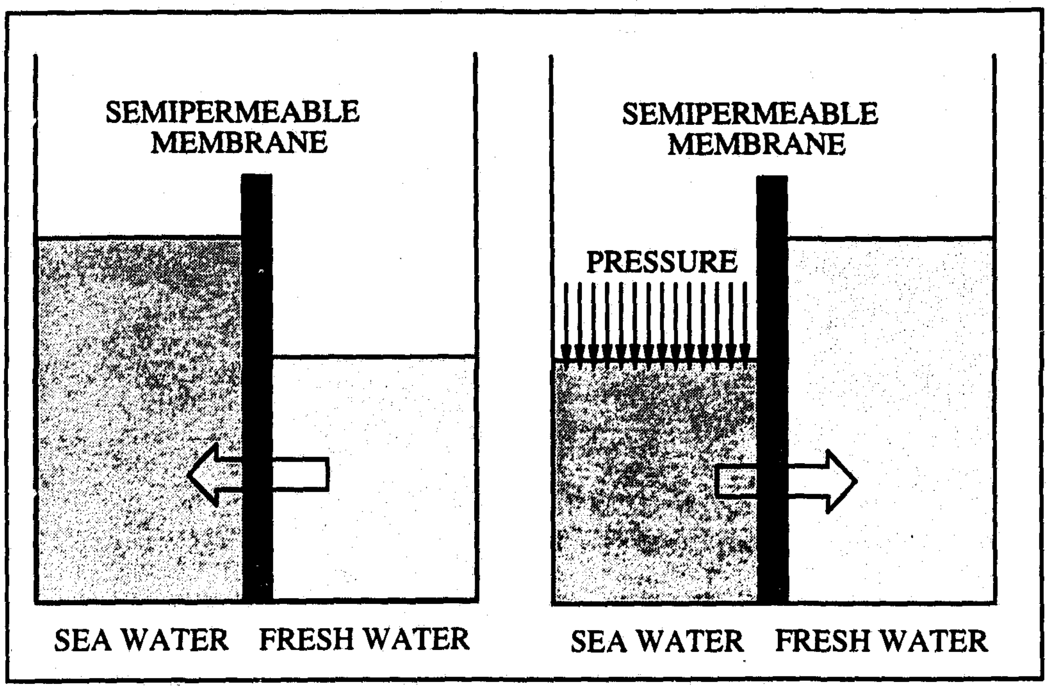

Figure 1.5 - Osmosis and Reverse-Osmosis

In practice, membranes are not ideal and some passage of the solute ions is inevitable. The flow of the solvent must, therefore, be sufficient to keep the concentration of these solute ions in the permeate at an acceptably low level. As the flux of solvent through the membrane increases with pressure, whereas the flux of solute ions is relatively constant with pressure, the feed solution must be raised to a pressure well above its osmotic pressure. In the case of sea water, reverse-osmosis systems typically operate at between 5.5 MPa (800 psi) and 6.9 MPa (1000 psi).

1.1.4 Concentration Polarisation

An important phenomenon which affects membrane performance is "concentration polarisation". Concentration polarisation refers to the formation of a high concentration boundary layer on the concentrate side of the membrane. Solute ions and particles are carried by convection toward the membrane surface, where the solvent, but not the dissolved species or particles, permeates through the membrane, as shown in Figure 1.6(a). The rate of convection toward the membrane is usually greater than the rate at which the dissolved species or particles diffuse away from the membrane and back into the main feed flow. As a consequence, a concentration gradient is created, as shown in Figure 1.6(b). The osmotic pressure of this high concentration layer is higher than the osmotic pressure of the main flow. The flux of permeate through the membrane is reduced accordingly. Concentration polarisation is controlled by the turbulent mixing of the flow of the feed stream across the membrane surface. It is, therefore, important that the flow rate through a membrane cartridge is sufficient to maintain turbulent flow.

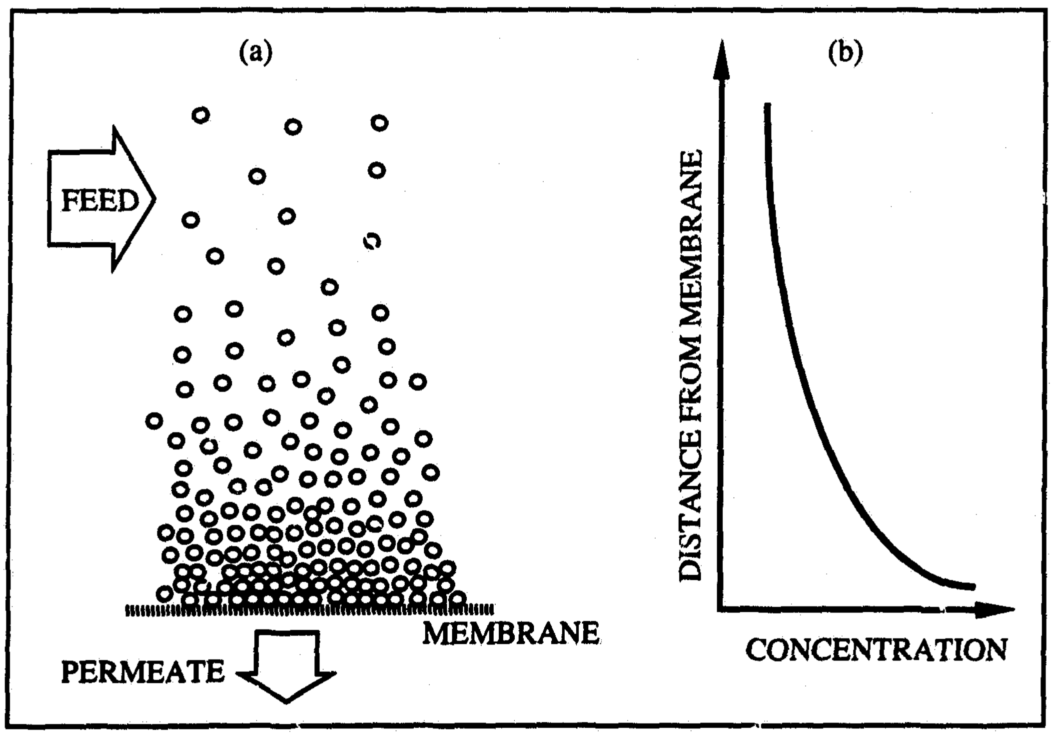

Figure 1.6 - Concentration Polarisation

1.1.5 RO Membranes and RO Membrane Packaging

The membranes which are used in sea water reverse-osmosis fall into two general categories: hollow fine fibre and flat sheet. Hollow fine fibres are 85 microns in diameter, or about the size of a human hair, and have a thin and dense external aramid skin which is the "membrane" part of the fibre. This skin is supported by a less dense and more porous sublayer, also of aramid. Pressurized sea water flows around the outside of the fibre and fresh water permeates through the outer skin and then flows, relatively unimpeded, through the porous sublayer to the hollow bore at the centre of the fibre. For commercial distribution, these fibres are bundled and assembled into cylindrical cartridges.

Flat sheet membranes are similar to hollow fine fibres in that there is a thin membrane layer which is supported by one or more porous layers. This membrane construction, called a "thin film composite", is then bonded to a porous fabric. For commercial distribution, these membrane/fabric sheets are wrapped into cylindrical "spiral-wound" cartridges, as shown in Figure 1.7. Two of these sheets, back to back and separated by a fine mesh spacer, are formed into an envelope and sealed on all but one edge. This fine mesh spacer is the fresh water carrier. The unsealed edge is bonded to a perforated plastic tube such that the fine mesh spacer is open to the perforations. A sheet of coarse mesh spacer is placed over the envelope and both are wound tightly around the perforated tube. Pressurised sea water flows through the cartridge axially in the coarse mesh spacer. Fresh water permeates across the membranes, into the fine mesh spacer and spirals inward to the perforated tube. Fresh water is collected from the ends of the perforated tube.

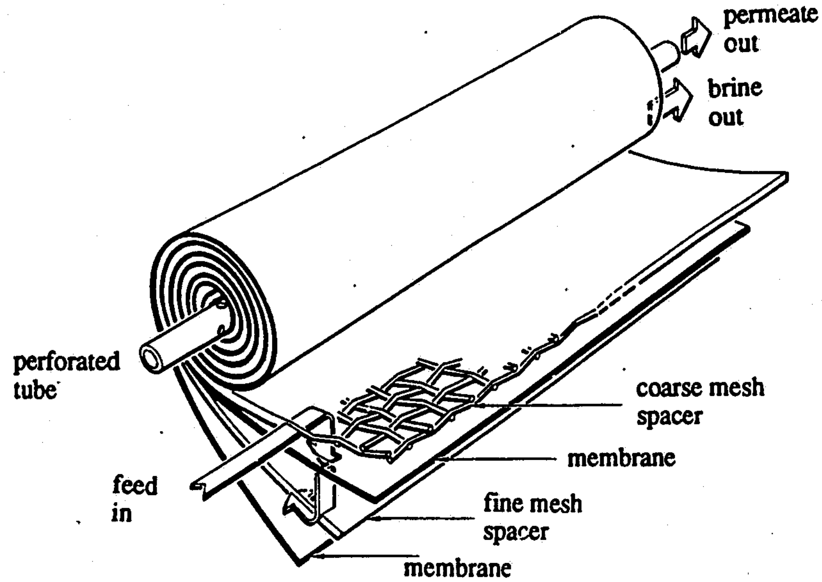

Figure 1.7 - Spiral Wound Membrane Cartridge

1.1.6 Conventional Reverse Osmosis System Design and Operation

In conventional RO desalination, process pressure is provided with a high pressure feed pump. The major components of a conventional reverse-osmosis desalination plant are shown in Figure 1.8. The low pressure feed pump draws feed sea water from the intake and feeds it through prefilters which remove impurities which would either foul the reverse-osmosis membranes or cause premature failure of the high pressure feed pump. The feed sea water is elevated to process pressure by the high pressure feed pump (5.5 MPa - 6.9 MPa for sea water desalination) and then passes through the membrane cartridge array.

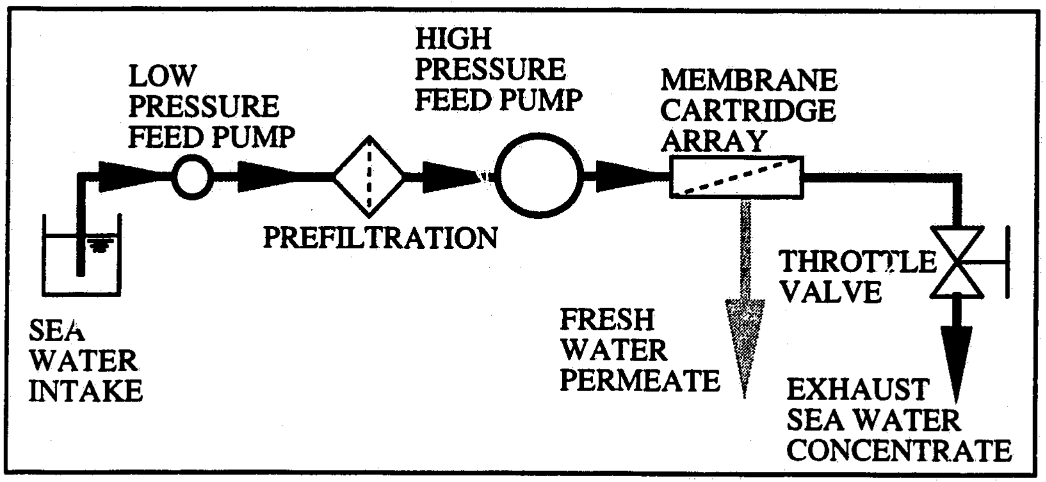

Figure 1.8 - Schematic of a Conventional Reverse-Osmosis Desalination System

Typically, the membrane cartridge array will have two or more stages of cartridges in series where each stage comprises a parallel set of pressure vessels, each of which contains one or more membrane cartridges in series, as shown in Figure 1.9.

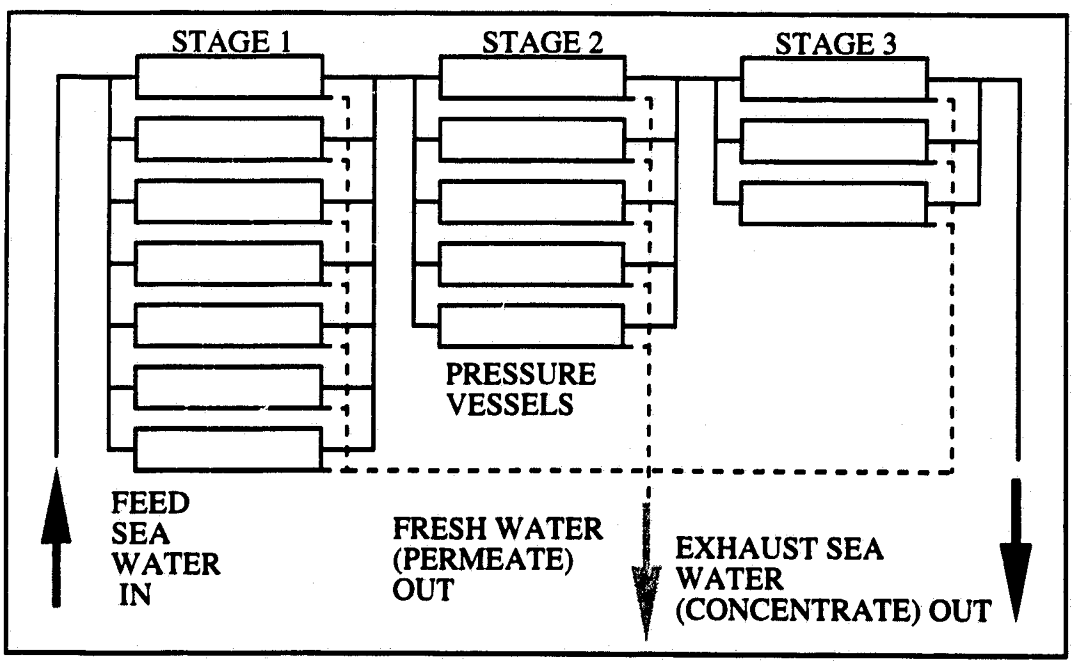

Figure 1.9 - Schematic of a Membrane Cartridge Array

The first stage receives the full feed flow while subsequent stages receive the full feed flow less the amount removed as product in the preceding stages. The overall recovery for a conventional RO system is typically 20% to 45%. The concentrated exhaust sea water, which is still at process pressure, is released across a throttle valve or, in some cases, directed into an energy recovery turbine.

High-pressure feed pumps are both the most expensive component and the greatest source of problems in a conventional RO plant. These pumps are, most often, of a reciprocating piston design. Critical to their operation, therefore, is the maintenance of a good seal on the sliding interface between the piston and the cylinder-bore. This interface is, however, highly susceptible to accelerated rates of corrosion and wear. As a consequence, these pumps are notoriously unreliable. In addition, the reciprocating nature of the design can produce levels of noise and vibration which, especially in military applications, are unacceptable.

Aside from the high-pressure pump, the principal disadvantage of a conventional reverse-osmosis desalination system is the wasted energy of the high-pressure brine exhaust. Pelton-wheel turbines are available which recover a portion of this exhaust brine energy, but the additional cost and complexity has prevented their widespread implementation, particularly in small plants. An alternative energy recovery device involves the redirection of the exhaust brine to the back side of the pistons in a reciprocating piston feed pump. Due to reliability difficulties with the additional valving, this system has been implemented only in small hand-pump units. A further difficulty with this system is that it limits operation to a single recovery ratio (the ratio of fresh water to feed sea water flow rates), dictated by the ratio of piston-rod to piston areas. Often, there is a need to vary recovery ratio, depending upon changes in feed water temperature and salinity and upon the condition of the membranes.

Conventional RO plants which do not have energy recovery are most economically operated at relatively high (30-40%) recovery ratios. This is because any sea water which is not recovered as fresh water leaves the system at high pressure and the energy associated with this high pressure flow is wasted. The principal means of increasing recovery ratio is to increase the membrane surface area to which a given quantity of feed sea water is exposed. This is accomplished either by increasing the number of stages of membrane cartridges or by increasing the number of membrane cartridges in each pressure vessel in one or more stages (see Figure 1.9). In either case, downstream membrane cartridges are exposed to a more concentrated feed solution. Due to the higher osmotic pressure of this more concentrated feed solution, the amount of product water recovered by these cartridges is reduced and its salinity is increased. To recover a given amount of product, therefore, a high recovery system will require more membrane cartridges and the quality of the product will be reduced relative to a conventional plant. As membrane costs typically represent one quarter to one third of the capital cost of a system, there is a significant cost premium associated with high recovery ratios.

A further disadvantage associated with high recovery ratios is that membrane cartridges exposed to higher concentration feed solutions require more frequent cleaning and replacement. Depending upon location, feed sea water contains concentrations of ions (such as Sr^{++}, Ca^{++} and Ba^{++}) which, upon further concentration in an RO plant, may precipitate out of the solution and form a scale which clogs the membrane surfaces. As the recovery ratio of an RO plant is increased, the likelihood of this kind of fouling also increases. As the solubility of these ions is increased by reducing the pH of the feed solution, most conventional RO systems include inject acid into the feed sea water to control this kind of fouling. Coagulating agents are also injected into the feed sea water to ensure that colloidal particles not removed by prefiltration do not foul the membranes. Since the concentration of these colloidal particles increases with increasing recovery ratio, the coagulating agent is more critical to high recovery ratio systems. High recovery systems must bear the cost and inconvenience of handling acid and coagulation agents.

1.2 Centrifugal Reverse Osmosis (CRO) Desalination

1.2.1 Conceptual Design of a CRO System

A promising new alternative to conventional RO is centrifugal reverse-osmosis (CRO) desalination. In CRO, process pressure is developed within a centrifuge rotor rather than with a high pressure feed pump. As in a conventional RO system, a low pressure feed pump draws feed sea water from the intake and forces it through prefilters which remove impurities which would, otherwise, foul the reverse-osmosis membranes, as shown in Figure 1.10. The filtered sea water then flows, at low pressure, into the spinning rotor at its axis via a rotary coupling. From the rotor axis, the sea water flows outward through radial passages to a membrane configuration at the periphery of the rotor. Rotor speed and radius are chosen so that process pressure is achieved in the membrane configuration. As the high pressure feed passes through the membrane configuration, the fresh water permeate is produced and then released from the rotor at its periphery. The remaining high pressure brine which is exhausted from the membrane cartridge is depressurized as it returns to the axis through radial passages, and then exits the rotor at low pressure via a rotary seal.

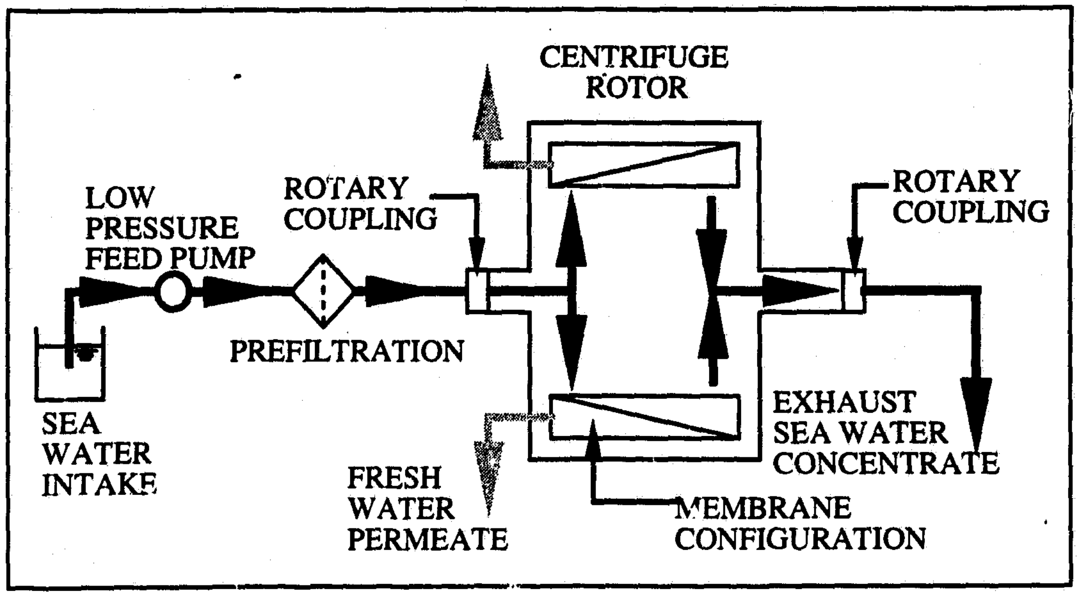

Figure 1.10 - Schematic of a Centrifugal Reverse-Osmosis Desalination System

1.2.2 The Potential Benefits of CRO

Without developing this conceptual design for a CRO system any further, it is apparent that CRO offers a number of potential benefits relative to conventional RO. The most important of these potential benefits is that the energy of the exhaust brine is recovered without the addition of an auxiliary turbine. The feed sea water enters the rotor axis at low pressure, relative to process pressure, and the exhaust brine exits the rotor at low pressure. The pressure drop from inlet to outlet is small compared with process pressure and is dictated by losses in the flow passages within the rotor. Energy recovery is, thus, an inherent rather than an optional feature of a centrifugal reverse osmosis system.

Another potential benefit of CRO is reliability. This reliability is derived from the absence of a high pressure feed pump. As is discussed Section 1.1.6, a major source of unreliability in a conventional reverse-osmosis plant is the high pressure feed pump and, in particular, its high pressure dynamic seals. The only dynamic seals in a centrifugal design are low pressure rotary seals at rotor inlet and outlet. Conventional mechanical seals provide reliable service in this sort of application.

Low levels of noise and vibration should also be characteristic of a centrifugal design. The high levels of noise and vibration of a reciprocating piston pump result from its inherently unbalanced design. Although the imbalance of a centrifuge rotor cannot be entirely eliminated, it can be controlled with dynamic balancing.

With respect to the membranes, CRO offers significant potential for the reduction of initial membrane requirements and membrane cleaning and replacement. As is discussed in Section 1.1.6, the wasted energy of the exhaust brine leads designers of conventional RO systems to specify plants having high recovery ratios (30% - 40%). Higher recovery ratios, however, lead to increased rates of membrane fouling and, as a result, reduced membrane life and more frequent membrane replacement. In addition, high recovery RO systems require more extensive pretreatment capabilities and for a given product flow rate, more membrane cartridges. Unlike a conventional RO system, however, there is no energy penalty associated with a low recovery ratio in a CRO system. Since the energy of the exhaust brine is recovered, the flow rate of the exhaust brine is of little consequence. A CRO plant can, therefore, operate at a low recovery ratio without incurring the energy penalty to which a conventional plant is subject. The number of membranes, the requirement for cleaning and replacement and the need to pretreat the feed sea water are reduced accordingly.

In either conventional or centrifugal RO, it is essential that the membrane surface remain unblocked and, thus, the removal of particles that could potentially block or "foul" the surface is of primary concern. This is accomplished by prefiltration of the feed stream and, in addition, by the turbulent action of the flow of the feed stream across the membrane surface.

CRO offers an additional means with which to combat both fouling and concentration polarisation. The membrane configuration, within a CRO rotor, could be constructed so that the feed sea water flow paths would be of a geometry and orientation, relative to the axis of rotation, such that suspended particles would be stripped away from the membrane surface by differential density separation. Concentration polarisation would also be addressed by this development as high concentration and, therefore, high density brine adjacent to the membrane would also be stripped away by differential density separation. Minimization of membrane fouling and concentration polarisation would lead to enhanced membrane performance and membrane life.

A less concrete but, nonetheless, promising benefit of CRO is its inherent simplicity. In CRO, the high pressure feed pump, membrane cartridge array and energy recovery turbine of a conventional RO plant are integrated into a single component, the rotor. If this conceptual simplicity can be retained in a functional design, the result will be low cost of manufacture and reliability of operation. The potential benefits of CRO are summarised in Table 1.2.

	CONVENTIONAL RO	CENTRIFUGAL RO
ENERGY CONSUMPTION	• Pressure energy of exhaust brine is wasted. • Additional capital cost and complexity of energy recovery turbine justified only for very large systems.	• Recovery of pressure energy of exhaust brine is an inherent feature of centrifugal reverse osmosis
RELIABILITY	• High pressure pump often a source of breakdown particularly dynamic high pressure seals. • High pressure piping requires exotic alloys to minimize corrosion.	• Simple design having only a single moving part • No dynamic high pressure seals. • Non-metallic construction, hence no corrosion problems
INITIAL AND REPLACEMENT MEMBRANE COSTS	• Operate at high recovery ratio in order to minimize power consumption. • High recovery ratio requires more initial membranes and reduces membrane life.	• Operate at low recovery ratio as energy consumption is independent of recovery ratio. •Low recovery ratio requires fewer initial membranes and replacement is less frequent.
DESIGN SIMPLICITY AND COST OF MANUFACTURE	• Complex high pressure pump and energy recovery turbine. • Expensive components which must be purchased from outside sources.	• Simply designed, single rotor integrates the high pressure pump, membrane array and the energy recovery turbine into a single component.
NOISE AND VIBRATION	• Vibration of reciprocating piston pumps can lead to failure of other components. • Noise levels which necessitate extensive abatement measures in Naval applications	• Rotors can be balanced to fine tolerances leading to low levels of noise and vibration.

Table 1.2 - The Potential Benefits of Centrifugal RO

1.3 Survey of Relevant Literature

Extensive searches have yielded only seven patents and no papers which bear directly on CRO. The design concepts described in four of these seven patents are based on fundamental misconceptions with respect to the operating principles of CRO and, therefore, are not implementable.

In the earliest patent, Huntington (1967) [7], identifies the potential of centripetal acceleration to reduce membrane fouling but suggests a design in which process pressure is developed by a high pressure feed pump rather than in the centrifuge itself. Grenci (1968) [8] is the first to suggest that process pressure be developed in the centrifuge and to identify the potential energy savings of a centrifugal system. Four subsequent patents are, as mentioned above, fundamentally flawed. Loeffler (1971) [9] modifies Grenci's design to provide for back-flushing of the membrane. This is accomplished with an impractical array of solenoid valves, slip rings and rotary seals. Berriman (1972 and 1975) [10, 11] contributes some interesting ideas with respect to the deployment of the membranes in the rotor but clearly fails to grasp the principle of a radial pressure gradient in a centrifuge. In his first patent [10], Berriman places the concentrate outlet at the rotor periphery, thus eliminating the recovery of energy from the concentrate. In his second patent [11], Berriman corrects this error by bringing the concentrate outlet back to the rotor axis. Unfortunately, he also returns the permeate outlet to the axis, thus eliminating the pressure difference across the membrane. The final of these four, Keefer (1980) [12] proposes a remarkable and completely unnecessary array of rotors and impellers to achieve energy recovery. It is apparent that neither Loeffler, Berriman nor Keefer constructed a functional unit. The most recent patent, Siwecki (1982) [13], proposes a design which, although, not as fundamentally flawed as its four predecessors, still fails to address the critical issues of rotor windage and pressure gradient.

Nowhere in these patents are the potential benefits of CRO, as delineated in Table 1.2, identified. Energy savings and reduced membrane fouling are discussed but the important issues of reduced membrane requirements, increased membrane life, reliability, noise and vibration, and design simplicity are entirely omitted.

In addition to these patents, there are papers which, although not relating to CRO in general, contain information which is relevant to specific aspects of the design of a CRO system. These are dealt with, in turn, in the context of the relevant chapters of this dissertation.

1.4 Scope of the Dissertation

The objective of the author's research has been to develop a practical design for a CRO system which realizes all of the potential benefits of CRO, as listed in Table 1.2. The initial research was in the form of a preliminary feasibility study which established the fundamental principles of CRO and identified the aspects of a CRO system which were likely to present the greatest design difficulty. A conceptual design for a functional CRO system was developed, incorporating features which addressed these aspects of the design. The findings of this study are presented in Chapter 2.

The preliminary feasibility study led to the development, design, construction and testing of a first prototype unit. This unit verified that the fundamental principles of CRO and the conceptual design, as identified in the feasibility study, were essentially sound. U.S. and

Canadian patents covering the enabling features of the design for this first prototype were issued to the author (see Appendix I and [14]). The development of a second prototype followed and the emphasis shifted toward optimization and refinement with respect to cost of manufacture and long term reliability. Subsequent to successful long-term land-based operation, this unit was installed aboard the CFAV St. Anthony where operational testing continues. Significant design features and performance data for the first and second prototypes are described in Chapter 3.

The operational performance of the first and second prototypes indicated areas in which significant improvement was required if the potential energy savings of CRO were to be fully achieved. Of particular concern were power consumption due to rotor windage losses and due to fluid flow losses through the rotor. Detailed experimental and computational studies of these losses were, therefore, undertaken. Chapter 4 discusses experimental and computational findings with respect to rotor windage. Chapter 5 reports experimental analyses of the flow losses in the feed flow-path through the centrifuge rotor. A relationship between two non-dimensional groups describing these losses and a critical modification to the second prototype design are determined.

One of the more difficult aspects of the design of the second prototype rotor was the specification of the outer filament wound composite shell. In order to assist in the optimization of this component in future designs, a method for the analysis of the stresses and deformations in this shell is developed. This method is based on the theory of elasticity for anisotropic materials. The details of this method and the findings for some specific cases are reported in Chapter 6.

Based on the experience with the first and second prototypes and the work detailed in Chapters 4 and 5, projections of the economics of CRO and a comparison with the economics of conventional RO are performed. The principal findings of this study are that CRO is, in general, more economical than conventional RO and that this advantage increases as system capacity increases. The method and findings of this analysis are presented in Chapter 7.

References

1. Stehling, K.R., Water: the Ocean's Greatest Resource, Sea Technology, June 1993, p. 105.

2. Freitas, R.A., Investing in Water, Special Report No. 104, Value Forecaster, Pilot Hill, CA.,.July 1991.

3. International Desalination Association Newsletter, May 1992

4. Leitner, G.F., Economic Feasibility of Reverse-Osmosis Process for Sea water Desalination, Desalination (Elsevier), 63, 1987, pp. 135-142.

5. Wangnick, K., 1990 International Desalination Association Worldwide Desalting Plants Inventory, Report No. 11, Topsfield MA.,May 1990

6. Desalination Systems Inc., Product Literature, Escondido Ca.

7. Huntington, M.G., Centripetal Acceleration Method and Apparatus, U.S. Patent No.3,355,382, 1967

8. Grenci, C.A., Centrifugal Reverse-Osmosis for Desalination, U.S. Patent No. 3,400,074, 1968.

9. Loeffler, R.L., Reverse Osmosis Apparatus, U.S. Patent No.3,567,030, 1971.

10. Berriman, L.P., Fluid Separation Method and Apparatus, U.S. Patent No. 3,669,879, 1972.

11.Berriman, L.P., Filtering Apparatus and Method, U.S. Patent No. 3,879,286, 1975.

12. Keefer, B.G., Rotary Reverse Osmosis Apparatus and Method, U.S. Patent No. 4,230,564, 1980

13. Siwecki, T.L., Andeen, G.L., Rotating Solution Separation System, , U.S. Patent No.4,333,832, 1982

14. Wild, P.M., Vickers, G.W., Moilliet, A., Hopkin, D.A., Centrifugal Reverse-Osmosis Desalination Unit, Canadian. Patent No.1,290,700, 1991.

Chapter 2
A Practically Feasible Design for CRO Incorporating Novel Design Solutions

2.0 Preliminary Feasibility Study

The author's development of CRO began with a preliminary study which addressed the issue of feasibility. This study consisted of both theoretical and experimental investigations intended to establish the fundamental operating principles of centrifuges and the application of these principles to CRO. Features which were expected to present design difficulties were identified and assessed for their potential impact on feasibility. Where these features were found to compromise the feasibility of CRO, novel design solutions were proposed and evaluated. The feasibility of CRO incorporating these solutions was then assessed and found to have significant advantages with respect to conventional RO. These solutions form the core of the U.S. and Canadian Patents granted to Wild et al (see Appendix I and [1]).

2.1 Survey of Literature Relevant to Centrifuge Design

With respect to the fundamental principles of centrifuge design, there is only a small body of literature as the majority of design data is retained "in-house" by centrifuge manufacturers. Furthermore, as the operating principles of CRO are fundamentally different than any existing centrifuge application, little of this small body of literature is relevant to CRO. Existing centrifuge applications are, almost exclusively, separation processes based on density differentials. These applications generally fall into one of three categories: gas/gas, liquid/liquid and liquid/solid separation. The majority of the literature related to centrifuge design focuses on the relative movement of these solution components under the influence of centrifugal action. In CRO, separation is driven strictly by pressure and, although a density differential can affect the process, it is not the driving force behind the process. As a result, little of the literature related to centrifuge design is applicable to CRO.

There are, however, two important design considerations, which are discussed in general terms in the literature: rotor windage and fluid flow losses [2]. These considerations are applicable to a wide range of centrifuge configurations, including CRO. Rotor windage is friction between the outer surface of the rotor and the surrounding air. Depending upon the operating speed and the diameter of the rotor, windage can be a significant component of the energy consumption of a centrifuge. For any continuous-flow centrifuge, there are losses associated with the flow of fluid through the centrifuge rotor. These losses will impact on the efficiency of CRO.

Beyond this small body of literature related to centrifuge design in general, there is literature related to the design of turbomachinery. Some of this has application to the design of a CRO system and is discussed in some detail in Chapters 4 and 5.

2.2 Membrane Configurations for CRO

The most fundamental component of the development of CRO is the specification of a membrane configuration to be incorporated into a CRO rotor. Two general categories of membrane configurations are considered here. The first, shown in Figure 2.1(a), is an array of commercially available cylindrical membrane cartridges, either spiral wound or hollow fine fibre, spaced evenly about the periphery of the rotor. This will be referred to as the "gattling gun" design. The second, shown in Figure 2.1(b), is a single annular cartridge which occupies the space at the rotor periphery.

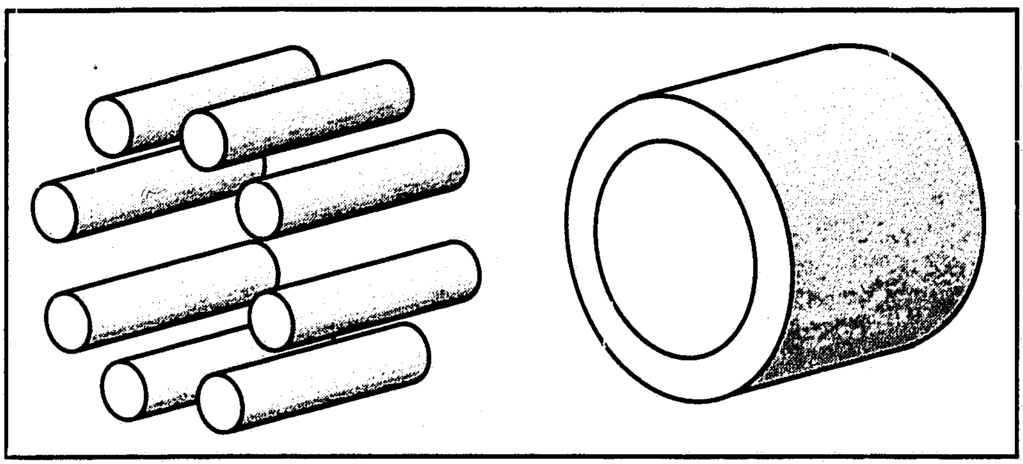

Figure 2.1 - Gattling Gun and Annular Membrane Configurations

Whether an annular or gattling gun design, the membrane configuration for CRO, is subject to conditions not experienced by the membrane configuration in a conventional RO plant. The centripetal acceleration of membrane, fresh water and sea water presents both problems and opportunities to the designer. In addition, therefore, to the constraints affecting the design of membrane configurations for conventional RO, there are constraints which affect the design of a membrane configuration specifically for CRO:

1. There is a radial pressure gradient which determines where, within a centrifuge rotor, a membrane configuration can be located.
2. In addition to pressure forces, the membrane configuration and its support structure must withstand the forces of centripetal acceleration.

3. Density gradients on the brine side of the membrane, caused by concentration polarization, will be affected by buoyancy forces due to centripetal acceleration.

2.2.1 Pressure Gradient Within a Centrifuge Rotor

For sea water desalination, the pressure differential across the reverse-osmosis membrane must be between 5.5 MPa (800 psi) and 6.9 MPa (1000 psi). If the pressure differential is less than 5.5 MPa, the salinity of the product water will be unacceptably high and the volume of product water produced will be unacceptably low. If the pressure differential exceeds 6.9 MPa, the membrane is prone to rupture.

Within a spinning rotor filled with sea water, the pressure increases as the square of rotor radius and speed of rotation.

$$P_{sw} = \frac{1}{2}\rho_{sw}\omega^2 r^2 \tag{2.1}$$

For a given CRO rotor operating at a fixed speed, there is an annular band within which the pressure in the sea water passages is between of 5.5 MPa and 6.9 MPa. The membrane configuration is, therefore, confined to this annular band. The ratio of the inner to outer radii of this annular band is a constant, given 5.5 MPa and 6.9 MPa at the inner and outer edges respectively.

$$\frac{r_{mc}^{in}}{r_{mc}^{out}} = \sqrt{0.8} \tag{2.2}$$

For any given rotor diameter and speed, a maximum of twenty percent of rotor volume is available for the membrane configuration and the maximum radial thickness of the membrane configuration is specified completely by rotor speed. These considerations are a significant constraint upon the design of a CRO rotor.

Consider a "gattling gun" design incorporating standard spiral wound membrane cartridges. These cartridges are manufactured in three diameters: 6.35, 10.15 and 20.3 cm. The rotor speeds for which the widths of the annular band are equal to the cartridge diameters are 1865, 1166 and 583 RPM respectively, as shown in Figure 2.2. The corresponding outer radii of the annular bands are the minimum allowable radii of rotors incorporating these cartridges, i.e. 0.60, 0.96, and 1.92 m respectively. These minimum rotor radii are conservative as no allowance has been made for rotor structure extending beyond the membrane cartridges themselves. Practically speaking, any rotor incorporating the largest size of membrane cartridge would have to be at least 4 m in diameter.

2.2.2 Forces Associated With Centripetal Acceleration

Conventional membrane cartridges are not, in and of themselves, pressure vessels. They are constructed so as to withstand the internal pressure differential between the feed and the permeate flow paths but the cartridge itself would rupture were it not immersed in pressurized sea water and housed within a pressure vessel. Similarly, membrane configurations for CRO must be immersed in pressurized in sea water.

The density of a membrane configuration for CRO is also an important issue. In the highly accelerated environment within the rotor, any material within the membrane configuration of density substantially greater than water will be subjected to tremendous positive radial forces. Similarly any materials of density substantially less than water will be subjected to tremendous negative radial forces. It is, therefore, important that a membrane configuration for CRO be either neutrally buoyant or, if not, be constructed so as to withstand the resulting forces.

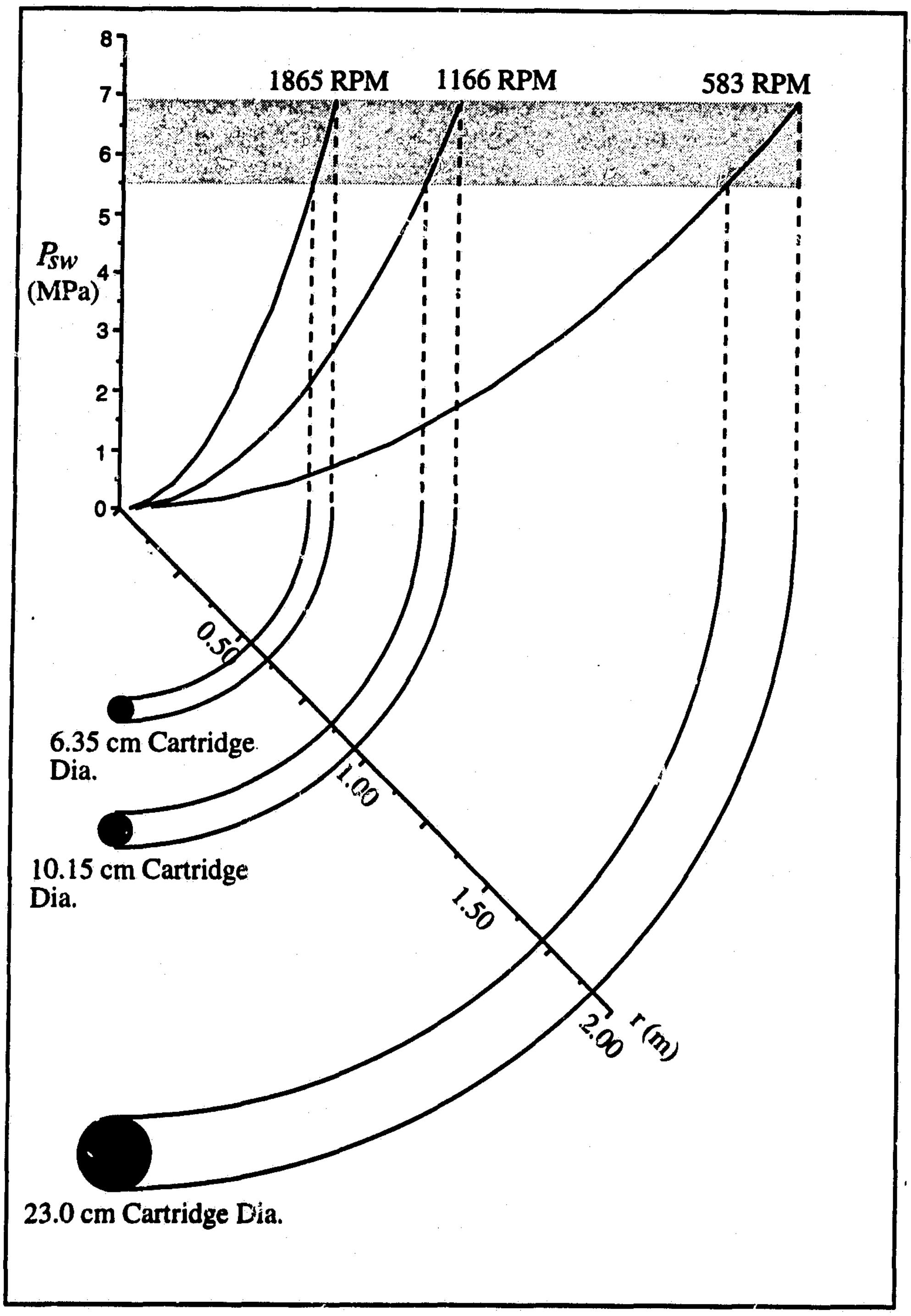

Figure 2.2 - Minimum Radii of Annular Band

In a gattling gun design, the buoyancy may impose a bending load on the membrane cartridges. A typical membrane cartridge has plastic end fittings which seat into the end plugs of the pressure vessels. The span of the cartridge between the end fittings is, however, supported only by the surrounding sea water. Depending whether the cartridge is positively or negatively buoyant, there is a buoyancy load which bends the cartridge either radially inward or radially outward.

2.2.3 Rotor Balance

For either an annular or a gattling gun design, the mass of the membrane configuration, the mass of fluid in which it is immersed and the mass of fluid which is contained within its flow passages must, in total, be dynamically balanced with respect to the axis of rotation of the rotor. Ideally, this condition should be maintained when a membrane cartridge or cartridges are replaced so that the rotor does not require rebalancing after membrane replacement.

2.2.4 The Influence of Centripetal Acceleration on Concentration Polarisation and Fouling

Just as the structure of the membrane configuration in CRO is subject to the considerable influence of centripetal acceleration, so also is the feed sea water solution. In the accelerated condition within a centrifuge rotor, the layer of higher concentration and, therefore, higher density brine next to the membrane surface is susceptible to buoyancy effects. If the sea water side of the membrane faces radially outward, this layer will "sink" away from the membrane, reducing concentration polarisation. If the sea water side of the membrane faces radially inward, this layer will "sink" toward the membrane, increasing concentration polarisation. Eid and Andeen [3] showed that, under the application of 500 g's of acceleration, outward facing membrane experiences a 52 % reduction in salt concentration, relative to a static membrane. Associated with this diminished salt concentration is a 21 % increase in product flow. Inward facing membrane experiences a 95 % increase in salt concentration. The acceleration in a functional CRO unit will be at least 1000 g's.

Within the membrane cartridges of a "gattling gun" configuration, those membrane surfaces which are oriented radially outward will benefit and those membrane surfaces which are oriented radially inward will suffer from the effect of acceleration on concentration polarisation.

There is potential for the development of membrane cartridges, specifically for incorporation into a centrifuge in which a "self scouring" effect could be created which would minimize both fouling and concentration polarization. Within these annular membrane cartridges, the feed flow paths would be of a geometry and orientation, relative to the axis of rotation, such that suspended particles would be stripped away from the membrane surface by centrifuge action, as shown in Figure 2.3. Brine layers of high concentration and, therefore, high density adjacent to the membrane would also be stripped away by the same centrifuge action, thus, minimizing the effects of concentration polarization. Minimization of membrane fouling and concentration polarization would lead to enhanced membrane performance and lifetime. Such a development would have a significant impact on the overall process cost of existing membrane separation applications, such as sea water RO and would, furthermore, open up new applications in which fouling and concentration polarization currently prevent practical implementation.

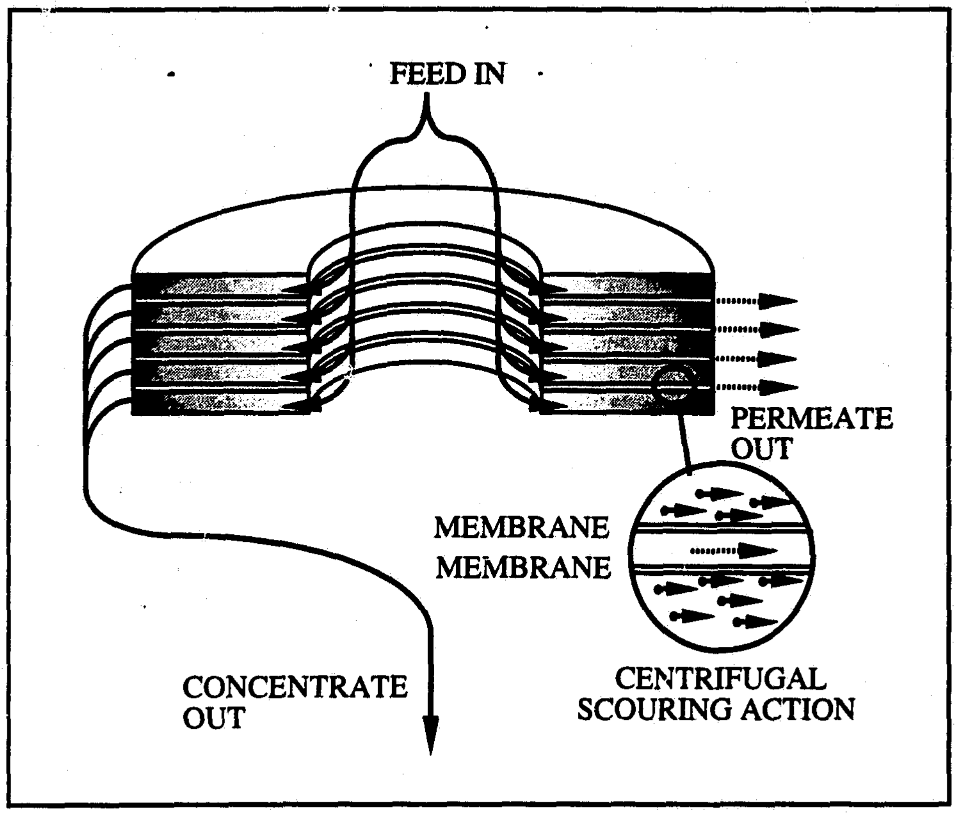

Figure 2.3 - Centrifugal Scouring Action

There are several examples of membrane configurations of the annular type in the patent literature. Berriman [4], [5] and Keefer [6] both describe membrane configurations of the annular type. However, each of these designs is, in some regard, flawed. The membrane configurations proposed by Keefer occupy only a small fraction of the available space within the rotor. The potential for increased productivity from a given size of rotor is, therefore, not capitalized upon (see Section 2.2.5). The various membrane configurations described by Berriman employ flow patterns which waste rather than recover the energy of the exhaust brine.

The author has filed Canadian and US Patent applications of designs for CRO which realize the potential benefits of a membrane cartridge as detailed above.

2.2.5 Volumetric Efficiency of Membrane Configurations for CRO

For the purposes of this discussion, a standard rotor design is adopted, as shown in Figure 2.4. The model is applicable to either the annular or to the gattling gun membrane configuration. Rotor diameters and speeds are selected so that the sea water pressure at the inner and outer edge of the annular band which contains the membrane configuration are 5.5 MPa (800 psi) and 8.3 MPa (1200 psi) respectively.

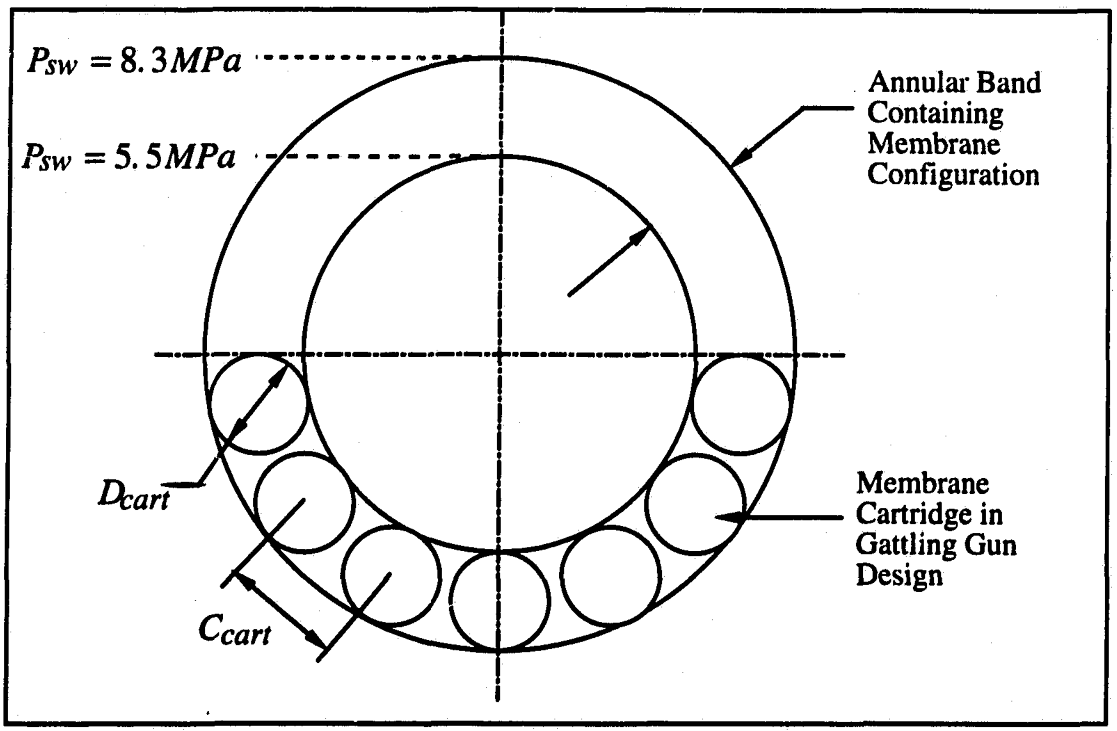

Figure 2.4 - Standard Model of CRO Rotor

As is discussed in Section 2.2.1, this higher pressure exceeds the allowable maximum but, based on the development described in Section 2.5.1, this difficulty can be circumvented. It is assumed that there is no support structure beyond the annular band and, therefore, the length and diameter of the rotor are taken as equal to the length and diameter of the annular band. The rotor is assumed to have a square profile, that is the length is equal to the diameter.

For a given diameter of rotor operating at a given speed, the percentage of rotor volume which can be occupied by productive membrane is significantly larger for an annular cartridge design than for a gattling gun design. The volumetric efficiency of the membrane configuration, η_{mc}, is here defined as

$$\eta_{mc} = \frac{N_{cart} V_{cart}}{V_{amc}} \tag{2.3}$$

Thus, $\eta_{mc} = 1$ for an annular design.

For a gattling gun design η_{mc} is a function of both the number of cartridges and of the cartridge center spacing, C_{cart}, as shown in Figure 2.5. The solid curve is the case where there are no gaps between adjacent membrane cartridges. The lower curves are cases where each membrane cartridge is spaced away from its neighbors by as much as a full cartridge diameter, in the case of the lowest curve. The solid curve, shows that the best possible efficiency for a gattling gun design is less than eighty percent of the efficiency of annular design. The efficiency decreases strongly as the spacing between adjacent cartridges increases and, particularly for $N_{cart} < 10$, as the number of membrane cartridges decreases.

Assuming that an annular membrane configuration has the same area of membrane material per unit of configuration volume as the individual membrane cartridges in a gattling gun design, a gattling gun design will require a larger diameter rotor to achieve the same product flow rate as an annular design.

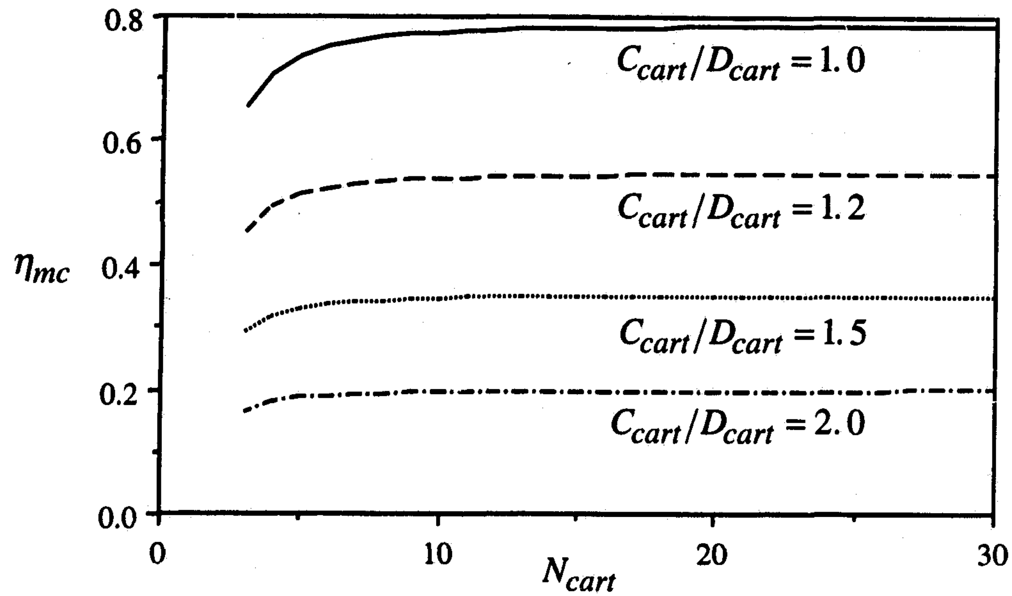

Figure 2.5 - Membrane Configuration Volume Ratio

2.3 Ideal Energy Savings of CRO Relative to RO

Consider the idealized continuous flow centrifuge rotor shown in Figure 2.6. The rotor is rotating with a constant angular velocity, ω, and is subjected to a drive torque, Γ_D. There is a flow in, at the axis, of Q_f at pressure P_{in}, and an equal flow out, also at the axis at pressure P_{out}. It is assumed, for the moment, that there are no frictional losses, external to the rotor, which are retarding its rotation. It is also assumed that the inlet and outlet flows are sufficiently close to the axis of rotation that the angular momentum of these flows is negligible.

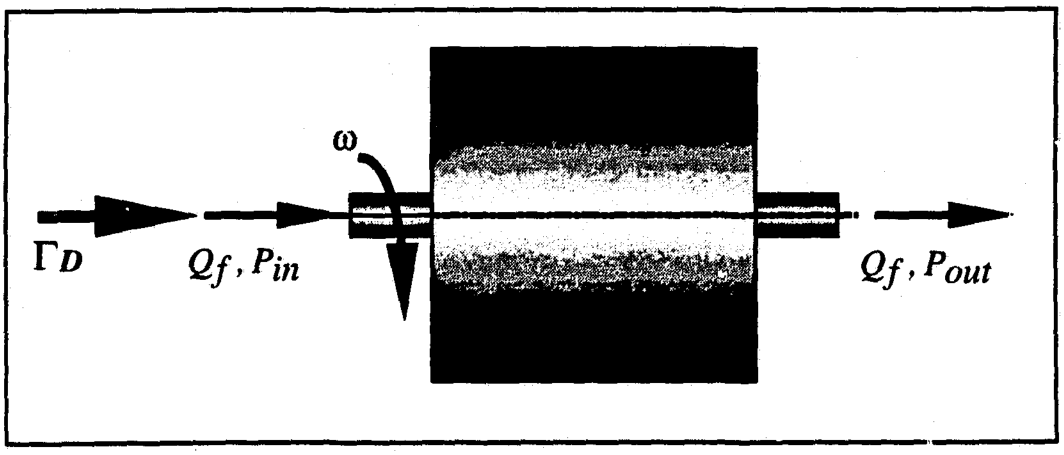

Figure 2.6 - Continuous Flow Centrifuge - Axial Inlet and Outlet

By conservation of angular momentum,

$$\Gamma_D = 0 \tag{2.4}$$

It is important to note that this statement is true regardless of the nature of the flow paths inside the centrifuge rotor. The pressure drop through the rotor is a function of the flow paths inside the rotor and of the flow rate, Q_f. In the absence of a driving pressure, that is if,

$$P_{in} - P_{out} = 0 \tag{2.5}$$

then there is no flow through the rotor.

Now consider the case where the flow is released from an orifice at a radius, R_{exit}, and that the orifice is aimed so as to direct the resulting jet in an axial direction, relative to the rotating frame of reference, as shown in Figure 2.7. Conservation of angular momentum for this case yields,

$$\Gamma_D = \rho Q_f \omega R_{exit}^2 \tag{2.6}$$

where, ρ, is the density of the fluid and drive power consumption, P_D, is simply,

$$P_D = \rho Q_f \omega^2 R_{exit}^2 \tag{2.7}$$

This expression for power does not describe cases where the outlet orifice is aimed so as to give the resulting jet a tangential component, relative to the rotating frame of reference.

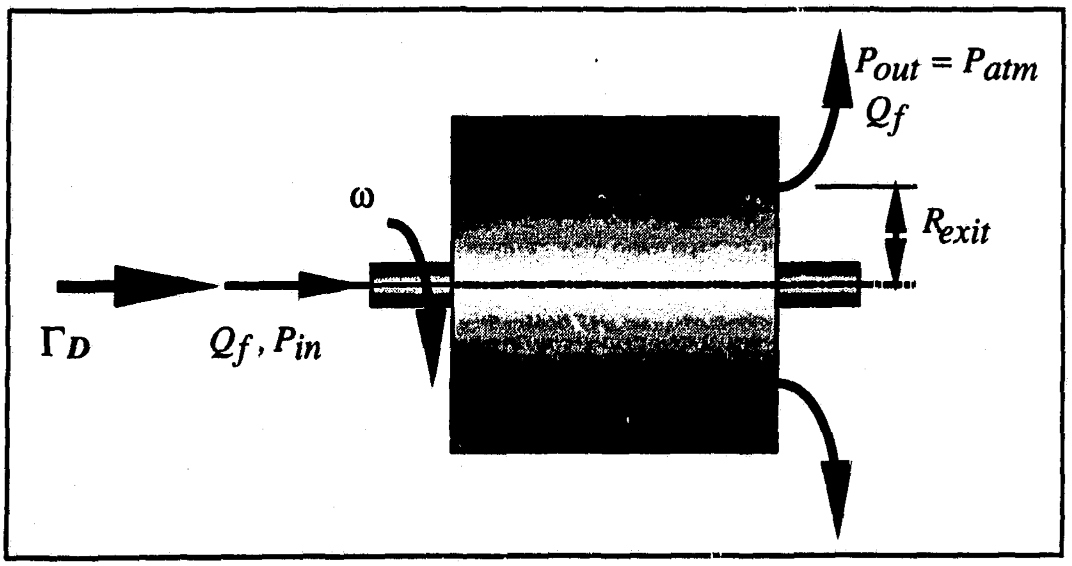

Figure 2.7 - Continuous Flow Centrifuge - Axial Inlet and Radially Displaced Outlet

Now consider the case where the flow at the exit is divided between a flow from the axis, $(1 - X) \cdot Q_f$, and a flow from an orifice, $X \cdot Q_f$, at the rotor periphery, as shown in Figure 2.8. As in the last case, the orifice is aimed so as to direct the resulting jet in an axial direction, relative to the rotating frame of reference.

Again, using conservation of angular momentum, the torque and power requirements are,

$$\Gamma_D = \rho X Q_f \omega R_{exit}^2 \tag{2.8}$$

$$P_D = \rho X Q_f \omega^2 R_{exit}^2 \tag{2.9}$$

As in the preceding case, this expression for power does not describe cases where the outlet orifice is aimed so as to give the resulting jet a tangential component, relative to the rotating frame of reference.

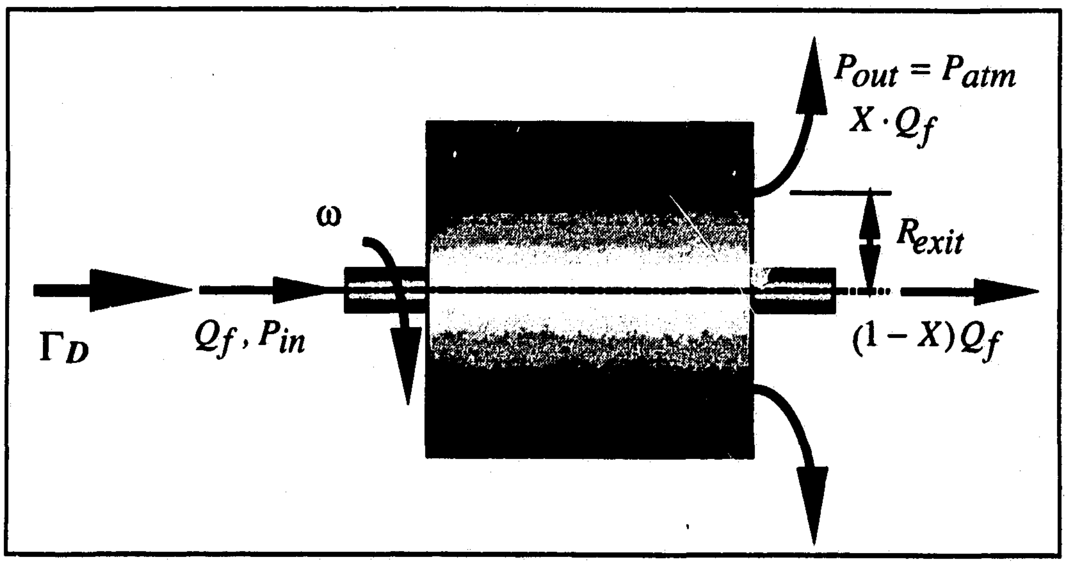

Figure 2.8 - Continuous Flow Centrifuge - Axial Inlet and Combined Axial and Radially Displaced Outlet

Now, consider a simple model of a CRO rotor, as shown in Figure 2.9. Assume that there is a single cylindrical layer of membrane within the rotor whose radius is equal to the exit radius of the fresh water permeate, R_{exit}. The fraction of the feed sea water which is converted to fresh water is the recovery ratio, RR, which corresponds to the fraction X, used in the preceding discussion.

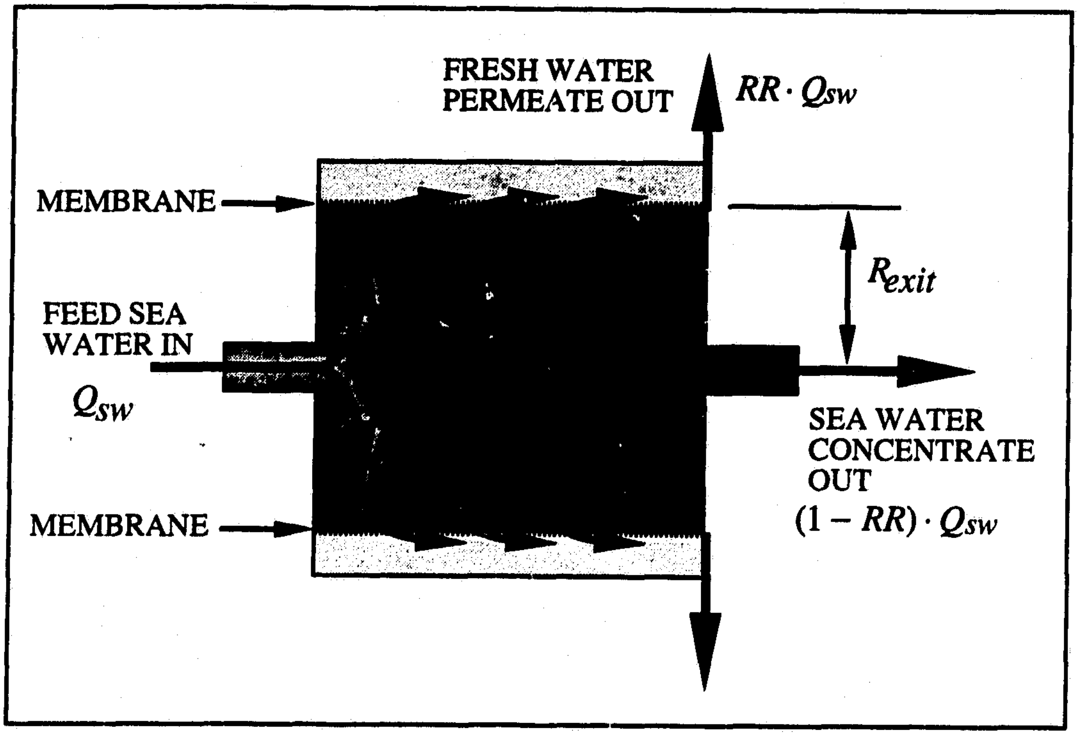

Figure 2.9 - Section of a Simplified CRO Rotor Incorporating a Single Layered Cylindrical Membrane

The angular velocity of the rotor is such that process pressure, P_p, is developed in the sea water on the surface of the membrane which faces toward the rotor axis. For the general case, the pressure, P, developed within a solid spinning disc of fluid is,

$$P = \frac{1}{2}\rho_f \omega^2 r^2. \tag{2.10}$$

For this case then, the process pressure, P_p, can be expressed as,

$$P_p = \frac{1}{2}\rho \omega^2 R_{exit}^2 \tag{2.11}$$

The fraction, RR, of the sea water which passes through the membrane as fresh water drops to a pressure only slightly above atmospheric pressure as a result of passing through the membrane. This fresh water is then released to atmosphere through an orifice, located adjacent to the fresh water side of the membrane. As the pressure drop across the orifice is negligible, the fresh water issues from the orifice with negligible velocity, relative to the rotating frame of reference. Orifice orientation is not important in this case.

Referring to equation 2.9, the power consumption of this process is,

$$P_D = \rho RRQ_{sw}\omega^2 R_{exit}^2 \tag{2.12}$$

Substituting 2.11 into equation 2.12, we obtain the following expression for the ideal power consumption of CRO,

$$P_D = 2\,RRQ_{sw}P_p \tag{2.13}$$

or

$$P_D = 2Q_{fw}P_p \tag{2.14}$$

In a conventional RO system, all of the feed sea water is elevated to system pressure and, in the absence of an energy recovery turbine, the concentrated sea water is exhausted at high pressure. The power consumption of a conventional RO plant, assuming no losses, is, therefore,

$$P_{conv} = Q_f P_p. \tag{2.15}$$

For sea water RO, the maximum practical recovery ratio is 35% or $X = 0.35$. For this case, the most favourable case for conventional RO, the power consumption of CRO is 70% of the power consumption of conventional RO. For lower recovery ratios, and it will be shown that there are compelling reasons for specifying lower recovery ratios, the power savings of CRO increase.

This is, of course a highly idealised assessment of the energy requirements of conventional RO and CRO. There are electrical, mechanical and fluid flow losses as well as other considerations that must be incorporated into a meaningful comparison of the energy consumption of these two processes.

2.4 Sources of Non-Ideal Power Losses in CRO

In a CRO system there are six sources of power losses which will cause a deviation from the idealised case discussed in Section 2.3: rotor windage, fluid friction along the feed sea water flow path in the rotor, rotor bearing friction, rotary seal friction, inefficiencies in the low pressure feed pump and drive motor inefficiencies. Estimates of bearing and seal friction and losses in the low pressure feed pump and drive motor are available from the manufacturers of these components. Rotor windage and fluid flow losses are more difficult to estimate. To gain an initial understanding of these losses, a used centrifugal cream separator, shown in Figure 2.10 was purchased and a series of experiments conducted.

The Westfalia Model 2004 centrifugal cream separator is a continuous-flow centrifuge. It is a "disc-type" centrifuge, so named for the stack of conical discs contained within the rotor. For density-based liquid-liquid separation, these discs increase the feed flow capacity which can be handled by a centrifuge rotor of a given volume. The interior diameter of the bowl is 0.13 m and the operation speed is 7386 rpm which, for water, yields a maximum pressure of 5.03 MPa (733 psi) at the rotor wall. As the operating pressure for RO is between 5.5 MPa (800 psi) and 6.9 MPa (1000 psi), the operational characteristics of this centrifuge were expected to be relevant to CRO. The experimental set up of the cream separator, shown in Figure 2.11 included a feed pump, pressure gages at the centrifuge inlet and outlet, a flow meter and watt meters measuring power to the centrifuge

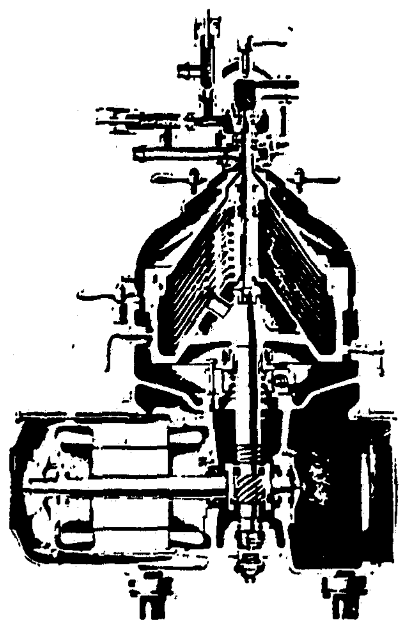

Figure 2.10 - The Westfalia Model 2004 Cream Separation Centrifuge

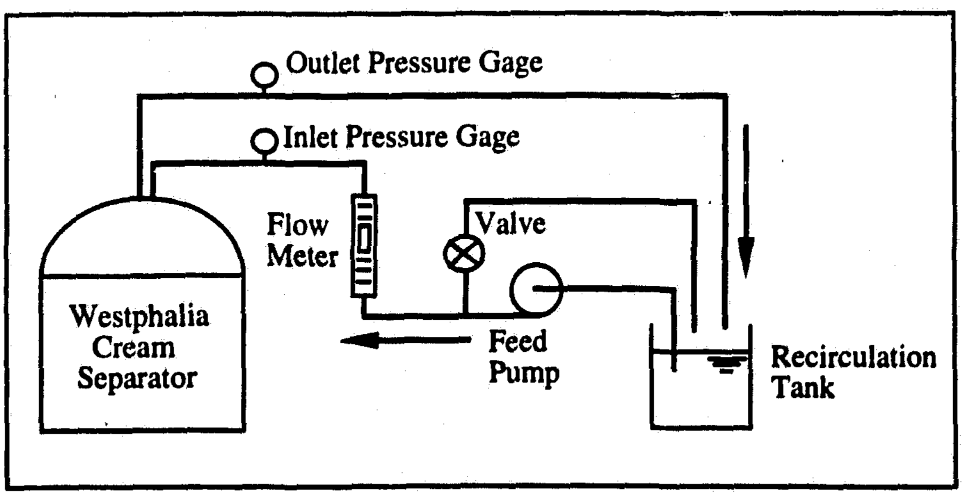

Figure 2.11 - Experimental Set-Up of Cream Separator

2.4.1 Rotor Windage

Tests conducted on the Westphalia centrifuge demonstrated that, in the absence of measures to reduce its effect, rotor windage could be the largest energy loss for a CRO system. With the rotor fully assembled and the rotor enclosure in place, the cream separator consumed 1400 W while, with the rotor removed, the cream separator consumed 540 W. Assuming that the contributions from increased bearing, gear and electrical losses associated with the higher load are relatively small, windage losses are 860 W. With the rotor enclosure removed, the cream separator consumed 1700 W, and windage losses are, therefore, 1140W. Clearly, windage losses are the most significant component of the energy consumption of the cream separator.

In order to obtain an estimate of the windage losses to be expected in an operational CRO unit, the literature was reviewed for a functional relationship predicting windage losses. This review is discussed in detail in Chapter 4. Bilgen and Boulos [7] presents a semi-empirical relation for the windage associated with a rotating cylinder of radius R_i, enclosed in a stationary cylindrical housing where g_r is the radial gap between the rotor and housing.

$$C_{M_{CYL}} = 0.515\, Re^{-0.5}\left(\frac{g_r}{R_i}\right)^{0.3} \qquad Re < 10^4 \qquad (2.16\text{ a})$$

$$C_{M_{CYL}} = 0.0325\, Re^{-0.2}\left(\frac{g_r}{R_i}\right)^{0.3} \qquad Re > 10^4 \qquad (2.16\text{ b})$$

$C_{M_{CYL}}$ is the moment coefficient and Re is the Couette Reynolds Number which are defined as follows:

$$C_{M_{CYL}} = \frac{M_{CYL}}{\pi \rho_{encl} \omega^2 R_i^4 L} \quad (2.17) \qquad Re = \frac{\rho_{encl} \omega R_i g_r}{\mu_{encl}} \quad (2.18)$$

M_{CYL} is the moment due to windage on the cylindrical surface of the rotor, ω is the angular velocity of the rotor, L is the length of the rotor and ρ_{encl} and μ_{encl} are the density and viscosity of the fluid (air) within the rotor enclosure. This relation accounts only for windage due to the outer cylindrical surface of the rotor and does not include windage due to the circular end surfaces of the rotor.

The windage due to these end surfaces can be approximated with Schlichting's [8] relation for the torque experienced by an enclosed rotating thin disc.

$$C_{M_{DISC}} = 0.0622\, \hat{Re}^{-1/5} \quad (2.19)$$

Here, $\hat{Re}$, refers to the Tip Reynolds number which is defined as,

$$\hat{Re} = \frac{\rho_{encl} \omega R_i^2}{\mu_{encl}} \quad (2.20)$$

The moment coefficient for a disc is defined as,

$$\hat{C}_{M_{DISC}} = \frac{M_{DISC}}{\frac{1}{2} \rho_{encl} \omega^2 R_i^5} \quad (2.21)$$

The windage moment associated with the entire rotor is approximated by the sum of the moments calculated for these two regions. This approach assumes that the flow in these two regions do not affect each other to any significant degree.

In order to verify the validity of these relations, windage data taken from the cream separator was compared with calculated values. The cream separator rotor and housing were modified to approximate, as nearly as possible, a simple cylindrical rotor enclosed in a concentric cylindrical housing as shown in Figure 2.12. This modification included the ability to vary the radial gap width. The power consumed by this configuration, at operating speed, was compared with the power consumed by the unit with the rotor removed.

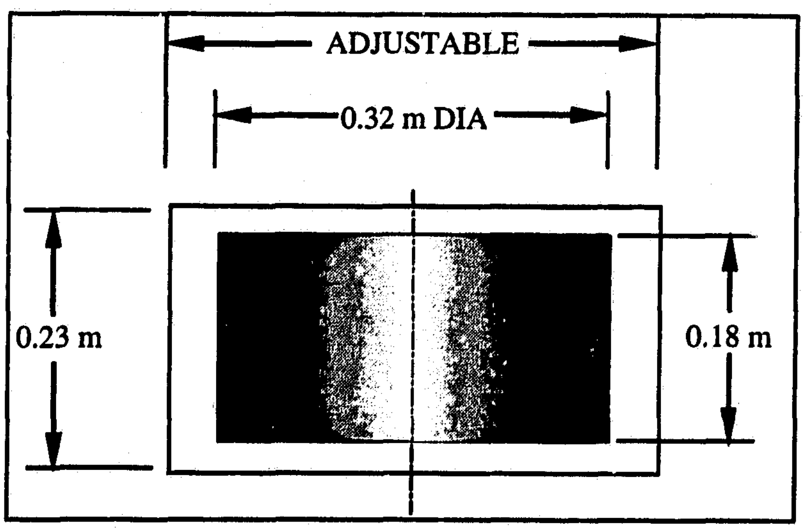

Figure 2.12 - Modified Cream Separator

As above, the difference was assumed to be due entirely to windage. Using the relations of Bilgen and Boulos [7] and of Schlichting [8], the windage due to the modified cream separator rotor were calculated. The calculated and measured data are both shown in Figure 2.13.

The assumptions underlying both the calculated and measured values of windage are rather crude but, at this point, the intention is only to determine the order of magnitude and, therefore, the significance of windage losses. With this in mind, it is apparent from Figure 2.13 that the relations of Bilgen and Boulos [7] and of Schlichting [8] may be used with some confidence to predict the order of magnitude of windage losses to be expected in a CRO system.

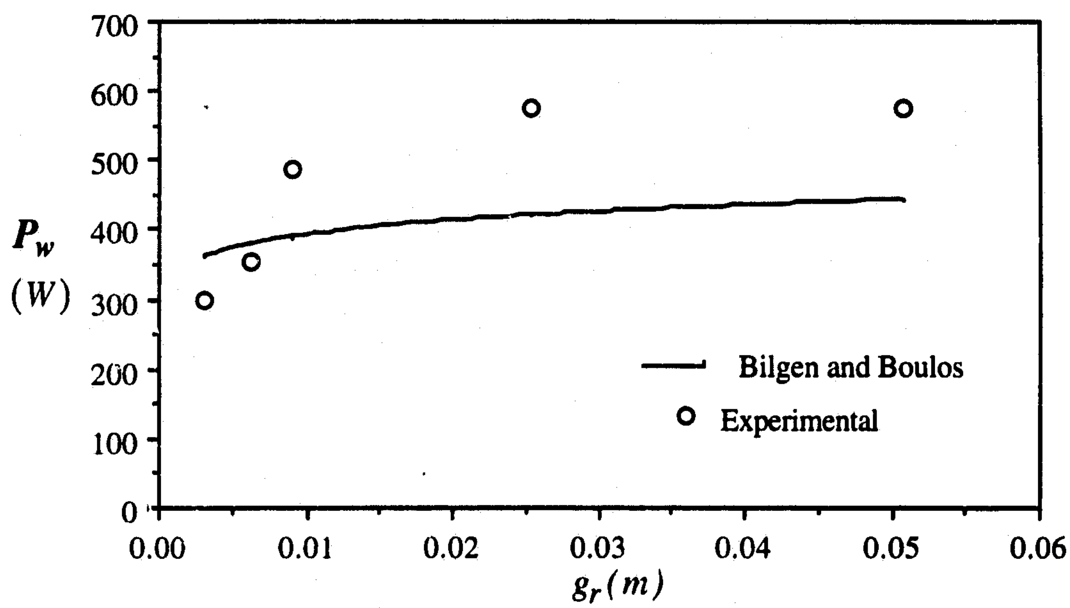

Figure 2.13 - Calculated and Measured Windage Power Versus Radial Gap Width

The magnitude of windage losses associated with a rotor of given physical dimensions and operating at a given speed has no significance in and of itself. It is only as a component of the "Specific Energy Consumption", $\overline{E}$, of a CRO system that windage power takes on any meaning. The specific energy consumption is the energy required to produce a fixed amount of fresh water, measured here in units of kWh/m^3. It is, therefore, critical to know the fresh water production capacity of the rotors for which windage power calculations are to be done.

The standard rotor design described in section 2.2.5 can be used to estimate these capacities. The capacity of a given membrane configuration is assumed to be a linear function of the volume of that configuration. The productivity per unit volume is assumed to be 717 m^3/day of fresh water per cubic metre of membrane configuration. This number is estimated from the specifications for the Filmtec SW30-8040 TFC membrane element.

Based on this standard design with the annular membrane configuration, the specific energy consumption due to windage, $\overline{E}_w$, was calculated for a range of system sizes, as shown in Figure 2.14.

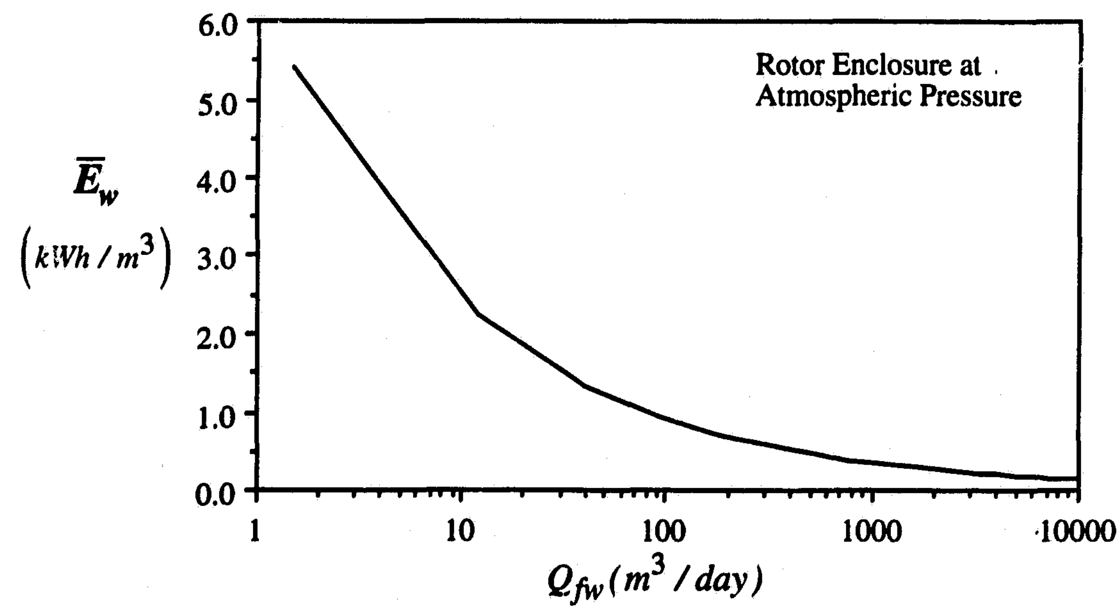

Figure 2.14 - Specific Energy Consumption of CRO due to Windage
(Membrane Cartridges of the Annular Design)

The principal component of CRO energy consumption is expected to be energy to the fresh water (equation 2.14). Expressed as specific energy consumption, this component has a value of 3.06 kWh/m^3 and, unlike windage losses, is not a function of system capacity. The windage losses shown in Figure 2.14 are, for all but the largest systems, significant, relative to the specific energy consumption of the fresh water. It is, therefore apparent that some measures must be taken to reduce windage losses below the levels indicated in Figure 2.14. Alternative windage abatement methods are evaluated in Section 2.5.2.

An important observation about Figure 2.14 is that specific energy consumption decreases as system size increases. This can be explained by consideration of the relationships between key parameters and rotor diameter. As rotor diameter, and system capacity, increase: the peripheral velocity of the rotor remains constant, the area of the outer cylindrical surface of a rotor increases linearly and the volume of productive membrane material which can be accommodated in the annular band increases as the square of rotor diameter. Intuitively and, as substantiated by inspection of the relations of Bilgen, rotor surface area and peripheral velocity are key factors controlling the calculated values of rotor windage. Rotor windage, therefore, does not increase as rapidly as the volume of productive membrane material and, thereby, fresh water capacity. As a result, specific energy consumption due to windage declines with system capacity.

2.4.2 Fluid Flow Losses

As is discussed in Section 2.3, there are losses associated with accelerating the fluid to the periphery of a centrifuge rotor and then returning it to the axis. These losses appear as a pressure drop from the inlet to the outlet of the rotor. It is expected that, for a given flow path within the rotor, these losses will be a function of feed flow rate and of angular velocity of the rotor.

The original flow path within the cream separator rotor was modified, as shown in Figure 2.15, so as to better model the anticipated flow path within a CRO rotor. That is, all feed water must flow to the periphery of the rotor which, in a CRO rotor, is where the membrane would be located and then return to the rotor axis prior to discharge. The original conical disc stack was replaced with two stacks of flat discs separated by a polyurethane foam spacer. The disc stack was intended to ensure tangential acceleration of the fluid as in a shear force pump [9]. Tests were also conducted with the disc stacks removed and the foam spacer in place. Flow configurations incorporating radial passages defined by vanes were not tested due to shortage of time and resources.

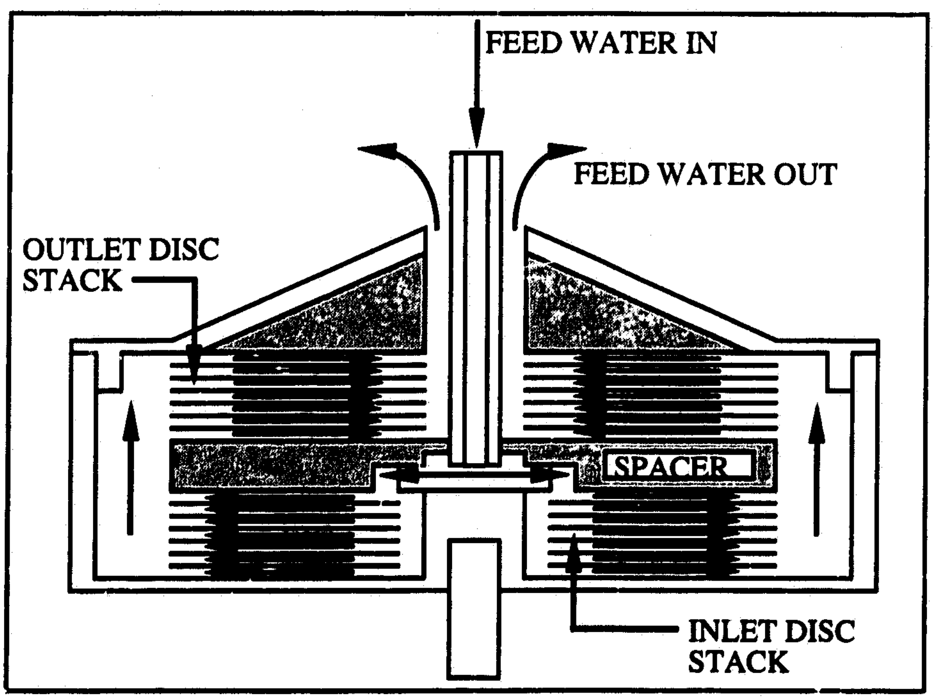

Figure 2.15 - Modified Fluid Flow Path in Cream Separator

The pressure drop across the rotor was measured over a range of flow rates with the rotor at rest and at full speed. The incremental pressure drop, from rest to full speed, was calculated and the results are plotted in Figure 2.16. The controls of the cream separator did not allow for operation at intermediate speeds. The removal of the discs resulted in a slight increase in the incremental pressure drop. Although this is a significant observation, further discussion of this point will be postponed to Chapter 5.

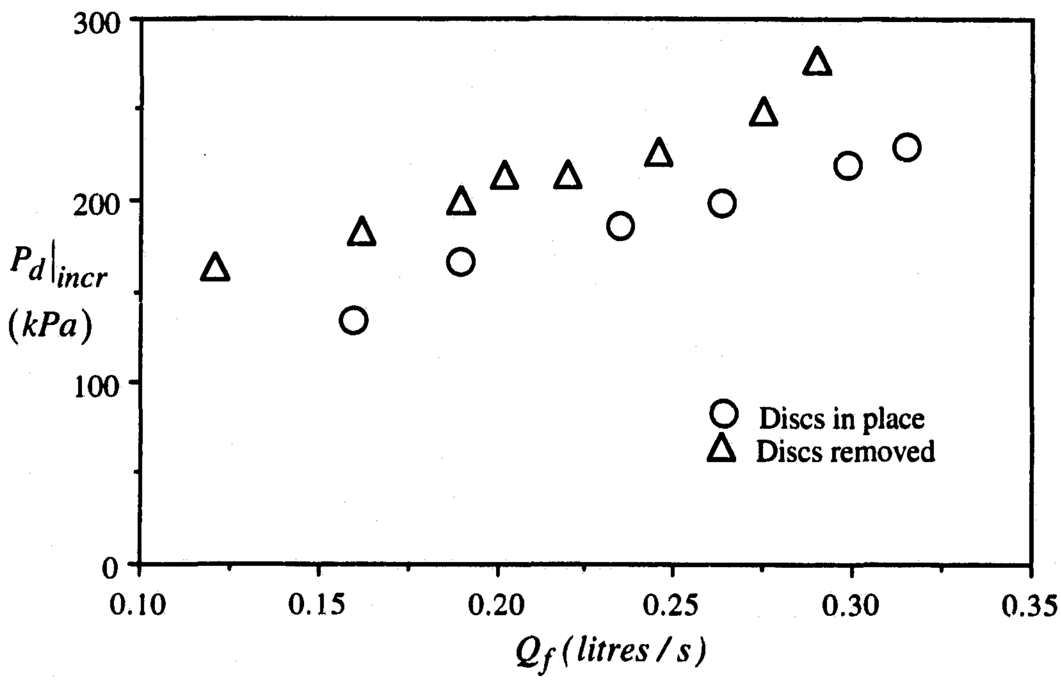

Figure 2.16 - Pressure Drop Across Cream Separator Rotor

In order to assess the significance of these losses in the context of CRO, consider a CRO system operating with the same feed flow rate as the cream separator. Such a CRO system operating with a feed flow of 0.29 litres/s (4.6 gpm) and at a recovery ratio of twenty percent would, in the absence of any losses (equation 2.13), consume 319 W. For a pressure drop across the rotor of 277 kPa (40 psi) the fluid power dissipated across the rotor is 80 W or 25% of the ideal power consumption of the system. To establish an understanding of the sources of these losses, an experimental assessment of fluid flow losses was conducted and the results are reported in Chapter 5.

It should be noted that, as expected, the centrifuge drive power at full speed was unaffected by variations in the feed flow rate for all flow configurations.

2.5 Novel Design Solutions Enabling CRO Feasibility

Many potential difficulties have been identified here which may compromise the feasibility of CRO. Some of these, such as the design of a suitable membrane configuration, have many possible solutions with favourable and unfavourable features associated with each alternative. There are, however, three design problems for which optimal solutions are apparent: provision of a uniform pressure differential, rotor windage abatement, and fresh water removal means.

2.5.1 Provision of a Uniform Pressure Differential

There are significant difficulties associated with the pressure gradient within the rotor of a CRO system, as detailed in Section 2.2.1, but it is possible to overcome these difficulties by the judicious selection of the radius at which the fresh water permeate exits the rotor. The discussion in Section 2.2.1 assumes that the fresh water permeate exits the rotor at a point within the membrane configuration furthest removed from the axis of rotation and that the permeate drains freely through the permeate channels to this point. The pressure on the permeate side of the membrane is, therefore, effectively equal to zero. Alternatively, if the fresh water permeate exits the rotor at a radius coincident with a point in the membrane configuration closest to the axis of rotation, then all of the permeate channels will be flooded with permeate and a "back pressure" will develop within these channels. This back pressure, P_{fw}, will increase with radius from the exit point of the permeate outward, as follows.

$$P_{fw} = \frac{1}{2}\rho_{fw}\omega^2\left(r^2 - R_{exit}^2\right) \quad (2.21)$$

$$\frac{\partial P_{fw}}{\partial r} = \rho_{fw}\omega^2 r \quad (2.22)$$

Neglecting the differences in the densities of sea water and fresh water, the rate of increase of pressure in the permeate channels will be equal to the rate of increase of pressure in the feed sea water channels, P_{sw}.

$$P_{sw} = \frac{1}{2}\rho_{sw}\omega^2\left(r^2\right) \quad (2.23)$$

$$\frac{\partial P_{sw}}{\partial r} = \rho_{sw}\omega^2 r \quad (2.24)$$

The pressure difference across the membrane will, therefore, be constant throughout the membrane configuration.

$$P_{sw} - P_{fw} = \frac{1}{2}\rho_{fw}\omega^2 R_{exit}^2 \quad (2.25)$$

This constant pressure differential will be equal to the pressure in the sea water channels at the inner radius of the annular band, as shown in Figure 2.17.

This design feature releases CRO from the considerable constraints which the pressure gradient within the rotor otherwise imposes. A CRO rotor incorporating this feature can make more than twenty percent of its volume (see section 2.2.1) available for a membrane configuration. In addition, the maximum radial thickness of the membrane configuration is not determined by rotor speed. For the "gattling gun" design, therefore, the pressure gradient no longer determines the minimum rotor diameter for a given diameter of cartridge. For the case of a 23 cm diameter cartridge, the minimum rotor radius was previously 1.92 m (see Figure 2.4). With this novel design feature it is possible to use these cartridges in a much smaller rotor, as shown in Figure 2.17. The outer radius of the rotor in this case is 0.83 m and the maximum absolute pressure in the sea water channels is 9.65 Mpa but the differential pressure across the membrane is only 5.5 Mpa and is constant throughout the membrane cartridge. This is an important feature of the author's patents.

In this discussion the density of sea water has been taken as equal to the density of fresh water. In fact, sea water is about 3% more dense than fresh water. For actual design calculations, therefore, this difference should be taken into consideration.

2.5.2 Rotor Windage Abatement

Three approaches to rotor windage abatement are investigated:

1. Adjustment of the radial gap width between the rotor
2. Operation of rotor in Helium filled enclosure
3. Operation of rotor in evacuated enclosure

The relations of Bilgen and Boulos [7] and of Schlichting [8] are used throughout these studies. The standard rotor design, developed in section 2.2.5, provides the necessary geometry and system capacity data.

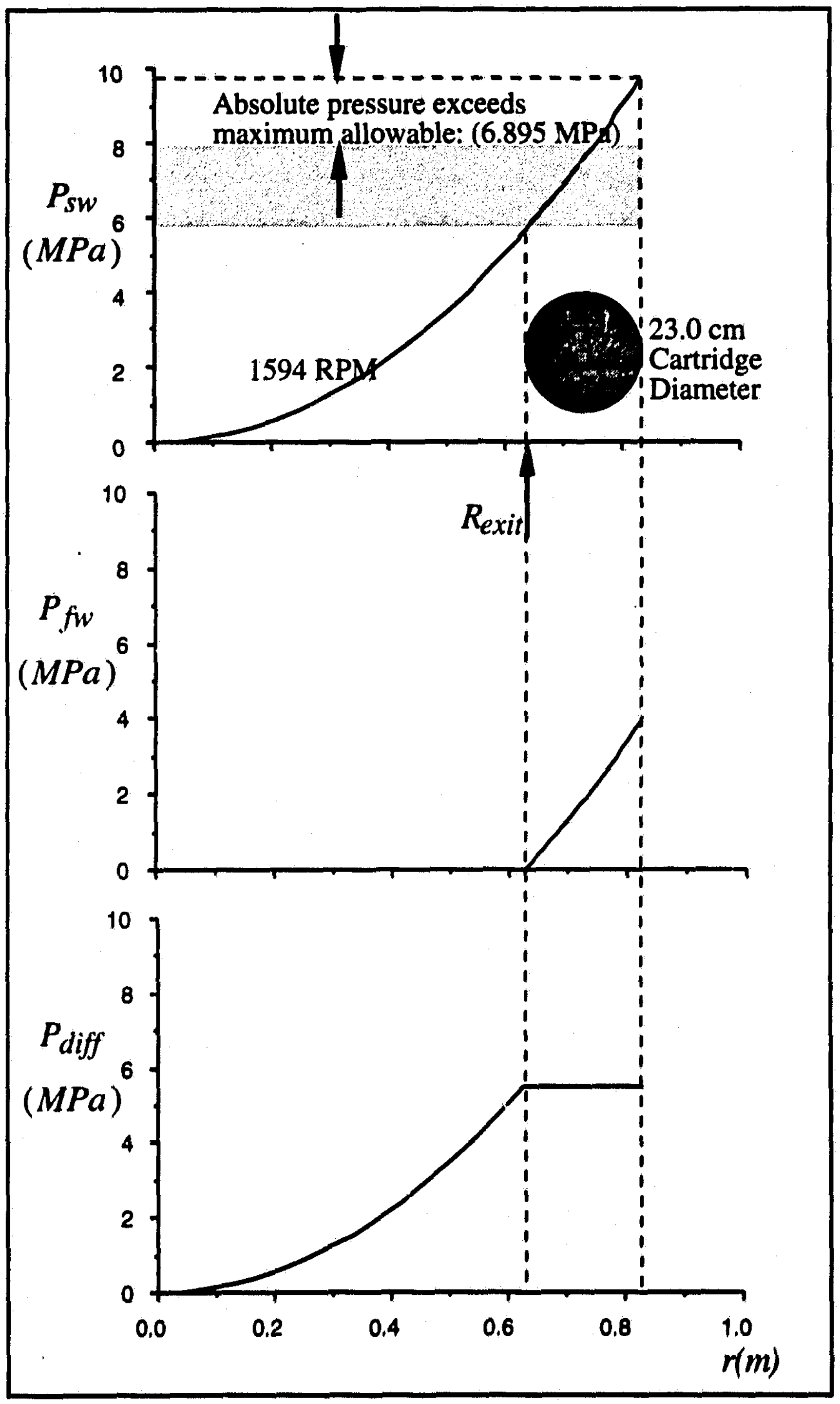

Figure 2.17 - Constant Pressure Differential Across Membrane

A CRO rotor of the standard design, having a diameter of one metre and incorporating an annular membrane cartridge, is used to evaluate the potential benefit of radial gap width reduction on windage power. The specific energy consumption due to windage torque, as predicted by the relations of Bilgen and Boulos [7] and of Schlichting [8], decreases as the radial gap width is reduced, as shown in Figure 2.18. The magnitude of the reduction is not, however, a significant proportion of total windage losses. The minimum gap width shown in Figure 2.18 is 1 mm. Reduction of the gap below this level is impractical from the point of view of the economical fabrication of the machinery.

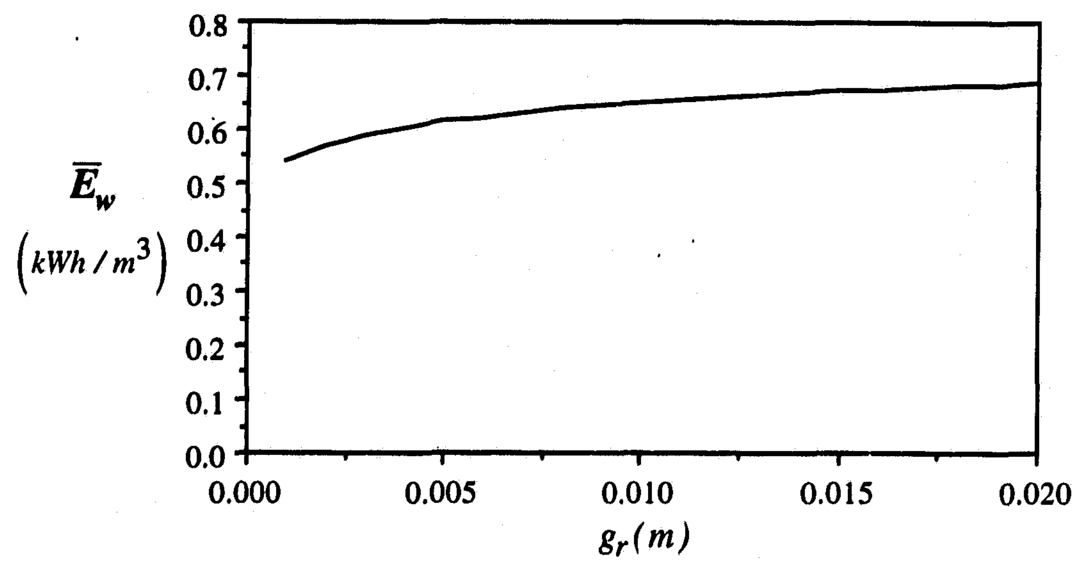

Figure 2.18 - Windage Torque Versus Gap Width for 1 m Diameter Rotor

Replacement of air with a lower molecular weight gas, with its associated lower density and lower viscosity, offers some potential for the reduction of rotor windage. Sato et al [10] have investigated the potential of helium-filled magnetic disc enclosures for computer applications. The motivation of this work was not only to reduce windage losses but also to reduce heating of the disc and the resulting distortion due to thermal expansion. In their application it was found that the disc operated in a helium-filled enclosure experienced twenty percent of the windage loss of the disc in an air-filled enclosure.

For the standard 1 m diameter rotor discussed above (with a 2 cm radial gap width), the relations of Bilgen and Boulos [7] and of Schlichting [8] are used to calculate the specific energy consumption due to windage associated with the a helium-filled rotor enclosure. The specific energy consumption due to windage is calculated to be 0.143 kWh/m^3 whereas, for an air filled rotor enclosure 0.685 kWh/m^3 is calculated. As reported by Sato [10], windage losses with a helium-filled enclosure are approximately twenty percent of the windage power with an air-filled enclosure. Although this is an attractive reduction in the power loss to windage, this is an impractical approach for CRO due to the mechanical complication of maintaining a sealed enclosure and, more importantly, the cost and inconvenience of maintaining a supply of helium.

The final option to be considered for the reduction of windage losses is the evacuation of the rotor enclosure. Again, using the relations of Bilgen and of Schlichting and the 1m diameter standard rotor design with an annular cartridge, windage power is calculated for pressures ranging from atmospheric to full vacuum, as shown in Figure 2.19.

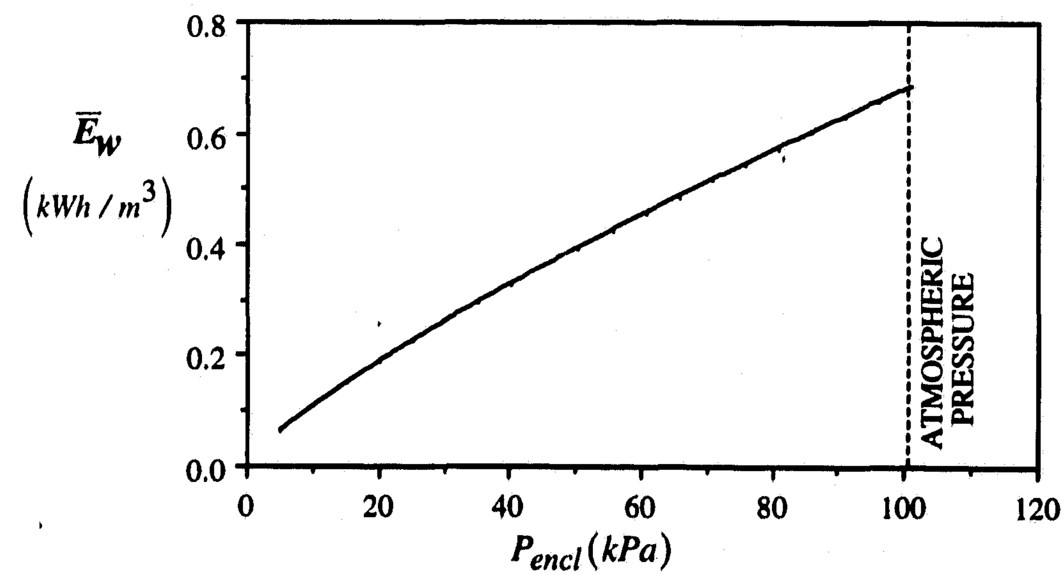

Figure 2.19 - Specific Energy Consumption due to Windage

It should be noted that these relations do not apply for high vacuum conditions as, at pressures below 10 microns of mercury (or 1.33 mPa), viscous losses must be modeled using kinetic rather than continuum theory [11].

Clearly, the potential energy savings to be realized from rotor housing evacuation are superior to the savings associated with either radial gap reduction or helium. The sole complication is the need for rotary seals to maintain an evacuated enclosure.

The specific energy consumption due to windage of CRO systems in which the rotor enclosure pressure is 8.13 kPa are calculated for rotors of the annular design and for rotors of the gattling gun design with $C_{cart}/D_{cart} = 1, 2$. For each of these rotor configurations, the specific power consumption due to windage decreases as system capacity increases, as shown in Figure 2.20.

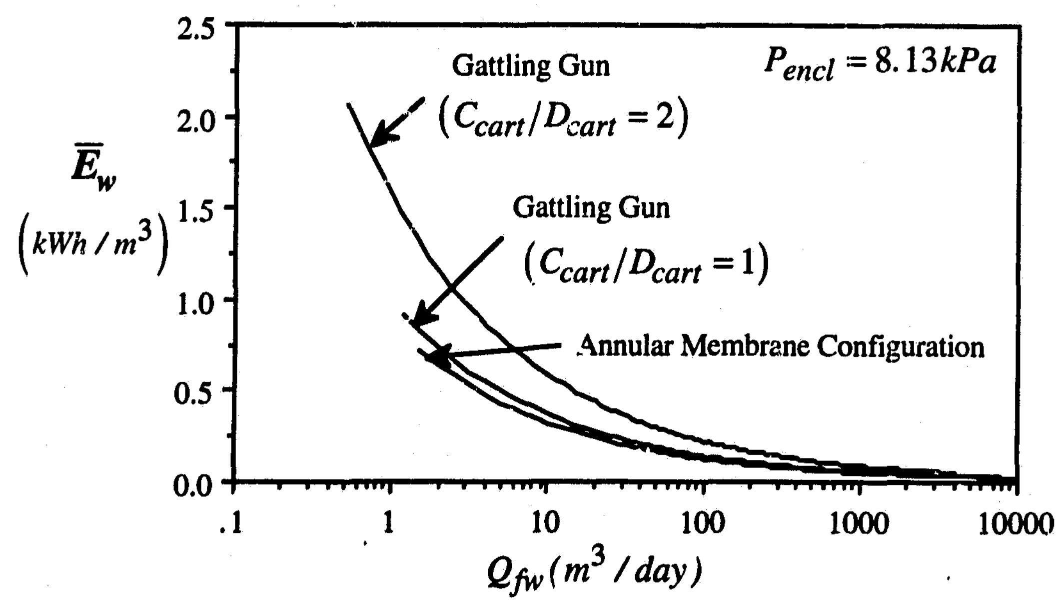

Figure 2.20 - Specific Energy Consumption Due to Windage Versus CRO System Capacity

Assuming these estimates of windage losses to be relatively accurate, it is possible to calculate the projected energy consumption of CRO systems of the standard gattling gun design, as shown in Figure 2.21. It is assumed that $C_{cart}/D_{cart} = 2$. These estimates include power to the fresh water (equation 2.13), windage losses and feed sea water pumping losses. Bearing, seal and electrical losses are neglected. The negative slope of this curve is due to the declining contribution due to windage, shown in Figure 2.20.

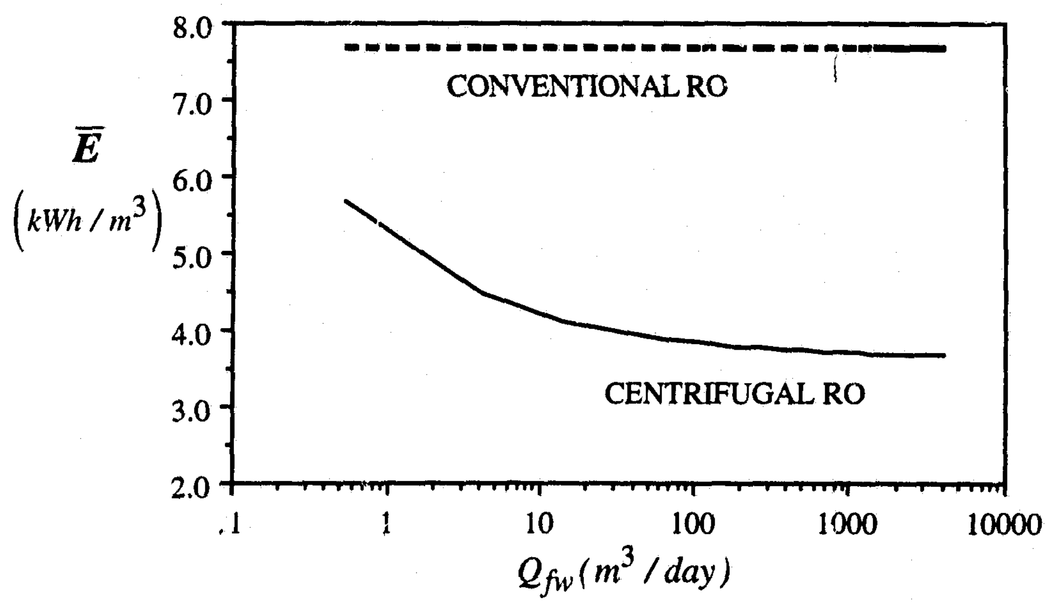

Figure 2.21 - Total Specific Energy Consumption of Conventional and CRO

The estimated power consumption of conventional RO is also shown in Figure 2.21. This estimate is derived from process pressure and flow rate. As in the estimate of CRO power, bearing, seal and electrical losses were neglected. It was also assumed that the high pressure feed pump operates at 100% efficiency. It is clear from this comparison that CRO has the potential to be significantly more energy efficient than conventional RO.

The discussion throughout this section has been constructed around the relations of Bilgen and Boulos [7] and of Schlichting [8]. The motivation for this was the convenience of functional relations and the fact that, for this assessment, only approximate estimates of windage are required. Chapter 4 is devoted to further experimental and computational investigations of windage in an effort to determine more accurate methods of predicting windage losses.

2.5.3 Fresh Water Removal Means

A matter which has not yet been discussed but which gains significance for the case of an evacuated rotor enclosure is the means by which fresh water permeate is to be collected from the rotor. If the rotor enclosure were at atmospheric pressure, the fresh water permeate could simply be released into the rotor housing and then be taken off through a drain. For an evacuated rotor enclosure, however, the fresh water permeate has to be pumped from the reduced pressure of the enclosure up to atmospheric pressure surrounding the enclosure.

A novel design feature which both recovers the fresh water permeate and which pumps it from the rotor enclosure is illustrated in Figure 2.22. The fresh water permeate is directed into an annular groove at one end of the rotor where it forms an annulus of fluid rotating as a solid body. A small pipe tip, like a pitot-static tube is introduced into the inner surface of this rotating annulus with its open end facing into the direction of rotor rotation. The moving fluid impinges on the open end of the tip, thus developing pressure which, if the other end of the tip is ducted to atmospheric pressure outside of the housing will drive a flow of fresh water permeate through the tip and out of the enclosure for collection.

If the external end of the pipe is blocked off, then the tip behaves like a pitot static tube and the pressure which it registers is equal to the stagnation pressure, P_s, of the stream in which it is inserted. At the surface of the annulus, this stagnation pressure is equal to the dynamic head of the stream.

$$P_s = \frac{1}{2}\rho_{fw}\left(\omega R_{exit}\right)^2 \tag{2.25}$$

Where, in keeping with the discussion of Section 2.5.1, the inner surface of the annulus is coincident with the inner edge of the membrane configuration at R_{exit}. Referring to equation (2.25), it is apparent that this stagnation pressure is equal to the differential pressure across the membrane. As the external end of the pipe is opened and flow begins, the pressure at the tip will drop. The result will be a "pump performance curve" which relates decreasing pressures at the tip to increasing flow rates through the tip.

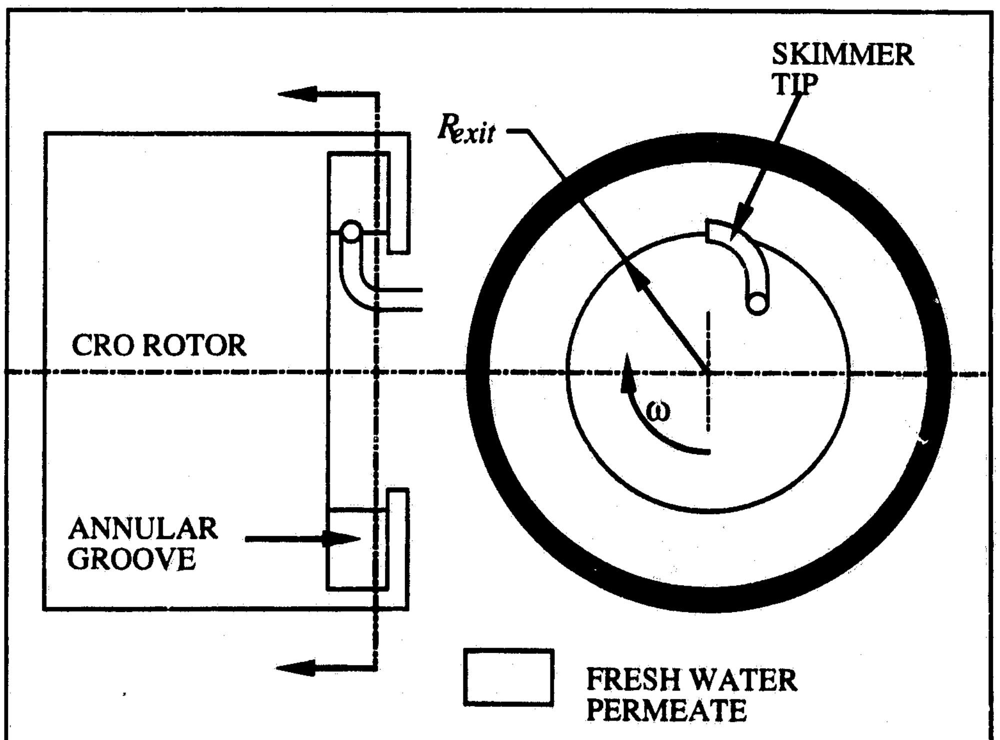

Figure 2.22 - Pitot-Type Skimmer Tip

This device could be modified so as to recover the velocity energy of the fresh water which is otherwise wasted. Recovery of this energy, possibly with the aid of a turbine connected to the outlet from the skimmer tip, would reduce the ideal energy consumption of CRO by 50%.

Alternatively, the pressure which is developed in the skimmer tip could be used to drive a second stage of RO filtration. Such second stages are commonly added on to conventional RO plants, but an additional pump is required to repressurize the fresh water permeate prior to entry into the second stage membrane filters. These two stage units are used to polish the permeate down to a level of ionization which is acceptable for industrial applications, such as process water for semiconductor manufacturing.

2.6 Assessment of CRO Feasibility

A first conceptual design for CRO, based on the discussions, data and novel design concepts presented in this chapter, can now be constructed. The key components of this conceptual design are:

1. a rotor incorporating a membrane configuration of either the gattling gun or annular design
2. radial passages to conduct the feed sea water from the rotor axis to the membrane configuration and to return the exhaust brine from the membrane configuration to the rotor axis.
3. an evacuated enclosure in which the rotor is housed
4. an annular groove at one end of the rotor into which the fresh water is directed.
5. a pitot-type skimmer tip to remove the fresh water from the rotor and to pump it from the rotor enclosure.

6. location of the skimmer tip such that the inner surface of the fresh water permeate annulus is radially coincident with the inner edge of the membrane cartridges.

This conceptual design, which forms the essence of the claims contained in the author's US and Canadian patents, represents a solid foundation upon which detailed designs for a practically feasible CRO system can be developed.

Considerable further development is required to determine the most favourable physical embodiment of this conceptual design. Given that this can be accomplished, the potential benefits of CRO, as detailed in Table 1.2, are now achievable. With respect to the most important of these benefits, reduced energy consumption, it is apparent that there could be significant energy consumption advantages associated with larger systems.

References

1. Wild, P.M., Vickers, G.W., Moilliet, A., Hopkin, D.A., Centrifugal Reverse-Osmosis Desalination Unit, Canadian. Patent No.1,290,700, 1991.

2. Ambler, C.M., Centrifugation Equipment, Industrial and Engineering Chemistry, Vol. 52, No. 6, June 1961, pp. 429-438

3. Eid, J. C.; Andeen, G. B., Effects of Acceleration On Particulate Fouling in Reverse-osmosis, Desalination, 47, May 1983.

4. Berriman, L.P., Fluid Separation Method and Apparatus, U.S. Patent No. 3,669,879, 1972.

5. Berriman, L.P., Filtering Apparatus and Method, U.S. Patent No. 3,879,286, 1975.

6. Keefer, Rotary Reverse Osmosis Apparatus and Method, U.S. Patent No. 4,230,564, 1980

7. Bilgen, E, Boulos, R, Functional Dependence of Torque Coefficient of Coaxial Cylinders on Gap Width and Reynolds Numbers, Journal of Fluids Engineering, March 1973, pp. 122-126.

8. Schlichting, H., Boundary Layer Theory, 4th ed.,McGraw-Hill, New York, 1960, p. 547.

9. Hasinger, S.H., Kehrt, L.G., Investigation of a Shear-Force Pump, Journal of Engineering for Power, July 1963, pp. 201-207

10. Sato, I., Otani, K, Oguchi, S., Hoshiya, K., Characteristics of Heat Transfer in a Helium-Filled Disk Enclosure, IEEE Trans. on Components, Hybrids and Manufacturing Technology, Vol II, No. 4, December 1988, p. 571-575.

11. Kuhlthau, A.R., Air Friction on Rapidly Moving Surfaces, Journal of Applied Physics, Vol. 20, February 1949, pp. 217-223.

Chapter 3
Development and Testing of First and Second Prototype CRO Systems

3.0 Prototype Development

Based on the positive findings of the feasibility study and with the continuing support of DND, development of a first prototype CRO unit, incorporating the novel design features introduced in Chapter 2, was undertaken. The objective of the first prototype was to demonstrate that the fundamental principles of CRO, as determined in the preliminary study, were correct and that there were no unanticipated problems which would affect process viability. The success of the first prototype was followed by the development of the second prototype, again supported by DND. This second unit went beyond feasibility, as the emphasis shifted toward optimization and refinement with respect to cost of manufacture and long term reliability.

3.1 The First and Second Prototype Designs.

Both prototype designs are based upon the conceptual design described in Section 2.6. A fundamental component of this conceptual design, which was unresolved in the feasibility study, is the selection of an annular or a gattling gun membrane configuration. Although an annular membrane configuration offers many potential benefits, as detailed in Section 2.2, the development of such a configuration requires membrane handling expertise and facilities which are not readily available to the author. The gattling gun design, on the other hand, incorporates commercially available membrane cartridges and, although it does not offer as many potential benefits as an annular design, it is a viable design option for CRO. For these reasons, a gattling gun membrane configuration is employed in both the first and the second prototypes.

Although the first and second prototypes are based on a common conceptual design, the details of the two embodiments differ substantially, as a brief comparison of the photographs shown in Figures 3.1 and 3.2 will verify. Much of this difference arises from the different philosophies under which these two units were designed. The first prototype was designed to verify feasibility whereas the second unit was a first attempt toward a commercially viable design. In addition, the design of the second prototype benefited significantly from the operational experience of the first prototype.

3.1.1 Prototype System Specifications

The design specification for the first prototype, as stipulated by DND, was 3785 litres/day (1000 gpd) from sea water of salinity 32,000 ppm at 25 C. This specification was met with eight Fluid Systems Model 7005 spiral wound membrane cartridges in parallel, each rated at 492 litres/day permeate flow rate.

The design specification for the second prototype, as stipulated by DND, was 11,355 litres/day (3000 gpd) from sea water of salinity 32,000 ppm at 25 C. This specification was met with sixteen Filmtec SW2521 membrane cartridges in parallel, each rated at 757 litres/day permeate flow rate.

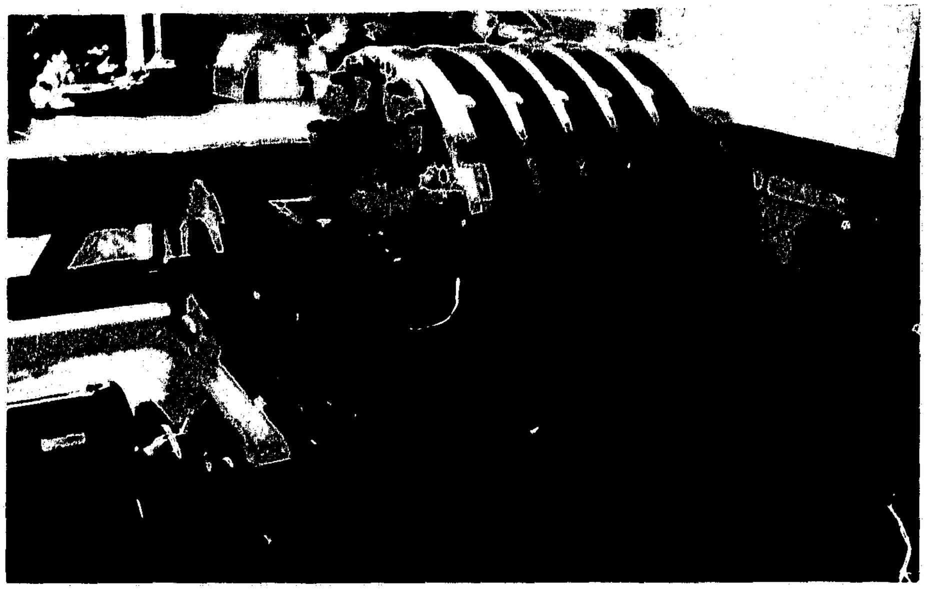

Figure 3.1 - Photograph of First Prototype

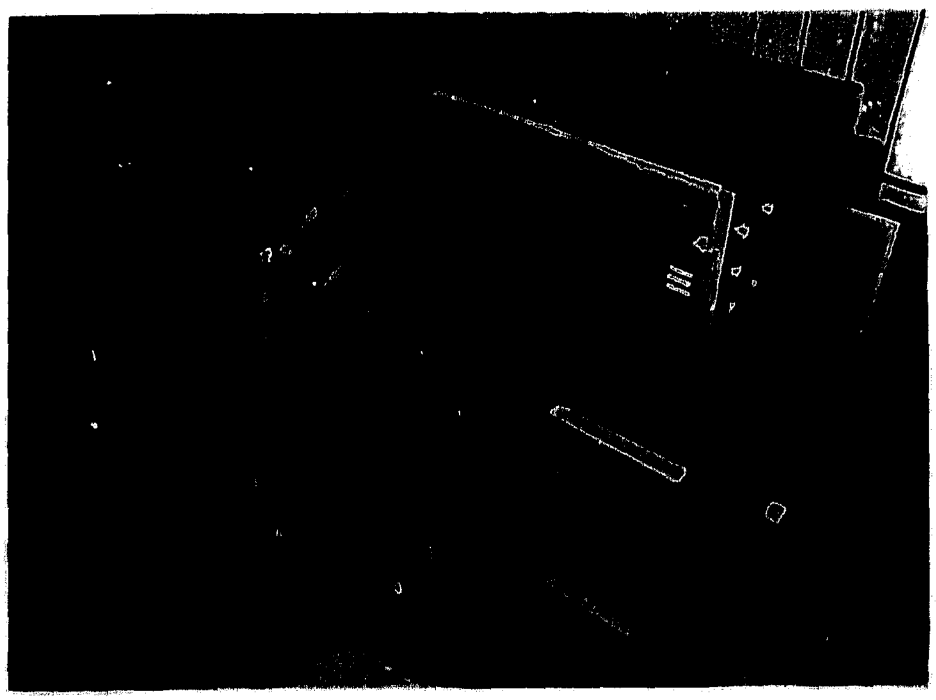

Figure 3.2 - Photograph of Second Prototype

3.1.2 Sea Water Flow Paths

As is discussed in Sections 2.4, the power consumption of the centrifuge drive motor is independent of the flow rate through the rotor. However, the pressure drop through the rotor and, thus, the power consumption of the feed pump, is dependent upon the flow rate through the rotor, rotor speed and the nature of the flow path through the rotor. The experimental work reported in Section 2.4.2 indicates that the feed pump power consumption is likely to be a significant component of the overall power consumption of a CRO unit. Compared with the potential power loss due to windage, however, the projected magnitude of fluid flow losses does not warrant special attention to this area of the design at the first prototype level. The fluid flow path through the rotor is, therefore, designed principally for ease of rotor manufacture and assembly rather than to minimize fluid flow losses.

The sea water flow path in both first and second prototypes consists of axial bores in either end of the rotor shaft, opposed radial holes, connecting these bores into flow diffusers which connect these radial holes to radial tubes which direct the flow to and from the pressure vessels. This flow path is shown schematically in Figure 3.3 and in detail in Figures 3.4 and 3.5. Referring to Figure 3.5, the feed sea water enters the bore in one end of the rotor shaft via a rotary coupling (1) and is directed from the bore (2) into the inlet diffuser (3) which divides the flow into the array of radial tubes (4) which pass the sea water into the pressure vessels (5) which contain the membrane cartridges (6). The sea water passes axially through the membrane cartridges and is then returned to the axis through the array of outlet tubes (7) and the diffuser (8) at the outlet end of the rotor.

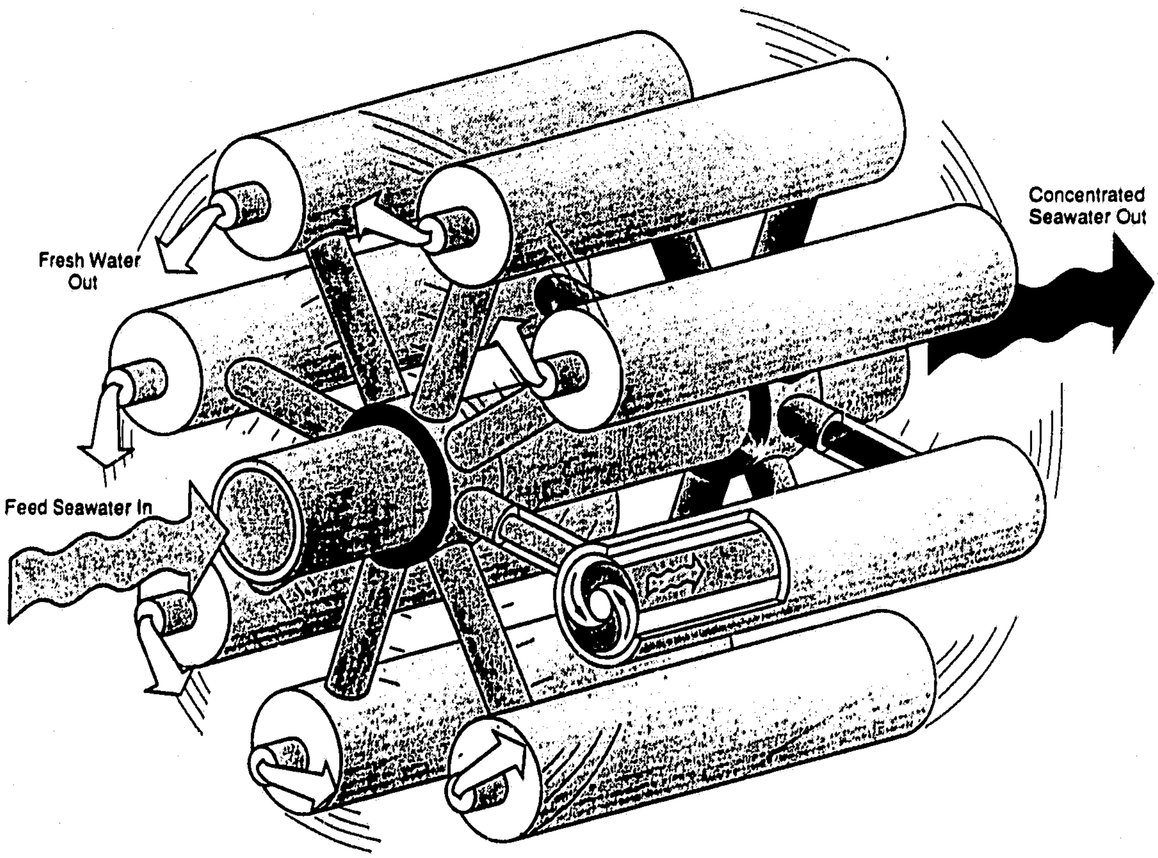

Figure 3.3 - Schematic View of Sea Water Flow Path

In the first prototype, the pressure vessels are located on a 0.548 m (21.6 inch) diameter pitch circle. The operational speed of the rotor, to provide 5.5 MPa at the inner edge of the membrane cartridges is 4100 rpm. In the second prototype, the pressure vessels are located on a 0.642 m (25.3 inch) diameter pitch circle. The operational speed of the rotor, to provide 5.5 MPa at the inner edge of the membrane cartridges is 3500 rpm.

3.1.3 Structure to Restrain Pressure Vessels Against Forces of Rotation

The assembly of pressure vessels and radial tubes shown in Figure 3.3 is the minimum component requirement for the rotors of the first and second prototypes. If this assembly could be endowed with sufficient structural integrity, the functional requirements of a CRO system would be satisfied. Under the loading due to forces of rotation, however, the radial tubes would be subjected to tremendous tensile loading and the pressure vessels would experience extreme bending loads between the points of connection with the radial tubes. In addition to this extreme centrifugal loading, the design criteria for the radial tubes and pressure vessels would also include the fluid pressure and corrosion resistance requirements accompanying the fluid handling functions of these components. The difficulty of simultaneously satisfying these many design criteria for the radial tubes and pressure vessels is a significant challenge.

In both the first and second prototypes, structural and fluid handling functions are separated. The role of the pressure vessels and radial tubes is strictly fluid handling and, in each case, there is an additional support structure which restrains these components against the forces of rotation. The only rotor component which serves both fluid handling and structural roles is the rotor shaft.

In the first prototype, the support structure consists of circular aluminum plates spaced along the length of the rotor shaft, as shown in Figure 3.4. These plates are bored in-line to accept the array of pressure vessels. One of the critical parameters in the design of these plates is the spacing between adjacent bores. This material in this region acts like a "spoke" which restrains the pressure vessels against centrifugal loading.

In the second prototype, the pressure vessels, are supported by a filament wound (S2 glass/vinyl-ester) cylindrical shell (9) which is located with respect to the rotor shaft by circular aluminum end plates (10) at either end of the rotor, as shown in Figure 3.5. The pressure vessels are also located by the end plates as they are seated, at either end, in rubber bushings (11) which are, in turn, seated in blind holes in the end plates. At speed, the outer shell experiences more radial deformation than the end plates and, as the pressure vessels move outward with the shell, the rubber bushings are compressed. Since the end plates do not carry a significant radial load due to the pressure vessels, the spacing between adjacent bores in the plates is not as critical as in the circular plates of the first prototype design. The pressure vessels can, therefore, be spaced more closely and, as a result, the volumetric efficiency of the membrane configuration (see Figure 2.5) can be much higher than in the plate design of the first prototype. Although this design addresses the problem of the different deformations experienced by the outer shell and by the end plates, it introduces flexibility which affects the dynamic balance of the rotor (see section 3.3.5).

3.1.4 Pressure Vessel Design

The pressure vessels of the first prototype are of anodized aluminum and the axial pressure force is contained by the axial rods which also locate the circular support plates. A standard circlip or retaining ring design is not acceptable owing to excessive bearing stress in the circlip groove.

The pressure vessels of the second prototype are of filament wound (S2-glass/epoxy) and the axial pressure force is contained by a three-piece segmented ring. As in the first prototype, a standard retaining ring design is not acceptable owing to excessive

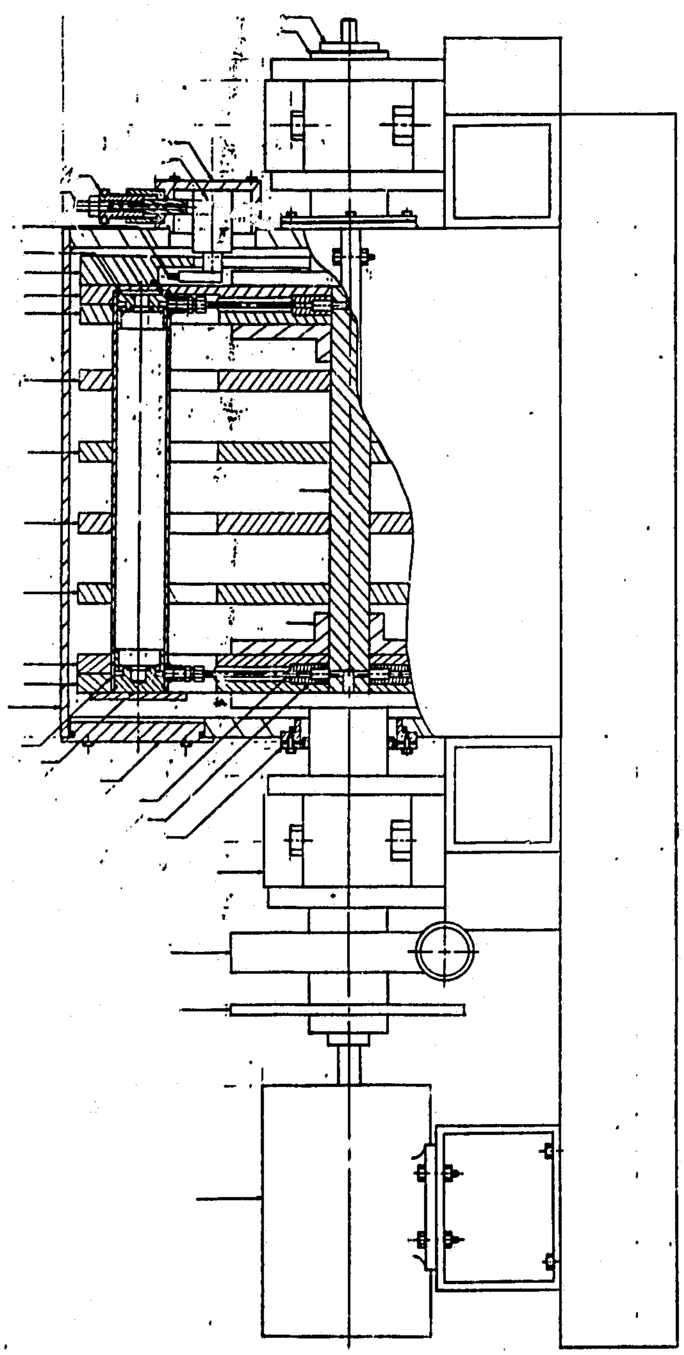

Figure 3.4 - Partial Section of First Prototype

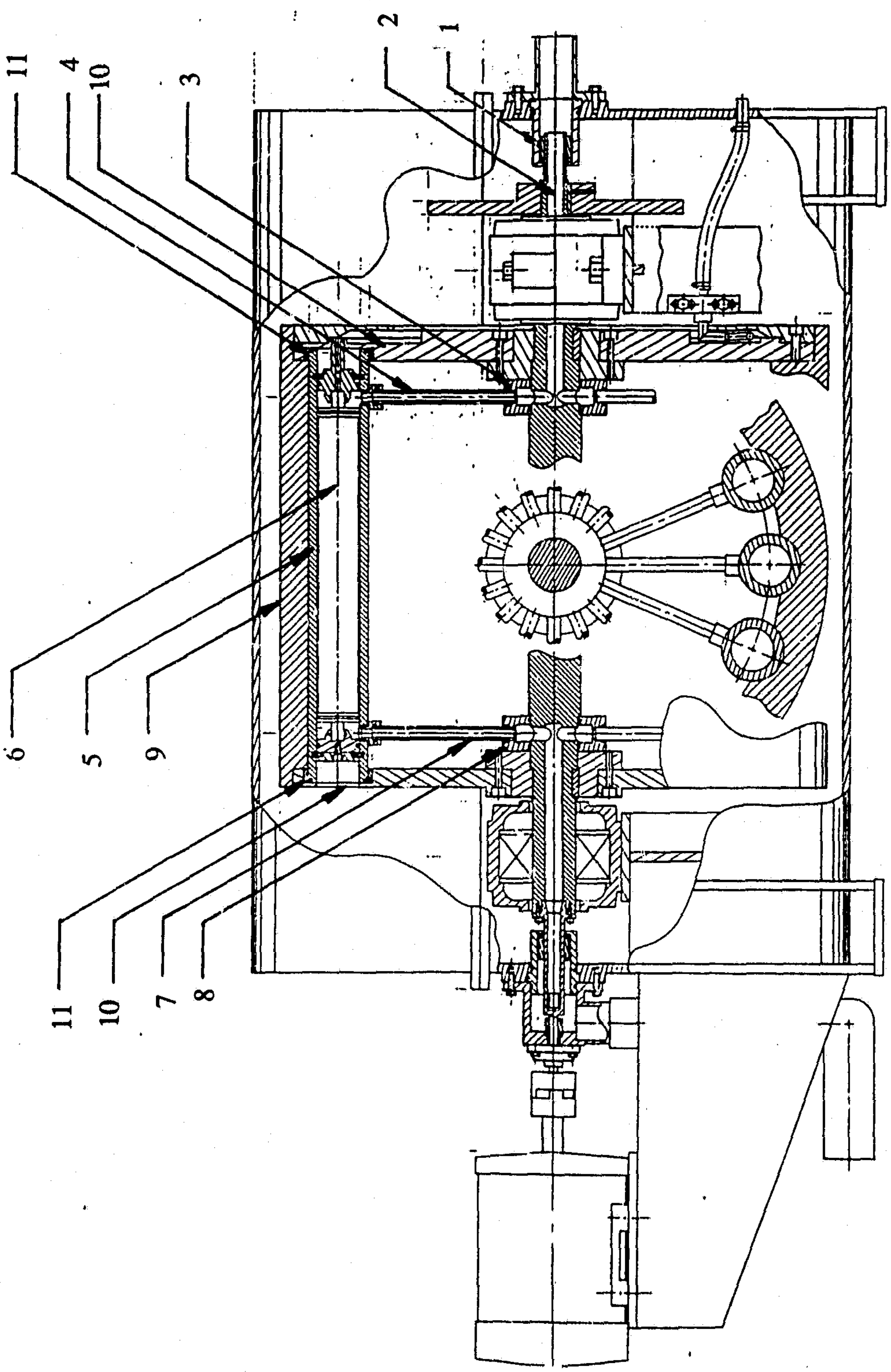

Figure 3.5 - Partial Section of Second Prototype

bearing stress in the circlip groove. The segmented ring design allows a greater depth of groove and, therefore, a larger surface for the segmented ring to bear upon.

3.1.5 Materials and Corrosion

In keeping with the conservative approach to the design of the first prototype, materials selection is restricted to readily available metals, as shown in Table 3.1. The rotor shaft, diffusers and radial tubes are constructed of 316 stainless steel. This material has excellent resistance to corrosion in sea water so long as minimum fluid velocities are maintained. If stagnation occurs, 316 SS is highly susceptible to crevice corrosion. Upon shutdown, therefore, it is essential that either fresh water or preserving solution be flushed through the system. The circular plates and pressure vessels and pressure vessel end closures are of 6061T6 aluminum. The pressure vessels and end closures are hard anodized to prevent corrosion. In spite being anodized, however, the pressure vessels suffer significant corrosion. This is partly due to scratching of the anodized coating but, judging from the locations of most severe corrosion, is principally due to galvanic interaction with the stainless steel radial tubes.

In the second prototype, all rotor components which contact sea water, with the exception of the rotor shaft, are non-metallic and impervious to corrosion, as shown in Table 3.1. The diffusers and radial tubes are of polycarbonate (lexan), the pressure vessels are of glass-epoxy filament-wound composite and the pressure vessel end-closures and spigots are of delrin. The rotor shaft is of Avesta 254SMO, a molybdenum rich stainless alloy which is not susceptible to corrosion in sea water. The rotor end plates are of 6061 T6 aluminum and the outer shell is of glass/vinyl-ester filament-wound composite.

Component	Material used in first prototype	Material used in second prototype
Pressure vessels	anodized aluminum (6061 T60)	filament wound glass/epoxy
Pressure vessel end closures	anodized aluminum (6061 T60)	delrin
Circular plates	aluminum (6061 T60)	aluminum (6061 T60)
Outer shell	N/A	filament wound glass/vinyl-ester
Main shaft	stainless steel (316)	stainless steel (Avesta 254SMO)
Radial Tubes	stainless steel (316)	polycarbonate
Inlet and outlet diffusers	stainless steel (316)	polycarbonate

Table 3.1 - Materials of First and Second Prototypes

3.1.6 Bearing and Seal Configurations

In the first prototype, the bearings are located outside of the rotor housing and there are rotary vacuum seals on the rotor shaft between the bearings and the ends of the rotor, as shown in Figure 3.4. Stress and vibration analyses indicate that the critical parameter controlling rotor shaft size is neither stress nor fatigue but the first natural frequency of vibration of the rotor/shaft system. The maximum operating speed of the unit must be less than this first natural frequency. As the distance between the bearings and the rotor ends increases, for a given shaft diameter, this natural frequency decreases. The axial length of the vacuum seals should, therefore, to be as small as possible. Although mechanical seals give superior service in this application, dry running teflon lip seals are specified in order to minimize the axial distance between the bearings and the rotor ends and, thus, to maximize the first natural frequency of the rotor/shaft system.

Unfortunately, the life of these lip seals proved to be impractically short (approximately 30 hours) owing to the high surface speed and lack of a lubricating/cooling fluid.

In the second prototype, the bearings are located inside the rotor housing eliminating the need for vacuum seals between the bearings and the rotor (see Figure 3.5). This reduces the span between the bearings and the ends of the rotor to a minimal distance. With this modification, the rotary seals run on the smaller non-weight-bearing extensions of the rotor shaft, outboard of the bearings and are sea water lubricated and cooled. As the axial length of these seals is no longer a concern, standard carbon/ceramic mechanical seals are used. These seals serve both to maintain rotor housing vacuum and to conduct the inlet and outlet sea water between stationary and rotating conduits.

3.1.7 Vacuum Systems

In the first prototype, the vacuum is drawn with an oil lubricated impeller-style pump. This pump is able to handle a small amount of water vapour but, under no condition, is it able to handle liquid water. The fresh water skimmer tip, however, sprays a small amount of water out of the annular groove and into the rotor housing and this can not be allowed to accumulate as it eventually impinges on the rotor. There is, therefore, a drain at the bottom of the housing which connects into a small chamber which was valved so as to operate as an air lock. The "overspray" collects in this chamber and is then manually drained without loss of housing vacuum. In spite of thi s measure, however, the vacuum pump oil requires frequent changing due to emulsification.

In a conventional RO system, fresh water does not permeate through the membranes until the osmotic pressure of sea water, relative to fresh water, is exceeded. For a CRO system this means that fresh water production does not commence until a certain speed of rotation, corresponding to the osmotic pressure, is exceeded. During rotor acceleration, therefore, there is a period during which the skimmer tip is not removing fresh water and could act as an open passage to atmosphere, frustrating the maintenance of a vacuum in the rotor housing. In the first and second prototypes, there is a check valve on the outlet from the skimmer tip assembly to prevent this from occurring.

In response to the difficulties with the oil lubricated vacuum pump, evacuation of the second prototype rotor housing is accomplished with a pneumatic venturi pump and a sea water actuated venturi pump. The pneumatic pump draws down the initial vacuum and is automatically shut down once the rotor has reached full speed. The sea water actuated vacuum pump then maintains the vacuum against minor leakages and also scours away the overspray from the fresh water skimmer tip.

3.1.8 Rotor Drive and Unit Instrumentation

In both the first and second prototypes, the rotary drive power is provided by a 5 Hp, 230 V, 3 phase, 3450 rpm synchronous induction motor which is coupled, in line, to the rotor shaft. The motor is sized for the load at full speed which is much less than the load which would be required to quickly accelerate the rotor using a conventional capacitor start device. The motor is controlled by a Toshiba frequency controller with which the frequency of the power which is delivered to the drive motor and, thereby, the rotational speed of the motor is controlled. In the first prototype, the rotor is accelerated to speed by manually incrementing the drive frequency at a rate which ensures that the allowable motor current is not exceeded. In the second prototype, an additional current feedback control circuit automatically ramps the unit to full speed.

Unit shut down is accomplished by cutting power to the frequency controller, and opening a valve on the rotor housing (automatically, in the case of the second prototype), thus admitting air to the housing and slowing the rotor. In addition, there is a brake disc/caliper which can be applied (automatically, in the case of the second prototype) if rapid deceleration is desired.

Both prototypes are instrumented to provide performance data during operation, as shown in Appendix II.

3.2 Performance of the First and Second Prototypes

3.2.1 Permeate Salinity and Flow Rates

Based on the membrane manufacturer's specifications the performance of the first prototype exceeds the projected performance of an equivalent conventional RO system. According to these specifications, the projected permeate flow rate at 25 °C is 3936 litres/day (based on 492 litres/day or 130 gpd per cartridge) and the projected salinity is 480 ppm (based on 98.5% salt rejection). At a feed sea water temperature of 12 °C, the permeate flow rate for the first prototype is 2,640 litres/day, as shown by the lower curve in Figure 3.8. The flux through a membrane is an increasing function of feed water temperature. Fluid Systems, the manufacturer of the membrane cartridges, specifies "temperature correction factors" (TCF) for temperatures ranging from 1 °C to 50 °C which can be used to calculate projected membrane performance relative to the standard performance at 25 °C. The TCF for 12 °C is 1.701 [1]. The permeate flow rate, when adjusted for the feed water temperature, converts to 4,490 litres/day at 25 °C, which exceeds the design specification of 3,785 litres/day, as shown by the upper curve in Figure 3.8.. These levels were maintained, within 5% throughout the testing period.

Note that the flow rate of fresh water permeate increases with feed flow rate. This trend is typical of conventional RO as the increasing fluid velocity across the membrane minimizes the effect of concentration polarisation.

The World Health Organization specifies 500 ppm as the maximum acceptable level of salinity in potable water. At the design flow rate for the first prototype, the permeate salinity is 453 ppm, which is within this standard, as shown in Figure 3.9. It is apparent from the slope of the curve in this figure that further increases is the feed sea water flow rate would result in further improvements in the purity of the fresh water permeate.

As was the case with the first prototype, the salinity and the flow rates of fresh water from the second prototype were within the range of values to be expected from a conventional RO plant. The projected permeate flow rate at 25 °C is 12,112 litres/day (based on 757 litres/day or 200 gpd per cartridge). Over the long term, approximately, 2,000 hours of intermittent operation, the fresh water flow rate has remained in the range of 5,677 to 7,570 litres/day and the fresh water salinity has remained between 200 and 300 ppm. Using a TCF of 1.701 for feed sea water at 12 °C, this corresponds to a flow of between 9,655 litres/day and 12,869 litres/day at 25 °C.

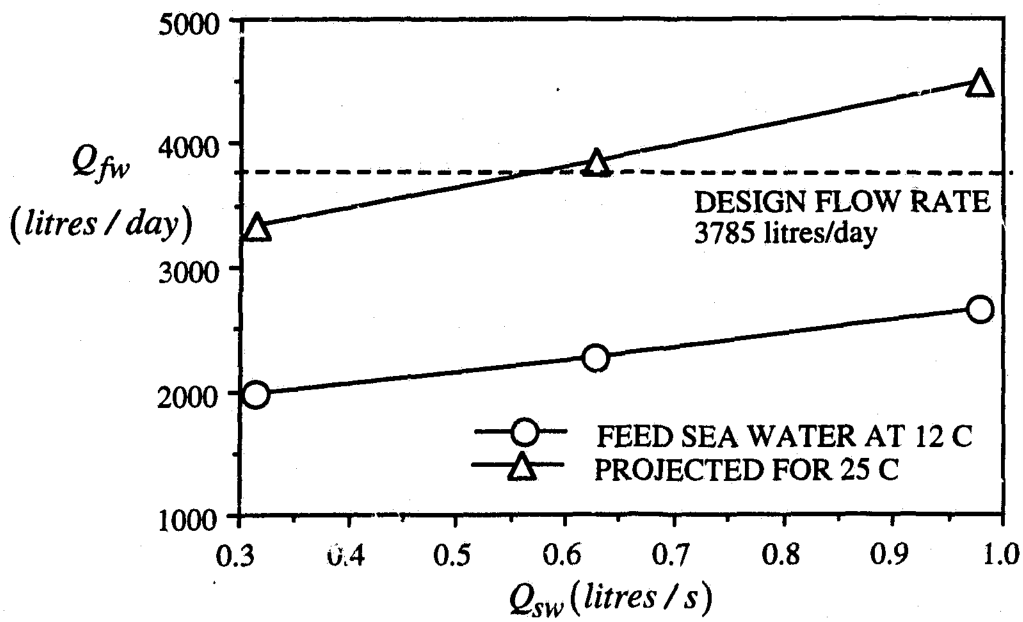

Figure 3.8 - Permeate Flow Rate vs Feed Sea Water Flow Rate for First Prototype

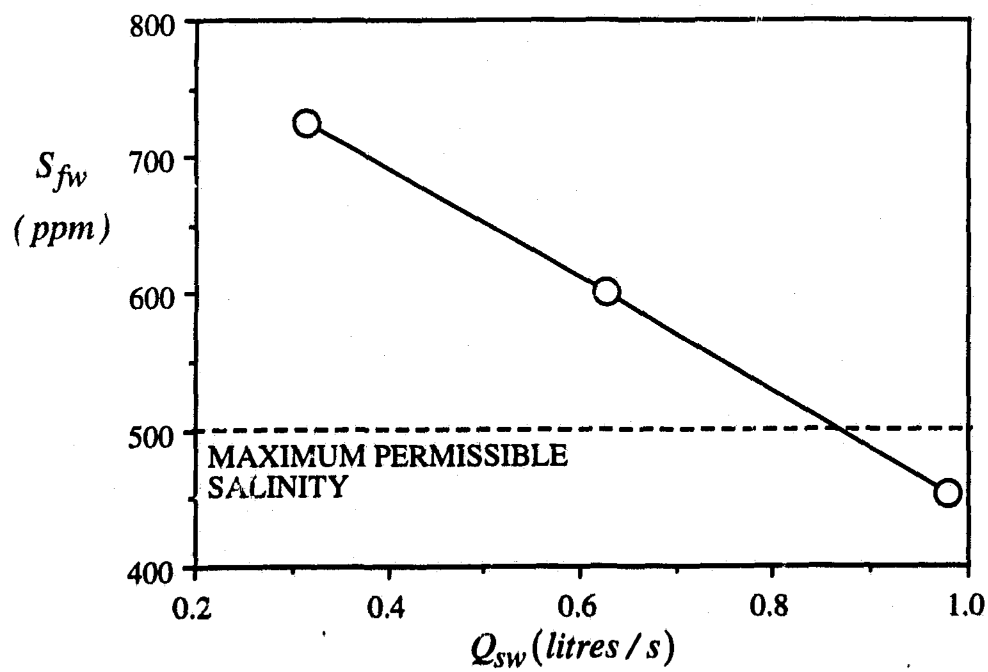

Figure 3.9 -Permeate Salinity vs Feed Sea Water Flow Rate for First Prototype

Fresh water salinity and flow rate show the same trends with feed flow rate as for the first prototype, as shown in Figures 3.10 and 3.11. At full speed, the maximum sea water flow rate which can be achieved with the feed flow rate available from the sea water supply system is 1.9 litres/s or 0.12 litres/s per membrane cartridge. The maximum allowable flow rate per cartridge is 0.38 litres/s. It is clear from Figures 3.10 and 3.11 that there would be additional benefits, both to quality and the quantity of fresh water production, associated with higher feed flow rates.

3.3.2 Power Consumption Due to Windage

The power consumption due to windage for the first prototype is estimated from operational data. The drive power consumption of the unit is measured over a range of levels of rotor enclosure evacuation and at a number of operating speeds, as shown in Figure 3.12. This data is taken without the membrane cartridges in place and, therefore, with no fresh water production. The power consumption attributable to windage is estimated by extrapolating the 4100 rpm curve to full vacuum. The difference between power at full vacuum and at $P_{encl} = 8.1 kPa$, 852W, is assumed to be due entirely to rotor windage.

The importance of rotor housing evacuation is reinforced by this figure and, in particular, by the slope of the 4100 rpm curve. As expected, the slopes of these curves become increasingly positive as rotor speed increases. A surprising feature of this figure is that the 1000 rpm curve has a negative slope. That is, drive power increases as rotor housing vacuum increases. This effect is due to friction in the vacuum seals.

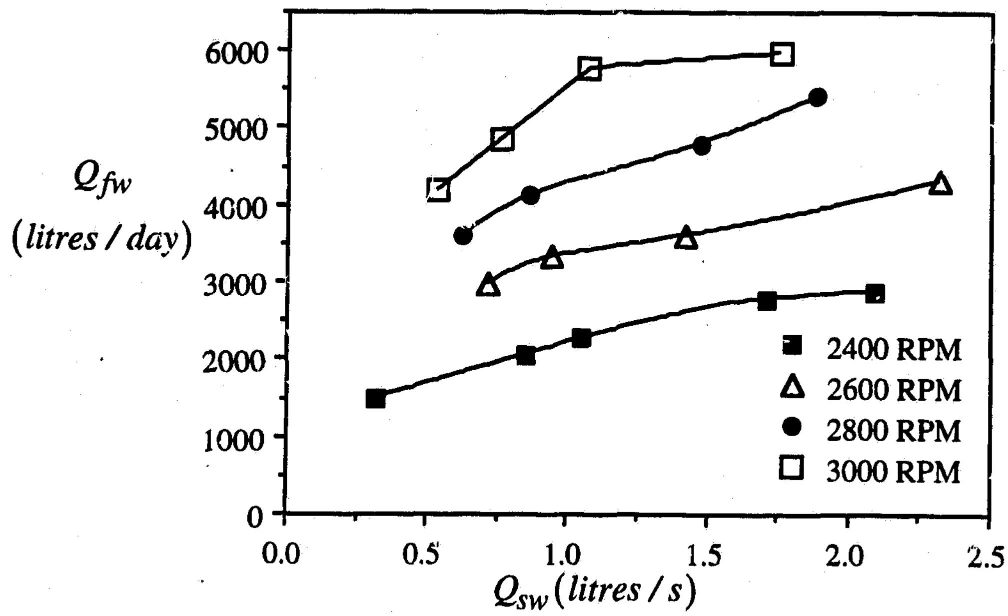

Figure 3.10 - Permeate Flow Rate vs Feed Sea Water Flow Rate for Second Prototype

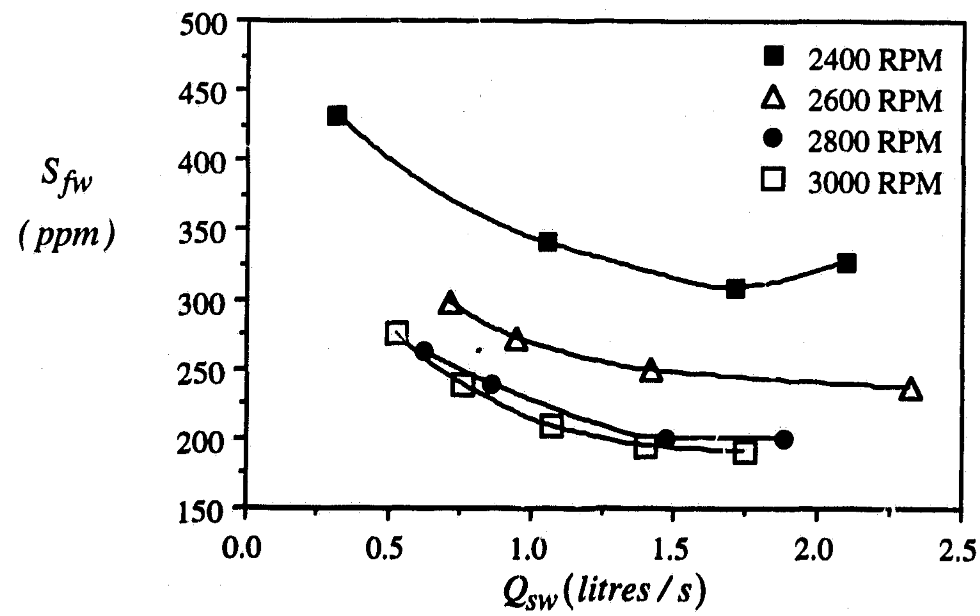

Figure 3.11 - Permeate Salinity vs Feed Sea Water Flow Rate for First Prototype

The vacuum seals are teflon lip seals and the force with which they are drawn down onto the rotor shaft is, in part, a function of the pressure differential from one side of the seals to the other. The resistance to rotation which these seals present is, therefore, a function of rotor housing vacuum, as shown in Figure 3.13. This data was taken with a plain shaft replacing the rotor in order to eliminate windage from the experiment. At 4100 rpm the drive power is 70% higher at 8.1 kPa than at atmospheric pressure. This effect accounts for the positive slope of the 1000 rpm curve in Figure 3.12. At higher speeds, windage washes out the effect of seal friction.

The power consumption due to rotor windage for the second prototype is estimated from operational data in the same manner as for the first prototype. The drive power consumption of the unit is measured over a range of levels of evacuation at the full operating speed, as shown in Figure 3.14. As with the first prototype, this data was taken without the membrane cartridges in place and, therefore with no fresh water production. The power consumption attributable to windage can be estimated by extrapolating the curve to full vacuum. The difference between the full vacuum value and the value at 4784 Pa, 636 W, is assumed to be due entirely to rotor windage.

A final observation with respect to windage is that the relations of Bilgen and Boulos [2] and of Schlichting [3], which were the basis of the windage discussion in Chapter 2, underestimate the windage power of the second prototype, as shown in Figure 3.15. The upper curve in this figure is extrapolated from the curve fit in Figure 3.14, less the zero pressure offset. This discrepancy may be due to discrepancies between the physical model for which these relations were developed. In particular, the bearing platforms interfere with the flow in the regions of the end gap and rotor enclosure is not concentric with the rotor.

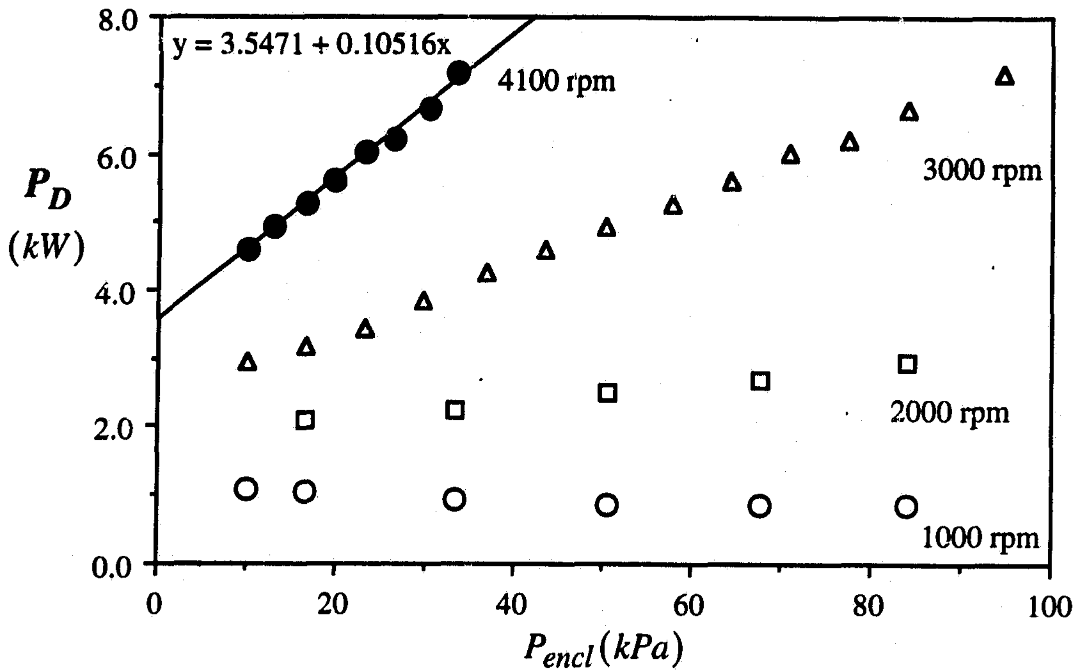

Figure 3.12 - Drive Power vs Rotor Enclosure Pressure and Rotor Speed

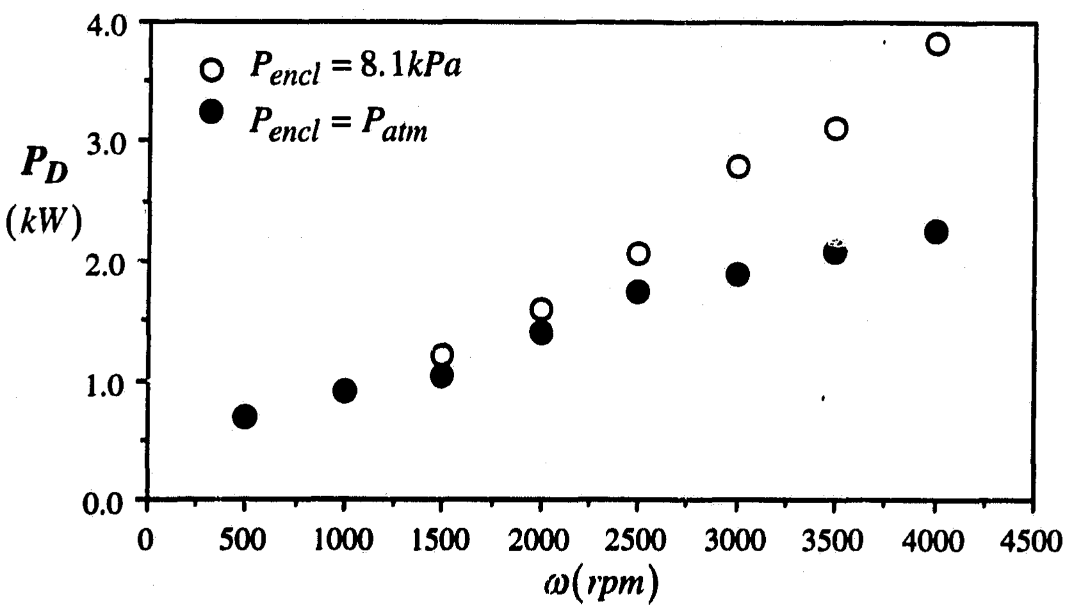

Figure 3.13 - Drive Power vs Rotor Speed for Plain Shaft

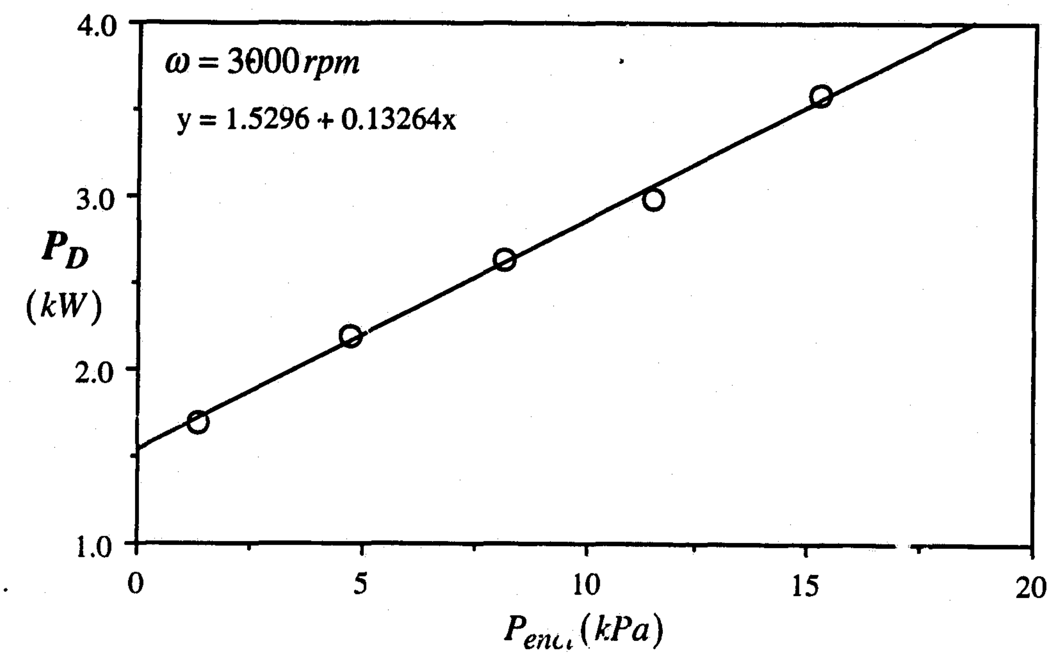

Figure 3.14 - Rotor Drive Power vs Rotor Enclosure Pressure for Second Prototype

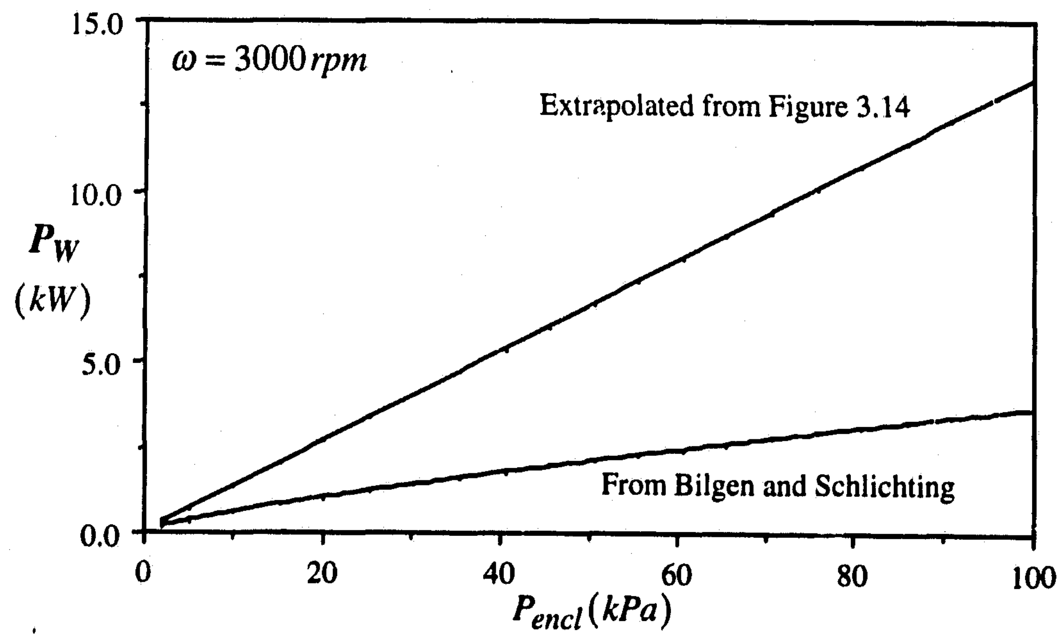

Figure 3.15 - Comparison of Test Data with
Data Calculated from Bilgen and Boulos[2] and Schlichting [3]

3.3.3 Fluid Flow Losses Through the Rotor

The fluid flow losses through the rotors of the first and the second prototypes are, as anticipated in the discussion in Section 2.4.1, an important component of the total power consumption of both the first and second prototypes. There is, in addition, a strong dependence of flow losses on rotor speed, as shown in Figure 3.16. The loss coefficient ratio is the ratio of the loss coefficient through the rotor at a given rotational speed divided by the loss coefficient at full operating speed. The loss coefficient itself is calculated from the pressure drop across the rotor, P_d, and the average velocity of the flow in the radial tubes, V_R.

$$C_L = \frac{P_d}{\frac{1}{2}\rho_f V_R^2} \tag{3.1}$$

The rotor speed ratio is the ratio of rotor speed to full operational speed.

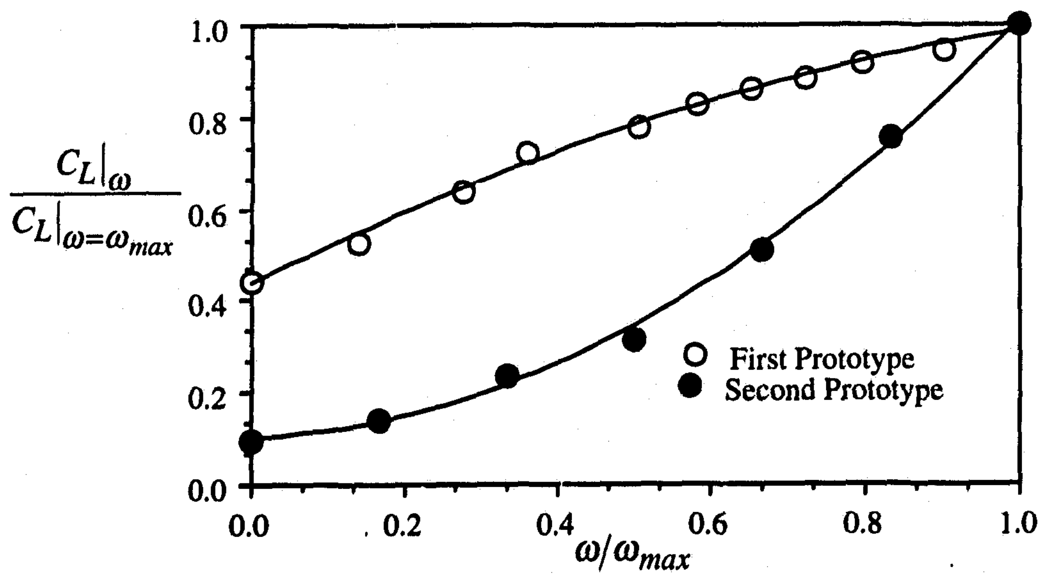

Figure 3.16 - Loss Coefficient Ratio vs Rotor Speed Ratio for First and Second Prototype

The flow losses in first prototype, when the rotor is at rest, are nearly half of the losses when the rotor is at full speed. This indicates that there are passages within the rotor which are excessively restrictive. The passages in the second prototype were, accordingly, enlarged and, as a result, the flow losses at rest were much smaller. However, the strong dependence of flow losses upon rotor speed remains. The pressure drop, for the normal operating sea water flow rate of 1.58 litres/s, increased from 90 kPa, when the rotor is at rest, to 695 kPa, when the rotor was at the normal operating speed of 3000 rpm. Assuming pump and motor efficiencies of 80% and 90% respectively, the sea water feed pump consumed 1.525 kW of power under normal operating conditions, which is 27.5% of the total energy consumption of the second prototype. Reductions in the flow losses through the centrifuge rotor would, therefore, have a significant impact on the overall power consumption of the CRO. To this end, an experimental study of flow losses was conducted, the results of which are reported in Chapter 5.

3.3.4 Total Power Consumption

In Chapter 2, the power consumption of the main centrifuge drive motor of a CRO system was projected to fall into three categories: power to the fresh water, windage losses, and bearing and seal friction. Experiments were conducted with the first and second prototype in order to determine the magnitude of each of these components. The sum was then compared with the total measured power consumption of the centrifuge drive motor in order to verify that the model of CRO power consumption, proposed in Chapter 2, was valid. The components of energy consumption for the prototypes are estimated as shown in Table 3.2.

	FIRST PROTOTYPE	SECOND PROTOTYPE
Power to fresh water (W) (equation 2.13)	417	1197
Windage losses (W) (Section 3.3.2)	852	636
Bearing and seal losses (W) (Section 3.3.2)	3547	1530
Total of Components of Drive Power (W)	**4816**	**3363**
Measured Drive Power (W)	**5976**	**3984**

Table 3.2 - Drive Power Consumption of First and Second Prototypes

Comparison of the final two rows of Table 3.2, shows that the sum of the components of power consumption is less than the measured value of power consumption for both units. This discrepancy is likely due to experimental inaccuracy. Watt meters of sufficient capacity were not available for these measurements and, as a result, the power data were derived from ammeter readings and using an assumed power factor of 0.95. The ammeter had resolution of ±0.25 amperes which results in a resolution of ±100 W on all power measurements. Possible variations in the power factor widen this error band still further.

The total and total specific energy consumptions of the first and second prototypes, inclusive of fluid flow losses, are shown in Table 3.3. The first prototype has specific energy consumption of 57.6 kWh/m^3 and the second prototype has specific power consumption of 17.5 kWh/m^3. The majority of the losses in the first prototype are due to the lip seals. Rearrangement of the bearing and seal placement, as discussed in Section 3.1.6, and replacement of the lip seals with carbon/ceramic mechanical seals accounts for most of the improvement in the specific power consumption of the second prototype.

With respect to total specific power consumption, inclusive of flow losses associated with the flow of feed sea water through the rotor, both prototypes are in excess of levels which were projected in Figure 2.21. This discrepancy is due principally to the exclusion of seal, bearing and electrical losses from idealised estimates in Chapter 2. In addition windage levels were well above those predicted in Chapter 2 using the relations of Bilgen and Boulos [2] and Schlichting [3].

	FIRST PROTOTYPE	**SECOND PROTOTYPE**
Fresh water Flow Rate (litres/day)	2640	7570
Measured Drive Power (W) (Table 3.2)	5976	3984
Fluid flow losses (W) (Section 3.3.3)	362	1525
Total Power (W)	**6338**	**5509**
Specific Energy Consumption (kWh/m^3)	**57.6**	**17.5**

Table 3.3 - Total Power Consumption of First and Second Prototypes

3.3.5 Rotor Balance

For a rigid rotor, a given level of unbalance at a speed well below the operational speed is easily extrapolated to the corresponding unbalance at operational speed. For such rotors, dynamic balancing is carried out at the lower speed to levels which, when extrapolated to full speed, are considered acceptable. This procedure is followed when balancing the first prototype rotor.

The second prototype rotor, however, has a degree of flexibility, as is discussed in section 3.1.3. It is, therefore, necessary to carry out dynamic balancing in a different manner. As the rotor comes to speed and the outer shell deforms, the center of mass of the rotor shifts. In addition, the annulus of fresh water affects rotor balance. Owing to machining inaccuracies, the annulus is not perfectly axisymmetric and, therefore, the mass of water in the annulus is not perfectly balanced.

Dynamic balancing of the second prototype rotor is carried out in stages. Initially, the rotor is accelerated until the level of vibration became unacceptable. The rotor is then balanced at that speed using an in-situ two-plane dynamic balancing procedure. The rotor is then accelerated to the next speed at which the level of vibration becomes unacceptable and the balancing procedure is repeated at this speed. This process is repeated until an acceptable level of balance is achieved at full speed. The principal effect of this process is that, although the rotor is balanced for operation at full speed, there are lower speeds at which there may be significant unbalances, as shown in Figure 3.17.

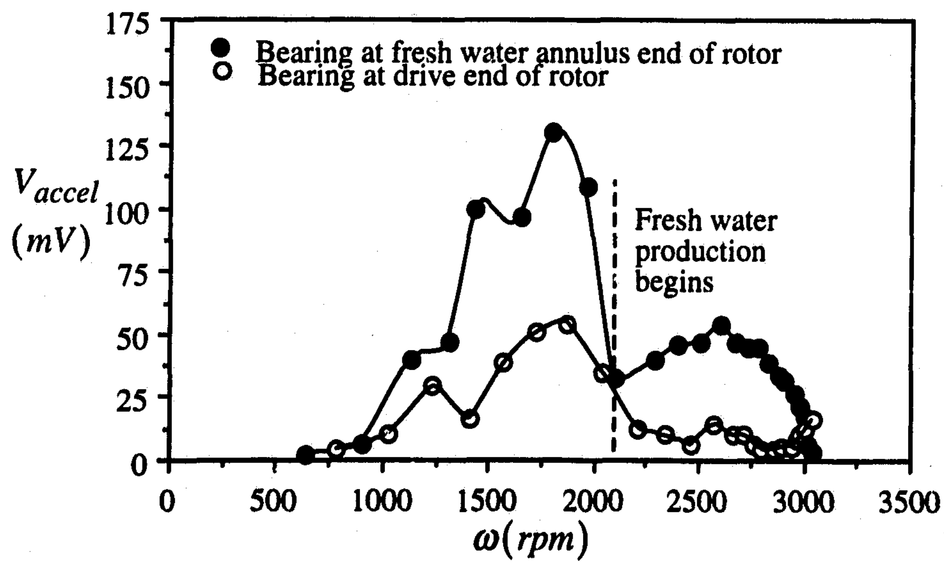

Figure 3.17 - Rotor Vibration vs Rotor Speed for Second Prototype

The relative magnitude of the RMS acceleration associated with the vibration at each of the rotor bearings is plotted against rotor speed. The peak value of vibration occurs just prior to the onset of fresh water production. The rotor is balanced to compensate for the annulus of fresh water and, therefore, the absence of fresh water at lower speeds results in an unbalance. The levels of vibration then decline to a minimum at the operating speed.

3.3.6 Noise Levels

One of the principal incentives for the development of CRO was the expectation that the noise levels associated with CRO would be significantly lower than the noise levels associated with conventional RO. The second prototype fulfills this expectation as its noise levels are below Airborne Noise Control level ANC 100, as shown in Figure 3.18. These measurements were taken in accordance with the Specification for Airborne Noise Levels in Canadian Forces Vessels (D-03-003-012/SF-000). ANC 100 is considered acceptable for auxiliary machinery rooms in which desalination systems are installed.

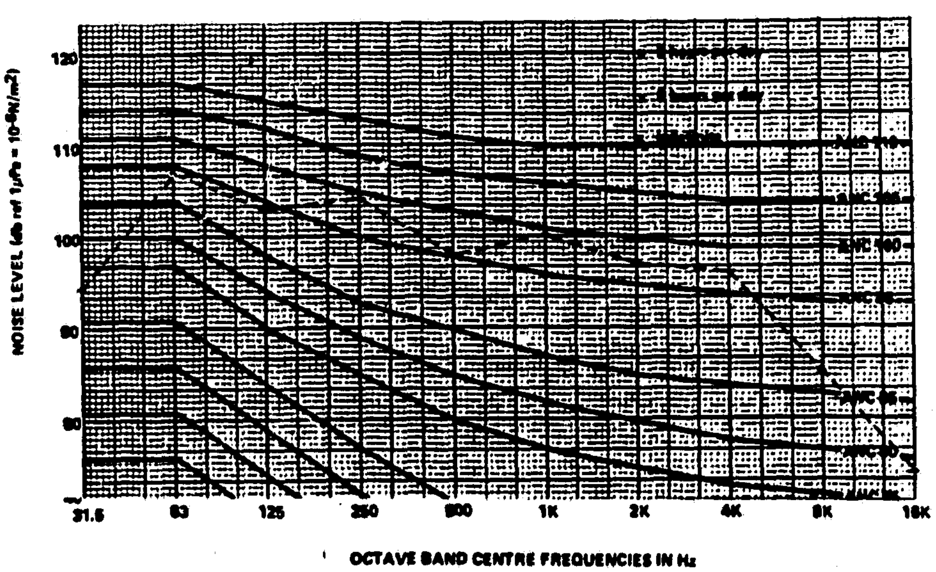

Figure 3.18 - Airborne Noise Levels of Second Prototype

Over the last decade, both the U.S. and Canadian Navies have spent a great deal of time and money bringing conventional RO systems within these noise and vibration specifications. The second prototype CRO unit, with no special noise abatement measures, is already within specification. The potential for reduction of the CRO noise levels to levels well below the specification is as yet untapped.

3.4 Assessment of First and Second Prototype and Potential for Further Development

The first prototype fulfilled its intended function in that it verified that CRO is an alternative means by which to develop the process pressure which is required to perform desalination of sea water with reverse-osmosis. Potable water was produced at levels of salinity and at flow rates which are equivalent to the salinities and flow rates which would be expected from a conventional reverse-osmosis unit. No fundamental difficulties, other than those which were anticipated and discussed in Chapter 2, were encountered. Furthermore, the design solutions to the difficulties which were identified in Chapter 2 proved to be successful.

The weaknesses in the design of the first prototype, relating principally to power consumption and to reliability were, for the most part, addressed in the design of the second prototype. Losses in the bearings and seals as well as the flow losses through the static rotor were significantly lower in the second prototype. The second prototype had a higher membrane configuration volume ratio, corrosion of key components was entirely eliminated and the vacuum system was more reliable.

Losses due to windage, bearings and seals require further reduction if the projected energy benefits of CRO are to be fulfilled. In order to gain a more complete understanding of windage losses, so that these losses can be accurately predicted in future designs, an experimental and computational study, as described in Chapter 4, has been conducted.

Another aspect of CRO energy consumption which requires detailed examination is losses resulting from fluid flow friction through the rotor. In both the first and second prototypes, these losses were strongly increasing functions of rotor speed. In order to gain a greater understanding of the nature of these losses and, subsequently, to reduce their magnitude, an experimental study was undertaken. The findings of this study are reported in Chapter 5.

With respect to refinement of the physical embodiment of the design, a detailed reassessment of the details of the second prototype is warranted. As part of this reassessment, a new method with which to assess the stresses and deformations in a filament wound composite shell under combined centrifugal and pressure loading has been developed. The results of this study are reported in Chapter 6.

References

1. Fluid Systems Product Literature, Temperature Effect, 1990

2. Bilgen, E, Boulos, R, Functional Dependence of Torque Coefficient of Coaxial Cylinders on Gap Width and Reynolds Numbers, Journal of Fluids Engineering, March 1973, pp. 122-126.

3. Schlichting, H., Boundary Layer Theory, 4th ed.,McGraw-Hill, New York, 1960, p. 547.

Chapter 4
An Experimental and Computational Investigation of Windage Losses Associated with a Rotating, Enclosed and Immersed Cylinder

4.0 Introduction

The nature of the flow in a viscous fluid contained between concentric cylinders, where the inner cylinder is rotating and the outer cylinder is stationary, is of general interest in many engineering applications. These applications include the design of rotating equipment such as turbines, pumps, motors, generators and centrifuges as well as the design of the journal bearings which, in some cases, support these various rotors. The flow characteristics which are of particular interest vary with the application. In motor design, heat transfer and frictional losses are the key parameters while, in journal bearings, the pressure distribution and, thus, the load carrying capability are of particular interest.

As is discussed in Chapters 2 and 3, windage losses are a significant component of the power consumption of CRO and the assessment of the effect of alternative design configurations have on these losses is, therefore, an essential component of the design process. A study has, therefore, been conducted, involving a comprehensive review of relevant literature and both computational and experimental analyses, whose objective is to establish a practical design approach to the problem of windage torque assessment.

4.1 Review of Relevant Literature

There is a vast body of literature related to the problem of flow around a cylindrical rotor immersed in a fluid and rotating within a stationary concentric cylindrical housing. Some of the incentive for this considerable volume of work has been the many engineering applications in which this geometry is encountered. Much of the work however, especially in recent years, has focused on transitions in the turbulent flow regimes and, as such, has been directed more toward a general understanding of turbulence than toward more specific engineering applications.

The geometry of concern, shown schematically in Figure 4.1, consists of an inner cylinder of radius, R_i, and of length, L, rotating with angular velocity, ω. This cylinder is enclosed in an outer stationary cylinder of radius, R_o. The axial gap width, g_a, is the distance between the end of the inner cylinder and the end of the outer cylinder. The radial gap width, g_r, is the distance from the outer surface of the inner cylinder to the inner surface of the outer cylinder.

With only a very few exceptions, researchers in this area have divided this geometry into two zones: the radial gap between the inner and outer cylinders, and the axial gap between the inner and outer cylinders. The first zone is often further simplified to an infinitely long annular chamber. The second zone, is generally addressed as a thin disc.

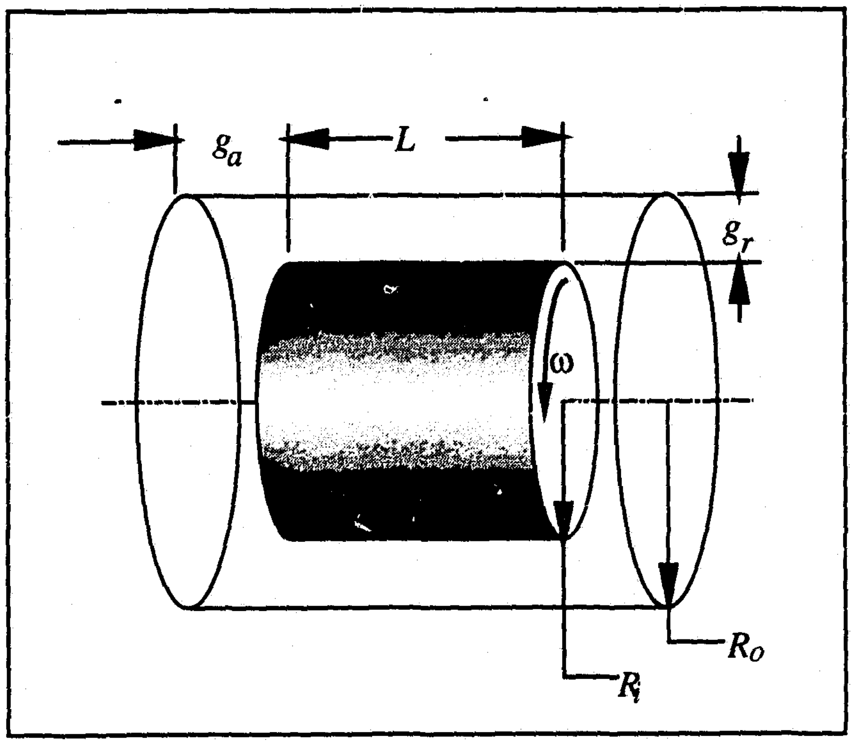

Figure 4.1 - Rotor and Enclosure Geometry and Notation

4.1.1 The Similarity Argument

Similarity analysis of the torque associated with the first zone, the annular chamber, produces certain dimensionless groups in terms of which most of the theoretical and experimental data in the literature are expressed. If end effects are neglected, which is equivalent to assuming a cylinder of infinite length, it is generally assumed that the moment, M_{CYL}, experienced by the outer surface of a cylindrical rotor immersed in a fluid and rotating in a stationary cylindrical housing is a function of rotor radius, R_i, radial gap width, g_r, rotor length, L, speed of rotation, ω, and the density , ρ_{encl} , and viscosity, μ_{encl} , of the fluid in the rotor enclosure.

One possible combination [1] of these parameters which emerges from similarity analysis is,

$$\frac{M_{CYL}}{\rho_{encl}\omega^2 R_i^4 L} \propto f\left(\frac{g_r}{R_i}, \frac{\rho_{encl}\omega R_i g_r}{\mu_{encl}}\right) \tag{4.1}$$

The moment coefficient, $C_{M_{CYL}}$, for a cylindrical rotor is commonly defined as the shear stress at the surface of the rotor divided by the pressure which is developed in an equivalent cylinder of rotating fluid.

$$C_{M_{CYL}} = \frac{\tau}{\frac{1}{2}\rho_{encl}\omega^2 R_i^2} \tag{4.2}$$

The shear stress at the rotor surface is,

$$\tau = \frac{M_{CYL}/R_i}{2\pi R_i L} \tag{4.3}$$

and, substituting this expression into (4.2),

$$C_{M_{CYL}} = \frac{M_{CYL}}{\pi\rho_{encl}\omega^2 R_i^4 L} \propto f\left(\frac{g_r}{R_i}, \frac{\rho_{encl}\omega R_i g_r}{\mu_{encl}}\right) = f\left(\frac{g_r}{R_i}, Re\right) \tag{4.4}$$

where Re is the Couette Reynolds Number defined as

$$Re = \frac{\rho_{encl}\omega R_i g_r}{\mu_{encl}} \tag{4.5}$$

From (4.4) it can be seen that, for a given ratio of rotor radius to gap width, there should be a one-to-one correspondence between the moment coefficient and the Couette Reynolds Number. In addition, the arguments of the function, f, combine to form a dimensionless group known as the Taylor number,

$$Ta = Re\sqrt{\frac{g_r}{R_i}} = \frac{\rho_{encl}\omega\sqrt{R_i}g_r^{3/2}}{\mu_{encl}} \tag{4.6}$$

The Taylor number is widely used in the analysis of this kind of flow.

4.1.2 Flow Regimes, Transitions and Stability

At low speeds, the flow between a rotating cylinder and a stationary concentric cylindrical housing is laminar and two dimensional but at a critical speed, this two dimensional flow becomes unstable and is superseded by a three dimensional steady flow. The pioneering work in this area was done by G.I. Taylor [2, 3, 4]. This three dimensional flow is characterized by pairs of annular vortices spaced axially along the gap between the inner and outer cylinder, as shown in Figure 4.2.

Taylor derived a relation for the critical speed at which this instability leads to the formation of these "Taylor vortices" for the case where the radial gap, g_r, is small compared with the radius of the rotor, R_i. This critical speed, ω_c, can be expressed as follows

$$\omega_c^2 = \frac{\pi^4\left(\frac{\mu_{encl}}{\rho_{encl}}\right)^2 (R_i + R_o)}{2Z \cdot g_r^3 R_i^2} \tag{4.7}$$

where,

$$Z = 0.0571(1 - 0.652 g_r / R_i) + 0.00056(1 - 0.652 g_r / R_i)^{-1} \quad (4.8)$$

The transition to Taylor vortices is usually referred to in terms of a critical Taylor number.

$$Ta_c = \frac{\rho \omega_c \sqrt{R_i} g_r^{3/2}}{\mu} \quad (4.9)$$

Taylor's own experimental results and those of many subsequent researchers [5, 6, 7, 8] verified the validity of Taylor's relation.

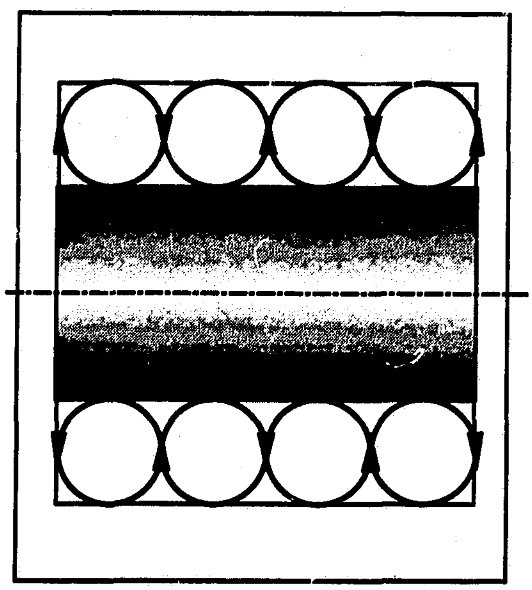

Figure 4.2 - Taylor Vortices

At a speed beyond the critical speed the Taylor vortices take on unsteady azimuthal oscillations known as "wavy vortices" [9, 10, 11]. At still higher speeds, these wavy vortices give way to a "noisy" turbulent flow in which the vortex structure persists but the azimuthal oscillations are extinguished [9, 12]. With respect to torque, the slope of a torque versus speed plot increases at the transition to steady Taylor vortices and then decreases slightly at the transition to wavy vortices [13, 14]

An important feature of Taylor vortex flow, in all three regimes, is that the spatial frequency of the vortices is not unique. Coles' experiments [9] showed that as many as twenty-six stable spatial states could exist at a given rotor speed. If the rotor is accelerated slowly from rest, there is a preferred spatial frequency called the primary mode. If initial conditions are varied, the resulting spatial frequency may be higher or lower, resulting in what are generally referred to as "anomalous modes" [15] In recent years, much of research related to the Taylor problem has dealt with the conditions of stability of the primary and of the anomalous modes. It was, however, observed by Cole [16] that measured torque was not affected by changes in mode of the Taylor flow at a given speed. This finding is of particular relevance to the present research.

Although most of the work on Taylor flow neglects the effect of the rotor ends by assuming cylinders of infinite length, some researchers have addressed aspects of the complications which the rotor ends introduce. The influence of end effects on Taylor vortex formation and transition was first investigated by Cole [14]. He showed that the onset of steady Taylor vortices was relatively insensitive to rotor length but that the onset of wavy vortices was relatively sensitive to the length of the rotor. Burkhalter [12] showed that the length of the vortex cells at the ends of an annulus was a function of both rotor speed and of the conditions at the ends of the annulus. Schaefer [17], Mullin [18] have conducted numerical investigations of the influence of end effects on the stability of anomalous modes. There is, however, no literature which deals directly with the influence of rotor length on windage torque.

4.1.3 Theoretical, Empirical and Semi-Empirical Functional Torque Relations

Considerable research has been done in an attempt to determine a functional relationship defining the moment experienced by the outer surface of the rotor. This work spans the range from purely theoretical to purely empirical and presents a variety of relations, each of which is intended to apply under certain conditions.

For simple, two dimensional laminar flow an expression for $C_{M_{CYL}}$ can readily be derived from the definition of viscosity and appears as,

$$C_{M_{CYL}} = \frac{4\mu R_o^2}{\rho\omega\left(R_o^2 - R_i^2\right)R_i^2} \tag{4.10}$$

where R_o is the inner radius of the rotor housing. It can be shown that this expression is a function only of the Couette Reynolds Number and of the ratio of rotor radius to gap width as is anticipated by the similarity analysis presented above. This relation has been shown to have good accuracy and is used as a basis for the measurement of viscosity.

For super critical speeds, the relations for the moment coefficient fall into two general categories. The first category assumes that the moment coefficient will scale with the Reynolds number, taken to some power.

$$C_{M_{CYL}} \propto Re^{-\kappa} \tag{4.11}$$

Note that equation (4.10) for laminar flow is a special case of this category where $\kappa = 1$. Relations falling into the second category assume that the nature of the drag on the rotating cylinder is fundamentally similar to the Prandtl-von Karman logarithmic velocity distributions and will, therefore, be characterized by a relation of the form,

$$\frac{1}{\sqrt{C_{M_{CYL}}}} = A + B\,ln\left(Re\sqrt{C_{M_{CYL}}}\right) \tag{4.12}$$

where A and B are constants.

The earliest relations of the first category were developed by Wendt [6]. These relations cover two ranges of Re above the critical speed.

$$C_{M_{CYL}} = 0.46\left[\frac{(R_o - R_i)R_o}{R_i^2}\right]^{\frac{1}{4}} Re^{-0.5} \qquad (400 < \mathrm{Re} < 10^4) \tag{4.13a}$$

$$C_{M_{CYL}} = 0.073\left[\frac{(R_o - R_i)R_o}{R_i^2}\right]^{\frac{1}{4}} Re^{-0.3} \qquad (\mathrm{Re} > 10^4) \tag{4.13b}$$

Stuart [19] developed a relation for the moment coefficient for speeds greater than but close to the critical speed. Based on experimental data, Donelly [1] recast Stuart's solution to apply over a range of supercritical speeds of up to several hundred times the critical speed.

$$C_{M_{CYL}} = a\omega^{-1} + b\omega^{n} \qquad \left(\frac{4}{3} < n < \frac{3}{2}\right) \tag{4.14}$$

The first term in this formulation accounts for the laminar component of the flow with $\kappa = 1$ while the second term accounts for the effects of the Taylor vortices. Donelly was able to achieve good fits with experimental data from a variety of researchers using $n = 1.36$. The coefficients, a and b, however were determined independently for each physical configuration by fitting the curve through the data points. As a predictive method, therefore, this relation is of little use.

For speeds well beyond the critical, Donelly suggests a relation of a form similar to that proposed by Wendt.

$$C_{M_{CYL}} \propto Re^{-0.5}\left(\frac{g_r}{R_i}\right)^{0.31} \tag{4.15}$$

This relation is developed further by Bilgen and Boulos [20] who refined the exponents and coefficient by fitting curves through the data collected by a number of previous researchers.

$$C_{M_{CYL}} = 0.515\, Re^{-0.5}\left(\frac{g}{R_i}\right)^{0.3} \qquad \mathrm{Re} < 10^4 \tag{4.16a}$$

$$C_{M_{CYL}} = 0.0325\, Re^{-0.2}\left(\frac{g}{R_i}\right)^{0.3} \qquad \mathrm{Re} > 10^4 \tag{4.16b}$$

Comparing the relations developed by Bilgen and Boulos in 1973 with those developed by Wendt in 1933 it is apparent that the pursuit of a functional relation of the first category progressed very little in the intervening forty years. In a recent paper, Lathrop

[21] used exceptionally sensitive torque measurements to determined that, contrary to Wendt and Bilgen, there are no ranges of Reynolds numbers over which a constant-exponent torque relation, such as 4.15, holds. Rather, Lathrop found that there were ranges over which the exponent varied continuously.

The first researcher to determine a relation of the second category, based on the Prandtl-von Karman logarithmic velocity distributions, was Theodorsen [22].

$$\frac{1}{\sqrt{C_{M_{CYL}}}} = -0.6 + 1.767\, ln\left(Re\sqrt{C_{M_{CYL}}}\right) \tag{4.17}$$

This relation applies only to a rotating cylinder which is not enclosed. Gazely [23] developed this form for an enclosed rotating cylinder,

$$\frac{1}{\sqrt{C_{M_{CYL}}}} = 5.466 + 3.536\, ln\left(Re\sqrt{C_{M_{CYL}}}\right) \tag{4.18}$$

Vrancik [24] also reported that this expression produced good agreement with his experimental data.

Ustimenko (cited in [25]), developed a relation which, at lower speeds, is of the first category and, at higher speeds, is of the second category. Where vortex flow dominates,

$$C_{M_{CYL}} = 0.476\, Re^{-0.5}\left(\frac{g_r}{R_i}\right)^{0.25} \tag{4.19}$$

and where turbulent flow dominates,

$$\frac{1}{\sqrt{C_{M_{CYL}}}} = 8.58 + 1.697\left(\frac{1+0.5(g_r/R_i)}{1+(g_r/R_i)}\right) ln\left(\frac{Re\sqrt{C_{M_{CYL}}}}{1.697(1+(g_r/R_i))}\right) \quad (4.20)$$

The transition between these two flow regimes is defined as the point at which the moment coefficient arising from the second relation exceeds the moment coefficient arising from the first.

Lathrop [21] also determined a relation of the second category,

$$\frac{1}{\sqrt{C_{M_{CYL}}}} = -\frac{(2.22+1.17\,ln(g_r/R_i))}{(g_r/R_i)} + \frac{1.17}{(g_r/R_i)} log\left(Re\sqrt{C_{M_{CYL}}}\right) \quad (4.21)$$

This relation gave good agreement for the particular geometry of Lathrop's experimental apparatus but it was not intended to be broadly applicable to other geometries. This is the most recent relation of the second category to appear in the literature.

Of these numerous relations, only Wendt, Bilgen and Boulos and Ustimenko are relatively consistent among themselves over a range of Reynolds numbers and radial gap width to radius ratios, as shown in Figure 4.3.

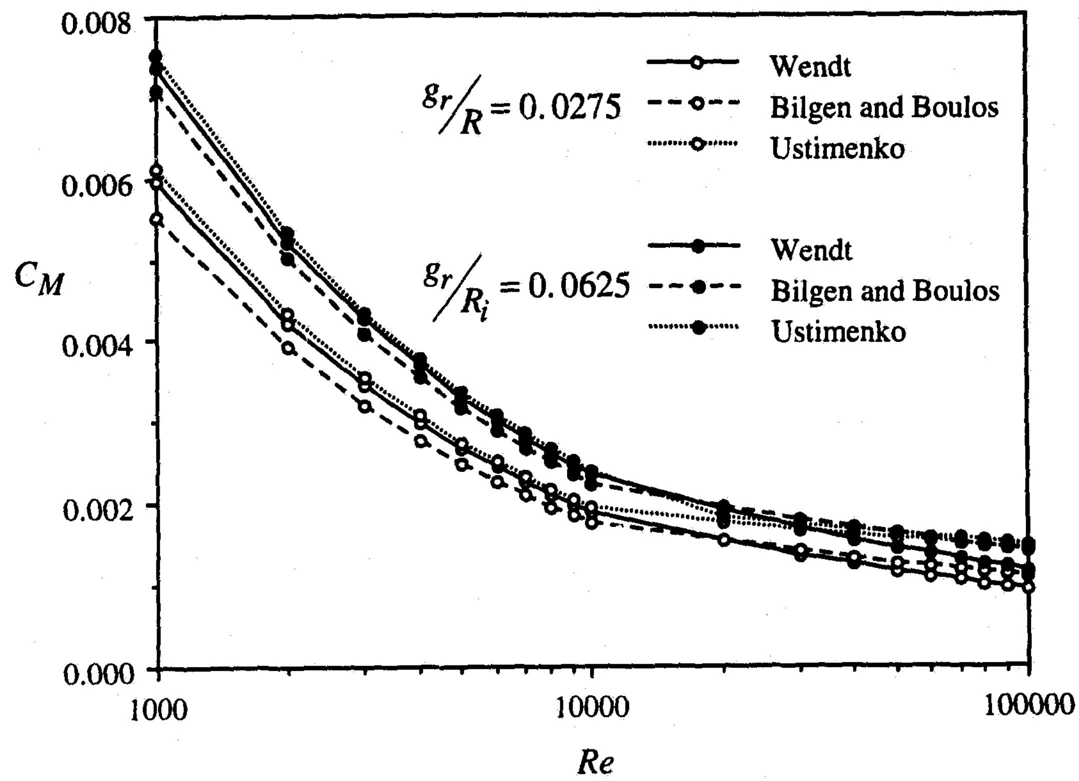

Figure 4.3 - A Comparison of the Functional Relations for Moment Coefficient

4.2 Experimental Apparatus

The windage test rig consists of a drive motor connected via a belt drive to a cantilevered cylindrical rotor, housed in a stationary cylindrical enclosure, as shown in Figures 4.4 and 4.5. The rotor enclosure is mounted on bearings at either end, and it is restrained from rotating by a length of 3.2 mm x 25.4 mm (0.125 x 1 inch) aluminum flat bar. For future work, the housing bearings are mounted on vertical and horizontal slides which allow the housing to be set eccentric to the rotor. The reaction torque of the rotor housing due to windage is measured via strain gages on the flat bar. The dimensions of the rotor and rotor enclosure were determined from similarity considerations with respect to proposed desalinator designs and are shown in Table 4.1. The maximum operating speed of the rotor was 4,750 rpm, corresponding to a Couette Reynolds Number of almost 15,000. The surfaces of the rotor and enclosure are machined to approximately 0.8 microns (32 microinches) of roughness. Torque data was taken repeatedly at 500 rpm intervals and the resulting moment coefficients were determined to have an uncertainty interval of ± 0.00012 (odds of 20 to 1).

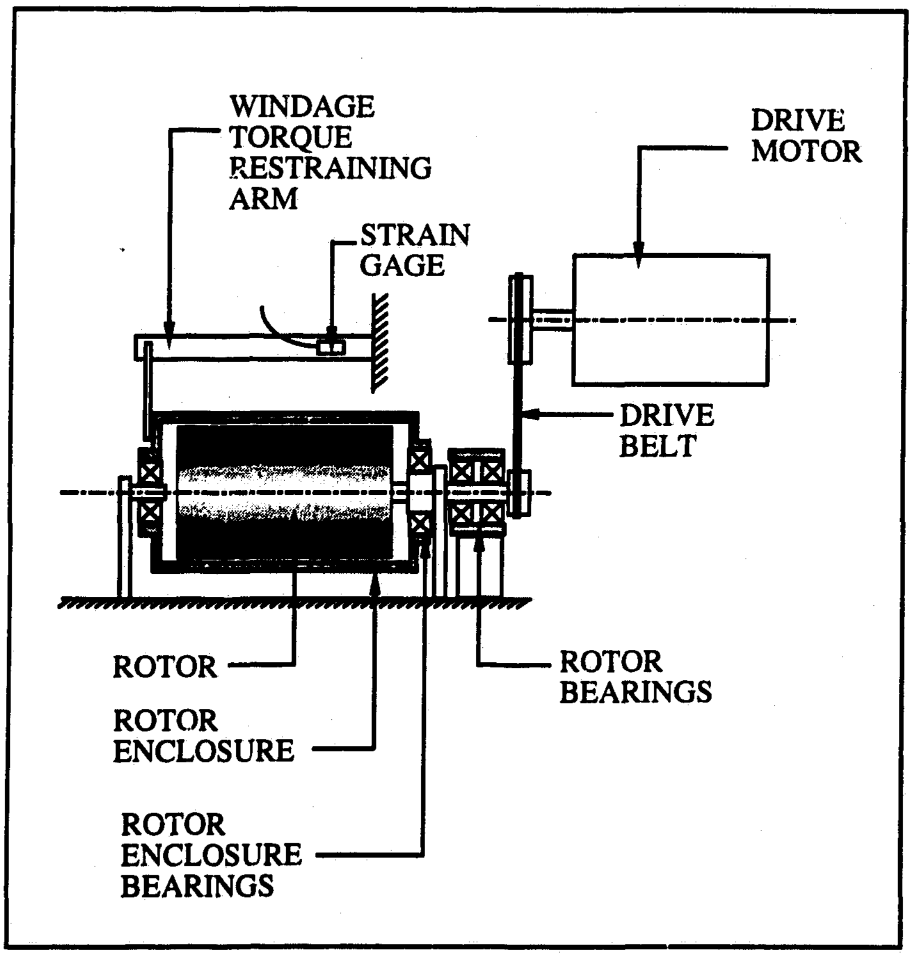

Figure 4.4 - Schematic View of Experimental Windage Apparatus

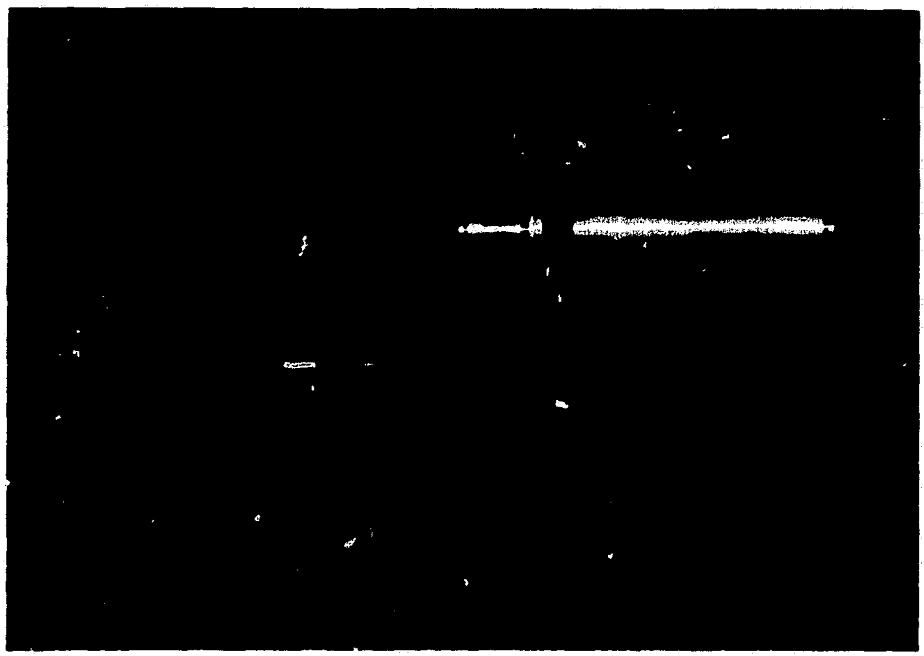

Figure 4.5 - Photograph of Experimental Windage Apparatus

	Small Rotor	Large Rotor
Rotor Radius (R_i)	0.1284 m (5.059 in)	0.1328 m (5.231 in)
Housing Inner Radius(R_o)	0.1364 m (5.375 in)	0.1364 m (5.375 in)
Radial Gap Width (g_r)	0.008 m (0.316 in)	0.0036 m (0.144 in)
Radial Gap Width to Rotor Radius Ratio $\left(g_r / R_i \right)$	0.0625	0.0275
Rotor Length (L)	0.2568 m (10.118 in)	0.2656 m (10.463 in)
Axial Gap Width (g_a) All dimensions ± 50 microns (0.002 inches) Maximum run-out 100 microns (0.004 inches)	0.0381 m (1.5 in)	0.0381 m (1.5 in)

Table 4.1 - Test Rig Rotors and Enclosure Dimensions

4.3 Computational Analyses

4.3.1 Problem Formulation

The computational analysis was conducted for the same geometry and operating conditions as the experimental analyses. The computational domain and coordinate system is shown in Figure 4.6.

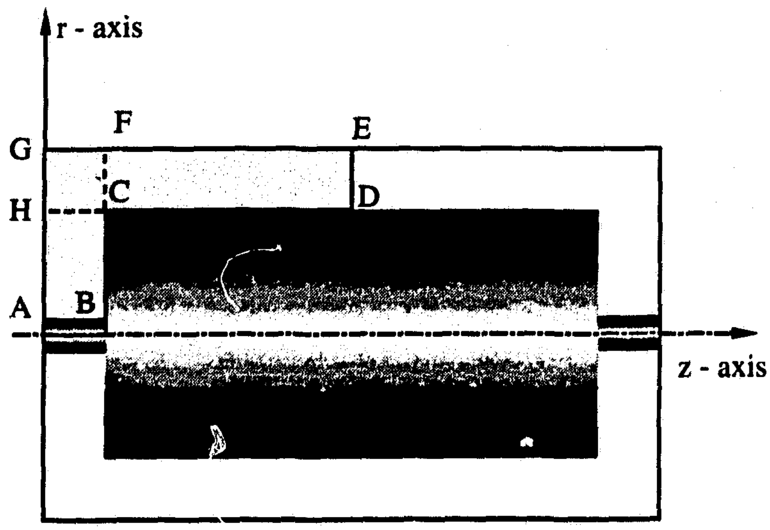

Figure 4.6 - Computational Domain

The flow is assumed to be steady, incompressible and turbulent, and all fluid properties are assumed constant. The flow is also assumed to be axisymmetric, and the problem can therefore be treated as a two-dimensional one, in the sense that gradients in the azimuthal direction are neglected, but all three velocity components are taken into account. With these assumptions, the time-averaged mass and momentum conservation equations may be written as:

$$\frac{\partial}{\partial x}(\rho u)+\frac{1}{r}\frac{\partial}{\partial r}(\rho r v)=0 \tag{4.21}$$

$$\frac{1}{r}\left[\frac{\partial}{\partial x}(\rho r u \phi)+\frac{\partial}{\partial r}(\rho r v \phi)\right]=\frac{\partial}{\partial x}\left(\mu_{eff}\frac{\partial \phi}{\partial x}\right)+\frac{1}{r}\frac{\partial}{\partial r}\left(r\mu_{eff}\frac{\partial \phi}{\partial r}\right)+S_{\phi} \quad (4.22)$$

where $\phi = u, v, w$ respectively for the three momentum equations in the x, r and θ directions, and S_{ϕ} is the source term defined in Table 4.2 for the three components of velocity.

The turbulent eddy viscosity μ_{eff} is modeled using the standard $k-\varepsilon$ model [24]. The details of the $k-\varepsilon$ model are discussed in Appendix III.

ϕ	S_{ϕ}
u	$-\frac{\partial p}{\partial x}$
v	$-\frac{\partial p}{\partial r}+\rho\frac{w^2}{r}-\mu_{eff}\frac{v}{r^2}$
w	$-\rho\frac{vw}{r}-\mu_{eff}\frac{w}{r^2}$

Table 4.2 - Source Terms in Momentum Equations

4.3.2 Boundary Conditions

The governing equations are solved in a computational domain shown in Figure 4.6, with the following boundary conditions:

(i) At the axis of symmetry (D-E), the normal gradients of all variables are set to zero, and the convective flux normal to the boundary is set to zero.

(ii) No slip condition is imposed at all walls for the velocity; the equilibrium wall function treatment is adopted to bridge the viscous sublayer. To ensure proper implementation of the wall functions, the grid points adjacent to solid boundaries were located such that $30 < y^+ = yu_\tau / \nu < 100$.

4.3.3 Numerical Solution Parameters

The equations were solved using the finite volume code FLUENT [26]. This code uses a collocated grid method. The higher order QUICK discretization scheme was employed in conjunction with the SIMPLEC algorithm. A block iterative solution method was used to together with a multigrid procedure to accelerate convergence. The calculation procedure was terminated when the normalized residuals were less than 5×10^{-4}.

4.3.4 Grid Refinement

The grid sensitivity of the solutions was assessed at a Couette Reynolds number of 1.58×10^3 (corresponding to 5000 rpm). Grid refinement was conducted in two stages. First computations were performed for a non-uniform base grid of 80 x 50 grid, and two successive refinements were performed. The predicted flow field and shear stresses in the radial gap region (CDEF) varied significantly, but the predictions in the axial gap region (ABFG) were essentially identical for the three grids as shown in Figs. 4.7 and 4.8.

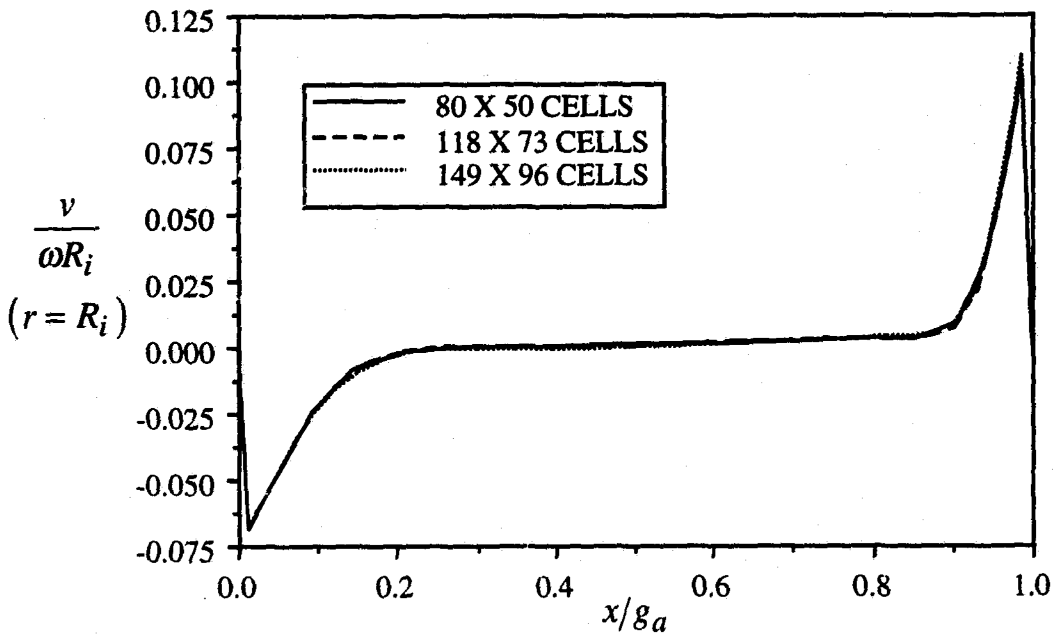

Figure 4.7 - Radial Velocity Profile Across Axial Gap at $(r = R_i),(g_r/R_i = 0.0625)$

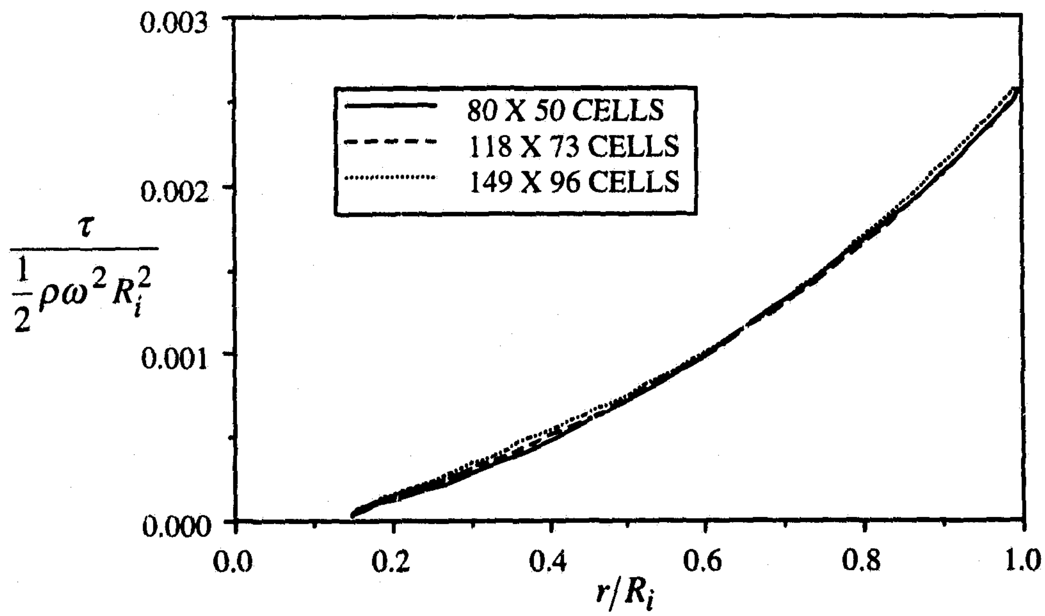

Figure 4.8 - Azimuthal Shear Stress on Rotor End Surface $(g_r/R_i = 0.0625)$

Based on these results, a second series of grid refinements was performed in region DEGH, while keeping the same 18 x 34 grid in the axial gap region. The results of this series of grid refinements are summarized in Table 4.3 in terms of the torques calculated for the different segments. A maximum difference of 2% is obtained between the finest and coarsest grid. The streamline patterns obtained with the 140 x 56 grid shown in Figure 4.9 clearly depict the Taylor vortices in the radial gap and the large counter-clockwise vortex in the axial gap.

	Wall Segment Designations			
Grid Size	B-C	C-D	G-E	A-G
109 X 56	-4.085E-05	-1.609E-04	1.769E-04	1.860E-05
140 X 56	-4.092E-05	-1.609E-04	1.780E-04	1.847E-05
170 X 56	-4.092E-05	-1.598E-04	1.775E-04	1.850E-05
230 X56	-4.091E-05	-1.584E-04	1.757E-04	1.854E-05

Table 4.3 - Average moment coefficients for four grid densities (5000 rpm)

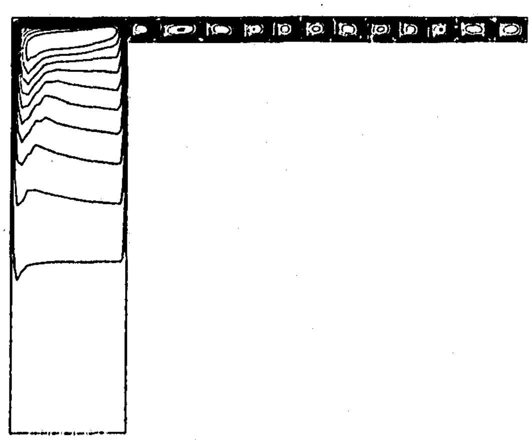

Figure 4.9 - Streamline Pattern (140 x 56 at 5000 rpm), $(g_r/R_i = 0.0625)$

The number of vortices obtained with all three grids were identical, but noticeable differences are observed in the wavelengths as shown by the axial distribution of the radial velocities and azimuthal shear stresses, as presented in Figures 4.10 and 4.11. When averaged along the cylinder, the shear stresses yield similar values for the moment coefficient as was seen in Table 4.3. In light of this relative insensitivity of azimuthal shear forces to grid density, the 140 x 56 grid was used for parametric studies of radial gap width, annulus length and rotor speed.

In order to assess the effect of assuming the symmetry boundary condition along ED (see Figure 4.6), calculations were performed for the entire length of the rotor with both end gaps using a 218 x 56 grid. The computed torques were within 1% of those obtained with the 109 x 56 computations for the half domain, but 11 instead 12 Taylor vortices were obtained. The non-uniqueness of the number of Taylor vortices has been observed in a number of instances during this study and in other experimental and computational studies in the literature. It is possible in this instance that the numerical perturbations associated with the two different computational domains result in two different physical solutions. It is also interesting to note that Cole [16] observed that measured torque was not affected by changes in mode of the Taylor flow at a given speed. Further analysis of the computational results will be presented with the measurements.

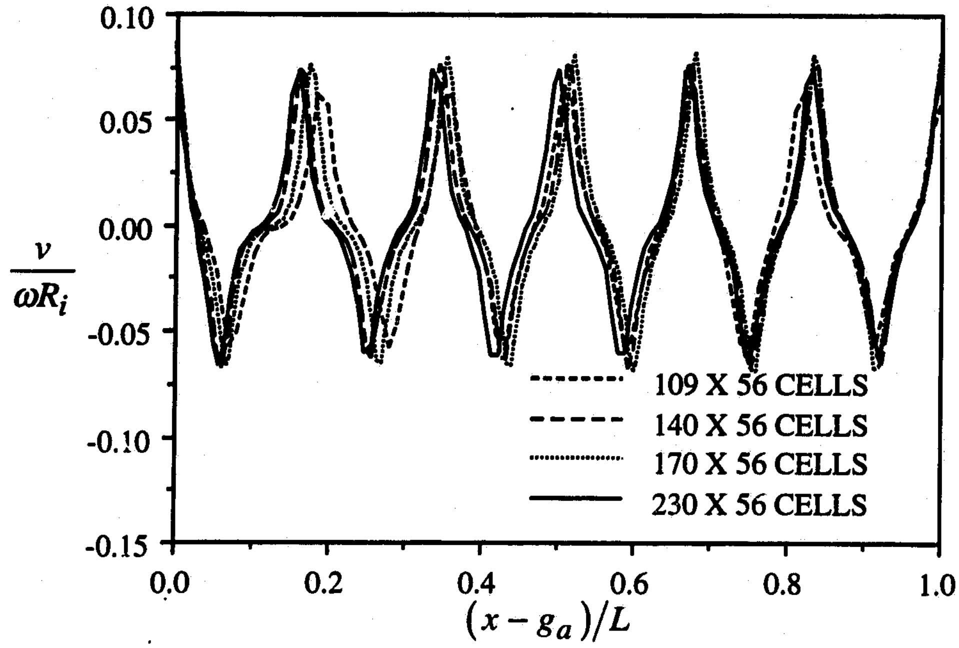

Figure 4.10 - Radial Velocity Along Center Line of Radial Gap $\left(g_r/R_i = 0.0625\right)$

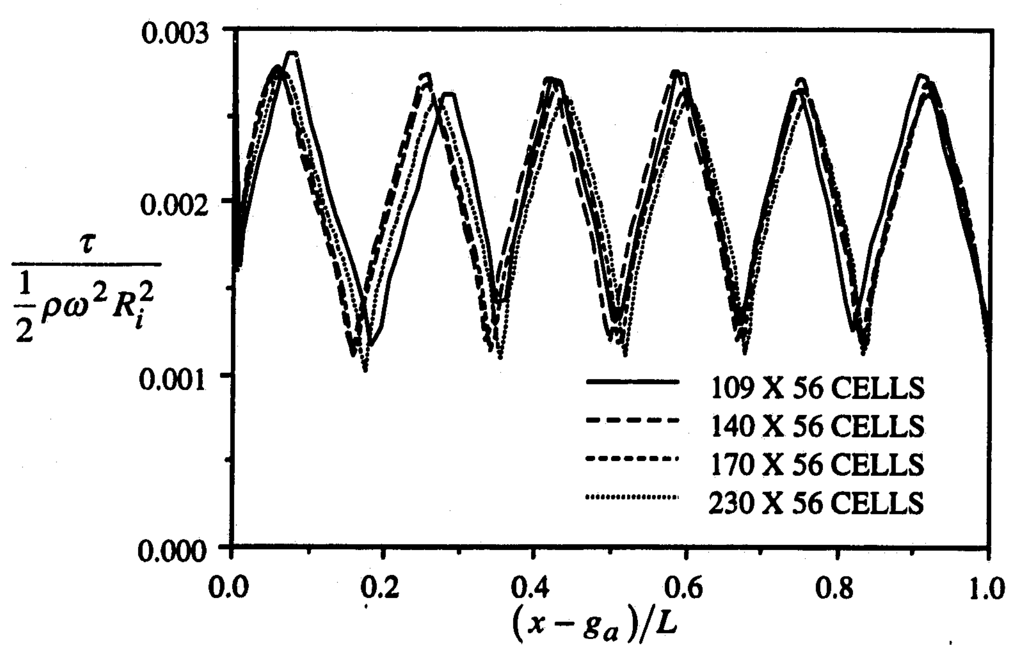

Figure 4.11 - Shear Force Along Outer Surface of Rotor $\left(g_r/R_i = 0.0625\right)$

4.4 Comparison of Windage Data Determined from Functional Relations, CFD Analysis and Experiments

The present computed and measured moment coefficients are compared to the relations of Wendt [6], Bilgen & Boulos [20] and Ustimenko [25] in Figures 4.12 and 4.13. Since these relations are for infinite cylinders, a correction for end effect was added. Following Schlichting [27], the additional torque due to end effects is assumed to be equal to that of an enclosed thin disk. The experimental data for $g_r/R = 0.0275$ spans $5,000 < Re < 17,000$ and the data for $g_r/R_i = 0.0625$ spans $18,000 < Re < 35,000$.

The semi-empirical relations and experiments are in relatively good agreement, while the present computations give values which are consistently on the order of 10% higher than the experiments. Between 25% and 27% of the CFD generated moment coefficients shown in Figures 4.12 and 4.13 is due to the moments on the end surfaces of the rotor whereas, for the functional relations, between 15.5% and 18.5% of the moment coefficients is due to the moments on the end surfaces. In order to eliminate any inconsistencies which these differences may be introducing, the CFD data and data calculated after Wendt, for the cylindrical surface of the rotor only, are plotted in Figures 4.14 and 4.15. The spread between these data sets is not significantly different than the spread shown in Figures 4.12 and 4.13.

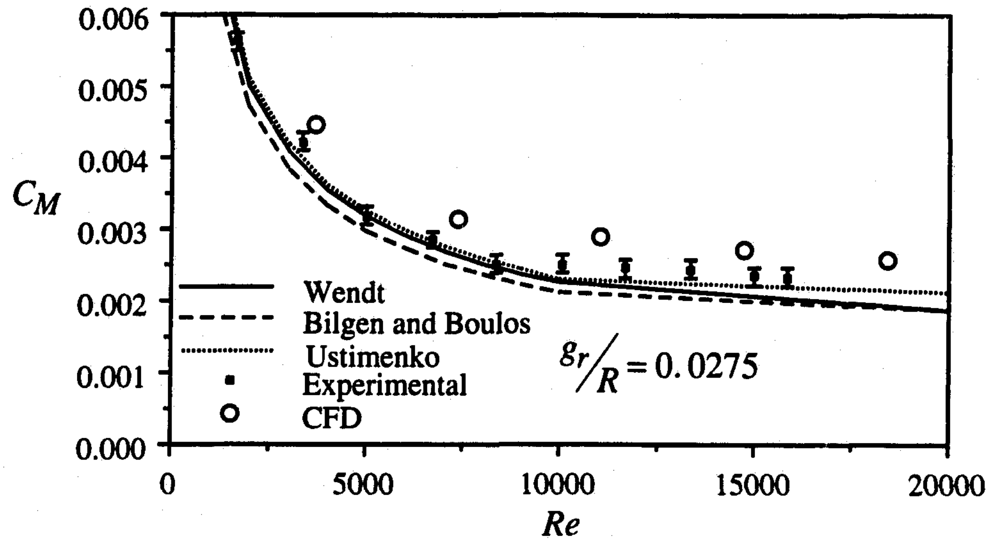

Figure 4.12 - Moment Coefficient versus Reynolds Number for $g_r/R = 0.0275$

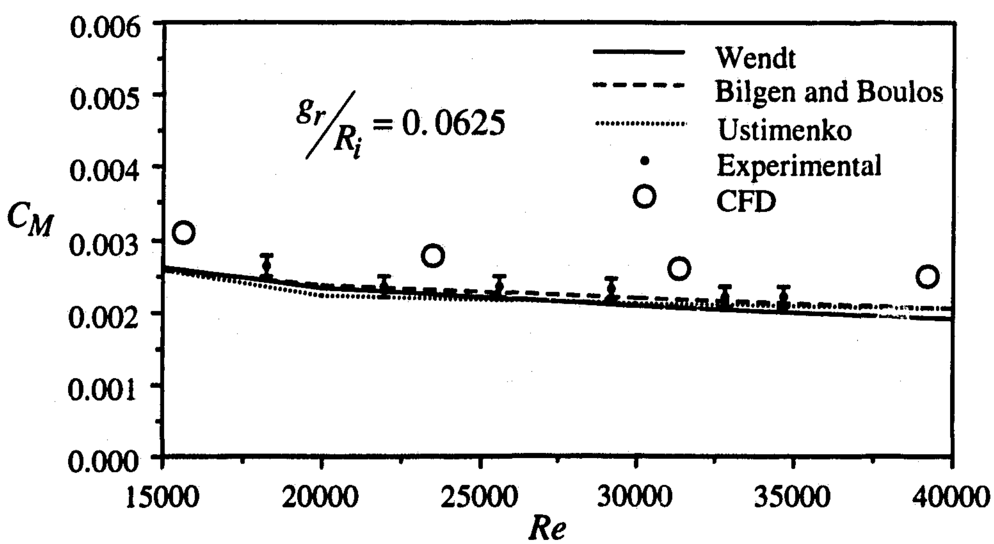

Figure 4.13 - Moment Coefficient versus Reynolds Number for $g_r/R_i = 0.0625$

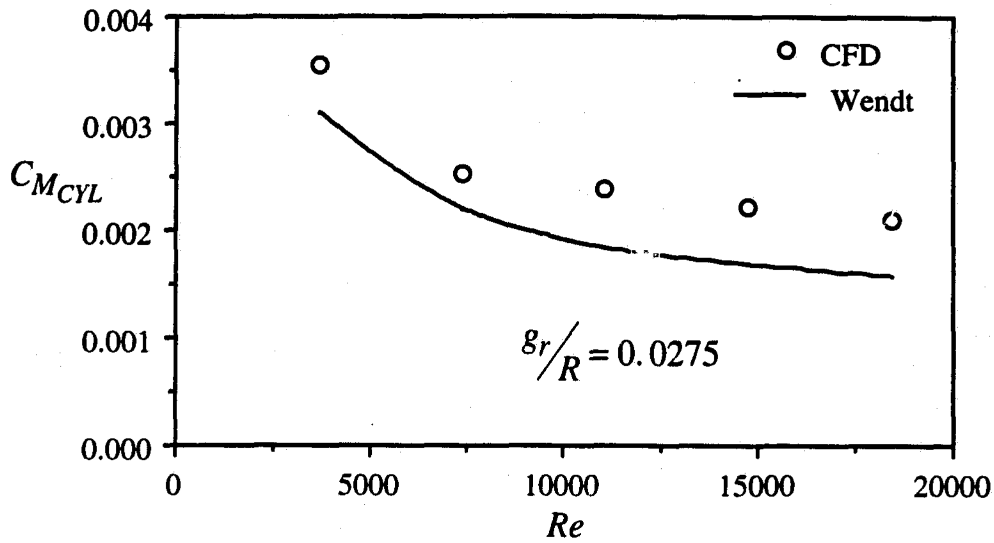

Figure 4.14 - Cylinder Moment Coefficient versus Reynolds Number for
$g_r/R = 0.0275$

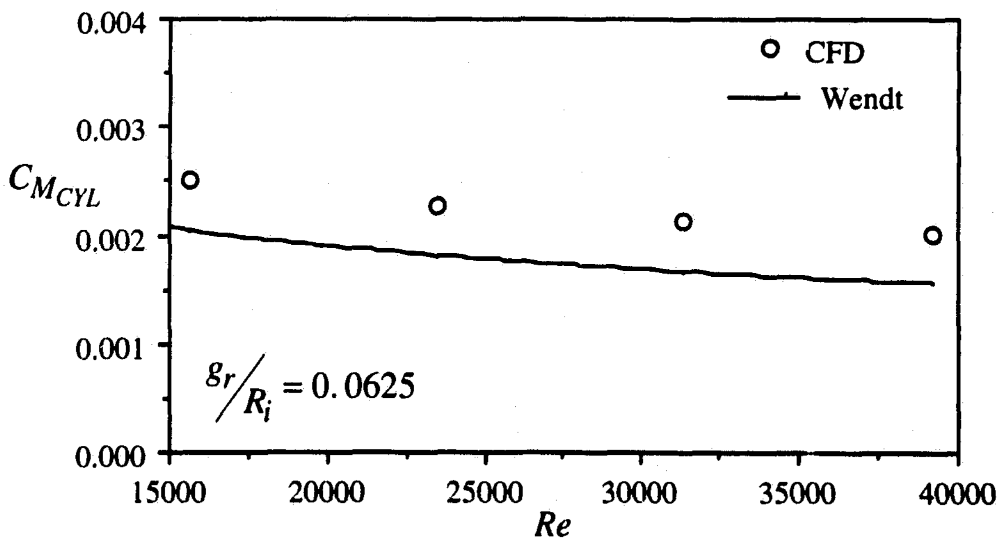

Figure 4.15 - Cylinder Moment Coefficient versus Reynolds Number for
$g_r/R_i = 0.0625$

The functional relations based on various forms of the log-law assume one-dimensional flow, i.e. the axial gradients associated with the Taylor vortices are neglected. Comparison of the log-law profile given in [25] with computed profiles at three different location in the Taylor vortex at the end of the rotor are presented in Figure 4.16. The log-law profile is fairly representative of the average CFD profiles, but does not reproduce the overshoots shown by the CFD profiles near the rotor and housing The higher gradients and shear stresses associated with these overshoots are consistent with the discrepancy between computed and theoretical moment coefficients.

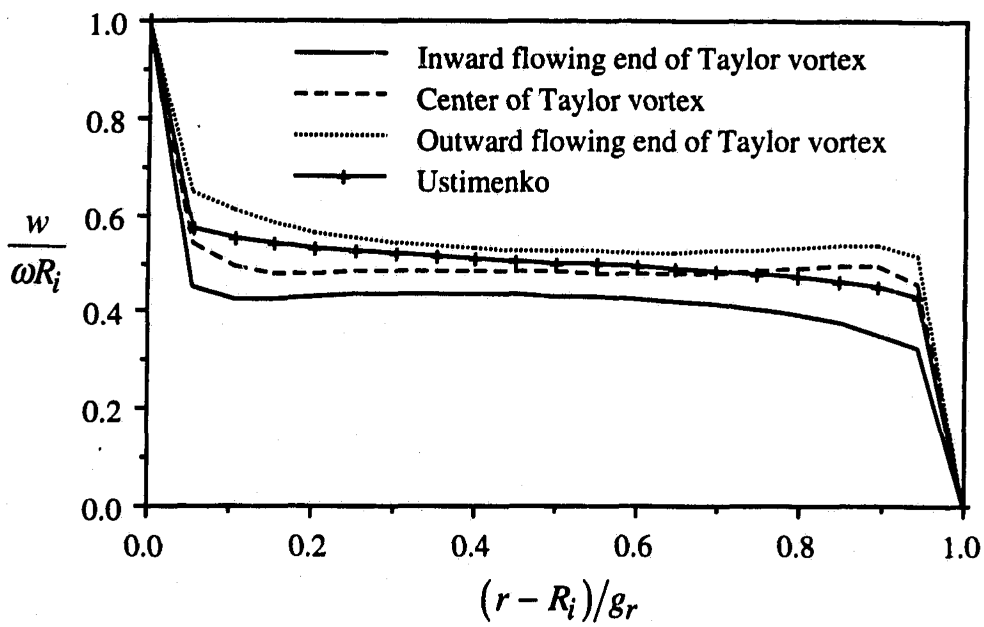

Figure 4.16 - Azimuthal Velocity Profiles Across Radial Gap

4.5 Parametric Study of Annulus Length Effects

In most experimental windage studies, the ratios of rotor length to rotor radius and to radial gap-width are set relatively high so as to minimize the effects of the rotor ends and, thereby, to approximate an infinite annulus. The torque due to the rotor ends is either neglected or is, in some manner, estimated and then subtracted from the total rotor torque. The functional relations discussed in Section 4.1.3 are founded upon data of this kind. In many engineering applications, however, these ratios are relatively low and the contribution to total rotor torque which is due to the rotor ends can be quite significant. If windage torque of such a rotor design is to be estimated using functional relations, the torque due to the rotor ends must also be approximated by a functional relation. In addition, it must be assumed that the flow in the axial gap is of negligible influence on the flow in the annular gap and visa versa.

Using the current CFD model, a numerical study of the effect of rotor length on the average windage torque at the outer cylindrical surface of the rotor and on the windage torque at the rotor ends was conducted. Although, as indicated in section 4.4, the quantitative results from the current CFD model are not in complete agreement with the experimental data, the model has shown sufficient accuracy that the trends shown in this study are expected to be reliable. The grid density of the 140 x 56 grid was maintained throughout this study. The results for the half-rotor model shown in Figure 4.6 are erroneous for small ratios of radial gap width to rotor length. The symmetry boundary condition at D-E consistently results in an outward flowing Taylor cell interface. This condition restricts the total number of Taylor cells, over the entire length of the rotor, to a multiple of 4. A complete Taylor cell is here defined as a single torroidal cell. In the absence of this condition, the total number of Taylor cells can be any multiple of 2, excepting anomalous modes [15]. Where the rotor is sufficiently long, this condition does not significantly affect either the individual cell structure or the average azimuthal shear stress. Where the rotor is sufficiently short, however, the individual cell structure becomes distorted, as is shown by comparison of the stream function patterns for the half rotor model with the results from a full-rotor model, see Figures 4.17 and 4.18.

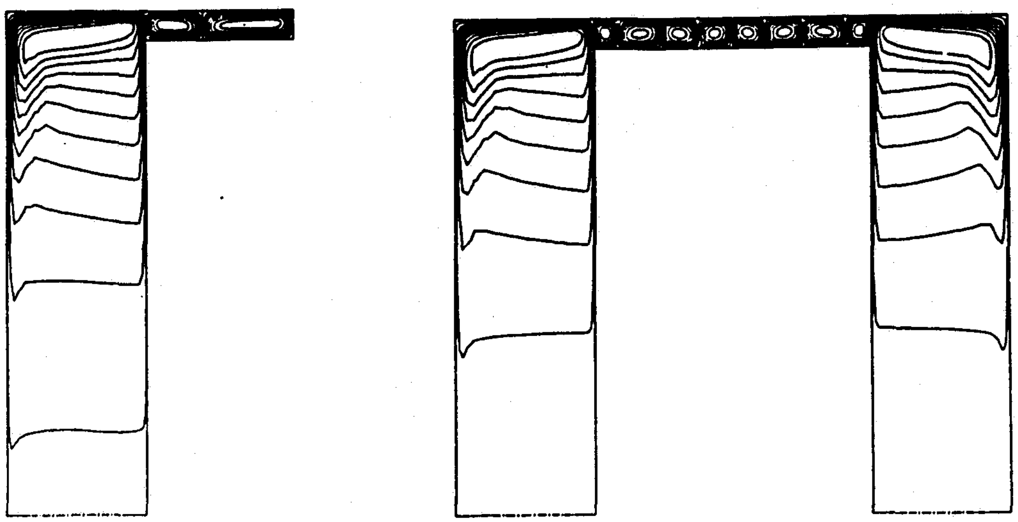

Figure 4.17 - Stream Function Patterns for half and full rotor models $\left(L/2\right)/g_r = 4.8$

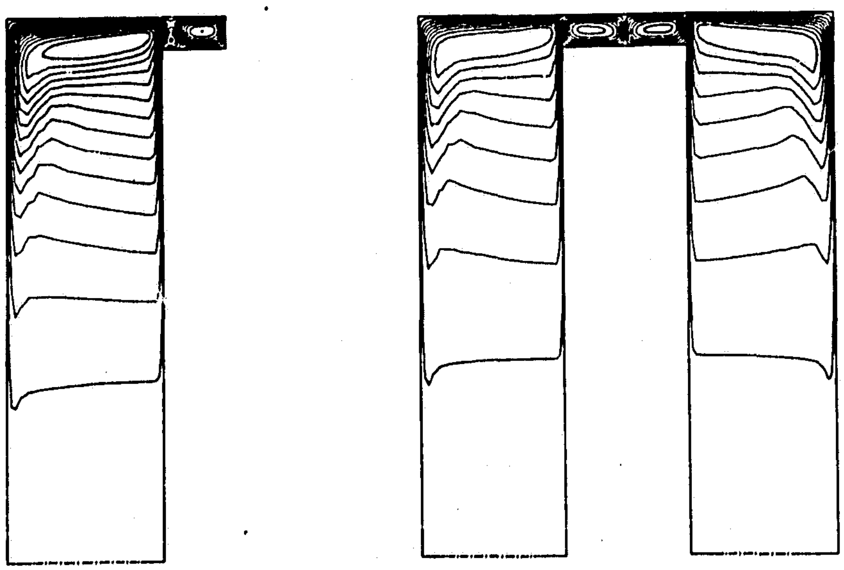

Figure 4.18 - Stream Function Patterns for half and full rotor models $\left(L/2\right)/g_r = 2.0$

The resulting average azimuthal shear stress is grossly underestimated by the half rotor model. This is shown by the divergence of the moment coefficient due to the outer cylindrical surface, $C_{M_{CYL}}$, for the half and full rotor models, shown in Figure 4.19.

Neglecting the erroneous half-rotor data, $C_{M_{CYL}}$ is a decreasing function of rotor length at relatively low ratios of rotor length to radial gap. At higher ratios of rotor length to radius, the moment coefficient is relatively independent of rotor length. The average azimuthal shear stress over the outer two Taylor cells (see the left-most peak in Figure 4.12) is higher than the average azimuthal shear stress over the inner cells. As the length of the rotor is increased the effect of these first cells becomes increasingly insignificant. As, however, the rotor becomes increasingly short, these cells significantly elevate the average azimuthal shear stress. The data calculated after Wendt [6], of course, is fully independent of rotor length.

The torque on the rotor ends, as determined by the numerical analysis, is relatively independent of the modeled flow in the annular region. As shown in Figure 4.20, the moment coefficients due to the rotor ends, $C_{M_{DISC}}$, (see equations 2.19 - 2.21) are sensitive neither to the ratio of rotor length to radial gap nor to the type of numerical model, namely: full or half rotor model. The data calculated after Schlichting [27], of course, is fully independent of rotor length.

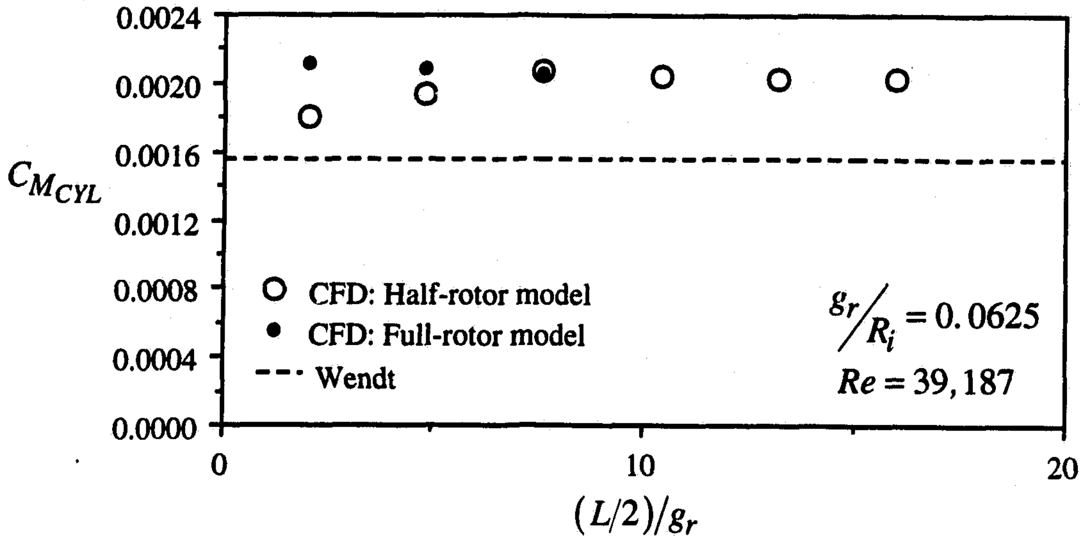

Figure 4.19 - Cylindrical Surface Moment Coefficient vs Ratio of Rotor Length to Radial Gap Width

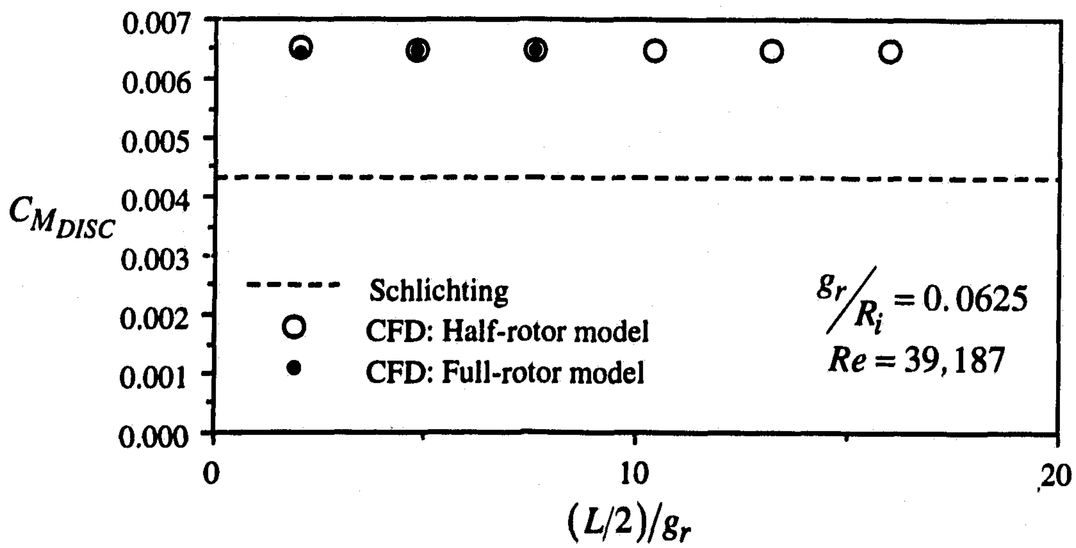

Figure 4.20 - Disc Moment Coefficient Due to Torque of Rotor Ends vs Ratio of Rotor Length to Radial Gap Width

4.6 Conclusions and Further Work

Of the various functional relations for windage torque, those of Wendt [6], Bilgen and Boulos [20] and Ustimenko [25] are the most broadly applicable and these relations, coupled with Schlichting's [27] relation applied to the rotor ends, showed good agreement with the experimental results. It should be noted that the current work has not included a detailed review of functional relations describing the moment on an enclosed rotating disc. Such a review should be undertaken in order to establish that these excellent results, calculated from Schlichting and Wendt, Bilgen and Boulos and Ustimenko, were not merely fortuitous.

The windage torques computed with the current CFD model, although consistently on the order of 10% higher than the experimental data, reproduced the observed declining trend of moment coefficient with Reynolds number. It is expected that this accuracy could be improved upon by using finer grids and alternative turbulence models.

The CFD model reproduced the expected Taylor vortices and it was shown that the azimuthal shear stress varies significantly through the axial length of a Taylor vortex. Where the ratio of rotor length to radial gap width is relatively large, this variation of the azimuthal shear stress distribution is averaged over the length of the rotor, and the resulting torque on the rotor is relatively insensitive to the number of vortices. Where the ratio of rotor length to radial gap width is relatively small, this variation of the azimuthal shear stress distribution results in a higher average azimuthal shear stress than for the case where the ratio of rotor length to radial gap width is relatively large. Accordingly, the functional relations of Wendt, Bilgen and Boulos and Ustimenko are expected to underestimate windage torque for cases where the ratio of rotor length to radial gap width is relatively small.

With respect to the design of the second prototype, it is now apparent that the lack of agreement between the measured windage and the values predicted by Bilgen and Boulos (see Figure 3.14) is principally due differences between the geometry within the rotor enclosure of the second prototype and the geometry for which the Bilgen and Boulos model is intended. Prior to the completion of this study, it was unclear whether some significant portion of this lack of agreement was due to inadequacies of the Bilgen and Boulos model. In order to reduce windage levels in future CRO units to the levels predicted by Bilgen and Boulos, the geometry of the rotor and enclosure must be modified. The rotor and enclosure should be smooth and concentric and the bearing platforms should be separated from the rotor by partitions which limit rotor induced air circulation about the bearing platforms.

References

1. Donelly, R.J. and Simon, N.J., An Empirical Torque Relation for Supercritical Flow Between Rotating Cylinders, Journal of Fluid Mechanics, vol. 7, 1960, p 401

2. Taylor, G.I., Fluid Friction Between Rotating Cylinders, Philosophical Transactions of the Royal Society of London, vol. 223, Feb. 8, 1923, pp. 289-343

3. Taylor, G.I., Distribution of Velocity and Temperature Between Concentric Rotating Cylinders, Proceedings of the Royal Society of London, Series A, vol. 151, no. 874, Oct. 1, 1935, pp. 494-512

4. Taylor, G.I., Fluid Friction Between Rotating Cylinders, Proceedings of the Royal Society of London, Series A, vol. 157, no.. 892, Dec. 2, 1936, pp. 546-578

5. Lewis, J.W., An Experimental Study of the Viscous Liquid Contained Between Two Coaxial Cylinders,. Proceedings of the Royal Society of London, Series A, vol. 117, 1927, pp 388-407.

6. Wendt, F., "Turbulente Stromungen Zwishen Zwei Rotierender Konaxialen Zylindern", Ingenieur-Archiv, vol IV, 1933,.p.577.

7. Kay, J., Elgar, E.C., Modes of Adiabatic and Diabatic Fluid Flow in an Annulus with an Inner Rotating Cylinder, Transactions of the ASME, April 1958, pp.753-765.

8. Pai, S.I., Turbulent Flow Between Rotating Cylinders, NACA Technical Note No. 892, March 1943.

9. Coles, D., Transition in Circular Couette Flow, Journal of Fluid Mechanics, vol. 21, 1965, pp.385-425.

10. Festermacher, P.R., Swinney, H.L., Gollub, J.B., Dynamical Instabilities and the Transition of Chaotic Taylor Vortex Flow, Journal of Fluid Mechanics, vol. 24, Part 1, 1979, pp. 103-128.

11. Shultz-Grunow, F, Hein, H, Bietrag zur Couettestromung, Zeitschrift fur Flugwissenshaften, 1956, vol. 4, pp. 28-30.

12. Burkhalter, J.E. and Koschmieder, E.L., Steady Supercritical Flow, Journal of Fluid Mechanics, 1973, vol. 53, Part 3, pp. 547-560.

13. Gulati, H.C., Ozogan, M.S., Mobbs, F.R., The Effect of Taylor Vortex Waves on Super Laminar Couette Flow Torques, Proceedings of the 7th Leeds Symposium on Tribology, 1980, pp. 255-61.

14. Cole, J.A., Taylor Vortex Instability and Annulus Length Effects, Journal of Fluid Mechanics, vol. 75, Part 1, 1976, pp. 1-15.

15. Benjamin, T.B., Mullin, T., Anomalous Modes in the Taylor Experiment, Proceedings of the Royal Society of London, Vol 377, Part A, July 1981, pp. 221-249.

16. Cole, J.A., Taylor Vortex Behaviour In Annular Clearances of Limited Length, Proceedings of the Fifth Australasian Conference on Hydraulics and Fluid Mechanics, Christchurch, New Zealand, December 1974, pp. 514-521.

17. Schaefer, D.G., Qualitative Analysis of a Model for Boudary Effects in the Taylor Problem, Mathematical Proceedings of the Cambridge Philosophical Society, Vol. 87, 1980, pp. 307-337.

18. Cliffe, K.A., Mullin, T., A Numerical and Experimental Study of Anolmalous modes in the Taylor Experiment, Journal of Fluid Mechanics, vol. 153, 1985, pp. 243-258.

19. Stuart, T.J., On the Non-Linear Mechanics of Hydrodynamic Stability, Journal of Fluid Mechanics, vol. 4, pp 1-21.

20. Bilgen, E, Boulos, R, Functional Dependence of Torque Coefficient of Coaxial Cylinders on Gap Width and Reynolds Numbers, Journal of Fluids Engineering, March 1973, pp. 122-126.

21. Lathrop, D.P., Fineberg, J., Swinney, H.L., Turbulent Flow Between Concentric Rotating Cylinders at Large Reynolds Number, Physical Review Letters, vol. 68, no. 10, March 1992, pp. 1515-1518.

22. Theodorsen, T, Regier, A., Experiments on Drag of Revolving Disks, Cylinders, and Streamline Rods at High Speeds, NACA Report No. 793, 1944.

23. Gazely, C., Heat Transfer Characteristics of the Rotational and Axial Flow Between Concentric Cylinders, Transactions of the ASME, January 1958, pp.79-89.

24. Vrancik, J.E., Predicition of Windage Power Loss in Alternators, NASA Technical Memorandum D-4849, October 1968.

25. Fluid Flow Data Book, Genium Publishing Corporation, 1969..

26. Fluent Users Guide, Fluent Inc., New Hampshire, 1992.

27. Schlichting, H., Boundary Layer Theory, 4th ed.,McGraw-Hill, New York, 1960, p. 547.

Chapter 5
An Experimental Analysis of the Dependence of Flow Losses Through a CRO Rotor on the Speed of Rotor Rotation

5.0 Introduction

It was anticipated that a CRO unit would require a low pressure sea water feed pump to provide pressure to overcome the flow losses which occur in the sea water flow path through the centrifuge rotor, as discussed in Section 2.5.2. It was not, however, anticipated that there would be the strong dependence of flow losses on rotor speed which was observed in both the first and the second prototypes. As shown in Figure 5.1, the pressure drop across the rotor of the second prototype increased from 90 kPa, when the rotor was at rest, to 695 kPa, when the rotor was at the normal operating speed. This pressure drop represented 27.5% of the total energy consumption of the second prototype, as detailed in Section 2.3.3. Reductions in the flow losses through the centrifuge rotor would, therefore, have a significant impact on the overall power consumption of CRO. To this end, an experimental study of flow losses was conducted to determine the regions within the flow paths of the first and second prototype rotors which were responsible for the strong dependence of flow losses upon rotor speed. The study also established design modifications which would reduce these losses to acceptable levels.

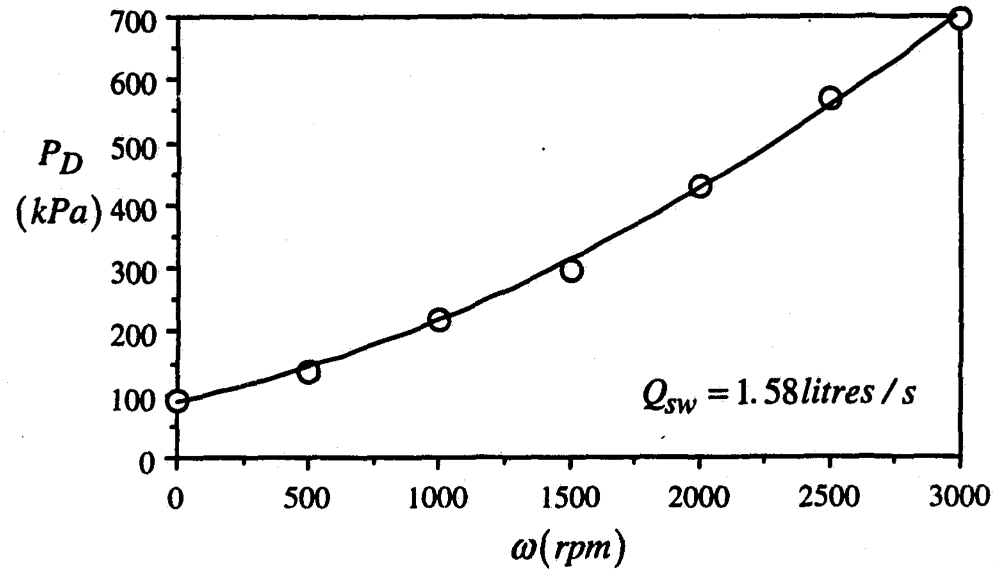

Figure 5.1 - Pressure Drop vs Rotor Speed

5.1 Flow Regions within the Centrifuge Rotor

The sea water flow paths in the first and second prototypes were based on the same basic geometry, shown in Figure 3.3. The individual details of the flow paths in the first and second prototypes are shown in the partial sections of the rotors shown in Figures 3.4 and 3.5. In order to simplify the complex problem of flow losses in the centrifuge rotor as a whole, the flow path through the rotor can be conveniently divided into nine distinct regions, as shown in Figure 5.2.

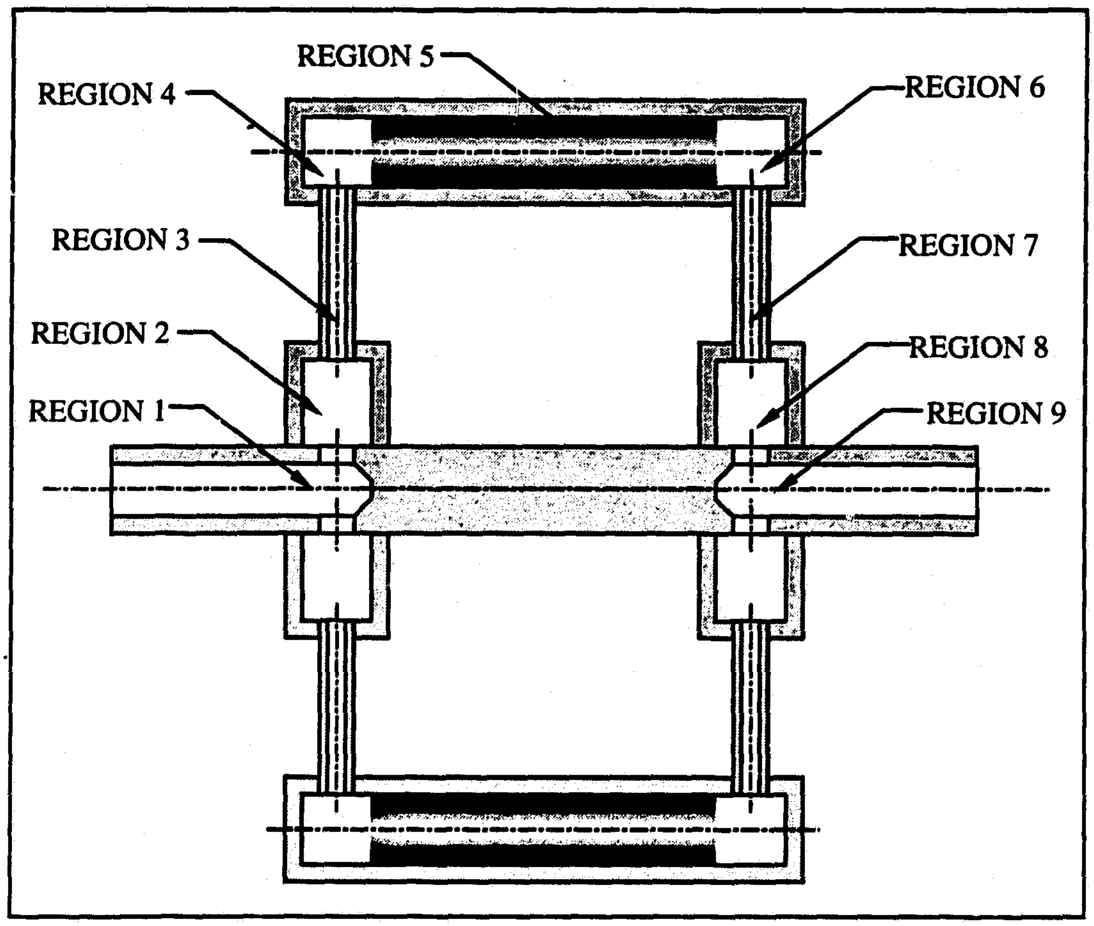

Figure 5.2 - Flow Regions Comprising Flow Path Through First and Second Prototype Rotors

The nine regions are:

1. **The transition from the bore in the rotor shaft to the two radial holes in the rotor shaft.** The length of the bore, from the transition between the non-rotating and rotating sections, is not expected to be sufficient for the tangential component of the flow to be fully developed when it reaches the radial holes. As a result, the flow undergoes not only an abrupt redirection due to the right angle between the bore and the radial holes but, in addition, an abrupt tangential acceleration as it enters the radial holes.

2. The transition of flow from the radial holes in the rotor shaft outward through the annular chamber in the diffuser and then into the radial tubes. As the tangential velocity of the outlet from the two radial holes is less than the tangential velocity of the inlet to the radial tubes, the flow must accelerate tangentially as it passes radially outward. In addition, the flow must distribute itself circumferentially so as to supply each of the sixteen pressure vessels.

3. The radial tubes connecting the diffuser to the pressure vessels. The velocity profile in these tubes is not expected to be axially symmetric as the rotation of the rotor will cause a pressure gradient across the tube cross section. This could lead to secondary flow patterns with re-circulation cells which would increase the resistance to flow.

4. The transition from the radial tubes into the pressure vessels. Referring to Figure 5.2, it can be seen that the geometry of this transition is quite complex. The effects of this geometry are difficult to forecast.

5. The flow path through the membrane cartridge. The sea water passage in the membrane cartridge forms a spiral, in end view, as shown in Figure 1.7. The width of this spiral passage is selected to create sufficient turbulence for the membrane surfaces within the cartridge to benefit from a turbulent scouring action. The membrane cartridge is supported at each end, by contact with the pressure vessel wall, and along its entire length by immersion in sea water. As the cartridge is not perfectly neutrally buoyant in sea water, there is a bending load on the cartridge due to centripetal acceleration. It is possible that, should the cartridge bend in response to this load, the sea water passages within the cartridge could become restricted or "pinched off". This would produce flow losses which would be strongly dependent upon rotor speed.

6, 7, 8, 9. These regions, at the outlet end of the rotor, are geometrically analogous to regions four, three, two and one, respectively, at the inlet end of the rotor. Some important aspects of the flow in these regions are expected to be similar.

To determine the impact of each of the nine regions described above on the flow losses through the centrifuge, experiments were conducted on the prototype rotor itself and on a small experimental rotor constructed so as to model the essential flow features of the prototype. The small experimental model was required to assess the effect of flow path geometry variations which could not be practically implemented in the prototype.

An important assumption which underlies this approach is that the flow losses in each of these regions occur independently of the flow losses in adjacent regions. In reality, the flow losses will be affected by upsteam and, to a lesser extent, by downsteam conditions. These effects are expected to alter the absolute losses but not the trends. For the purposes of this work it is assumed that the flow losses in a given region are a function only of flow rate and of rotor speed.

5.2 Dimensionless Parameters

In order to compare the results obtained from the experimental model with the results from the prototype, it is critical that the data be non-dimensionalised in a manner which is both convenient and meaningful. Buckingham-Pi analysis of the critical parameters leads to a number of possible non-dimensional groups and reference to fundamental literature [1, 2, 3] regarding centrifugal pumps and turbines indicates which non-dimensional groups are likely to be most relevant to this application.

In the analysis of turbomachinery, head versus flow rate plots of "geometrically similar machines" can be collapsed onto a single curve by plotting a dimensionless “head coefficient”,

$$\Omega = \frac{\hat{g}H_{turbo}}{\omega^2 R_{imp}^2} \tag{5.1}$$

against a dimensionless “flow coefficient”,

$$\Psi = \frac{Q_{turbo}}{\omega R_{imp}^3} \tag{5.2}$$

where H is head, ω is speed of rotation, R_{imp} is impeller radius and Q is volumetric flow rate. For geometrically similar machines, the ratios of critical dimensions, within each machine, are equal.

For a pump, the head coefficient can be thought of as a measure of the efficiency with which the maximum stagnation enthalpy available upon outlet from the impeller is converted into useful pressure. At impeller outlet, the stagnation enthalpy, h_0, is,

$$h_0 = \frac{V_{outlet}^2}{2} + \frac{P_{outlet}}{\rho_f} \tag{5.3}$$

where V_{outlet} is the velocity of the fluid at impeller outlet and ρ_f is the density of the fluid. The pressure at outlet from the impeller, P_{outlet}, is assumed to be due entirely to the body force of rotation and can be expressed as follows

$$P_{outlet} = \frac{1}{2}\rho_f \omega^2 R_{imp}^2 \qquad (5.4)$$

where ω is the angular velocity of the impeller. If the tangential component dominates the velocity, V_{outlet}, then

$$V_{outlet} \approx \omega R_{imp} \qquad (5.5)$$

Thus the expression for stagnation enthalpy reduces to

$$h_0 = \omega^2 R_{imp}^2 \qquad (5.6)$$

The ratio of the head which is available at the outlet from a pump, $\hat{g}H_{turbo}$, to the stagnation enthalpy is, therefore, a measure of the efficiency of the pump. This ratio is, furthermore, equal to the head coefficient, $\boldsymbol{\Omega}$, discussed above.

$$\frac{\hat{g}H}{h_0} = \frac{\hat{g}H_{turbo}}{\omega^2 R_{imp}^2} = \boldsymbol{\Omega} \qquad (5.7)$$

For a continuous flow centrifuge, such as a CRO, the measurable pressure parameter is the incremental pressure drop through the rotor, $P_d\big|_{incr}$. The incremental pressure drop, $P_d\big|_{incr}$, is defined as the pressure drop through the rotor, for a given flow rate and rotational speed, less the pressure drop for the same flow rate when the rotor is stationary.

This is to minimize the effect of variations, from one experimental configuration to another, in the viscous flow losses due simply to flow restrictions. Thus, $P_d\big|_{incr}$ is a measure of the pressure drop due solely to the effect of rotation. The head coefficient for a centrifuge can, therefore, be conveniently defined as

$$\Omega_c = \frac{P_d\big|_{incr}}{P_{C_{max}}} \tag{5.8}$$

where $P_{C_{max}}$ is the maximum pressure developed within the centrifuge.

$$P_{C_{max}} = \frac{1}{2}\rho_f \omega^2 R_{max}^2 \tag{5.9}$$

In the discussions which follow, $\boldsymbol{\Omega_c}$ will be referred to as the "pressure coefficient".

The flow coefficient, $\boldsymbol{\Psi}$, is a ratio of the radial velocity, in a purely radial flow machine, to the tangential velocity. The radial velocity, V_R, at the outlet from the impeller of a radial flow pump is,

$$V_{outlet}\big|_{radial} = \frac{Q_{turbo}}{2\pi R_{imp} kt} \tag{5.10}$$

where t is the width of the flow passages in the impeller and k is a constant, of value less than one, which adjusts for the space occupied by the impeller vanes. The ratio, k', defined as,

$$k' = \frac{2\pi kt}{R_{imp}} \tag{5.11}$$

must be constant for geometrically similar machines. For geometrically similar machines, therefore, k' is a constant and 5.10 can be rewritten as,

$$V_{outlet}\big|_{radial} = \frac{Q_{turbo}}{k'R_{imp}^2} \tag{5.12}$$

The tangential velocity at the outlet from the impeller is

$$V_{outlet}\big|_{tan} = \omega R_{imp} \tag{5.13}$$

where ω is angular velocity. The ratio of radial velocity to tangential velocity can now be shown to be equivalent to the flow coefficient, ψ,

$$\frac{V_{outlet}\big|_{radial}}{V_{outlet}\big|_{tan}} = \frac{Q_{turbo}}{\omega k' R_{imp}^3} \propto \Psi \tag{5.14}$$

An equivalent dimensionless group can be derived for the CRO. A flow coefficient, which relates radial to tangential velocities is expressed as

$$\Psi_c = \frac{\left(Q_f / A_r\right)}{\omega R_{max}} \tag{5.15}$$

where A_r is the area of the flow passages in the radial direction. In the discussions which follow, Ψ_c will be referred to as the "velocity coefficient".

5.3 Experiments Conducted on Second Prototype CRO Rotor

The experiments which could be conducted using the second prototype CRO rotor itself were limited, as the geometry of the flow path within the rotor could not be substantially modified without undertaking a major and expensive redesign. There are, however, two flow regions whose contribution to total flow losses can be assessed without excessive modifications to the prototype rotor. These are: region one, the transition from the bore in the rotor shaft to the two radial holes in the rotor shaft, and region five, the flow path through the membrane cartridge.

The impact of region one was assessed by the placement of a vaned insert into the bore in the rotor shaft, as shown in Figure 5.3. The insert was tapered so as to provide a gradual tangential acceleration of the flow as it passed through the rotor shaft bore. The vaned insert ensured that the tangential velocity of the flow through the bore in the rotor was fully developed when it reached the radial holes, thus minimizing any abrupt tangential acceleration as the flow entered the radial holes. It was anticipated that, if this abrupt tangential acceleration was responsible for a significant component the flow losses through the rotor, then the vaned insert would cause a significant reduction in the pressure drop through the rotor.

The loss coefficient data taken with the insert in place showed no significant variation from the data which was obtained without the insert in place, as is shown in Figure 5.4. The dimensionless flow loss coefficient, C_L is defined as,

$$C_L = \frac{P_d}{\frac{1}{2}\rho_f V_R^2} \tag{5.16}$$

where P_d is the pressure drop through the rotor at maximum flow rate and V_R is the corresponding velocity of the flow in the radial tubes. It is concluded that the flow losses in this region either do not represent a significant portion of the total flow losses through the rotor and/or are due to a mechanism other than sudden radial acceleration.

The impact of region five was assessed by simply removing the membrane cartridges and recording the resulting pressure drop data. As can be seen from Figure 5.5, the loss coefficient in the absence of the membrane cartridges is offset from the loss coefficient with the membrane cartridges by a consistent amount which is independent of rotor speed. The flow losses through the membrane cartridge can, therefore, be characterised as viscous flow losses having no dependence upon rotor speed.

It has been shown that regions one and five do not contribute significantly to the flow losses through the centrifuge rotor. Experimental investigations of the remaining flow regions were conducted with the experimental test rig.

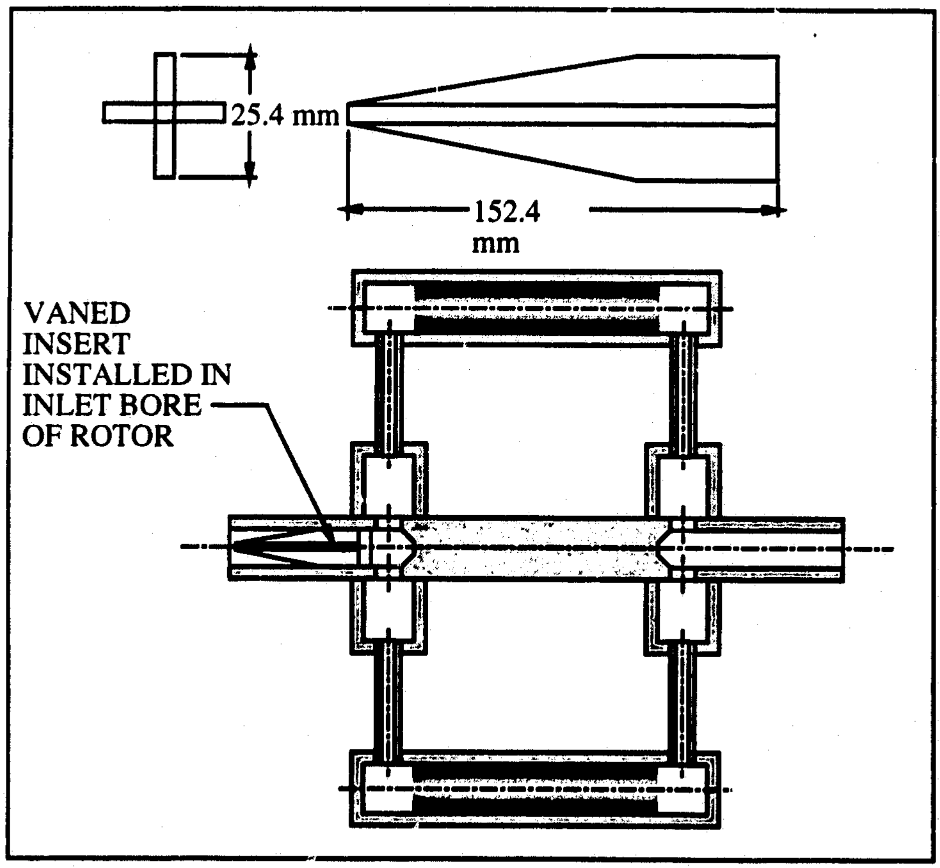

Figure 5.3 - Vaned Insert in Second Prototype Inlet Bore

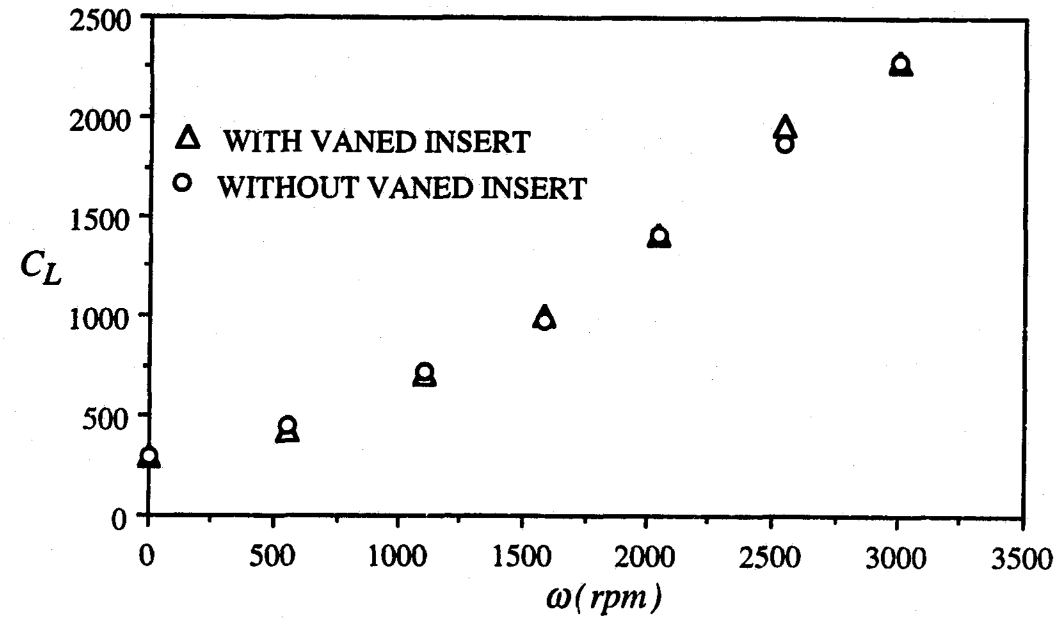

Figure 5.4 - Loss Coefficient vs Rotor Speed for Second Prototype (With and Without Vaned Insert)

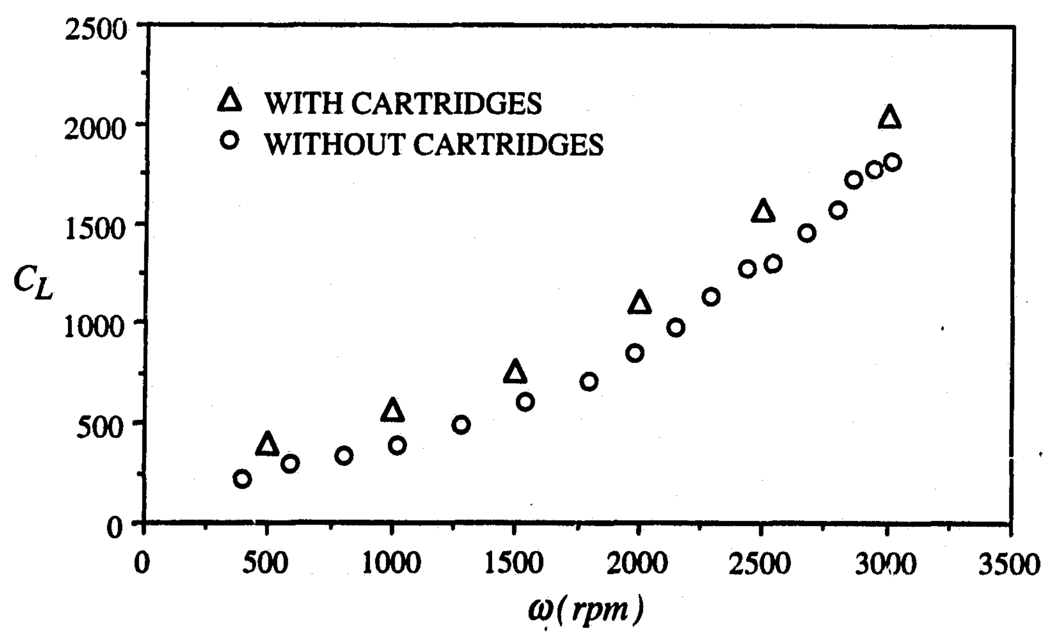

Figure 5.5 - Loss Coefficient vs Rotor Speed for Second Prototype (With and Without Membrane Cartridges)

5.4 The Experimental Model

In order to assess the relative impact of each of the remaining regions on the flow losses through the second prototype rotor, an experimental model was designed and constructed which included a rotor incorporating flow paths which modeled the flow paths in the prototype rotor. The layout of the experimental model, as shown in Figure 5.6, includes a cantilever mounted rotor which is belt driven from a 2 hp DC motor with a variable speed control. The maximum rotor speed is 5000 rpm. The pressure drop through the rotor is measured with pressure gages at inlet to and outlet from the rotor. The flow rate of water through the rotor is measured by timing the fill duration of a vessel of known volume.

The experimental rotor is of a modular design so as to facilitate the variation of flow path geometry. A photograph of the rotor is shown in Figure 5.7. The following flow path configurations were examined:

Configuration #1 (Figure 5.8 - centre and left) In this configuration, the test rig rotor models the flow paths of the prototype, in the absence of the diffusers and the membrane cartridges. The flow path consists of an axial bore at inlet which connects into two radial holes which extend into two radial tubes which are curved into 180 degree arcs. These radial tubes return to the main body of the rotor and connect to radial holes which return to the outlet bore at the rotor axis. Three sets of radial tubes were constructed to provide maximum radii of 184 mm (7.25 in), 165 (6.5 in), 140 mm (5.5 in). A fourth and smallest radius of 70 mm (2.75 in) is achieved by sealing off the radial outlet from the main rotor body, removing the radial tubes and opening the axial passages close to the periphery of the rotor body. For the other radii, where radial tubes are attached, these axial passages are blocked off.

Configuration #2. (Figure 5.8 - center and right) This is a slight variation on configuration #1 in which the radial holes intercept the axial bores at inlet and outlet tangentially rather than radially. The tangential path is shown in the full section of the rotor on the right of Figure 5.8

Configuration #3 (Figure 5.9) This configuration models the prototype flow path, including the diffusers at inlet and outlet. The number of radial tubes is six rather than two, to more accurately represent the geometry of the prototype.

5.4.1 Similarity of Experimental Model to Prototype

The experimental model was designed to be, where possible, geometrically similar to the prototype and, where possible, was operated in ranges of flow rate and rotational speed that where dynamically similar to the second prototype. Dynamic similarity exists between two turbomachines operating at different speeds when the ratio of fluid velocity, with respect to the rotating frame of reference, to "blade velocity" is equivalent. Thus, by operating the test rig so that the range of the velocity coefficient, Ψ_c, is equivalent to the range of the velocity coefficient in the second prototype, dynamic similarity is ensured.

5.4.2 Assessment of the Losses in the Nine Flow Regions of the Experimental Model.

Geometrically, the flow regions within the experimental model and the prototype rotor are symmetric about a plane intersecting the midpoint of the rotor axis. That is, regions one and nine are symmetric, regions two and eight are symmetric, and so on. The assessments which follow address these regions as pairs and do not attempt to distinguish the losses in one member of the pair from the losses in the other member.

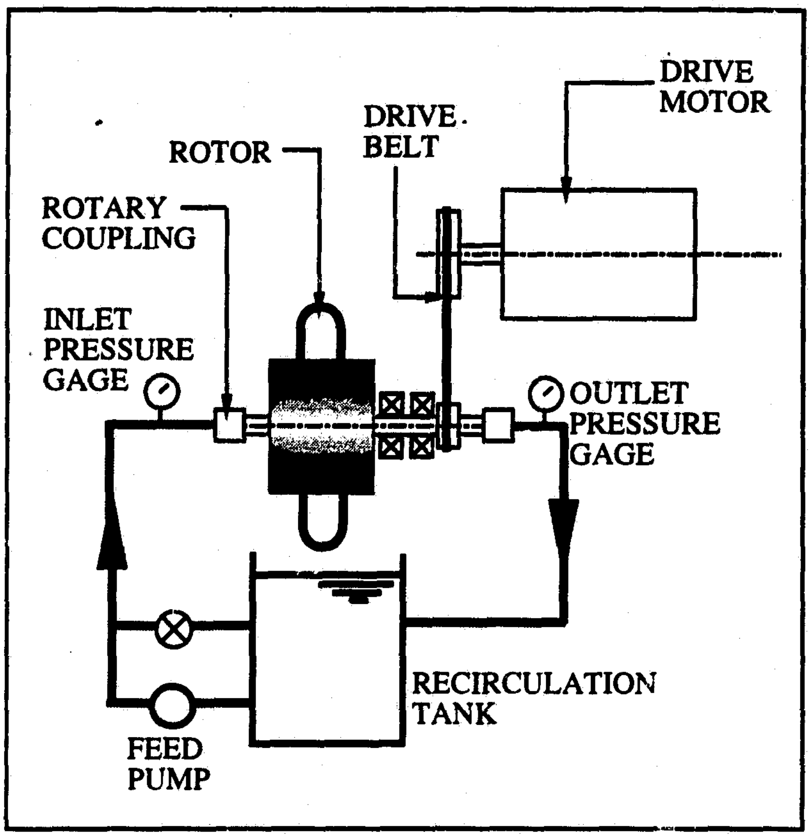

Figure 5.6 - Layout of Experimental Test Rig

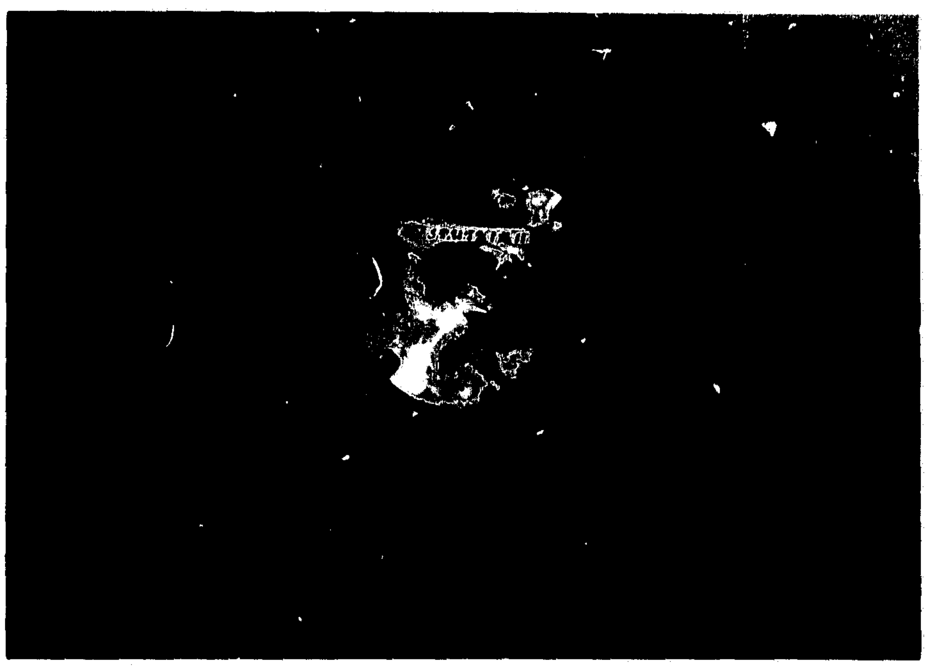

Figure 5.7 - Photograph of Test Rig Rotor

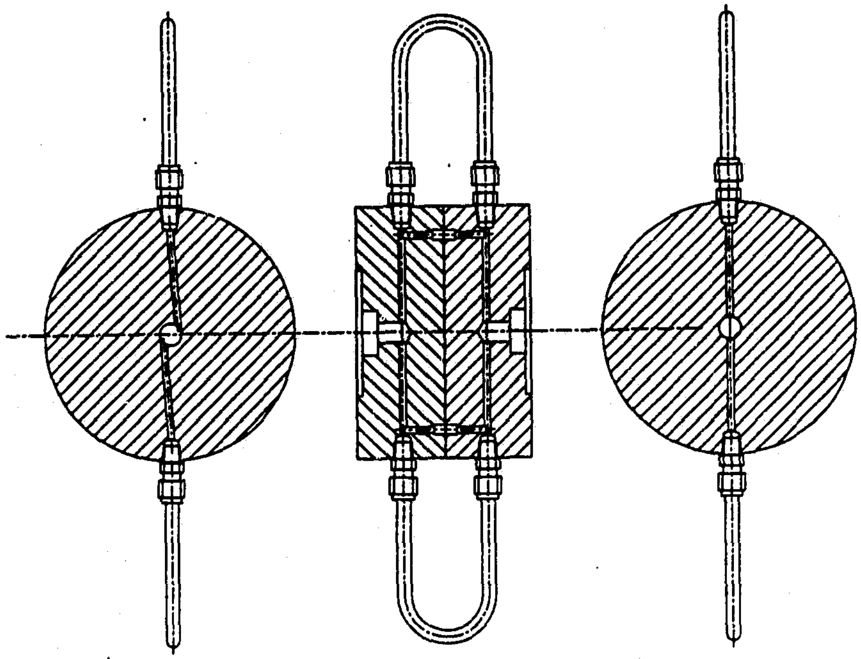

Figure 5.8 - Test Rig Rotor Configuration #1 & #2

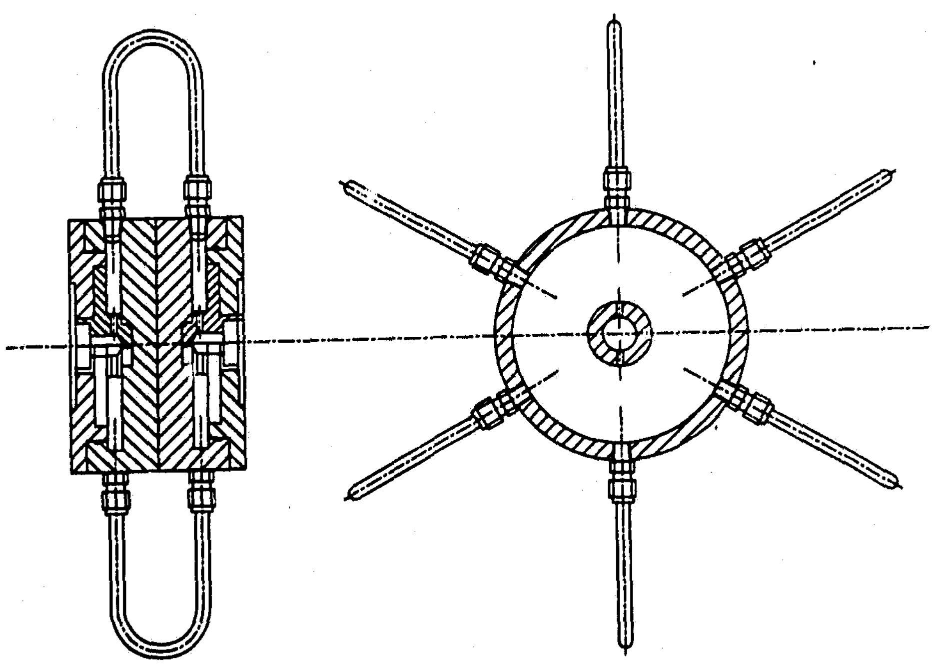

Figure 5.9 - Test Rig Rotor Configuration #3

Regions One and Nine- The Transition From Axial Bore To Radial Holes

Although the tests with the vaned insert in the prototype rotor indicated that the losses in this region were not significant, tests were conducted with the experimental model to determine the effect of the geometry at the transition from axial to radial passage. Two geometries were tested, Configuration #1 and Configuration #2. Configuration #2 was tested in both clockwise and counter-clockwise directions, see Figure 5.10. If the tangential velocity profile in the axial bore is not fully developed at the radial holes, then clockwise rotation of the holes about the non-rotating core of fluid will tend to induce flow into the holes. On the other hand, counter-clockwise rotation of the holes about the non-rotating core of fluid will tend not to induce flow into the holes. Accordingly, it was expected that flow losses would be lower for rotation in the clockwise direction than for rotation in the counter-clockwise direction. As is shown in Figures 5.11 and 5.12, the data displays these expected trends. The units of the ordinates in these figures are the difference between the incremental pressure drops of configuration #1 and the incremental pressure drops of configuration #2 for clockwise and counter-clockwise rotation.

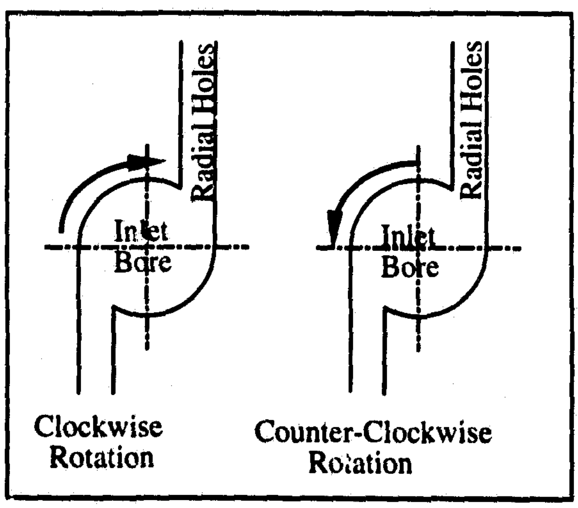

Figure 5.10 - Clockwise and Counter-Clockwise Rotation of Configuration #2

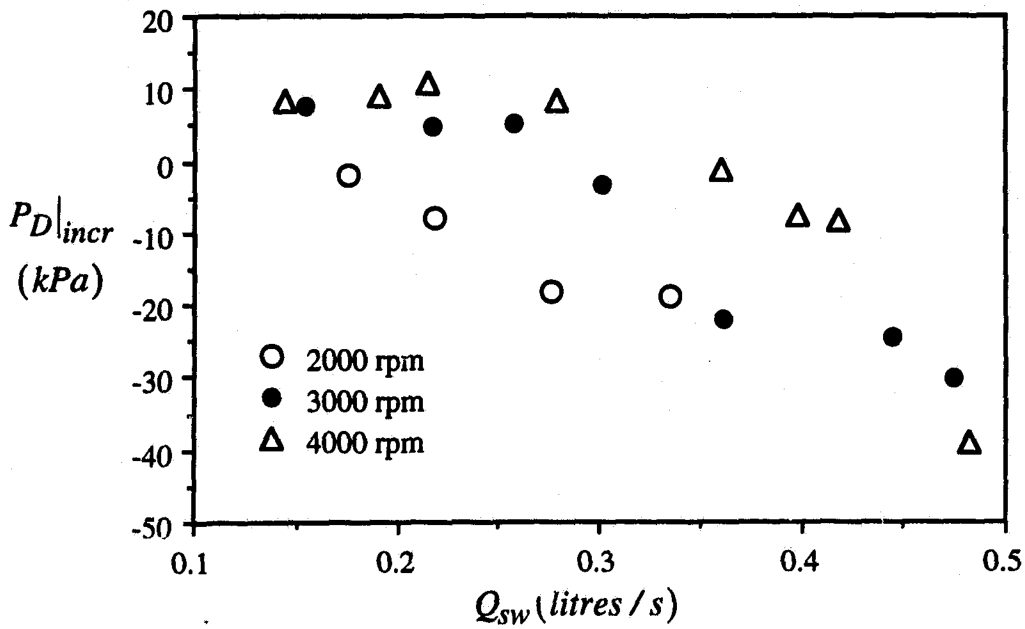

Figure 5.11 - Incremental Pressure Drop Differential vs Flow Rate for Configuration #2 Clockwise Rotation (R=70 mm)

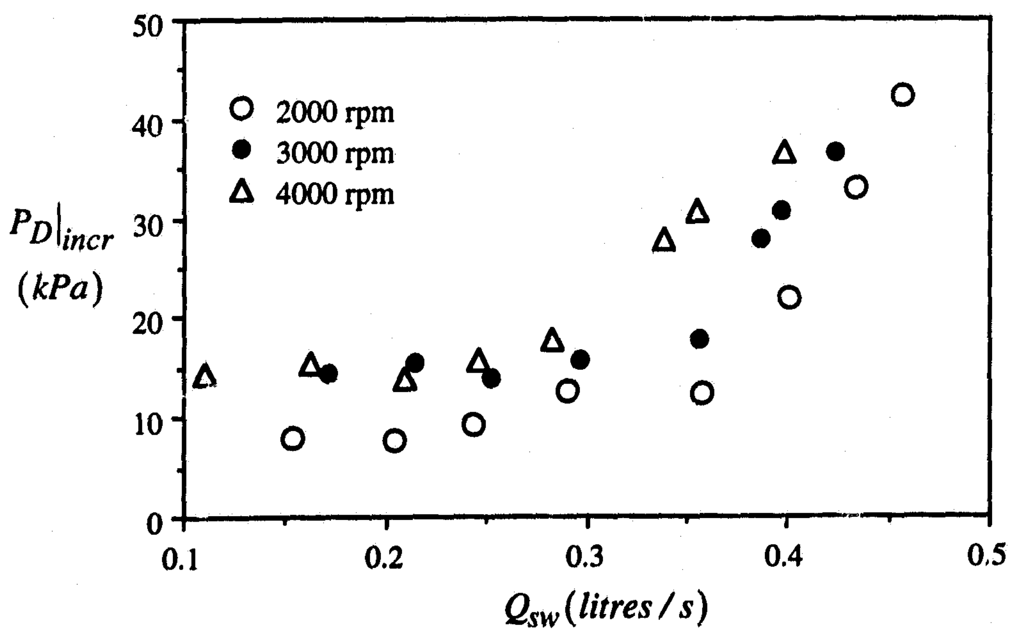

Figure 5.12 - Incremental Pressure Drop Differential vs Flow Rate for Configuration #2 Counter-Clockwise Rotation (R=70 mm)

Regions Three and Seven- The Radial Tubes

The state of the flow and, therefore, the resistance to flow within the radial tubes of the rotor are assumed to be a function of, among other things, the length of the radial tubes and the speed of rotation of the rotor. The maximum peripheral pressure in the rotor also varies as a function of both rotor speed and radial tube length.

$$P_{C_{max}} = \frac{1}{2}\rho_f \omega^2 R_{max}^2 \quad (5.17)$$

As a question of design, it is important to understand whether a particular combination of rotor speed and radial tube length can deliver a given peripheral pressure more efficiently than other combinations of rotor speed and radial tube length.

To address this question, pressure drop data was gathered for three lengths of radial tubes, two Reynolds numbers and rotor speeds ranging from 1,500 rpm to 4,500 rpm. The Reynolds Numbers are referenced to the flow in the radial tubes of the test rotor. The smaller number, Re=9,900, corresponds to the Reynolds numbers of the flow in the radial tubes of the prototype. The larger number, Re=52,800, corresponds to the Reynolds numbers of the flow in the radial holes that connect the shaft bore to the diffuser in the prototype.

For any given maximum peripheral pressure and for both Reynolds numbers, the pressure drop through the rotor does not vary significantly with the length of the radial tubes, as shown in Figure 5.13. It appears, therefore, that, if there are significant losses in the radial tubes, these losses are not affected by the combination of rotor speed and radial tube length which deliver a given peripheral pressure.

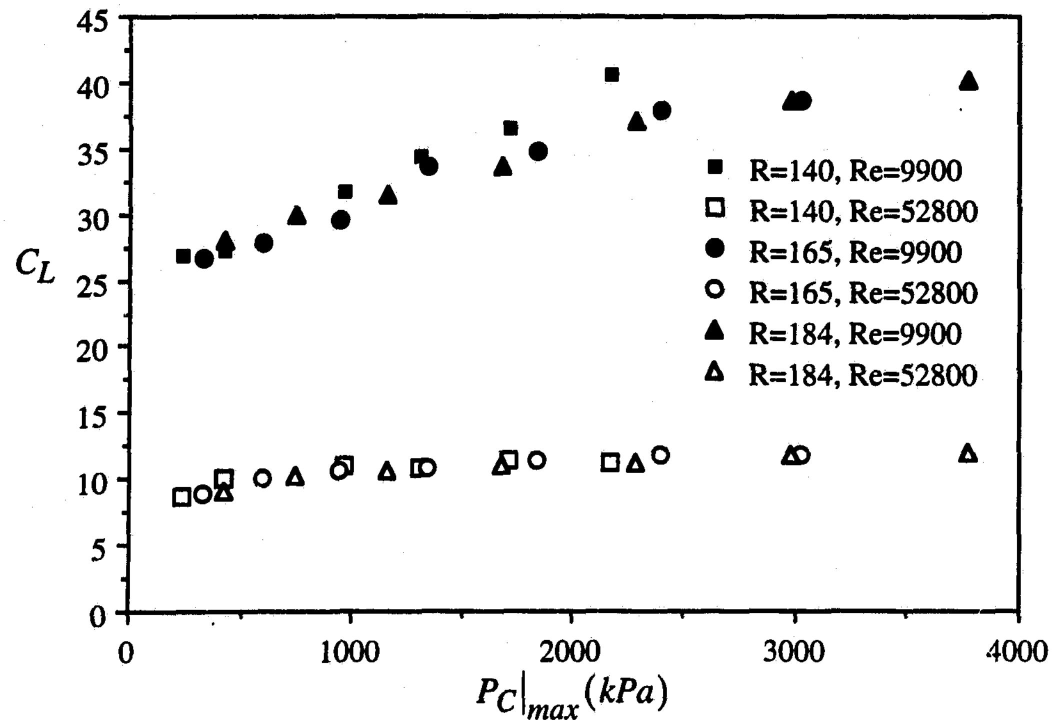

Figure 5.13 - Loss Coefficient vs Maximum Peripheral Pressure Configuration #1

Regions Two and Eight- The Diffuser

The key difference between Configuration #1 of the experimental rotor and the prototype is the absence of a diffuser in the former. Accordingly, it is significant that there is a dramatic difference between the flow losses exhibited in the prototype and in Configuration #1, as shown in non-dimensional form in Figure 5.14.

In order to confirm the inevitable conclusion that the elevated pressure losses of the prototype are due to the diffuser, tests were conducted using Configuration #3, which includes a model of the diffuser. These results, shown in Figure 5.15, demonstrate conclusively that region two, the diffuser, is the single largest source of flow losses in the prototype. The data from Configuration #3 shows approximately the same values of the pressure coefficient as the data from the prototype and, in addition, it shows a similar coherence at low values of the velocity coefficient. It is apparent from Figures 5.14 and 5.15 that the dimensionless parameters, pressure coefficient and velocity coefficient, are important to the characterisation of the performance of a centrifuge. The data from the experimental model, for a range of speeds, radii and flow rates, collapses into a relatively narrow field as does the data from the prototype.

In calculating the velocity ratio, it is important that the radial velocity be calculated so as not to bias the results of one configuration with respect to another. It is established that the losses in the radial tubes do not exhibit a strong dependence on speed of rotation. It is, furthermore, apparent that the losses in the region of the diffuser are strongly dependent upon rotor speed. It is, therefore, reasonable to expect that the radial velocity at entrance to the annular diffuser chamber will show some correlation with losses. Accordingly, the radial velocity which is used to calculate the velocity ratio for the prototype is the velocity through the radial holes connecting the bore in the shaft to the diffuser. For the experimental model in configuration #3, the velocity in the radial holes in the diffuser insert are used. In configuration #1, the velocity in the radial tubes is used.

It should be noted that the conclusions which are drawn from this work are insensitive to the choice of radial velocity. If the radial velocity in the radial tubes is used throughout this analysis, the apparent severity of the losses in the diffuser become even more acute, as indicated in Figure 5.16.

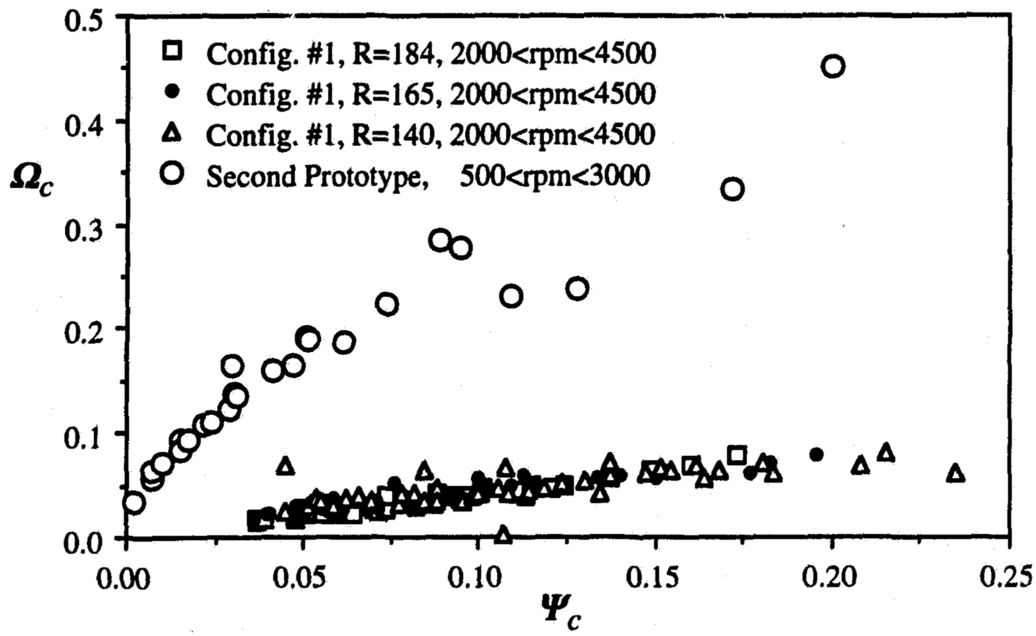

Figure 5.14 - Pressure Coefficient vs Velocity Coefficient (Second Prototype and Test Rig Configuration. #1)

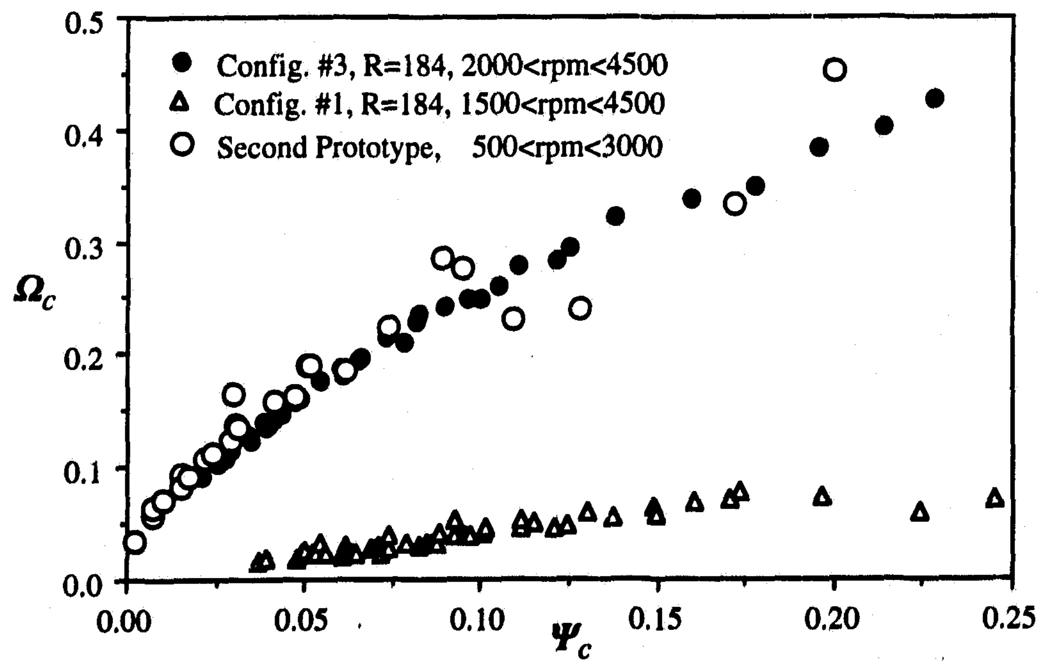

Figure 5.15 - Pressure Coefficient vs Velocity Coefficient (Second Prototype and Test Rig Configuration. #1 and #3)

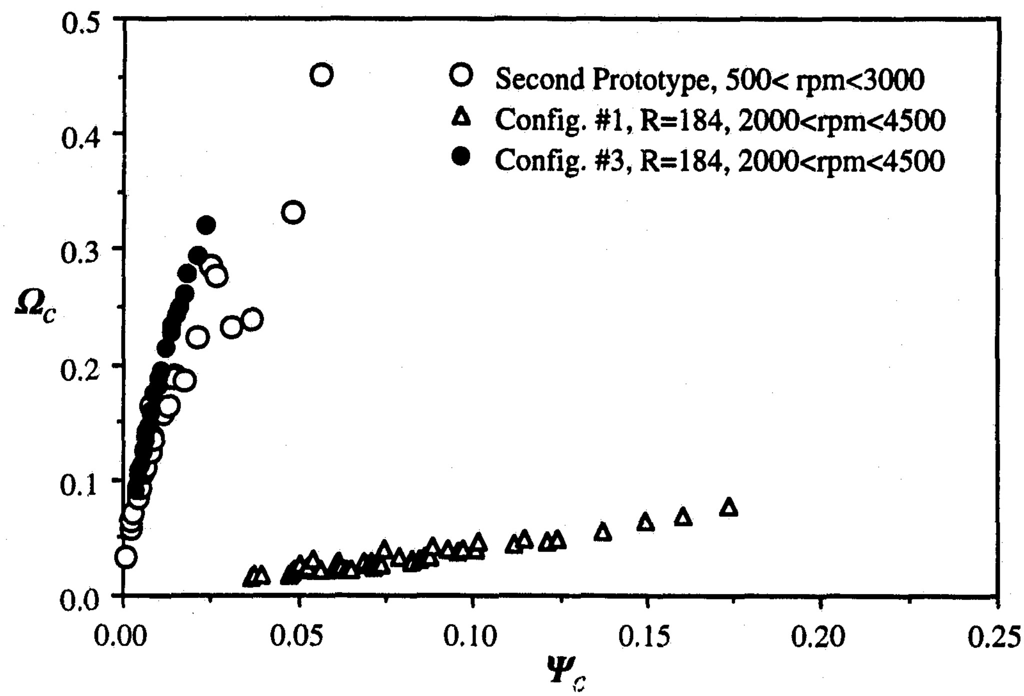

Figure 5.16 - Pressure Coefficient vs Velocity Coefficient Based on Velocity in Radial Tubes (Second Prototype and Test Rig Configuration. #1 and #3)

Regions Four and Six-The transition from the radial tubes into the pressure vessels

These regions were not studied as it had been shown that the majority of losses were associated with the diffuser.

5.4.4 Design Modifications to Model

To confirm that the majority of the pressure drop is occurring in the diffuser and to assist in the design of a practical modification which would reduce these losses in future CRO units, the test rotor was reconfigured as follows:

Configuration #4 (Figure 5.17) This configuration is identical to #3 except that the radial passages in the diffusers have been "extended" with the curved tubes shown. The inside diameter of the curved tubes is 2.75 mm (0.108 in).

Configuration #5 This configuration is identical to #4 except that the inside diameter of the curved tubes is larger, 4.57 mm (0.180 in).

This design modification was predicated on the assumption that the losses in the diffuser are due principally to flow separation and turbulent eddies associated with the viscous shear forces that accelerate the flow tangentially as it passes radially outward within the annular diffuser chamber. The extended radial passages effectively reduce the radial span of the annular diffuser chamber, thus, ensuring that virtually no tangential acceleration is required within the diffuser chamber. Rather, this acceleration is achieved in a relatively "ordered" fashion within the extended radial passages. The motion of the fluid contained within the annular diffuser chamber is closer to a solid body rotation.

The pressure coefficients for these configurations are lower than for any previous configurations, as shown in Figure 5.18. These results confirm not only that the diffuser is the principal source of flow losses but also the mechanism by which these losses occur. The addition of the extensions to the radial holes reduces the flow separation and turbulence in the annular diffuser chamber and the resulting flow losses are even lower than were observed for configuration #1, in which there was no diffuser.

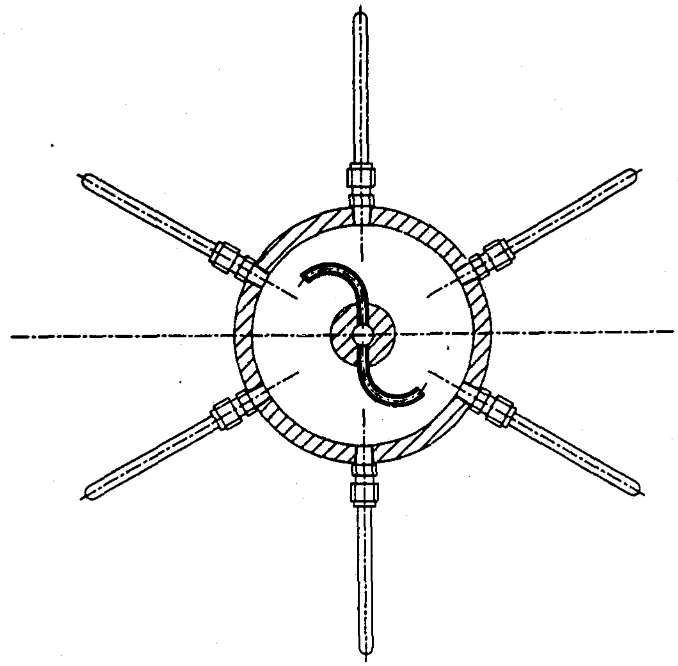

Figure 5.17 - Test Rig Rotor Configuration #4

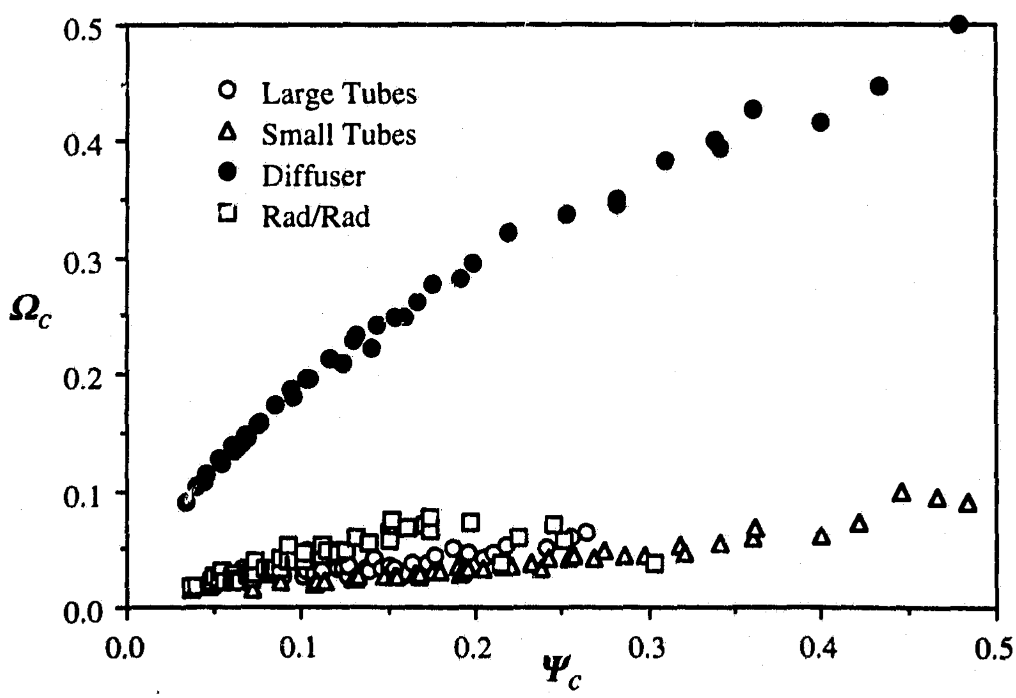

Figure 5.18 - Pressure Coefficient vs Velocity Coefficient

5.5 Conclusions and Further Work

The results of the work with the experimental model and the second prototype clearly indicate that the majority of the flow losses, caused by rotor rotation, are associated with the diffuser. The work also indicates that these losses can be minimized either by eliminating or reducing the radial span of the diffuser chamber. It is also apparent that some small benefit could be derived from positioning the radial holes connecting the shaft bore to the diffuser "tangentially" rather than "radially".

The losses in the radial tubes are relatively independent of the combination of tube length and rotor speed which are used to achieve a given pressure at the centrifuge periphery. This is an important finding as it suggests that the flow losses through a CRO unit should be relatively independent of the rotor diameter.

This study focused on the incremental flow losses caused by rotor rotation. However, future designs must also consider the flow losses when the rotor is at rest as these are the "base line" to which the rotational losses are added. The greatest restriction to flow in the prototype design is the radial holes from the rotor shaft bore to the diffuser chamber. In the second prototype design, however, the size of these holes is limited by their effect on the strength of the rotor shaft. Future diffuser designs should address these apparently conflicting design objectives.

REFERENCES

1. Dixon, S.L., Fluid Mechanics, Thermodynamics of Turbomachinery, 2nd Ed. Permagon Press, Toronto, 1975.

2. Lobanoff, V.S., Ross, R.R., Centrifugal Pumps: Design and Application, Gulf Publishing Company, Houston, 1985.

3. Daugherty, R.L., Franzini, J.B., Fluid Mechanics With Engineering Applications, 7th Ed., McGraw-Hill, Toronto, 1977

Chapter 6

A New Method of Analysis of the Stresses and Strains in a Filament-Wound Cylindrical Shell Under Combined Loading

6.0 The Unique Loading Conditions of a Centrifuge Rotor

The loading conditions on the outer shell of a centrifuge rotor, in particular of a CRO rotor, are unlike the loading conditions of any other conventional application of filament-winding technology. Filament-wound pipe and pressure vessels are widely used in applications in which internal/external pressures, bending and torsion may be present. Manufacturers of filament-wound pipe and pressure vessels have well-established methods for the analysis of stresses and strains in their products. These methods are based on a combination of the theory of orthotropic cylindrical shells and practical experience. Given specific loading conditions, these manufacturers can recommend suitable materials, wind angles and wall thicknesses. Loading due to centrifugal force, however, is not widely understood in the filament-winding industry.

The one exception to this statement is the emerging technology associated with energy-storage flywheels incorporating filament-wound rims. Filament-wound materials are suited to this application by virtue of their relatively high stiffness-to-density and strength-to-density ratios. Since the energy crisis of the early 1970's, energy storage flywheels have received intermittent attention as an alternative to conventional battery applications. As the properties of composite materials have advanced, so also has the potential of filament-wound flywheel energy-storage devices. The methods for the analysis of stresses and strains in filament-wound flywheels are also based on the theory of orthotropic cylindrical shells and practical experience. This expertise, however, is restricted to the few emerging companies and researchers who are working in this field.

The outer shell of a CRO rotor, based on the design of the second prototype, is subjected to radial loading only. Part of this loading is a radial body force due to centripetal acceleration and part is an internal pressure distribution (modeled as uniform) due to the contact forces between the pressure vessels and the inner surface of the outer shell (see Figure 3.5). Future designs are anticipated, possibly including an annular membrane configuration, in which considerable axial loading will also be present. This particular combination of loading conditions does not occur in any of the applications of filament-winding discussed earlier.

A new analytical procedure has, therefore, been developed to assess the stresses and deformations under this combination of loading conditions. This procedure is based on classical laminated plate theory and models both plane stress and plane strain states of a cylindrical shell comprised of a number of cylindrical sublayers, each of which is cylindrically orthotropic. Available loading conditions are: internal and external pressures, axial force (as either an imposed external force or as the force due to pressure vessel end closures) and radial loading due to rotation about the cylinder axis. Material strength analysis is based on the quadratic failure criteria using either the "First Ply Failure" or the "Last Ply Failure" criteria. This procedure, which has been implemented into a FORTRAN 77 program, may be used for stress and deformation analysis of filament wound pressure vessels, flywheels and centrifuge rotors.

6.1 Relations for Stress and Strain

Netting analysis [1] is a simplified approach to the design of cylindrical filament wound structures under internal pressure loading. Netting analysis assumes that all strength and stiffness properties are derived from the fibres alone. Since, in reality, fibre and matrix interact to provide superior properties, netting analysis is a conservative approach to design.

Lekhnitskii [2] developed relations for the problem of *plane stress* in a cylindrical shell which is cylindrically orthotropic and which is subjected to internal and external pressures. By layering a number of such shells and by matching the radial deformations of adjacent shells at their interfaces, he developed relations describing the stresses and strains in a cylindrical shell which is composed of a number of cylindrical layers, each of which has its own particular elastic properties. Lekhnitskii's work was intended for application to wood which is, roughly speaking, cylindrically orthotropic.

Tsai [3] has extended Lekhnitskii's work to the case of *generalised plane strain,* in which the axial deformation of the pressure vessel can be non-zero, and applied it to a composite filament-wound pressure vessel where each layer of Lekhnitskii's model corresponds to a "winding layer" of the pressure vessel. Each winding layer consists of a number of helical winding passes in the positive α orientation alternating with the same number of helical winding passes in the negative α orientation, as shown in Figure 6.1. Winding layers are assumed to be homogenous and cylindrically orthotropic. The properties of each layer, in the tangential plane, are determined from the two-dimensional laminated plate theory while the properties in the radial direction are determined using one of a number of possible models.

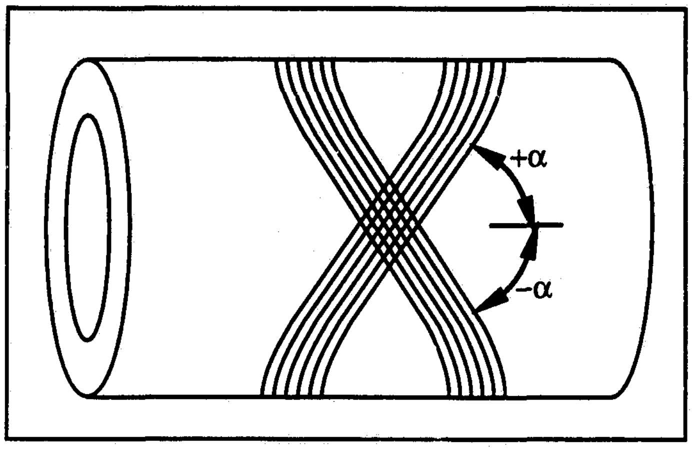

Figure 6.1 - Filament Winding

Lekhnitskii also developed a solution for the problem of *plane stress* in a single and then in a multi-layered thin circular shell which is cylindrically orthotropic and which is subjected to a body force due to rotation. A number of researchers have applied Lekhnitskii's solution in their investigations of the strength of high speed composite flywheels [4,5,6,7].

The present work extends the work of Lekhnitskii and Tsai, by considering the state of *generalised plane strain* in a thick-walled multi-layered filament-wound cylindrical shell which is subjected to both internal pressure and centrifugal loads The axial deformation of each layer is equal to a constant such that the integral of axial stress over the end surfaces is equal to the total axial load. Each layer is considered to be homogeneous and cylindrically orthotropic and variations in wind-angles, from layer to layer, are modeled by variations of the elastic properties, from layer to layer.

6.2 A Model for the State of Stress and Strain in a Multi-Layer Cylindrically Orthotropic Cylindrical Shell

6.2.1 Derivation of the Model

Lekhnitskii [2] derives relations for plane stress in a ring of cylindrically orthotropic material subjected to internal and external pressure and to body forces due to rotation, as shown in Figure 6.2. These relations can be extended to the case of generalised plane strain using the "reduced strain coefficients", also proposed by Lekhitskii [8]. The details of this derivation are shown in Appendix IV.

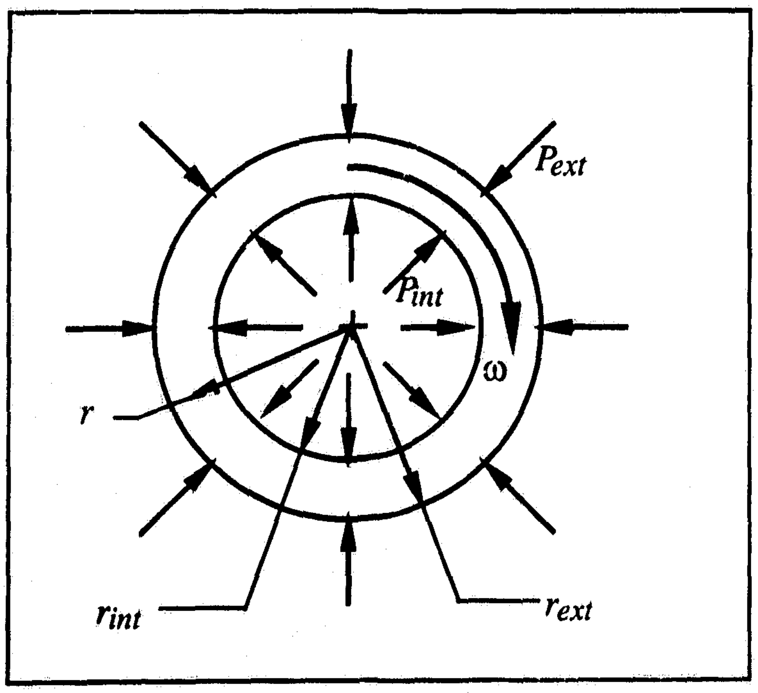

Figure 6.2 - Rotating Shell Under Internal and External Pressure

After Lekhnitskii, the following stress relations are determined

$$\sigma_r = \rho\omega^2 r_{ext}^2 \left(\frac{3+\nu_{\theta r}}{9-g^2}\right)\left(\begin{array}{l}\left(\frac{1-c^{g+3}}{1-c^{2g}}\right)\left(\frac{r}{r_{ext}}\right)^{g-1} + \\ \left(\frac{1-c^{g-3}}{1-c^{2g}}\right)c^{g+3}\left(\frac{r_{ext}}{r}\right)^{g+1} - \left(\frac{r}{r_{ext}}\right)^2\end{array}\right) +$$
$$\left(\frac{P_{\text{int}}c^{g+1}}{1-c^{2g}}\right)\left(\left(\frac{r}{r_{ext}}\right)^{g-1} - \left(\frac{r_{ext}}{r}\right)^{g+1}\right) +$$
$$\left(\frac{P_{ext}}{1-c^{2g}}\right)\left(c^{2g}\left(\frac{r_{ext}}{r}\right)^{g+1} - \left(\frac{r}{r_{ext}}\right)^{g-1}\right)$$

(6.1)

$$\sigma_\theta = \left(\frac{\rho\omega^2 r_{ext}^2}{9-g^2}\right)\left(\begin{array}{l}(3+\nu_{\theta r})g\left(\begin{array}{l}\left(\frac{1-c^{g+3}}{1-c^{2g}}\right)\left(\frac{r}{r_{ext}}\right)^{g-1} \\ -\left(\frac{1-c^{g-3}}{1-c^{2g}}\right)c^{g+3}\left(\frac{r_{ext}}{r}\right)^{g+1}\end{array}\right) \\ -\left(g^2+3\nu_{\theta r}\right)\left(\frac{r}{r_{ext}}\right)^2\end{array}\right)$$
$$\left(\frac{P_{\text{int}}c^{g+1}g}{1-c^{2g}}\right)\left(\left(\frac{r}{r_{ext}}\right)^{g-1} + \left(\frac{r_{ext}}{r}\right)^{g+1}\right) -$$
$$\left(\frac{P_{ext}g}{1-c^{2g}}\right)\left(\left(\frac{r}{r_{ext}}\right)^{g-1} + c^{2g}\left(\frac{r_{ext}}{r}\right)^{g+1}\right)$$

(6.2)

$$\sigma_z = \frac{\varepsilon_z}{a_{33}} - \frac{1}{a_{33}}\left(a_{13}\sigma_r + a_{23}\sigma_\theta\right) \tag{6.3}$$

where $\nu_{\theta r}$ is an effective Poisson ratio,

$$\nu_{\theta r} = -\frac{\beta_{12}}{\beta_{22}} \tag{6.4}$$

and c and g are ratios defined as

$$c = \frac{r_{\text{int}}}{r_{ext}} \qquad\qquad g = \sqrt{\frac{\beta_{11}}{\beta_{22}}} \tag{6.5}$$

β_{ij} are the "reduced strain coefficients" and are defined as,

$$\beta_{ij} = a_{ij} - \frac{a_{i3}a_{j3}}{a_{33}} \qquad (i, j = 1, 2) \tag{6.6}$$

and a_{ij} are the coefficients of the compliance matrix which, for a cylindrically orthotropic material reduces to,

$$\begin{Bmatrix} \varepsilon_r \\ \varepsilon_\theta \\ \varepsilon_z \\ \gamma_{\theta z} \\ \gamma_{zr} \\ \gamma_{r\theta} \end{Bmatrix} = \begin{bmatrix} a_{11} & a_{12} & a_{13} & & & \\ a_{12} & a_{22} & a_{23} & & & \\ a_{13} & a_{23} & a_{33} & & & \\ & & & a_{44} & & \\ & & & & a_{55} & \\ & & & & & a_{66} \end{bmatrix} \begin{Bmatrix} \sigma_r \\ \sigma_\theta \\ \sigma_z \\ \tau_{\theta z} \\ \tau_{zr} \\ \tau_{r\theta} \end{Bmatrix} \tag{6.7}$$

The components of displacement are,

$$
\begin{aligned}
u_r &= r(\beta_{12}\sigma_r + \beta_{22}\sigma_\theta - \nu_{z\theta}\varepsilon_z) \\
u_\theta &= 0 \qquad\qquad (6.8\text{-}6.10) \\
u_z &= z\varepsilon_z
\end{aligned}
$$

where,

$$\nu_{z\theta} = -\frac{a_{23}}{a_{33}} \qquad (6.11)$$

This solution can be extended to the case of a multi-layered cylinder, as shown in Figure 6.3, in which each layer is cylindrically orthotropic but in which the elastic constants vary from layer to layer. This models a filament-wound shell in which the wind angle varies from layer to layer and where each layer is assumed to be homogeneous and cylindrically orthotropic. It is assumed that the pressure vessel is in a state of plane strain and, therefore, that the axial deformation of all layers is equal to a consant, ε_z^0.

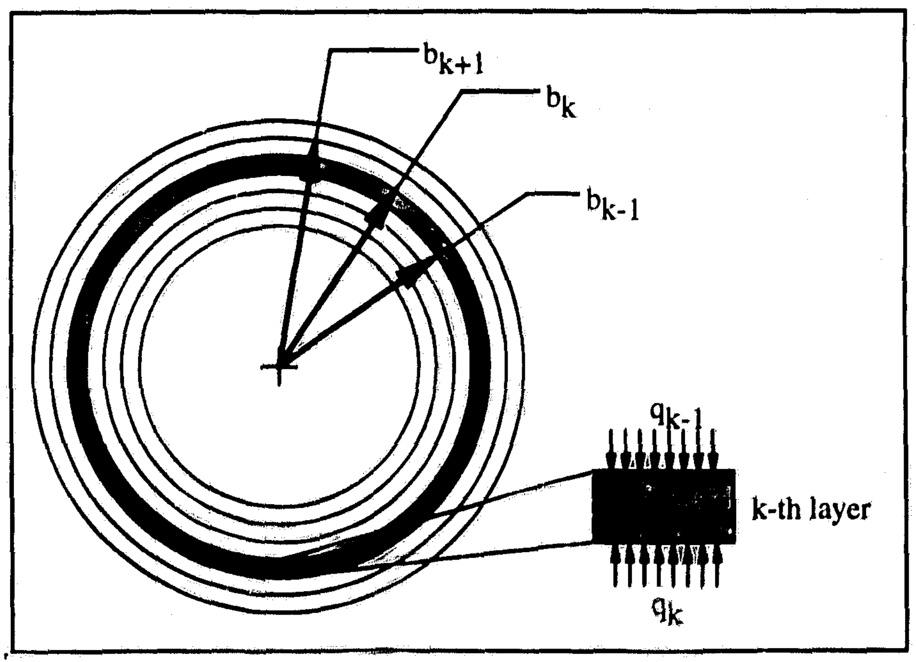

Figure 6.3 - Multi-layered cylinder showing layer notation

After Lekhnitskii, the stresses in the k-th layer are as follows,

$$\sigma_r^{(k)} = \rho_k \omega^2 b_k^2 \left(\frac{3+\nu_{\theta r}^{(k)}}{9-g_k^2}\right)\left(\left(\frac{1-c_k^{g_k+3}}{1-c_k^{2g_k}}\right)\left(\frac{r}{b_k}\right)^{g_k-1} + \left(\frac{1-c_k^{g_k-3}}{1-c_k^{2g_k}}\right)c_k^{g_k+3}\left(\frac{b_k}{r}\right)^{g_k+1} - \left(\frac{r}{b_k}\right)^2\right) +$$
$$\left(\frac{q_{k-1}c_k^{g_k+1}}{1-c_k^{2g_k}}\right)\left(\left(\frac{r}{b_k}\right)^{g_k-1} - \left(\frac{b_k}{r}\right)^{g_k+1}\right) +$$
$$\left(\frac{q_k}{1-c_k^{2g_k}}\right)\left(c_k^{2g_k}\left(\frac{b_k}{r}\right)^{g_k+1} - \left(\frac{r}{b_k}\right)^{g_k-1}\right) +$$

(6.12)

$$\sigma_\theta^{(k)} = \left(\frac{\rho_k \omega^2 b_k^2}{9-g_k^2}\right)\left(\left(3+\nu_{\theta r}^{(k)}\right)g_k\left(\left(\frac{1-c_k^{g_k+3}}{1-c_k^{2g_k}}\right)\left(\frac{r}{b_k}\right)^{g_k-1} - \left(\frac{1-c_k^{g_k-3}}{1-c_k^{2g_k}}\right)c_k^{g_k+3}\left(\frac{b_k}{r}\right)^{g_k+1}\right) - \left(g_k^2+3\nu_{\theta r}^{(k)}\right)\left(\frac{r}{b_k}\right)^2\right) +$$
$$\left(\frac{q_{k-1}c_k^{g_k+1}g_k}{1-c_k^{2g_k}}\right)\left(\left(\frac{r}{b_k}\right)^{g_k-1} + \left(\frac{b_k}{r}\right)^{g_k+1}\right) -$$
$$\left(\frac{q_k g_k}{1-c_k^{2g_k}}\right)\left(\left(\frac{r}{b_k}\right)^{g_k-1} + c_k^{2g_k}\left(\frac{b_k}{r}\right)^{g_k+1}\right)$$

(6.13)

$$\sigma_z^{(k)} = \frac{\varepsilon_z^{\mathbf{0}}}{a_{33}^{(k)}} - \frac{1}{a_{33}^{(k)}}\left(a_{13}^{(k)}\sigma_r^{(k)} + a_{23}^{(k)}\sigma_\theta^{(k)}\right) \tag{6.14}$$

where,

$$c_k = \frac{b_{k-1}}{b_k} \quad (6.15) \qquad g_k = \sqrt{\frac{\beta_{11}^{(k)}}{\beta_{22}^{(k)}}} \quad (6.16) \qquad \nu_{\theta r}^{(k)} = -\frac{\beta_{12}^{(k)}}{\beta_{22}^{(k)}} \quad (6.17)$$

and

$$\beta_{ij}^{(k)} = a_{ij}^{(k)} - \frac{a_{i3}^{(k)}a_{j3}^{(k)}}{a_{33}^{(k)}} \quad (i,j=1,2) \tag{6.18}$$

The displacements are as follows,

$$\begin{aligned} u_r^{(k)} &= r\left(\beta_{12}^{(k)}\sigma_r^{(k)} + \beta_{22}^{(k)}\sigma_\theta^{(k)} - \nu_{z\theta}^{(k)}\varepsilon_z^{\mathbf{0}}\right) \\ u_\theta^{(k)} &= 0 \\ u_z^{(k)} &= z\varepsilon_z^{\mathbf{0}} \end{aligned} \qquad (6.19\text{-}6.21)$$

where

$$\nu_{z\theta}^{(k)} = -\frac{a_{23}^{(k)}}{a_{33}^{(k)}} \tag{6.22}$$

Axial equilibrium of each layer is satisfied by the following relation,

$$\sum_{k=1}^{n} 2\pi \int_{b_{k-1}}^{b_k} \sigma_z^{(k)} r dr = \pi\left(P_{int} r_{int}^2 - P_{ext} r_{ext}^2\right) + F_A \qquad (6.23)$$

Substituting equations 6.12 and 6.13 for $\sigma_r^{(k)}$ and $\sigma_\theta^{(k)}$, respectively, into equation 6.14 for $\sigma_z^{(k)}$ and then evaluating the integral in equation 6.23, the following relation for $\varepsilon_z^{\mathbf{o}}$ is determined,

$$\varepsilon_z^{\mathbf{o}} = \frac{1}{\Delta}\left(\left(P_{int} r_{in}^2 - P_{ext} r_{ext}^2\right) + {}^{F_A}\!/_{\pi} - \sum_{k=1}^{n}\left(q_{k-1}\delta_k + q_k\mu_k + \omega^2\psi_k\right)\right) \qquad (6.24)$$

This is similar to the relation developed by Tsai [2], except for the additional term ψ_k which accounts for the effect of rotation. δ_k, μ_k and Δ are as defined by Tsai,

$$\delta_k = \frac{-2}{a_{33}^{(k)}\left(1 - c_k^{2g_k}\right)} \begin{pmatrix} \dfrac{b_k c_k^{g_k+1}}{1+g_k}\left(a_{13}^{(k)} + g_k a_{23}^{(k)}\right)\left(b_k - c_k^{g_k} b_{k-1}\right) \\ -\dfrac{b_{k-1}}{1-g_k}\left(a_{13}^{(k)} - g_k a_{23}^{(k)}\right)\left(b_k c_k^{g_k} - b_{k-1}\right) \end{pmatrix} \qquad (6.25)$$

$$\mu_k = \frac{-2}{a_{33}^{(k)}\left(1 - c_k^{2g_k}\right)} \begin{pmatrix} \dfrac{-b_k}{1+g_k}\left(a_{13}^{(k)} + g_k a_{23}^{(k)}\right)\left(b_k - c_k^{g_k} b_{k-1}\right) \\ +\dfrac{b_k c_k^{g_k}}{1-g_k}\left(a_{13}^{(k)} - g_k a_{23}^{(k)}\right)\left(b_k c_k^{g_k} - b_{k-1}\right) \end{pmatrix} \qquad (6.26)$$

$$\Delta = \sum_{k=1}^{n} \frac{b_k^2 - b_{k-1}^2}{a_{33}^{(k)}} \qquad (6.27)$$

and the new term, ψ_k, is as follows,

$$\psi_k = \frac{2\rho_k b_k^2\left(3+\nu_{\theta r}^{(k)}\right)}{9-g_k^2}\left(\begin{array}{l} \left(\dfrac{a_{13}^{(k)}}{a_{33}^{(k)}} + \dfrac{a_{23}^{(k)}}{a_{33}^{(k)}} g_k\right)\left(\dfrac{1-c_k^{g_k+3}}{\left(1-c_k^{2g_k}\right)\left(1+g_k\right)}\right)\left(b_k^{-g_k+1} b_{k-1}^{g_k+1} - b_k^2\right) + \\ \left(\dfrac{a_{13}^{(k)}}{a_{33}^{(k)}} - \dfrac{a_{23}^{(k)}}{a_{33}^{(k)}} g_k\right)\left(\dfrac{\left(1-c_k^{g_k-3}\right)c_k^{g_k+3}}{\left(1-c_k^{2g_k}\right)\left(1-g_k\right)}\right)\left(b_k^{g_k+1} b_{k-1}^{-g_k+1} - b_k^2\right) + \\ \left(\dfrac{a_{13}^{(k)}}{a_{33}^{(k)}} + \dfrac{a_{23}^{(k)}}{a_{33}^{(k)}} \dfrac{\left(g_k^2 + 3\nu_{\theta r}^{(k)}\right)}{\left(3+\nu_{\theta r}^{(k)}\right)}\right)\left(\dfrac{1}{4b_k^2}\left(b_k^4 - b_{k-1}^4\right)\right) \end{array}\right)$$

(6.28)

Now, substituting $\sigma_r^{(k)}$, $\sigma_\theta^{(k)}$ and ε_z^{0} from equations 6.12, 6.13 and 6.24, respectively, into equation 6.19, a new expression for $u_r^{(k)}$, in terms of the interface pressures, q_i ,is determined. The radial displacements of adjacent layers, at their interface, must be equal, or,

$$u_r^{(k)}(b_k) = u_r^{(k+1)}(b_k) \qquad (6.29)$$

Upon substitution of this new expression for $u_r^{(k)}$ into 6.29, a set of simultaneous equations in q_i, one for each of the n-1 interfaces, are defined.

$$\phi_k q_{k+1} + \gamma_k q_k + \eta_k q_{k-1} + \omega^2 \lambda_k + \left(\frac{v_{z\theta}^{(k)} - v_{z\theta}^{(k+1)}}{\Delta}\right)\left(\sum_{i=1}^{n}\left(q_{i-1}\delta_i + q_i\mu_i + \omega^2 \psi_i\right)\right) = \left(\frac{v_{z\theta}^{(k)} - v_{z\theta}^{(k+1)}}{\Delta}\right)\left[\left(P_{in} r_{\mathrm{int}}^2 - P_{ext} r_{ext}^2\right) + F/\pi\right]$$

(6.30)

Again, this relation is similar to the relation developed by Tsai [3], except for the additional terms ψ_k and λ_k which account for the effect of rotation. ϕ_k, γ_k and η_k are as defined by Tsai,

$$\phi_k = \frac{2 g_{k+1} \beta_{22}^{(k+1)} c_{k+1}^{(g_{k+1}-1)}}{1 - c_{k+1}^{2 g_{k+1}}} \qquad (6.31)$$

$$\gamma_k = -\beta_{12}^{(k)} - \frac{g_k \beta_{22}^{(k)}\left(1 + c_k^{2 g_k}\right)}{\left(1 - c_k^{2 g_k}\right)} + \beta_{12}^{(k+1)} - \frac{g_{k+1} \beta_{22}^{(k+1)}\left(1 + c_{k+1}^{2 g_{k+1}}\right)}{\left(1 - c_{k+1}^{2 g_{k+1}}\right)} \qquad (6.32)$$

$$\eta_k = \frac{2 g_k \beta_{22}^{(k)} c_k^{g_k+1}}{1 - c_k^{2 g_k}} \qquad (6.33)$$

and the new term, λ_k, is as follows,

$$\lambda_k = b_k^2 \left\{ \begin{array}{l} \dfrac{\rho_k \beta_{22}^{(k)}}{\left(9 - g_k^2\right)} \left\{ \begin{array}{l} g_k \left(3 + \nu_{\theta r}^{(k)}\right) \left(\dfrac{\left(1 - 2c_k^{g_k+3} + c_k^{2g_k}\right)}{\left(1 - c_k^{2g_k}\right)} \right) - \\ \left(g_k^2 + 3\nu_{\theta r}^{(k)}\right) \end{array} \right\} + \\ \dfrac{\rho_{k+1} \beta_{22}^{(k+1)}}{\left(9 - g_{k+1}^2\right)} \left\{ \begin{array}{l} g_{k+1} \left(3 + \nu_{\theta r}^{(k+1)}\right) \left(\dfrac{\left(1 - 2c_{k+1}^{g_{k+1}-3} + c_{k+1}^{2g_{k+1}}\right)}{\left(1 - c_{k+1}^{2g_{k+1}}\right)} \right) + \\ \left(g_{k+1}^2 + 3\nu_{\theta r}^{(k+1)}\right) \end{array} \right\} \end{array} \right\}$$

(6.34)

Once the simultaneous equations, 6.30, are solved for the q_k's, equations 6.12, 6.13, 6.14, 6.19 and 6.24 are used to determine $\sigma_r^{(k)}$, $\sigma_\theta^{(k)}$, $\sigma_z^{(k)}$, $u_r^{(k)}$ and ε_z^0 respectively. $\sigma_r^{(k)}$, $\sigma_\theta^{(k)}$ and $\sigma_z^{(k)}$ are then transformed to the coordinates of the individual lamina which lie at $\pm\alpha$ with respect to the cylinder coordinates. The Quadratic or "Tsai-Hahn" failure criteria (see section 6.2.4), in used to calculate a strength ratio, $S^{(k)}$, for each lamina. The strength ratio can be calculated for "First Ply Failure" or for "Last Ply Failure". For either failure model, the lamina with the lowest $S^{(k)}$ value determines the limiting load.

6.2.2 Plane Stress

The case of plane stress can easily be recovered from the plane strain model developed in section 6.2.1 by converting the reduced strain coefficients to the corresponding coefficients of the compliance matrix, namely,

$$\beta_{ij}^{(k)} = a_{ij}^{(k)} \qquad (i, j = 1, 2) \tag{6.35}$$

Equation 6.30 then reduces to,

$$\phi_k q_{k+1} + \gamma_k q_k + \eta_k q_{k-1} + \omega^2 \lambda_k = 0 \tag{6.36}$$

where ϕ_k, γ_k , η_k and λ_k are as defined by equations 6.31-6.34. Once the simultaneous equations, 6.36, have been solved for the q_k's, equations 6.12 and 6.13 are used to determine $\sigma_r^{(k)}$ and $\sigma_\theta^{(k)}$. In addition, we now have,

$$\sigma_z^{(k)} = 0 \tag{6.37}$$

$$\varepsilon_z^{(k)} = a_{13}^{(k)} \sigma_r^{(k)} + a_{23}^{(k)} \sigma_\theta^{(k)} \tag{6.38}$$

$$u_r^{(k)} = r\left(\beta_{12}^{(k)} \sigma_r^{(k)} + \beta_{22}^{(k)} \sigma_\theta^{(k)}\right) \tag{6.39}$$

6.2.3 Effective Elastic Properties for the Laminate

In general, a laminated composite, or "laminate", is comprised of a number of anisotropic layers or "laminae", each possessing its own elastic properties. These elastic properties, tensile and shear moduli and Poisson ratios, describe the response of each lamina to applied loads. The "effective" elastic properties of a laminate describe the response of the laminate, as a unit, to applied loads. The "in-plane" effective elastic properties of a laminate can be determined from the "in-plane" elastic properties of the individual laminae using the theory of laminated plates [9]. ("In-plane" refers to the plane which is normal to stacking direction of the laminate.) The in-plane constitutive relation of the laminate is, thus, determined from the in-plane constitutive relations of the individual laminae.

An "angle-ply" laminate is a special class of laminates having alternating lamina placed at angles $+\phi$ and $-\phi$. A filament-wound cylindrical shell, having a wind angle of $\pm\alpha$, is an angle-ply laminate. In the multi-layered shell that is the subject of this investigation, each layer is an angle-ply laminate with its own wind angle, $\pm\alpha_{(k)}$, as shown in Figure 6.4. Neglecting the effect of curvature, the effective elastic properties of each of these layers, in the tangential plane, are equivalent to the in-plane properties of the equivalent angle-ply laminate. The in-plane effective elastic properties for an angle-ply laminate can, thus, be calculated from the theory of laminated anisotropic plates [9].

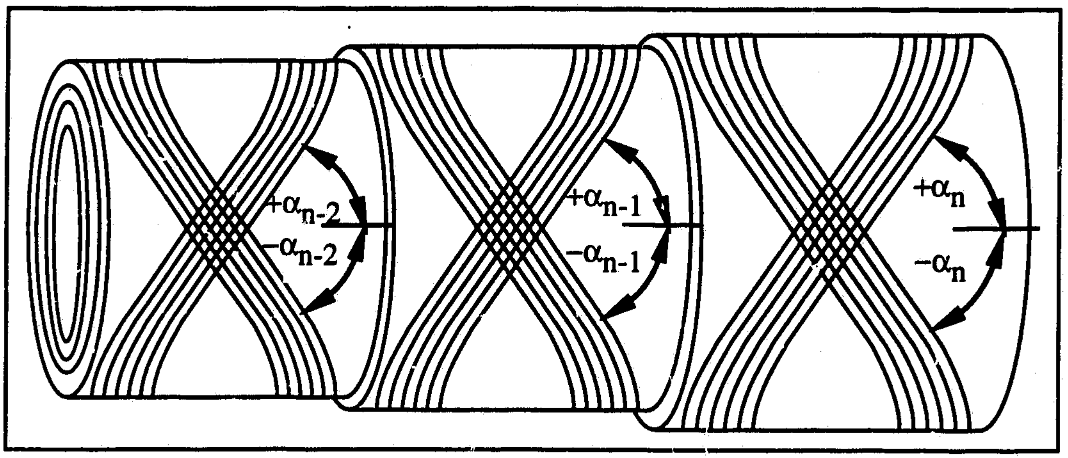

Figure 6.4 - Multi-Layered Filament Wound Cylinder

As this investigation is concerned with stresses and strains in three dimensions, effective elastic properties in all three dimensions are required. Unfortunately, there is no well established analytical method for determining the effective elastic properties of a laminate in the interlaminar direction. Given the three-dimensional elastic properties of the uniaxial laminae of which the laminate is comprised, there are a number models in the literature which will approximate the three-dimensional effective elastic properties of the laminate [10,11,12,13,14]. The method of Sun and Li [10], see Appendix V, is used in this work as it shows good correlation with experimental data and is relatively easy to implement.

6.2.4 Failure Criteria

It has been shown that the modes of failure in filament-wound composite pipes vary with wind angle, material, wall thickness and loading conditions [15,16,17,18]. It is not, however, the intention of this work to explore the subtleties of failure mode analysis, but rather to provide a model with which to calculate levels of stress and strain, within the bounds of linear deformation. This information can then be used as input for any given failure criteria.

In a recent survey of macroscopic failure criteria [19], Tsai concluded that the quadratic failure criteria is more suitable for use with composite materials than the maximum stress or maximum strain criteria. For the cases considered in his study, all three criteria show good agreement with experimental data but, whereas the maximum stress and strain criteria are defined by seven inequalities, the quadratic failure criteria is expressed in a single equation.

$$F_{ij}\sigma_i\sigma_j + F_i\sigma_i = 1 \quad i,j = 1,2....6 \qquad (6.40)$$

This equation consists of a scalar products of tensor components. These tensors lend themselves to the kind of coordinate transformations which are commonly performed in composites analysis. For this study, therefore, the quadratic or "Tsai-Hahn" failure criteria is used. A detailed description of the quadratic failure criteria, as applied to a three-dimensional state of stress in a composite, is given in Appendix VI.

In general, every ply in a composite does not fail at the same time. Assuming no delamination occurs, there is a sequence of ply failures leading to the ultimate failure of the composite. The load to failure can be calculated for "First Ply Failure" (FPF), which is self explanatory, or for "Last Ply Failure" (FPF) in which it is assumed that the composite matrix has failed in every ply but the fibres are intact [3]. This condition is modeled by applying a "degradation factor" (DF) to the matrix modulus of every layer, thus, reducing the transverse modulus of the unidirectional laminate of which each ply is comprised. The transverse strength properties are, however, not degraded. This has the effect of suppressing the transverse failure mode. Since, in most cases, transverse failure is the first mode of failure, LPF generally occurs at a higher loading that FPF.

6.2.5 Model Verification

The analytical procedures developed in sections 6.2.1 and 6.2.2, augmented by the model of elastic properties and by the failure criteria described in sections 6.2.3 and 6.2.4 respectively, have been incorporated into a FORTAN 77 program which allows the user to input geometric parameters and material properties for each layer and the loading conditions for the shell as a whole.

The stresses and deformations determined by the program were first verified for the case of a multi-layer shell comprised of an isotropic material. These results were verified against the closed form solutions for a single layer shell subject to both internal pressure loading and to the forces of rotation [20]. The program was then verified for the case of a multi-layer shell comprised of cylindrically orthotropic layers with the same elastic properties. For both internal pressure loading and rotational loading, the program was verified against the thin-walled pressure vessel approximation where the circumferential and axial stresses are assumed constant through the thickness of the pressure vessel wall. A comparison of results is shown in Figure 6.5.

6.3 Applications of the Procedure

The procedure is applied to examples of three different applications: pressure vessels, centrifuge rotors, and flywheels. In each of these examples, the material on which the analysis is based is a graphite/epoxy composite (T300/N5208). The properties of the unidirectional laminate are given in Appendix VII.

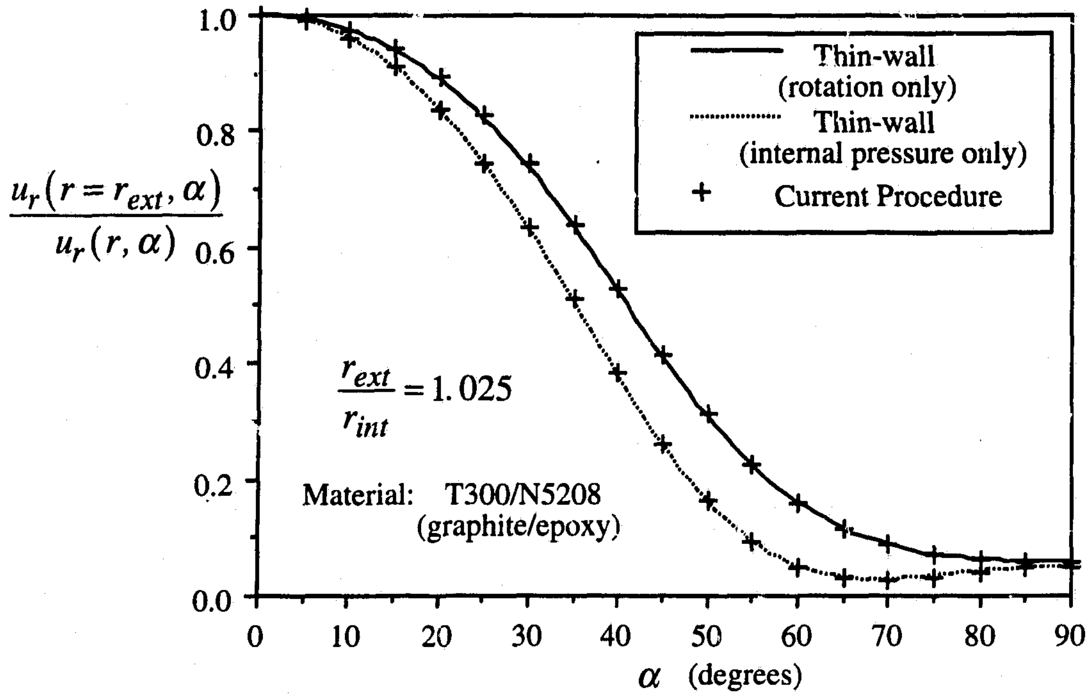

Figure 6.5 - Radial Deformation vs Wind Angle for Thin-wall model and Current Model

6.3.1 Application #1 - Pressure Vessel Design

Consider a filament wound pressure vessel with closed ends and wound at a constant wind angle. For this application, netting analysis can be used to determine the wind angle for which the fibres bear all of the axial and circumferential loading and for which the matrix is, therefore, unstressed. Netting analysis [1] shows that this wind angle should be related to the average through-the-thickness axial and circumferential stresses, as follows.

$$\tan^2 \alpha = \frac{\bar{\sigma}_\theta}{\bar{\sigma}_z} \tag{6.41}$$

In reality, of course, the matrix is subject to stresses but this is an approximate means by which to minimize that stress. As the matrix failure is, almost without exception, the weakest mode of failure in a composite structure, this wind angle should be close to the optimal wind angle for the pressure vessel.

For a thin-walled pressure vessel with closed ends, it can be shown that,

$$\frac{\overline{\sigma}_\theta}{\overline{\sigma}_z} = 2 \tag{6.42}$$

and, using equation 6.41,

$$\alpha_{opt} = \pm 54.74^{\circ} \tag{6.43}$$

Using the current procedure, optimum wind-angles have been shown to range from 54° to 56° for radius ratios of 1.025 to 1.5.

In general, of course, the stress distribution through the wall of a filament-wound vessel will not be uniform but will vary, depending upon geometry, materials, method of construction and loading. Consider, for example, single layer cylindrically orthotropic shells under internal pressure loading only, with end closures and with $1.025 \leq R_{ext}/R_{\text{int}} \leq 1.5$. As wall thickness increases, the stress distribution through the thickness of the wall becomes increasingly non-uniform, as shown in the calculated stress profiles shown in Figure 6.6. For each wall thickness, the appropriate optimum wind angle has been used, as discussed earlier.

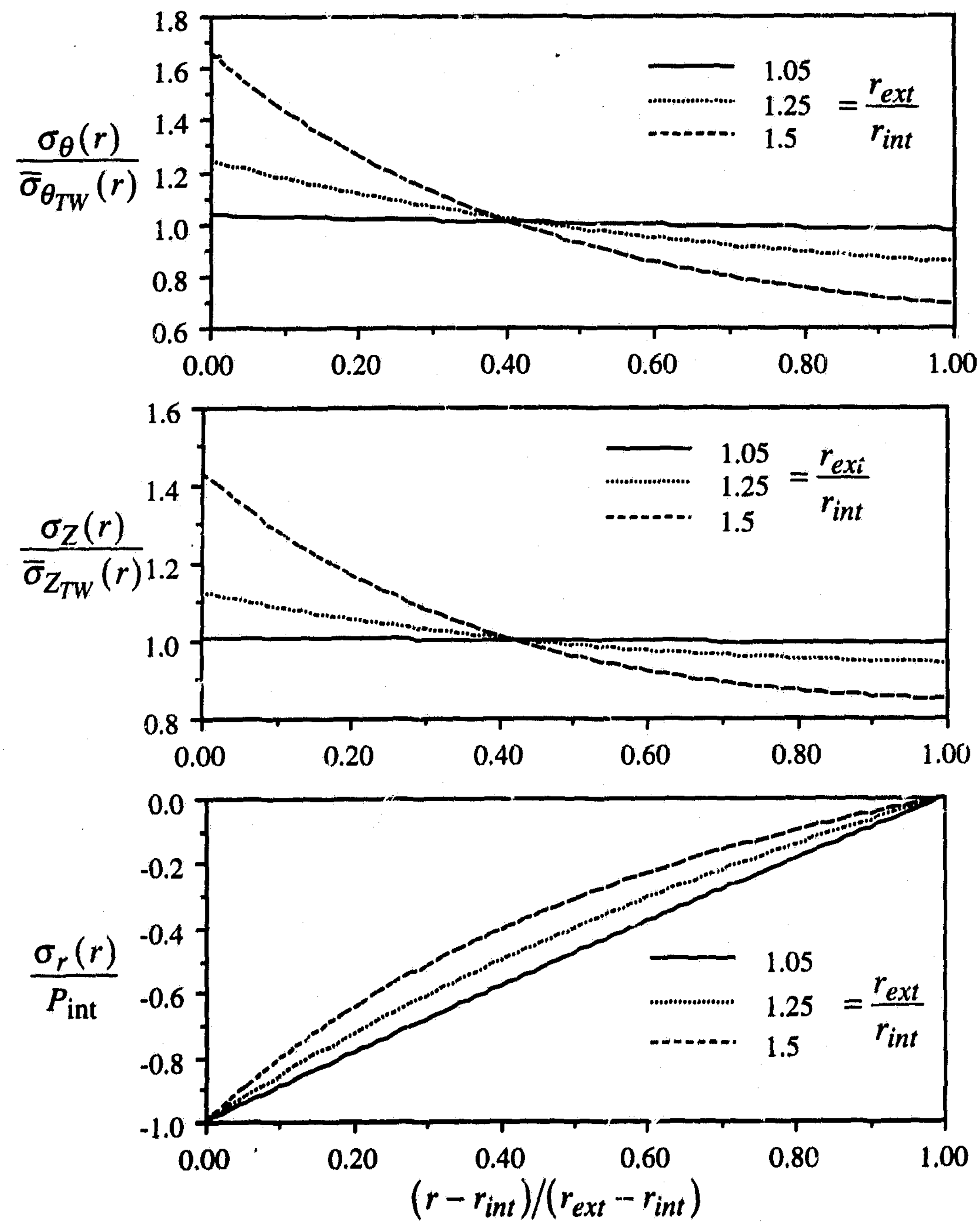

Figure 6.6 - Circumferential, Axial and Radial Stress Profiles (Material: T300/N5208 - graphite/epoxy)

These stress distributions result in strength ratio distributions which also vary through the wall of a filament-wound vessel, as shown in Figure 6.7. The load bearing capability of the material in regions of high strength ratio, S, is not as well utilized as in regions of low strength ratio.

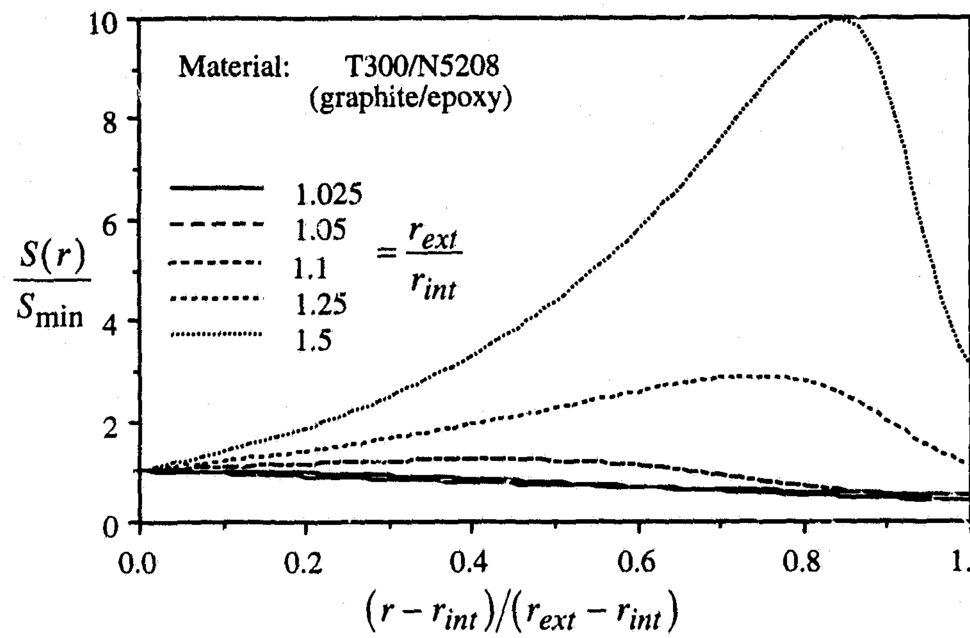

Figure 6.7 - Strength Ratio vs Radial Position (Last Ply Failure, DF=0.3)

Consider again the case of a pressure vessel with closed ends and under internal pressure loading. Rather than a single wind angle through the thickness of the vessel wall, consider now a multitude of layers wound at different angles. The wind angles in each layer can be specified so as to provide both a more even distribution of strength ratio and a higher failure pressure. For example, the wind angles of shells having three layers have been tuned, by trial and error, to provide the increases in failure pressures listed in Table 6.1. These wind angle combinations are not optimal but they do provide an indication of the potential benefit of variable wind angles.

$\frac{R_{ext}}{R_{int}}$	Optimum Constant Wind-angle α	Alternative Wind-Angle Combination $(\alpha_1 / \alpha_2 / \alpha_3)$	LPF Failure Pressure Percentage Increase
1.1	55°	68°/56°/38°*	7.6%
1.25	55°	35°/55°/75°*	9.7%
1.5	56°	25°/60°/75°	5.4%

*Tsai [2] also found these wind-angle combinations to be beneficial

Table 6.1 - Increase in Burst Pressure Associated with Variable Wind Angles

(Last Ply Failure, DF=0.3)

Tsai [3] has identified the potential benefits to filament-wound pressure vessel efficiency, based on the LPF criteria, associated with variable wind angles . Although the current procedure uses a different model for the elastic constants than was used in Tsai's work, the results presented here confirm the trends and design principles identified by Tsai.

It is important to note that, for the FPF criteria, the benefits of wind angle variation are much less significant. The maximum improvement to FPF-criteria failure pressure, achieved by trial and error variation of the wind angles, was less than one percent. The LPF criteria degrades the matrix modulus, reducing the transverse modulus of the unidirectional laminate, but leaves the transverse strength properties intact. This has the effect of suppressing the transverse failure mode. In the biaxial loading of a pressure vessel, therefore, the fibres in an individual layer can be oriented to provide maximum strength with respect to hoop or axial loading without transverse failure of that layer due to axial or hoop strain respectively. The intact transverse modulus of the FPF criteria, however, produces significant transverse stresses if the wind angle varies from the netting analysis optimum.

6.3.2 Application #2 - Centrifuge Rotor Design

Consider a centrifuge rotor which consists of a cylindrical filament-wound pressure vessel with closed ends, filled with liquid and rotating about its axis of symmetry. The average, or thin-walled hoop stress, $\overline{\sigma}_\theta$, is comprised of a component due to the internal fluid pressure and a component due to the forces of rotation on the rotor material, as follows,

$$\overline{\sigma}_\theta\Big|_{pressure} = \frac{P_p r_{int}}{\left(r_{ext} - r_{int}\right)} \tag{6.44}$$

where,

$$P_p = \frac{1}{2}\rho_f \omega^2 r_{int}^2 \tag{6.45}$$

and

$$\overline{\sigma}_\theta\Big|_{rotation} = \frac{\rho_c \omega^2 \left(r_{ext}^3 - r_{int}^3\right)}{3\left(r_{ext} - r_{int}\right)} \tag{6.46}$$

The average axial stress, $\overline{\sigma}_z$, is due to the internal fluid pressure only.

$$\overline{\sigma}_z = \frac{P_p r_{int}}{4\left(r_{ext} - r_{int}\right)} \tag{6.47}$$

The ratio of average axial stress to average circumferential stress and, therefore, the optimum netting analysis wind-angle is as follows,

$$tan^2 \alpha_{opt} = \frac{\overline{\sigma}_\theta}{\overline{\sigma}_z} = \frac{\overline{\sigma}_\theta|_{pressure} + \overline{\sigma}_\theta|_{rotation}}{\overline{\sigma}_z} \tag{6.48}$$

$$tan^2 \alpha_{opt} = \frac{\overline{\sigma}_\theta}{\overline{\sigma}_z} = \frac{4\left(2\rho_c\left(r_{ext}^3 - r_{int}^3\right) + 3\rho_f r_{int}^3\right)}{3\rho_l r_{int}^3} \tag{6.49}$$

This ratio is higher than for the case of a static pressure vessel. The total axial force is lower because the pressure on the end closures decreases from the pressure at the inner wall of the rotor to zero at the axis of the rotor. The total hoop force is higher because of the additional loading due to the forces of rotation on the rotor material. Not only is the resulting optimum wind angle higher than for the case of a static pressure vessel, but it is also an increasing function of rotor wall thickness, as shown in Figure 6.8. The differences between the netting analysis results and the results of the current procedure, also shown in Figure 6.8, are due to the stiffness and strength of the composite in the transverse and shear directions. Netting analysis neglects these properties.

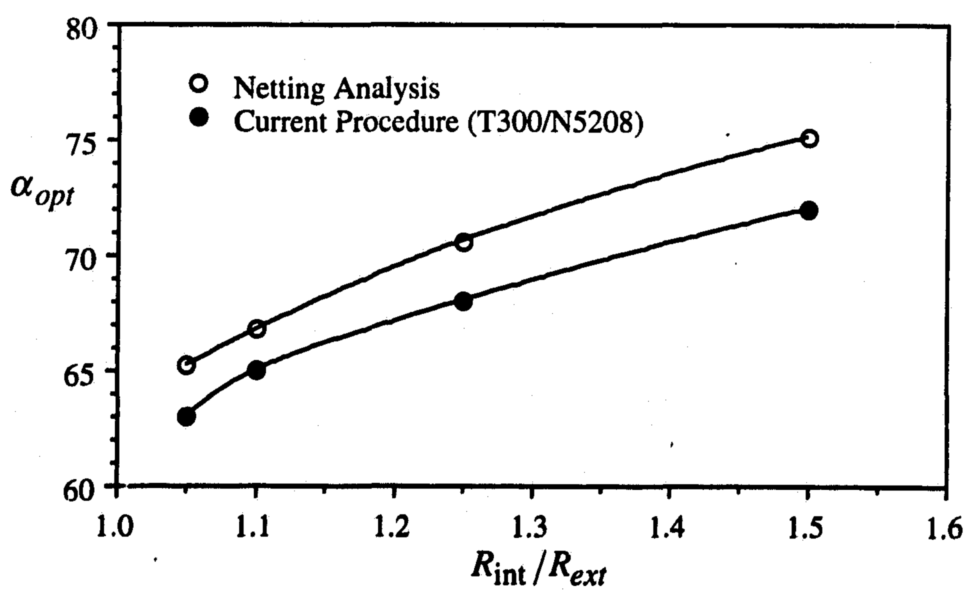

Figure 6.8 - Optimum Wind Angle vs Radius Ratio

As is the case for a static pressure vessel, the benefits of wind angle variation in a centrifuge rotor are more significant for LPF than for FPF. For safety reasons, however, the LPF criteria is not appropriate for rotor design if, indeed, it is appropriate for pressure vessel design. For the graphite/epoxy composite considered here, therefore, optimum constant wind-angle is effectively an optimum design. For composites having lower matrix moduli, relative to the fibre moduli, there may be some benefit associated with wind-angle variation.

6.3.3 Application #3 - Energy Storage Flywheel Design

The mode of failure most commonly reported in the literature is interlaminar failure due to positive radial stresses. A number of solutions to this problem have been proposed, including:

i) ballasting of the inner layers with lead particles [5]

ii) reinforcement with quasi-isotropic discs on either side of the flywheel. [21]

iii) radial tapering of the flywheel [22, 23]

iv) interference fit with internal hub [24]

An alternative solution is to vary the wind angles such that the inner layers are relatively compliant in the hoop direction while the outer layers remain relatively stiff. In this manner the inner layers will move with the outer layers maintaining small or negative radial stresses.

Consider the case of a filament-wound graphite/epoxy flywheel with an inner radius of 0.5 m and an outer radius of 1.0 m consisting of five layers of equal thickness. By changing the wind angles from a constant 90° to 68°/73.5°/79°/84.5°/90°, the kinetic energy capacity increases by 45.7% as determined by plane stress analysis and 36.6% as determined by plane strain analysis based on FPF criteria. As in Section 6.4.1, this combination has been determined by trial and error and is not optimal. It does, however, provide an indication of the potential benefit of variable wind angles to flywheel design.

Stress analysis of high-speed composite rotors for energy storage flywheels is generally based on the assumption of plane stress. Most researchers [4,5,6,7,21,22,23,24] have, therefore, based their analysis on the relations of Lekhnitskii [2]. This assumption requires that there is no stress in the axial direction and, in addition, that the disc is free to deform in the axial direction. Although this assumption is only exactly satisfied for infinitesimally thin discs, practically useful results can be obtained for discs which have a relatively large radius to thickness ratio [25], if the wind-angle does not vary through the radial thickness of the rotor. If, however, there are variations in wind angle, axial stresses will be induced due to the associated transitions in the Poisson ratio $\nu_{\theta z}^{(k)}$. Neglecting end-effects, therefore, plane strain should be a more accurate model of this application where wind angle is not constant. As neither the plane stress nor the plane strain model presented here addresses the state of stress near the ends, further analysis is these regions is warranted.

6.4 Conclusions and Further Work

A new analytical procedure is developed to assess the stresses and deformations under loading conditions particular to centrifuge rotors. This procedure is based on classical laminated plate theory and models both plane stress and plane strain states of a cylindrical shell comprised of a number of cylindrical sublayers, each of which is cylindrically orthotropic. Available loading conditions are: internal and external pressures, axial force (as either an imposed external force or as the force due to pressure vessel end closures) and radial loading due to rotation about the cylinder axis. Material strength analysis is based on the quadratic failure criteria using either the "First Ply Failure" or the "Last Ply Failure" criteria. This procedure, which has been implemented into a FORTRAN 77 program, may be used for stress and deformation analysis of filament wound pressure vessels, flywheels and centrifuge rotors.

Preliminary results indicate that for FPF of a cylinder of graphite/epoxy composite with biaxial loading, such as a pressure vessel with closed ends, the benefit of wind angle variation is relatively small. If, however, the loading is only in the hoop direction, such as a thick-rimmed flywheel, there are significant benefits associated with wind angle variation. Other materials may show greater benefit for the biaxial loading case if the matrix is sufficiently compliant.

An expression for the optimal constant wind angle in centrifuge rotor with closed ends is developed using netting analysis. The new procedure gives similar optima with differences being due to the stiffness and strength properties of the composite matrix which are neglected in netting analysis.

Further development to this procedure should include routines for the selection of optimal wind angles, inclusion of residual stresses due to composite curing, and interference fits between adjacent layers. In addition, sensitivity studies of alternative failure criteria and methods of determining elastic constants in three dimensions should be conducted and verified against experimental data.

REFERENCES

1. Engineering Materials Handbook, ASM International, p. 508

2. Lekhnitskii, S.G., Anisotropic Plates, Gordon and Breach Science Publishers, London, 1968.

3. Tsai, S.W., Composites Design, Fourth Edition, Think Composites, Ohio, 1988

4. Florin, G., Stress and Deformation in Circular Rotor Discs made from an Anisotropic Material, FOA Reports, Vol. 5, No. 4, 1971, pp. 1-11.

5. Pardoen, G.C., Achieving Desirable Stress States in Thick Rim Rotating Discs, International Journal of Science, Vol. 23, No. 6, 1981, pp367-382.

6. Morganthaler, G.F., Bonk, S. P., Composite Flywheel Stress Analysis and Materials Study, 12th National SAMPE Symposium, Paper D-5, 1967.

7. Shiratori, E., Ikegami, K., Hattori, T., Rotating Strength of Circumferentially Fibre-Reinforced Composite Discs, Bulletin of the JSME, Vol 21, No 153, March 1978, Paper No. 153-4

8. Lekhnitskii, S.G., Theory of Elasticity of an Anisotropic Body, MIR Publishers, Moscow, 1981.

9. Tsai, S. W. and Hahn, T.H., Introduction to Composites Design, Technomic Publishing Company, Lancaster PA, 1980

10. Sun, C.T., Li, S., Three-Dimensional Effective Elastic Constants for Thick Laminates, Journal of Composite Materials, Vol. 22, July 1988, pp. 629-639

11. Chou, P.C., Carleone, J., Elastic Constants of Layered Media, Journal of Composite Materials, Vol. 6, 1972, pp. 80-93

12. Roy, A.K., Kim, R.Y., Experimental Determination of Transverse Shear Stiffness of a Thick Laminate, Proceedings of the 1989 SEM Spring Conference on Experimental Mechanics, May 29 - June 1, 1989, Cambridge Mass.

13. Knight, M., Three-Dimensional Elastic Moduli of Graphite/Epoxy Composites, Journal of Composite Materials, Vol. 16, March 1982, pp. 153-159

14. Roy, A.K., Tsai, S.W., Three Dimensional Effective Moduli of Orthotropic and Symmetric Laminates, Journal of Applied Mechanics, Vol. 59, March 1992, pp. 39-47.

15. Rosenow, M.W.K., Wind Angle Effects in Glass Fibre-Reinforced Polyester Filament Wound Pipes, Composites, Vol. 15, No. 2, April 1984, pp. 144-152.

16. Hull, D., Legg, M.J., Spencer, B., Failure of Glass/Polyester Filament Wound Pipe, Composites, January 1978, pp. 17-23.

17. Hull, D., Spencer, B., Effect of Winding Angle on the Failure of Filament Wound Pipe, Composites, October 1978, pp. 263-271.

18. Carswell, W.S., Ainsworth, L., The Behaviour of Glass Filament Wound Tubes Under Internal Pressure, Proceedings of the 2nd International Conference on Composite Materials, pp. 472-483.

19. Tsai, S. W., A Survey of Macroscopic Failure Criteria for Composite Materials, Journal of Reinforced Plastics and Composites, Vol 3, January 1984, pp. 40-62

20. Roark, R.J., Young, W.C., Formulas for Stress and Strain, Fifth Ed., McGraw Hill, Montreal, 1982

21. Tsuda, S.,Shiratori, E., Ikegami, K., Rotating Strength of Laminated Composite Discs, Bulletin of the JSME, Vol 23, No 180, June 1980, Paper No. 180-5

22. Genta, G., The Shape Factor of Composite Material Filament Wound Flywheels, Composites, Vol. 12, No. 2, April 1981, pp. 49-55.

23. Genta, G., On the Design of Thick Rim Composite Material Filament Wound Flywheels, Composites, Vol. 15, No. 1, January 1984, pp. 49-55.

24. Huntington, R. A., Kirk, J.A., Stress Redistribution for the Multiring Flywheel, ASME Paper No. 77-WA/DE-26, ASME 1977 Winter Annual Meeting.

25. Timoshenko, S.P., Goodier, J.N., Theory of Elasticity, 3rd Ed., McGraw-Hill, New York, 1977.

Chapter 7
Projected Economics of CRO

7.0 Introduction

Chapters 4 through 6 address three technical issues which are fundamental to the CRO technology. There are, in addition many other areas in which further research and development is required before CRO will be truly "market ready". As this work will require substantial up-front investment, there must be a clear indication that, once it is market ready, CRO will have competitive advantages sufficient to ensure a reasonable return on that investment. A comparative assessment of the economics of conventional RO and the projected economics of CRO follows.

7.1 The Economics of Conventional RO

The total cost of water desalinated by conventional RO is comprised of four major components: energy consumption, capital charges, membrane replacement and plant operation. A typical distribution among these four cost components as shown in Table 7.1. Other researchers have reported similar distributions [2, 3].

Cost Component	Cost Proportion
Energy	29.2%
Capital Charges	24.3%
Membrane Replacement	23.9%
Plant Operation (Chemicals, maintenance, labour)	22.6%

Table 7.1 - Typical Breakdown of the Cost of Water Desalinated by Conventional RO [1]

In addition, the total cost per unit of water desalinated by conventional RO is a decreasing function of system capacity, as shown in Table 7.2.

Desalination Plant Capacity (m^3/day)	Total Cost per Gallon of Fresh Water ('91 US $/$m^3$)
37.85 (10,000 US gpd)	$4.49
378.5 (100,000 US gpd)	$3.30
3785 (1,000,000 US gpd)	$2.48

Table 7.2 - Total Cost Of Water Desalinated by Conventional RO [4]

7.2 The Projected Economics of CRO

The four components of the cost of water desalinated by CRO are estimated for plants of five sizes, 10,000, 25,000, 50,000, 86,000 and 172,000 gpd. It is assumed that the conventional RO and CRO plants are operating at recovery ratios of 30% and 20% respectively. Although it is not shown that these are optimal recovery ratios, it is apparent from industry specifications that 30% is perceived to be an optimal recovery ratio for many conventional RO applications. CRO, on the other hand, can operate at lower recovery ratios with little increase to energy consumption and with greatly reduced membrane costs, as is discussed in Section 1.2.2, . The optimal recovery ratio for CRO will, therefore, be lower than for conventional RO and is estimated here to be 20%.

7.2.1 Power Consumption

As discussed in Chapter 2, the principal components of CRO energy consumption are energy to the fresh water, windage, fluid flow losses through the rotor, bearing and seal losses and pump and motor inefficiencies. These components of energy consumption as well as total and specific energy consumptions for the five plant sizes are given in Table 7.3. It is important to note that specific power consumption decreases with increasing system capacity. This is due to the decreasing specific power consumption due to windage, bearing and seal losses. The details of these estimates are given in Appendix VIII.

Unit Capacity (m3/day)	38	95	189	326	651
Unit Capacity (US gallons/day)	10,000	25,000	50,000	86,000	172,000
Windage Losses (kW)	1.47	2.27	2.82	4.86	3.70
Bearing Losses(kW)	0.16	0.35	0.29	0.53	0.82
Seal Losses (kW)	1.20	2.60	1.85	3.02	2.49
Power To Fresh Water (kW)	5.44	13.59	27.18	46.76	93.52
Feed Pump Power (kW)	0.53	1.32	2.64	4.55	9.09
Vacuum Pump Power (kW)	1	1	2	2	2
Motor Efficiency	90%	90%	90%	90%	90%
Total Power (kW)	10.87	23.47	40.87	68.57	124.02
Specific Power Consumption (kWh/m3)	6.893	5.954	5.183	5.055	4.572

Table 7.3 - Projected Power Consumption For CRO Plants

The power consumption of a conventional RO plant is less sensitive to system capacity as the efficiency of the positive displacement pumps is relatively independent of pump size. For the purposes of this comparison, a specific power consumption of 7.47 kWh/m^3 for conventional RO will be assumed. The calculation of this number is based on assumptions which are equivalent to the assumptions underlying the estimation of CRO power consumption (see Appendix VIII). Power consumption estimates published in the literature [1] and by conventional RO system manufacturers [5] support this estimate.

The energy costs for CRO are, thus, projected to be 39% lower for CRO than for conventional RO.

7.2.2 Capital Cost

The capital cost of CRO, once the technology has been developed to the point of market readiness, is difficult to estimate as reduction of manufacturing costs will be a major thrust of this development. A cost estimate for a 150,000 gpd CRO plant was, however, performed by WaterGroup Canada Inc. as part of their assessment of the technology. They found that, for this plant, the estimated manufacturing costs of a CRO and of a conventional RO plant were within 2% of each other.

It is assumed here that the capital costs of CRO and conventional RO are equivalent

7.2.3 Membrane Replacement Cost

Membrane replacement costs are affected both by the number of membrane cartridges in a given plant and by the replacement interval for those cartridges. Both of these factors are, in turn, affected by the recovery ratio of the desalination plant. Recovery ratio is elevated by increasing the number of membrane cartridges in series (see Figure 1.10) and, thereby, extracting greater amounts of fresh water from a given feed sea water flow rate. In such a series connection, the amount of fresh water recovered per cartridge diminishes in the seawater flow direction as successive cartridges receive lower flow rates at higher salinities. The higher osmotic pressures of the higher salinities reduces the net pressure driving the reverse-osmosis process and the lower flow rates reduce the scouring action which otherwise prevents excessive concentration polarisation and minimizes membrane fouling. The fresh water flow rate, per cartridge, decreases from cartridge to cartridge in the seawater flow direction. Accordingly, the average fresh water flow rate per cartridge decreases and the number of cartridges increases as recovery ratio increases. In addition, the driving pressure for a high recovery ratio system must be higher so as to ensure that downstream cartridges do not produce excessively saline permeate. The minimum number of Filmtec 8040 cartridges, N_{cart}, required to produce 326 m^3/day (86,000 gpd) of desalinated water for a range of recovery ratios, RR, as determined using Filmtec's own system analysis program [6], is shown in Figure 7.1.

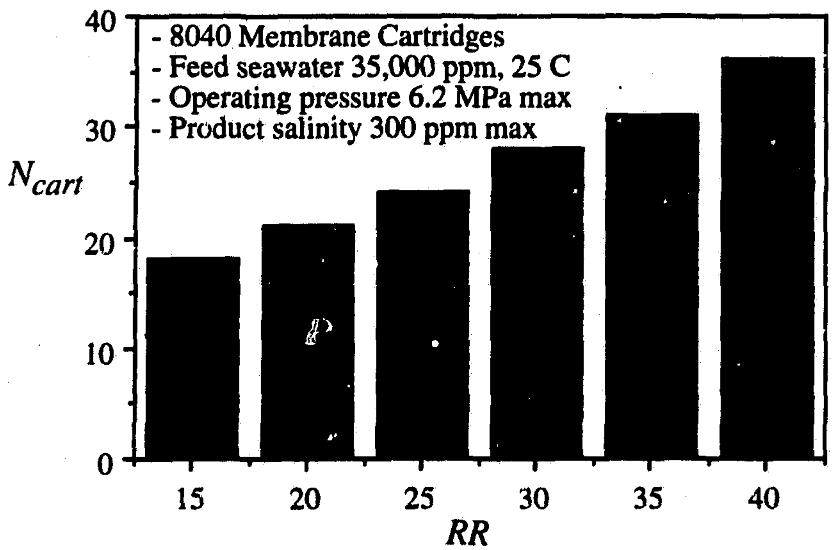

Figure 7.1 - Number of Membrane Cartridges versus Recovery Ratio

The life span of a membrane cartridge, L_{mem}, is also adversely affected by high recovery ratios. This is caused by irreversible membrane blockage and membrane compaction which result from increased fouling and increased operating pressure respectively, both of which are associated with higher recovery ratios. Unfortunately, there is little quantitative data in the literature which documents this phenomena and membrane manufacturers are understandably reluctant to release their data. The only published data is for recovery ratios of between 30% and 40% [7]. For use in the current comparison, this data has been extrapolated to a recovery ratio of 20%, as shown in Figure 7.2.

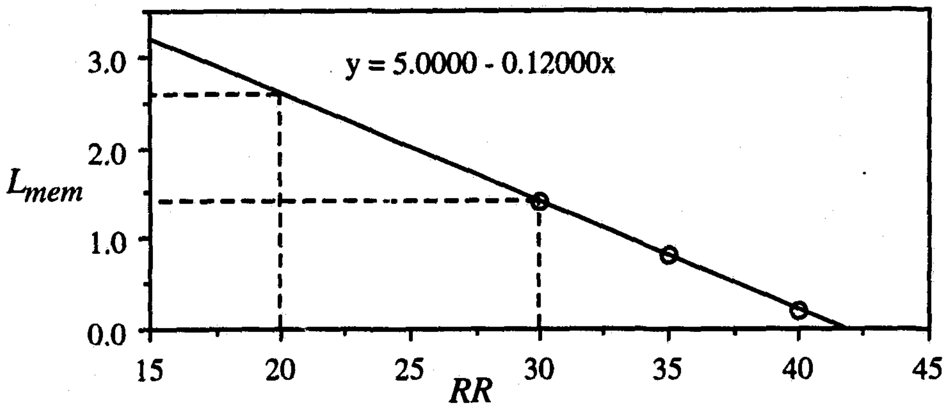

Figure 7.2 - Membrane Life Versus Recovery Ratio [7]

Taken together, the trends shown in Figures 7.1 and 7.2 show that, over the ten year life of an RO plant, the number of membrane cartridges is 60% lower for a plant operating at 20% recovery relative to a plant operating at 30%.

The membrane costs for CRO are, thus, projected to be 60% lower for CRO than for conventional RO.

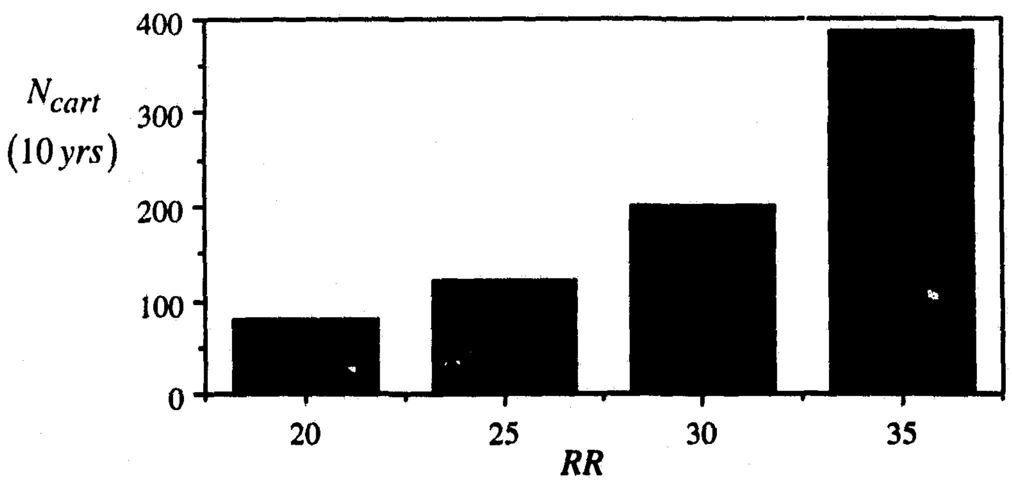

Figure 7.3 - Number of Membrane Cartridges Over Ten Year Life Of Plant Versus Recovery Ratio

7.2.4 Operating Cost

The major components of operating cost, apart from energy consumption and membrane replacement, for either conventional or centrifugal RO systems are chemicals, maintenance and labour for plant operation, as shown in Table 7.4. Conventional RO, operating at 30% recovery ratio, will require higher concentration dosages of antiscalants to prevent membrane fouling than a CRO system operating at 20% recovery. The higher feed flow rate of the CRO system may, however, result in an equivalent volume of antiscalant injection. CRO should have an advantage with respect to maintenance costs as there are no dynamic high pressure seals. These are a frequent replacement item in a conventional RO system. Operation costs should be equivalent as either type of system will be largely automated with PLC controls.

It is assumed here that the operating costs of conventional RO and CRO are equivalent.

COST COMPONENT	CONVENTIONAL RO	CENTRIFUGAL RO
Chemicals	•Higher dosages of antiscalant at higher recovery ratio	•Higher feed flow-rates to be dosed at lower recovery ratio
Maintenance	•Cartridge cleaning and replacement •High pressure feed pump tear downs •Corrosion of high pressure piping	•Cartridge cleaning and replacement •Bearing lubrication •Seal inspection and replacement
Operation (labour)	•Automated, PLC controls	•Automated, PLC controls

Table 7.4 - Operating Costs of Conventional and Centrifugal RO

7.2.5 Total Cost of Water Produced by CRO

As there are substantial similarities between the details of construction and operation of CRO and conventional RO plants, the relative proportions of the total cost of water desalinated by conventional RO, shown in Table 7.1, are assumed as a basis for this comparison. Consider a conventional and a centrifugal RO plant having the capacity of the largest plant shown in Table 7.3, 651 m^3/day. The cost of water desalinated by a conventional RO plant of this size is estimated to be \$3.23/m^3, interpolating the data shown in Table 7.2. By adjusting the individual cost components according to the findings of sections 7.2.1 to 7.2.4, the cost of water desalinated by CRO is estimated to be \$2.39/m^3 or 25.9% lower than the cost of water desalinated by conventional RO, as shown in Table 7.5.

	Conventional RO Cost Components ('91 US \$/m^3)	Projected Relative Costs for CRO Cost Components	Centrifugal RO Cost Components ('91 US \$/m^3)
Energy	\$0.94	61%	\$0.58
Capital	\$0.78	100%	\$0.78
Membranes	\$0.77	40%	\$0.31
Operation	\$0.73	100%	\$0.73
Totals	\$3.23	74%	\$2.39

Table 7.5 - Projected Costs of Water Desalinated by Conventional RO and CRO

7.4 Conclusions and Recommendations

Although this economic analysis is based upon a relatively unsophisticated model, the predicted advantage of CRO, 25.9% cost savings, is sufficient to warrant further development in order to verify the economics of CRO experimentally. This further development should focus on scale-up to large scale plants, for which lower energy consumption is projected, and design for manufacture, so as to minimize capital cost. If, subsequent to this development, the projected savings, or even a fraction of the projected savings can be achieved, there is a large and rapidly growing market for desalinated water which will welcome a new competitive technology.

References

1. Al-Zubaidi, A.A.J, Parametric Cost Analysis of Seawater Reverse-Osmosis Systems Design In Kuwait, Desalination, 76, 1989, pp. 241-280

2. Leitner, G.F., Economic feasibility of the Reverse-Osmosis Process for Seawater Desalination, Desalination, 63, 1987, pp. 135-142.

3. Wade, N.M., Hornsby, M.R., Distillation and Reverse-Osmosis Energy Consumption and Costs, Desalination, 1982, 245-247.

4. Freitas, R.A., Investing in Water, Special Report No. 104, Value Forecaster, Pilot Hill, CA, July 1991.

5. Village Marine Tech, Product Literature, Gardena Ca.

6. The Dow Chemical Company, FILMTEC Reverse-Osmosis System Analysis, Minneapolis Mn.

7. Awerbach, L., May, S., Soo-Hoo, R, Van Der Mast, V., Hybrid Desalting Systems, Desalination, 76, 1989, 189-197.

Chapter 8
Summary of Conclusions

8.0 Introduction

The objective of the work detailed in this dissertation was the development, implementation and optimization of the design for a centrifugal reverse-osmosis desalination system. The key findings of this work are, therefore, related principally to CRO. As a result of studies related to specific aspects of CRO design, however, findings relevant to other engineering applications have also been determined. These two categories of findings or conclusions are summarized here.

8.1 Conclusions of General Interest

• Relations of Bilgen and Boulos [1], Ustimenko [2] and Wendt [3] provide estimates of windage losses for a rotating cylinder within a stationary concentric cylindrical enclosure which are within 10% of experimentally determined values. These relations are preferred for rotors which have a relatively large ratio of length to diameter.

• Computational model developed with Fluent [4], also provides estimates of windage losses for a rotating cylinder within a stationary concentric cylindrical enclosure which are within 10% of experimentally determined values. The computational model is preferred for rotors which have a relatively small ratio of length to diameter.

• A new method is developed for the analysis of the state of stress and strain in a cylindrical filament wound vessel which is subjected to internal and external pressure, axial force and a radial body force due to rotation. This method allows the wind angle to be varied through the thickness of the cylinder wall. This method has applications in design of filament wound centrifuge rotors and of filament wound flywheels.

• The benefit of wind angle variation for applications in which there is biaxial loading (i.e. significant axial and hoop stresses) is shown to be significant only for the first ply failure criteria. The benefit of wind angle variation for applications in which there is uniaxial loading (i.e. either significant axial or significant hoop stresses) is significant for either the first or for the last ply failure criteria.

8.2 Conclusions Related Specifically to CRO

8.2.1 Comparison of Centrifugal and Conventional RO

• A relatively large scale CRO system (172,000 gpd) is projected to produce desalinated water at a cost 26% less than the cost of water desalinated by conventional RO. This saving is due to lower energy and membrane costs.

• The energy consumption of a CRO system is less than the energy consumption of a conventional RO system and the magnitude of the energy advantage of CRO increases as system capacity increases. It is projected that the energy consumption of a 172,000 gpd CRO system will be 39% less than the energy consumption of a 172,000 gpd conventional RO system

• The energy consumption of a CRO system is principally a function of fresh water production and is virtually independent of the feed sea water flow rate and of the system recovery ratio. A CRO system can, therefore, operate at a lower recovery ratio than a conventional reverse-osmosis system with only a very small associated energy penalty.

• By operating at a lower recovery ratio, both the number of membranes required and the frequency of membrane replacement is reduced. It is projected that the cost of membranes, over the life of a plant, is 60% lower for CRO at 20% recovery than for conventional RO at 30% recovery. (It is assumed that these recovery ratios are the respective optimal recovery ratios for each process.)

In summary, centrifugal reverse-osmosis offers the following general benefits relative to Conventional reverse-osmosis.

- Lower energy consumption
- Lower membrane requirements
- Improved reliability
- Lower levels of noise and vibration
- Design simplicity
- Lower total cost per gallon of desalinated water

8.2.2 Novel Design Features: Developed, Implemented, Verified and Patented

• "Gattling Gun" membrane configuration

• Location of fresh water exit at inner edge of membrane configuration so as to provide a uniform differential pressure across the membrane and throughout the membrane configuration.

• Evacuation of rotor enclosure so as to minimize energy consumption due to windage.

• Removal of fresh water from rotor using pitot-type skimmer tip.

• "Pumping" of fresh water from inside evacuated enclosure to surrounding ambient pressure using pressure developed at entrance to skimmer tip.

8.2.3 Design Refinements Arising from Prototype Development and Subsequent Design Studies

• Flexible composite rotor design in which outer shell provides structural requirements associated with centrifugal loading from pressure vessels.

• Smooth rotor and rotor enclosure surfaces (separation of bearing platforms from the rotor by partitions which limit rotor induced air circulation about the bearing platforms)

• Replacement of open annular chamber in diffuser with radial passages to accelerate the flow in a relatively ordered manner.

8.2.4 Further Novel Design Features: Identified and Requiring Development

• Membrane cartridge designed specifically for incorporation into a CRO rotor and in which the membrane is oriented so as to minimize the effects of fouling and of concentration polarization by the action of centrifugal force.

• Recovery of the velocity energy of the fresh water either by the addition of a second RO stage on the outlet from the skimmer tip or by the addition of a "turbine" to return this energy to the rotor drive.

References

1. Bilgen, E, Boulos, R, Functional Dependence of Torque Coefficient of Coaxial Cylinders on Gap Width and Reynolds Numbers, Journal of Fluids Engineering, March 1973, pp. 122-126.

2. Fluid Flow Data Book, Genium Publishing Corporation, 1969..

3. Wendt, F., "Turbulente Stromungen Zwishen Zwei Rotierender Konaxialen Zylindern", Ingenieur-Archiv, vol IV, 1933,.p.577.

4. Fluent Users Guide, Fluent Inc., New Hampshire, 1992.

Appendix I

Wild et al, <u>Centrifugal Reverse-Osmosis Desalination Unit,</u> U.S Patent 4,886,597

United States Patent [19]
[11] Patent Number: 4,886,597
[45] Date of Patent: Dec. 12, 1989

Wild et al.

[54] CENTRIFUGAL REVERSE-OSMOSIS DESALINATION UNIT

[75] Inventors: Peter M. Wild; Geoffrey W. Vickers; David A. Hopkin; Antony Moilliet, all of Victoria, Canada

[73] Assignee: Her Majesty the Queen in right of Canada, Ontario, Canada

[21] Appl. No.: 243,273

[22] Filed: Sep. 12, 1988

[30] Foreign Application Priority Data

Sep. 24, 1987 [CA] Canada 547791

[51] Int. Cl.[4] B01C 13/00
[52] U.S. Cl. 210/321.68; 210/321.84
[58] Field of Search 210/321.6, 321.68, 321.84

[56] References Cited

U.S. PATENT DOCUMENTS

3,385,769	5/1968	Brose	210/321.84 X
4,230,564	10/1980	Keefer	210/321.6 X

Primary Examiner—Frank Spear
Attorney, Agent, or Firm—Nixon & Vanderhye

[57] ABSTRACT

The invention disclosed is a desalination apparatus for removing salt from seawater. The apparatus operates on the principle of reverse-osmosis whereby a feed solution containing seawater is separated into a product solution of decreased salt concentration and an exhaust solution of increased concentration. An evacuated enclosure is included to reduce windage losses and power consumption.

13 Claims, 4 Drawing Sheets

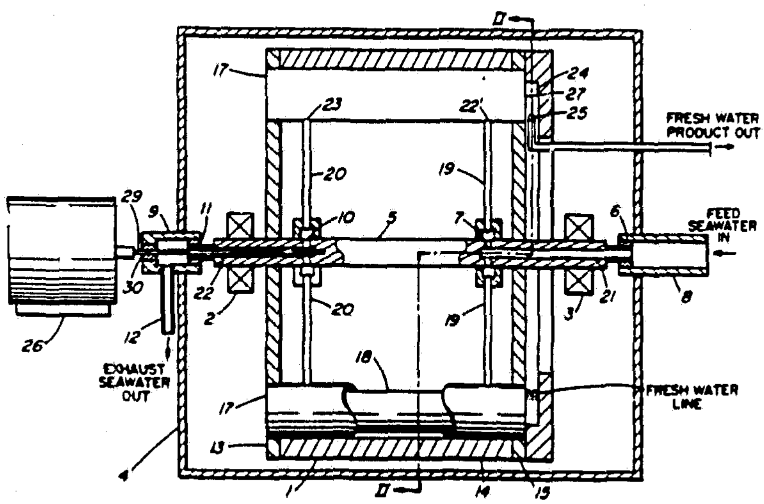

U.S. Patent Dec. 12, 1989 Sheet 1 of 4 **4,886,597**

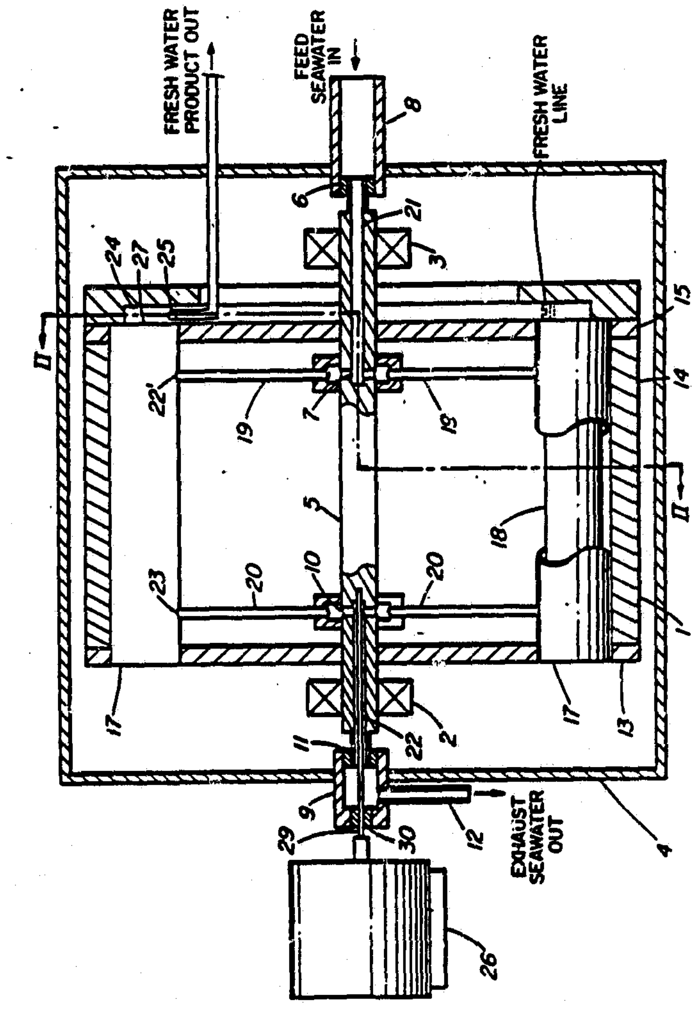

FIG. 1

U.S. Patent Dec. 12, 1989 Sheet 2 of 4 4,886,597

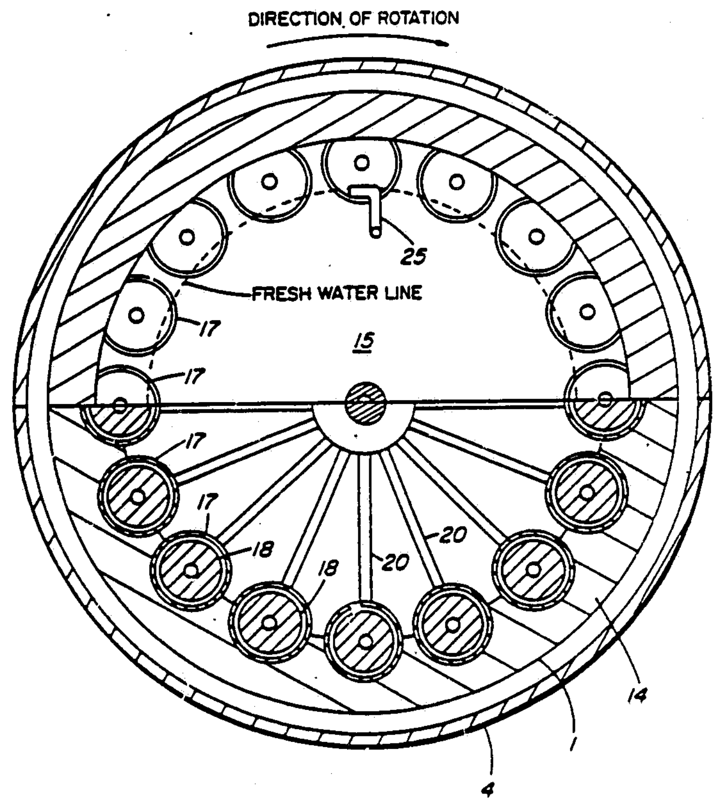

FIG. 2

U.S. Patent Dec. 12, 1989 Sheet 3 of 4 **4,886,597**

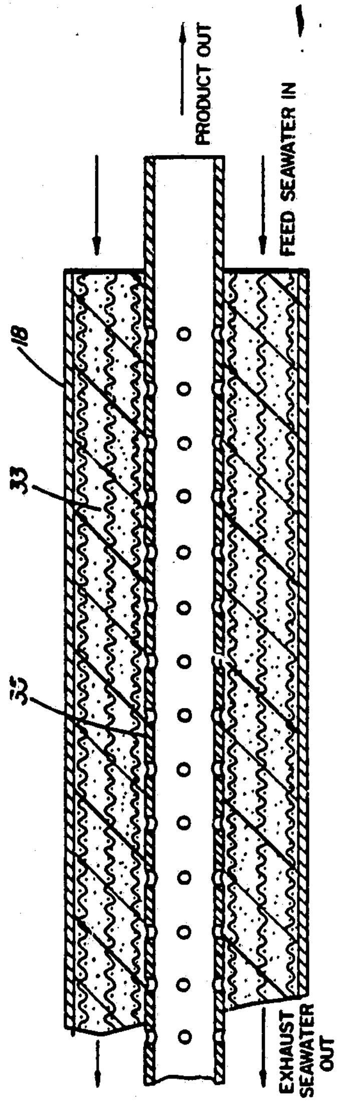

FIG. 3

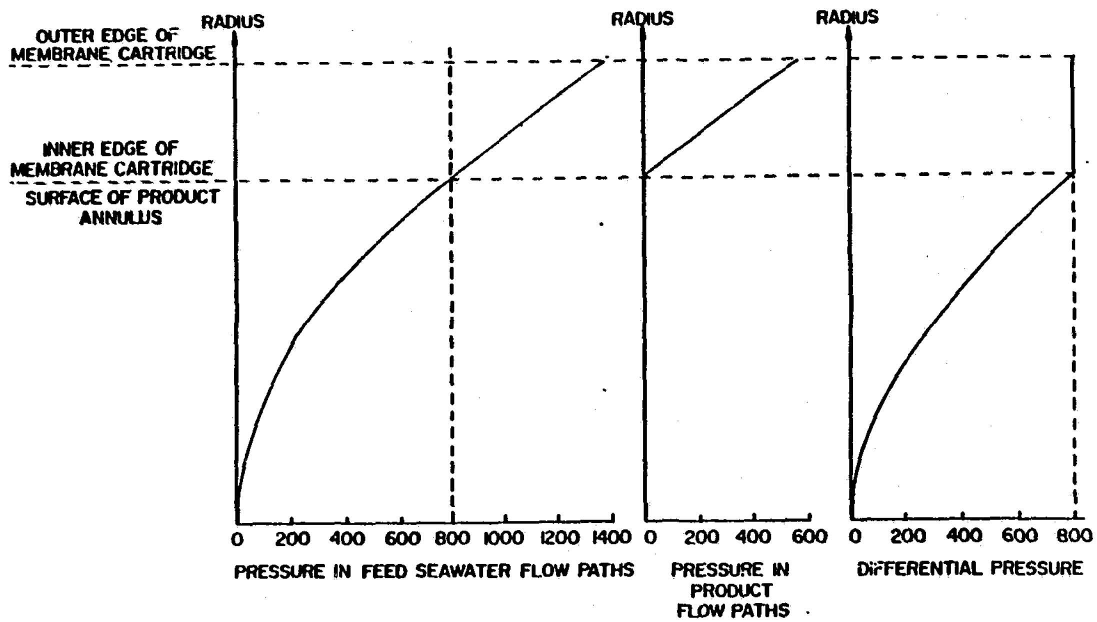

FIG. 4A FIG. 4B FIG. 4C

CENTRIFUGAL REVERSE-OSMOSIS DESALINATION UNIT

This invention relates to desalination method and apparatus and in particular to an apparatus for removing salt from water by reverse-osmosis.

Reverse-osmosis is a high pressure process, e.g., 800 psi in the case of desalination of seawater. Traditionally, there have been two techniques for developing this high pressure, namely, high pressure pumps and centrifuges. Although a centrifuge offers theoretically higher efficiencies, commercial systems, almost without exception, have employed pumps. Practical difficulties have prevented widespread development of centrifugal reverse-osmosis desalination systems.

One of these difficulties is the design of a membrane configuration suitable for a centrifuge. For example, U.S. Pat. No. 3,669,879 of 13 June 1972 in the name of L. P. Berriman proposes various means for deploying a reverse-osmosis membrane within a single cylindrical rotating pressure vessel.

U.S. Pat. No. 4,333,832 by Siwecki et al employs, on the other hand, a number of smaller pressure vessels located about the periphery of a rotating structure or rotor. Each vessel contains a single cartridge of reverse-osmosis membrane material. This is a practical design but it is feasible only for relatively large rotor diameters. The reasons for this are twofold:

1. Pressure Gradient: The pressure within the pressure vessels is not uniform. There is a radial pressure gradient, with respect to the rotor axis. As commercially available membrane cartridges are effective only between 800 and 1000 psi, the pressure within a vessel should not exceed this range, i.e., the pressure should be 800 psi, at the edge closest to the rotor axis, and 1000 psi, at the edge furthest from the rotor axis. For any given cartridge diameter, there is a corresponding minimum rotor diameter which will satisfy these pressure conditions.

2. Windage: Windage is friction between the peripheral surface of the rotor and the surrounding air. At the speeds required to develop process pressure, the power lost to windage is significant.

Windage power per unit product diminishes with increasing unit capacity. The volume of membrane accommodated and, therefore, the productivity of a centrifugal ROD increases as the square of rotor diameter whereas the surface area and, therefore, windage increase only linearly with rotor diameter. The proportion of unit power attributable to windage, therefore, decreases with increasing unit size.

The Siwecki patent describes a stationary shroud enclosing the rotor. This restricts the circulation of air about the rotor, thereby reducing windage. As Siwecki states, however, only for large units can windage be "held to a small fraction of power costs" by this technique.

It is an object of the invention to separate a single solution, by means of a reverse-osmosis membrane, into two solutions; one of higher and one of lower concentration than the original solution. In this discussion the original solution is called the "feed", the reduced concentration solution is the "product" and the increased concentration solution is the "exhaust".

According to the invention, an apparatus for separating an original feed solution into a product solution of decreased concentration and an exhaust solution of increased concentration is provided, comprising

reverse-osmosis membrane means;

supply means for supplying the original feed solution to said reverse-osmosis membrane means;

exhaust means for removing the exhaust solution of increased concentration from said reverse-osmosis membrane means;

product removal means for removing the product solution of decreased concentration from said reverse-osmosis membrane means;

means for creating a pressure differential within said reverse-osmosis membrane means to separate the original feed solution into the product solution and the exhaust solution; and

evacuated enclosure means for said reverse-osmosis membrane means.

In the drawing which illustrates a preferred embodiment of the invention,

FIG. 1 is a side elevation partly in section of the apparatus according to the invention;

FIG. 2 is an end-view of the apparatus according to the invention, partly in section taken along line II—II in FIG. 1;

FIG. 3 is a side elevation in section of a state-of-the-art spirally wound reverse-osmosis membrane cartridge used in the apparatus, according to the invention; and

FIG. 4A, 4B and 4C are graphs depicting the radial pressure gradients in the apparatus according to the invention.

Referring to the drawing, a reverse-osmosis means is provided in a rotor assembly 1. The rotor assembly 1 is supported for rotation about axle 5 in bearings 2 and 3 within an evacuated enclosure means in the form of a close-fitting cylindrical stationary shroud 4. Vacuum means (not shown) is used to evacuate the shroud. The rotor assembly 1 consists of a circular array of tubular pressure vessels 17 radially spaced evenly about its periphery equidistant from axle 5. Each pressure vessel 17 contains a single cylindrical reverse-osmosis membrane cartridge 18 including a reverse-osmosis membrane. The pressure vessels 17 are supported radially about axle 5 by support means in the form of a cylindrical support shell 14. The pressure vessels 17 and shell 14 are located with respect to the axle 5 by circular end plates 13 and 15.

Means for creating a pressure differential within the reverse-osmosis membrane means is provided by the centrifugal force created by rotating the rotor assembly 1 at high speed.

The rotational drive is communicated to axle 5 from drive means 26, typically an electric motor, to the rotor assembly 1 through drive shaft 29. Evacuation of the shroud reduces windage, thereby permitting use of a much smaller motor than would otherwise be required, e.g. 5 H.P. as opposed to 50 H.P. without the evacuated shroud.

Supply means is provided for supplying the original "feed" solution to the reverse-osmosis membrane means. Specifically, the "feed" is admitted to the rotor assembly 1 through stationary inlet conduit 8. It passes into bore 21 in the axle 5 via rotating coupling 6. Radial openings 7 in the axle 5 conduct the "feed" from the bore 21 into radial inlet conduits 19 and, thence, into pressure vessels 17 via "feed" inlet 22'. The "feed" is then directed axially into the membrane cartridge 18 as indicated in FIG. 3.

Exhaust means is provided for removing the "exhaust" solution from the reverse-osmosis membrane means. Specifically, the "exhaust" (not having passed through the reverse-osmosis membrane) returns to the axle bore 22 via exhaust outlet 23, radial outlet tubes 20 and through radial outlet openings in axle bore 22. The "exhaust" exits the rotor assembly through rotating coupling 11 and is directed from the system by stationary exhaust outlet assembly 9 and exhaust outlet conduit 12. Rotary seal 30 seals between drive shaft 29 and stationary outlet assembly 9.

Product removal means is provided for removing the "product" solution from the reverse-osmosis membrane means. Specifically, the "product" (having passed through the reverse-osmosis membrane) is directed axially from the membrane cartridges 18 as indicated in FIG. 3 through product outlet opening 27 into an annular inwardly facing groove 24 about the periphery of one end of the rotor assembly. The open "product" receiving end of conduit 25 resides in groove 24 and faces into the direction of rotation of rotor assembly. The other (exit) end of the conduit 25 is bent, so as to pass out of the groove 24 and out of the shroud 4. Product removal conduit 25 is provided within groove 24 to remove the "product" from the system. Specifically, the "product" is collected and retained within the groove by centripetal force. The inner surface of the spinning annulus of "product", thus formed, impinges on the open end of the outlet conduit 25 developing pressure therein. When this pressure exceeds ambient pressure, the "product" flows out through the conduit, thus acting as a "pump".

Commercially available reverse-osmosis membrane cartridges are produced in two styles, a first employing a spiral wound membrane and a second employing a hollow fibre membrane. Both styles of cartridges contain a configuration of adjacent "product" and "feed" flow-paths separated by a reverse-osmosis membrane. It is the pressure differential between these paths that drives the separation process.

In a typical spiral-wound cartridge, as manufactured by UOP Fluid Systems or Filmtec, the membrane is bonded to a sheet of porous support fabric. Two of these sheets, back to back and separated by a mesh spacer, are formed into an envelope and sealed on all but one edge. The mesh spacer is the "product" flow-path. The unsealed edge of the envelope is bonded to a central perforated plastic tube such that the carrier is open to the perforations. A sheet of coarser mesh is placed over the envelope and both are wound tightly around the perforated tube. This coarser mesh is the "feed" flow path.

FIG. 3 is a side elevation of such a spiral wound cartridge showing the spiral configuration of membranes and meshes 33 and the perforated central tube 35 in section. The "feed" solution is admitted axially into cartridge 18 from inlet 22 (FIG. 2) and flows axially through the coarse mesh or "feed" flow path. As the "feed" passes through this mesh, the "product" fraction permeates through the membrane material and into the mesh spacer or "product" flow path. The mesh spacer directs the "product" spirally inwardly and into the perforated central tube 35 and, thence, from the cartridge. One end of this central tube is plugged, i.e. the end opposite to the "product" outlet. The remaining "exhaust" is expelled from the cartridge at the other end.

The "feed" flow-paths in the cartridges are continous with the "feed" flow paths in the rotor, i.e. bores 21, 22 and radial conduits 19, 20. The pressure in these "feed" flow-paths, therefore, increases continuously with displacement from the rotor axis as shown in FIG. 4A.

The "product" flow-paths in the cartridge are continuous with the "product" water held in the annular groove 24. The pressure in the "product" water flow-paths, therefore, depends upon the radius of the surface of the "product" water annulus. Pressure is zero at this surface. Pressure is positive at any location in the "product" flow-paths which is at a radius greater than this surface radius. As shown in FIG. 4B, this pressure increases with displacement from the rotor axis.

The applicant has found that the rate of increase of pressure in the "feed" water flow-paths is equal to the rate of increase of pressure in the "product" water flow-paths at any radius beyond the surface of the "product" water annulus.

As shown in FIG. 4C, the pressure differential across the membrane, from "feed" to "product" water flow paths is, therefore, constant from the surface of the "product" water annulus outward.

The radial pressure gradient within the "feed" flow-paths is described by the equation:

$$P_F=(p/2)w^2R^2$$

"P_F" is pressure within the "feed" flow-paths, "p" is fluid density, "w" is the angular velocity of the rotor assembly and "R" is displacement from the rotor assembly axis. The pressure within the "product" flow-paths (P_P) increases according to the same relation:

$$P_P=(p/2)w^2(R^2-R_A^2)$$

"R_A" is the radius of the surface of the "product" annulus. The differential pressure (P_D), therefore, is:

$$P_D=P_F-P_P$$

$$P_D=(p/2)w^2R_A^2$$

The differential pressure is uniform and equal to the pressure in the "feed" flow-paths, at radius R_A.

If the surface of the "product" water annulus is coincident with the innermost edge of the membrane cartridges, then the pressure differential across the membrane is uniform throughout the cartridge and equal to the pressure in the "feed" flow-path at that innermost edge.

In the case of desalination of seawater, the pressure differential across the membrane is generally restricted to between 800 and 1000 psi. Below 800 psi, the "product" salinity is unacceptably high and above 1000 psi, the membrane is prone to rupture.

In this embodiment of the invention, the "product" receiving opening in conduit 25 is located so as to maintain the surface of the "product" annulus coincident with the innermost edge of the membrane cartridges. The rotor speed is controlled so as to ensure that the uniform pressure differential which results is between the required 800 and 1000 psi. For example:

If R = 12 in

If R = 12 in	
Rotor speed	P Diff
(RPM)	(psi)
3293	800
3493	900
3682	1000

The embodiments of the invention in which an exclusive property or privilege is claimed are defined as follows:

1. An apparatus for separating an original feed solution into a product solution of decreased concentration and an exhaust solution of increased concentration, comprising:

reverse-osmosis membrane means;

a single rotor assembly housing said reverse osmosis means, said rotor assembly comprising an array of pressure vessels each containing a reverse-osmosis membrane and support means for said array including axle means about which the assembly is rotatable, wherein said pressure vessels are radially spaced from said axle means about the periphery of said assembly;

supply means for supplying the original feed solution to said reverse-osmosis membrane means;

exhaust means for removing the exhaust solution of increased concentration from reverse-osmosis membrane means;

product removal means for removing the product solution of decreased concentration from said reverse-osmosis membrane means;

means for creating a pressure differential within said reverse-osmosis membrane to separate the original feed solution into the product solution and the exhaust solution; and

evacuated enclosure means for said reverse-osmosis membrane means, said evacuated enclosure means being in the form of a shroud which closely fits over said rotor assembly to minimize windage losses.

2. Apparatus according to claim 1, wherein said means for creating a pressure differential is provided by drive means for imparting rotational drive to said rotor assembly.

3. Apparatus according to claim 1, wherein said pressure vessels are in a circular array spaced evenly about said assembly equidistant from said axel means.

4. Apparatus according to claim 3, wherein said supply means includes means for admitting the original

feed solution at said axel means and to conduct it radially to said pressure vessels.

5. Apparatus according to claim 4, wherein said exhaust means includes means for returning the exhaust solution to said axel means where it is removed from the apparatus.

6. Apparatus according to claim 5, wherein said product removal means includes means for collecting the product solution.

7. Apparatus according to claim 6, wherein said product collecting means is in the form of an annular inwardly-facing groove about the periphery of one end of the rotor assembly for collecting said product solution in the vicinity of said pressure vessels.

8. Apparatus according to claim 7, wherein said product removal means further includes product receiving conduit means located in said annular groove, said conduit means having an open end facing into the direction of rotation of the rotor assembly, the other end being located outside of said evacuated enclosure means, whereby the product solution flows out of the assembly through the conduit due to the pressure differential induced by the impingement of the product solution on the open end of said conduit.

9. Apparatus according to claim 8, wherein said pressure vessels comprise a tubular casing and an inner concentric cylindrical reverse-osmosis membrane cartridge structure defining adjacent product solution and feed solution flow paths separated by a reverse-osmosis membrane, whereby said feed solution enters said feed solution flow path at one end of said pressure vessel and flows axially along said feed flow paths and is separated into said exhaust solution which exits at the other end of said casing, and said product solution which permeates through said reverse-osmosis membrane into said product solution flow path and is directed into said annular groove where it forms a spinning annulus of product solution therein which is removed from the pressure vessels at said one end.

10. Apparatus according to claim 9 wherein the pressure differential across said reverse-osmosis membrane is substantially uniform throughout.

11. Apparatus according to claim 10, wherein the pressure differential is between 800 and 1000 psi.

12. Apparatus according to claim 10, wherein the product receiving open end of said conduit means is located to maintain the inner surface of the annulus of product solution within said annular groove coincident with the surface of the reverse-osmosis cartridge nearest to the rotor assembly axel.

13. Apparatus according to claim 1, wherein said original feed solution is brine and wherein said product solution is potable water.

* * * * *

Appendix II

Experimental Set-up for First and Second Prototypes

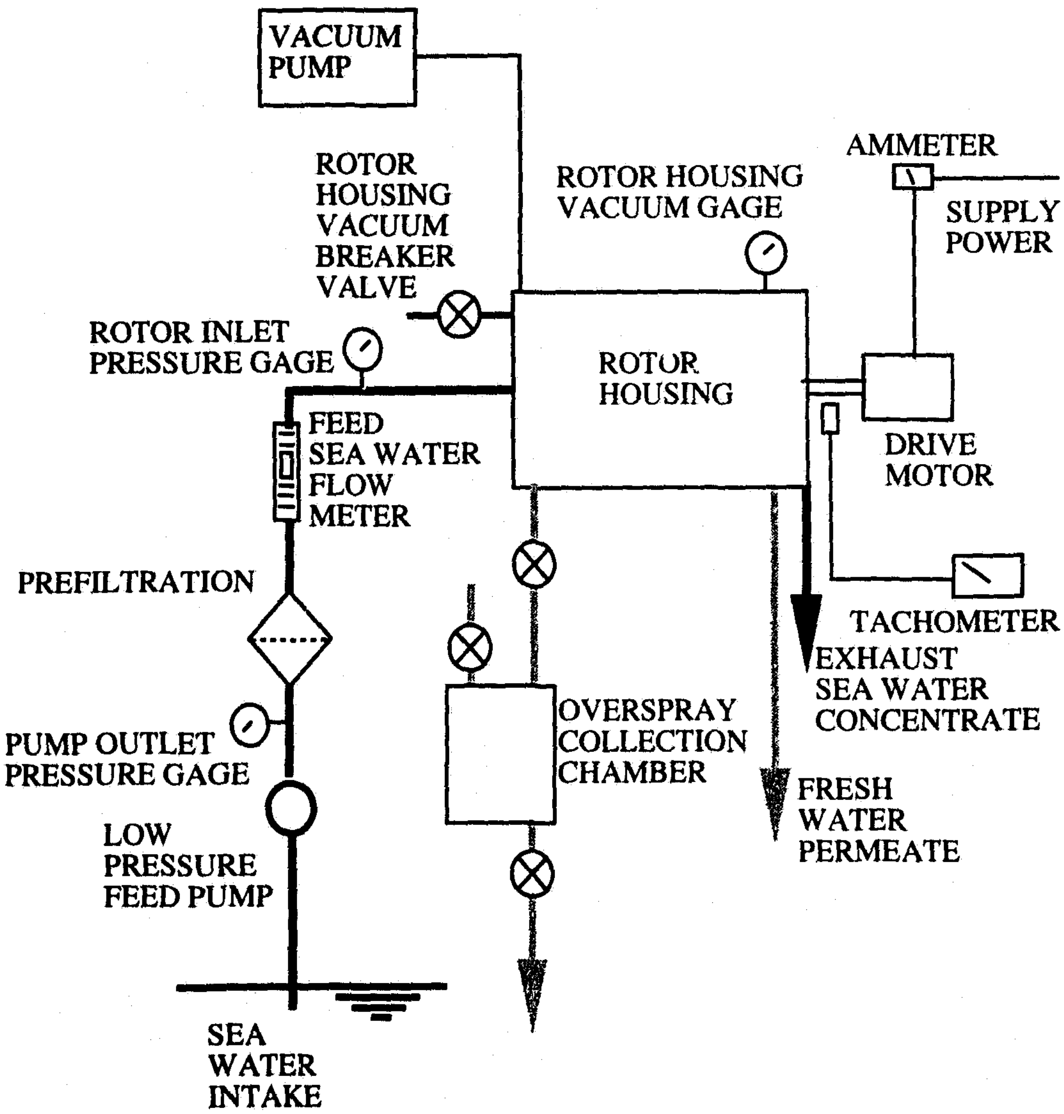

Figure II.1 - Experimental Set-up for First Prototype

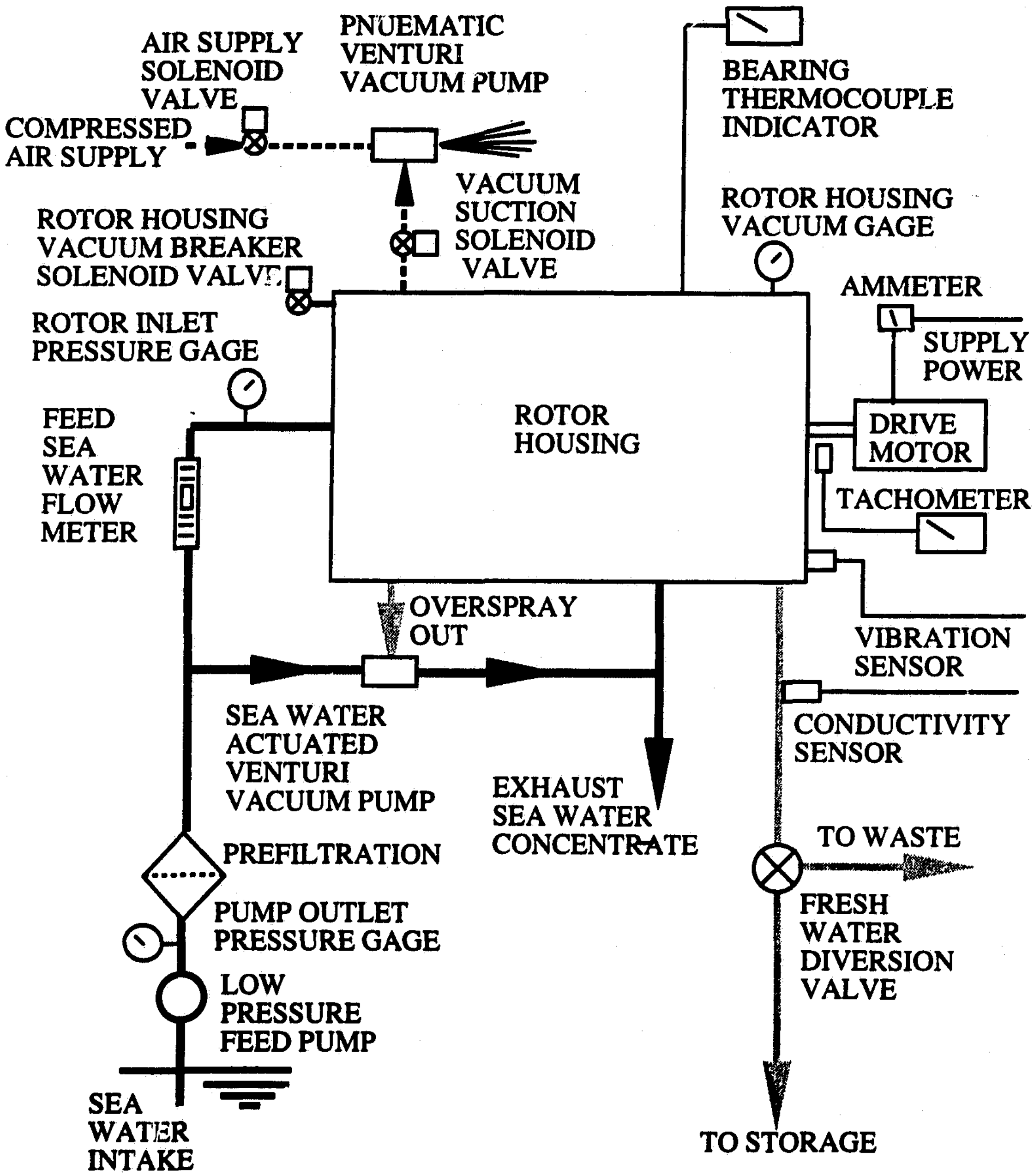

Figure II.2 - Experimental Set-up for First Prototype

Appendix III

The k- ε Turbulence Model

(Rodi, W, Turbulence models and their Application in Hydraulics--A State of the Art Review, International Association for Hydraulics Research, Delft, the Netherlands, 1884)

The continuity and momentum equations, valid for laminar and turbulent incompressible flow, flow are expressed as,

$$\frac{\partial U_i}{\partial x_i} = 0 \qquad \text{(III.1)}$$

$$\rho \frac{\partial U_i}{\partial t} + \rho \frac{\partial}{\partial x_j}\left(U_i U_j\right) = -\frac{\partial p}{\partial x_i} + \frac{\partial}{\partial x_j}\left\{\mu\left(\frac{\partial U_i}{\partial x_j} + \frac{\partial U_j}{\partial x_i}\right)\right\} \qquad \text{(III.2)}$$

where $U_i \quad (i = 1, 2, 3)$ and p are the instantaneous velocities and pressures respectively.

For turbulent flows, the general instantaneous variable, ϕ, may be replaced by the sum of a time- averaged component, $\overline{\phi}$, and a fluctuating component, φ,as follows

$$\phi = \overline{\phi} + \varphi \qquad \text{(III.3)}$$

where the time-averaged value, $\overline{\phi}$, is defined as.

$$\overline{\phi} = \frac{1}{\Delta t} \int_t^{t+\Delta t} \phi dt \qquad \text{(III.4)}$$

and the duration of the averaging time Δt is long compared with the longest time scales of the turbulent motion.

The velocities U_i and pressure p in II.1 can be decomposed into mean and fluctuating components as in II.3 and, time averaging, we obtain, for a statistically steady flow,

$$\frac{\partial}{\partial x_j}\left(U_i U_j\right) = -\frac{\partial p}{\partial x_i} + \frac{\partial}{\partial x_j}\left\{\mu\left(\frac{\partial U_i}{\partial x_j} + \frac{\partial U_j}{\partial x_i}\right) - \rho\overline{u_i u_j}\right\} \qquad \text{(III.5)}$$

where, for convenience, the overbars defining mean variables have been dropped. This expression contains six new unknowns involving correlations between the fluctuating components of the velocities, $\rho\overline{u_i u_j}$. Physically, these terms, called Reynolds stresses, represent the transport of momentum due to the velocity fluctuations. In order to obtain closure of this new set of equations, relationships between the Reynolds stresses and the existing variables must be established. Turbulence modeling attempts to establish these relationships.

The $k - \varepsilon$ turbulence model requires the solution of two additional transport equations: one for the turbulent kinetic energy, k, and one for the rate of dissipation of turbulent kinetic energy, ε. The model is founded upon the eddy-viscosity concept which can be expressed as,

$$-\rho\overline{u_i u_j} = \mu_t\left(\frac{\partial U_i}{\partial x_j} + \frac{\partial U_j}{\partial x_i}\right) - \frac{2}{3}\rho k \delta_{ij} \qquad \text{(III.6)}$$

where μ_t is the turbulent eddy-viscosity which, unlike the molecular viscosity, μ, is not a fluid property but is rather a function of the state of turbulence and may, therefore, vary from one point to another and from one flow to another.

The term involving the Kronecker delta, δ_{ij}, is included to ensure that the continuity equation is satisfied. In the absence of this term, the sum of the normal Reynolds stresses, where $i = j$, is equated to zero since

$$\frac{\partial U_i}{\partial x_i} = 0 \qquad \text{(III.7)}$$

Inclusion of this term, however, ensures that the sum of the normal Reynolds stresses is correctly equated to twice the kinetic energy of the fluctuating motion.

$$2k = \overline{u_1^2} + \overline{u_2^2} + \overline{u_3^2} \qquad \text{(III.8)}$$

The sum of the normal stresses is a scalar which can be incorporated into the pressure gradient term in the momentum equation.

The definition of the Reynolds stresses is now reduced to the definition of the turbulent eddy viscosity μ_t . In the eddy viscosity concept, the eddy viscosity is assumed to be proportional to a velocity characterising the fluctuating motion, $\hat{V}$, and to a typical length of this motion, L.

$$\mu_t \propto \hat{V}L \qquad \text{(III.9)}$$

The most physical meaningful scale for characterising the velocity scale is $\sqrt{k}$ and accordingly, II.9 becomes,

$$\mu_t \propto \rho\sqrt{k}L \tag{III.10}$$

The rate of dissipation of turbulent kinetic energy, ε, is related to k and L using dimensional analysis,

$$\varepsilon \propto \frac{k^{3/2}}{L} \tag{III.11}$$

By combining II.10 and II.11, the following expression for μ_t is obtained,

$$\mu_t = \frac{C_\mu \rho k^2}{\varepsilon} \tag{III.12}$$

where C_μ is an empirically determined constant of proportionality.

The definition of the Reynolds stresses is now reduced to determining k and ε. Exact transport equations for k and ε can be derived from II.2 but the result contains undefined higher order correlations which render it impractical. In the "standard" $k-\varepsilon$ model, transport equations for k and ε are modeled based on a combination of empirical data and dimensional arguments. The resulting equations for statistically steady flow take the form,

$$\rho U_k \frac{\partial k}{\partial x_k} = \frac{\partial}{\partial x_k}\left(\frac{\mu_{eff}}{\sigma_k}\frac{\partial k}{\partial x_k}\right) + \mu_{eff}\left(\frac{\partial U_i}{\partial x_k} + \frac{\partial U_k}{\partial x_i}\right)\frac{\partial U_i}{\partial x_k} - \rho\varepsilon$$

(III.13)

$$\rho U_k \frac{\partial \varepsilon}{\partial x_k} = \frac{\partial}{\partial x_k}\left(\frac{\mu_{eff}}{\sigma_\varepsilon}\frac{\partial \varepsilon}{\partial x_k}\right) + C_1\mu_{eff}\frac{\varepsilon}{k}\left(\frac{\partial U_i}{\partial x_k} + \frac{\partial U_k}{\partial x_i}\right)\frac{\partial U_i}{\partial x_k} - \frac{C_2\varepsilon^2}{k}$$

(III.14)

The effective viscosity, μ_{eff}, is the sum of the laminar and eddy viscosities,

$$\mu_{eff} = \mu + \mu_t \qquad \text{(III.15)}$$

The empirical constants in equations II.13 and II.14 are as defined in Table II.1

C_μ	C_1	C_2	σ_k	σ_ε	κ
0.09	1.44	1.92	1.0	$\frac{\kappa^2}{(C_2 - C_1)\sqrt{C_\mu}}$	0.4187

Table III.1 Empirical Constants for the $k-\varepsilon$ Model

The governing set of equations for the $k-\varepsilon$ model is comprised of equations II.14 and II.15, the continuity equation, II-1, and the momentum equation updated to include the effective viscosity, as follows,

$$\frac{\partial}{\partial x_j}\left(U_i U_j\right) = -\frac{\partial p^*}{\partial x_i} + \frac{\partial}{\partial x_j}\left\{\mu_{eff}\left(\frac{\partial U_i}{\partial x_j} + \frac{\partial U_j}{\partial x_i}\right)\right\} \qquad \text{(III.16)}$$

where

$$p^* = p + \frac{2}{3}\rho k \tag{III.17}$$

Appendix IV

Derivation of Stress and Strain Relations for a State of Generalised Plane Strain in a Circular Ring of a Cylindrically Orthropic Material

(after Lekhnitskii, S.G., Anisotropic Plates, Gordon and Breach Science Publishers, London, 1968.)

The equations of equilibrium for a homogeneous body in cylindrical coordinates are as follows:

$$\begin{aligned} \frac{\partial \sigma_r}{\partial r} + \frac{1}{r}\frac{\partial \tau_{r\theta}}{\partial \theta} + \frac{\partial \tau_{rz}}{\partial z} + \frac{\sigma_r - \sigma_\theta}{r} + \boldsymbol{R} &= 0 \\ \frac{\partial \tau_{r\theta}}{\partial r} + \frac{1}{r}\frac{\partial \sigma_\theta}{\partial \theta} + \frac{\partial \tau_{\theta z}}{\partial z} + \frac{2\,\tau_{r\theta}}{r} &= 0 \\ \frac{\partial \tau_{rz}}{\partial r} + \frac{1}{r}\frac{\partial \tau_{\theta z}}{\partial \theta} + \frac{\partial \sigma_z}{\partial z} + \frac{\tau_{rz}}{r} &= 0 \end{aligned} \qquad \text{(IV.1 - IV.3)}$$

Where $\boldsymbol{R}$ is a body force in the radial direction.

Now, consider an homogeneous cylindrical body having cylindrical orthotropy which is subjected to normal forces distributed over the cylindrical surface and a radial body force $\boldsymbol{R}$, Both body forces and surface forces are constant along the length of the cylinder. In addition, the forces distributed over the ends of the cylinder reduce to an axial force located at the cylinder axis. These forces are distributed such that the end surfaces remain planar. As there is nothing to distinguish one cross section from another, along the length of the cylinder, the states of stress and strain must not vary with z. and all cross sections perpendicular to the cylinder axis must, therefore, remain planar. This is a state of *generalised plane strain*.

If the body forces are defined by a potential, $\overline{U}(r)$ such that:

$$\boldsymbol{R} = -\frac{\partial \overline{U}}{\partial r} \tag{IV.4}$$

then equations IV.1 - IV.3 can be rewritten, for this case, as,

$$\begin{aligned}
\frac{\partial\left(\sigma_r - \overline{U}\right)}{\partial r} + \frac{1}{r}\frac{\partial \tau_{r\theta}}{\partial \theta} + \frac{\sigma_r - \sigma_\theta}{r} &= 0 \\
\frac{\partial \tau_{r\theta}}{\partial r} + \frac{1}{r}\frac{\partial \sigma_\theta}{\partial \theta} + \frac{2\,\tau_{r\theta}}{r} &= 0 \\
\frac{\partial \tau_{rz}}{\partial r} + \frac{1}{r}\frac{\partial \tau_{\theta z}}{\partial \theta} + \frac{\tau_{rz}}{r} &= 0
\end{aligned} \tag{IV.5 - IV.7}$$

The six equations describing the generalised Hookes Law for a material having cylindrical orthotropy are:

$$\begin{Bmatrix} \varepsilon_r \\ \varepsilon_\theta \\ \varepsilon_z \\ \gamma_{\theta z} \\ \gamma_{zr} \\ \gamma_{r\theta} \end{Bmatrix} = \begin{bmatrix} a_{11} & a_{12} & a_{13} & & & \\ a_{12} & a_{22} & a_{23} & & & \\ a_{13} & a_{23} & a_{33} & & & \\ & & & a_{44} & & \\ & & & & a_{55} & \\ & & & & & a_{66} \end{bmatrix} \begin{Bmatrix} \sigma_r \\ \sigma_\theta \\ \sigma_z \\ \tau_{\theta z} \\ \tau_{zr} \\ \tau_{r\theta} \end{Bmatrix} \tag{IV.8}$$

These strains can also be expressed in terms of displacements, as follows,

$$\varepsilon_r = \frac{\partial u_r}{\partial r}$$

$$\varepsilon_\theta = \frac{1}{r}\frac{\partial u_\theta}{\partial \theta} + \frac{u_r}{r}$$

$$\varepsilon_z = \frac{\partial u_z}{\partial z}$$

$$\gamma_{\theta z} = \frac{\partial u_\theta}{\partial z} + \frac{1}{r}\frac{\partial u_z}{\partial \theta}$$

$$\gamma_{zr} = \frac{\partial u_z}{\partial r} + \frac{\partial u_r}{\partial z} \qquad \text{(IV.9 - IV.14)}$$

$$\gamma_{r\theta} = \frac{1}{r}\frac{\partial u_r}{\partial \theta} + \frac{\partial u_\theta}{\partial r} - \frac{u_\theta}{r}$$

so that IV.8 can be rewritten as,

$$\begin{Bmatrix} \dfrac{\partial u_r}{\partial r} \\ \dfrac{1}{r}\dfrac{\partial u_\theta}{\partial \theta} + \dfrac{u_r}{r} \\ \dfrac{\partial u_z}{\partial z} \\ \dfrac{\partial u_\theta}{\partial z} + \dfrac{1}{r}\dfrac{\partial u_z}{\partial \theta} \\ \dfrac{\partial u_z}{\partial r} + \dfrac{\partial u_r}{\partial z} \\ \dfrac{1}{r}\dfrac{\partial u_r}{\partial \theta} + \dfrac{\partial u_\theta}{\partial r} - \dfrac{u_\theta}{r} \end{Bmatrix} = \begin{bmatrix} a_{11} & a_{12} & a_{13} & & & \\ a_{12} & a_{22} & a_{23} & & & \\ a_{13} & a_{23} & a_{33} & & & \\ & & & a_{44} & & \\ & & & & a_{55} & \\ & & & & & a_{66} \end{bmatrix} \begin{Bmatrix} \sigma_r \\ \sigma_\theta \\ \sigma_z \\ \tau_{\theta z} \\ \tau_{zr} \\ \tau_{r\theta} \end{Bmatrix}$$

(IV.15)

The expression for ε_z from IV.8 can be rearranged as follows,

$$\sigma_z = \frac{\varepsilon_z}{a_{33}} - \frac{1}{a_{33}}\left(a_{13}\sigma_r + a_{23}\sigma_\theta\right) \quad \text{(IV.16)}$$

and then substituted into IV.15,

$$\begin{aligned}
\frac{\partial u_r}{\partial r} &= \beta_{11}\sigma_r + \beta_{12}\sigma_\theta + \frac{a_{13}}{a_{33}}\varepsilon_z \\
\frac{1}{r}\frac{\partial u_\theta}{\partial \theta} + \frac{u_r}{r} &= \beta_{12}\sigma_r + \beta_{22}\sigma_\theta + \frac{a_{23}}{a_{33}}\varepsilon_z \\
\frac{\partial u_z}{\partial z} &= \varepsilon_z \\
\frac{\partial u_\theta}{\partial z} + \frac{1}{r}\frac{\partial u_z}{\partial \theta} &= \beta_{44}\tau_{\theta z} \\
\frac{\partial u_z}{\partial r} + \frac{\partial u_r}{\partial z} &= \beta_{55}\tau_{rz} \\
\frac{1}{r}\frac{\partial u_r}{\partial \theta} + \frac{\partial u_\theta}{\partial r} - \frac{u_\theta}{r} &= \beta_{66}\tau_{r\theta}
\end{aligned} \quad \text{(IV.17 - IV.22)}$$

where, β_{ij} are the "reduced strain coefficients" and are defined as,

$$\beta_{ij} = a_{ij} - \frac{a_{i3}a_{j3}}{a_{33}} \qquad (i,j = 1,2,4,5,6) \qquad \text{(IV.23)}$$

Integrating IV.19 with respect to z, we obtain the following relation for axial displacement,

$$u_z = z\varepsilon_z + W(r,\theta) \qquad \text{(IV.24)}$$

Substituting this result into IV.20 and IV.21 and then integrating these with respect to z again, the following relations for radial and tangential displacements are obtained,

$$u_r = (\beta_{55}\tau_{rz})z - \frac{1}{2}z^2\frac{\partial \varepsilon_z}{\partial r} - z\frac{\partial W}{\partial r} + U(r,\theta)$$
$$u_\theta = (\beta_{44}\tau_{\theta z})z - \frac{1}{2}\frac{1}{r}z^2\frac{\partial \varepsilon_z}{\partial \theta} - \frac{1}{r}z\frac{\partial W}{\partial \theta} + V(r,\theta)$$

(IV.25 - IV.26)

where the functions $U(r,\theta)$, $V(r,\theta)$ and $W(r,\theta)$ arise as "constants of integration". By substituting these displacements into IV.17, IV.18 and IV.22 and then equating coefficients of zeroth, first and second order terms in z the following sets of equations are obtained,

$$\frac{\partial U}{\partial r} = \beta_{11}\sigma_r + \beta_{12}\sigma_\theta + \frac{a_{13}}{a_{33}}\varepsilon_z$$
$$\frac{1}{r}\frac{\partial V}{\partial \theta} + \frac{U}{r} = \beta_{12}\sigma_r + \beta_{22}\sigma_\theta + \frac{a_{23}}{a_{33}}\varepsilon_z$$
$$\frac{1}{r}\frac{\partial U}{\partial \theta} + \frac{\partial V}{\partial r} - \frac{V}{r} = \beta_{66}\tau_{r\theta}$$

(IV.27 - IV.29)

$$\frac{1}{r}\frac{\partial W}{\partial \theta} = \beta_{44}\tau_{\theta z}$$
$$\frac{\partial W}{\partial r} = \beta_{55}\tau_{rz}$$

(IV.30 - IV.31)

$$\frac{\partial^2 \varepsilon_z}{\partial r^2} = 0$$

$$\frac{1}{r}\frac{\partial^2 \varepsilon_z}{\partial \theta^2} + \frac{\partial \varepsilon_z}{\partial r} = 0$$

$$\frac{\partial^2 \varepsilon_z}{\partial \theta \partial r} - \frac{1}{r}\frac{\partial \varepsilon_z}{\partial \theta} = 0$$

(IV.32 - IV.34)

The solution of IV.27-IV.29 is of the form,

$$\varepsilon_z = Ar\cos\theta + Br\sin\theta + C \qquad \text{(IV.35)}$$

Equations IV.25 - IV.27, can be simplified using IV.31, IV.32 and IV.36 with the following results,

$$u_r = -\frac{1}{2}z^2(A\cos\theta + B\sin\theta) + U$$

$$u_\theta = -\frac{1}{2}\frac{1}{r}z^2(-A\sin\theta + B\cos\theta) + V \qquad \text{(IV.36 - IV.38)}$$

$$u_z = z(Ar\cos\theta + Br\sin\theta) + zC + W$$

If the loading due to body forces and surface forces are further restricted such that they do not vary circumferentially, then all longitudinal cross-sections which intersect the z-axis are identical. The states of stress and deformation are, therefore, independent of θ. This requires that,

$$A = B = 0 \qquad \text{(IV.39)}$$

and equations IV.37 - IV.39 reduce to

$$u_r = U$$
$$u_\theta = V \qquad \text{(IV.40 -}$$
$$u_z = zC + W$$

IV.42)

Where U, V and W are now functions of r alone. However, recalling that all cross sections, perpendicular to the cylinder axis, must remain planar, W cannot be a function of r alone and, therefore,

$$W = 0 \text{ and } \tau_{\theta z} = \tau_{rz} = 0 \qquad \text{(IV.43)}$$

In addition, the end condition that the forces distributed over the ends of the cylinder reduce to an axial force located at the cylinder axis, requires that

$$\tau_{r\theta} = 0. \qquad \text{(IV.44)}$$

Equation IV-29 reduces to

$$\frac{\partial V}{\partial r} - \frac{V}{r} = 0 \qquad \text{(IV.45)}$$

and, thus,

$$V = 0 \qquad \text{(IV.46)}$$

Now, IV.40-IV-42 reduce as follows,

$$u_r = U(r)$$
$$u_\theta = 0 \qquad \text{(IV.47-IV.49)}$$
$$u_z = z\varepsilon_z^{\mathbf{0}}$$

where $\varepsilon_z^{\mathbf{0}}$ is a uniform axial strain.

Equations IV-27 and IV-28 reduce to

$$\frac{\partial U}{\partial r} = \beta_{11}\sigma_r + \beta_{12}\sigma_\theta + \frac{a_{13}}{a_{33}}\varepsilon_z^0$$
$$\frac{U}{r} = \beta_{12}\sigma_r + \beta_{22}\sigma_\theta + \frac{a_{23}}{a_{33}}\varepsilon_z^0 \qquad \text{(IV.50-IV.51)}$$

and using the identity

$$r\frac{\partial}{\partial r}\left(\frac{\partial U}{\partial r}\right) - r\frac{\partial^2}{\partial r^2}(U) = 0 \qquad \text{(IV.52)}$$

these reduce to

$$\left(r\frac{\partial}{\partial r}\right)\left(\beta_{11}\sigma_r + \beta_{12}\sigma_\theta + \frac{a_{13}}{a_{33}}\varepsilon_z^0\right) -$$
$$r\frac{\partial^2}{\partial r^2}\left(r\left(\beta_{12}\sigma_r + \beta_{22}\sigma_\theta + \frac{a_{23}}{a_{33}}\varepsilon_z^0\right)\right) = 0 \qquad \text{(IV.53)}$$

The stresses must satisfy the equilibrium equations IV.5 - IV.7. These equations are satisfied if the stresses are described by the Airy stress functions $\boldsymbol{F}$ and ψ as follows,

$$\sigma_r = \frac{1}{r}\frac{\partial \boldsymbol{F}}{\partial r} + \frac{1}{r^2}\frac{\partial^2 \boldsymbol{F}}{\partial \theta^2} + \overline{U}$$
$$\sigma_\theta = \frac{\partial^2 \boldsymbol{F}}{\partial r^2} + \overline{U}$$
$$\tau_{\theta z} = -\frac{\partial \psi}{\partial r}$$
$$\tau_{rz} = \frac{1}{r}\frac{\partial \psi}{\partial \theta} \qquad \text{(IV.54-IV.58)}$$
$$\tau_{r\theta} = -\frac{\partial^2}{\partial r \partial \theta}\left(\frac{\boldsymbol{F}}{r}\right)$$

Since, for the current loading conditions,

$$\tau_{\theta z} = \tau_{rz} = \tau_{r\theta} = 0, \qquad \text{(IV.59)}$$

it follows that,

$$\psi = 0 \text{ and } \boldsymbol{F} = \boldsymbol{F}(r). \qquad \text{(IV.60 - IV.61)}$$

Substituting the Airy stress functions, IV.54 and IV.58, into IV.53,

$$\frac{\partial^2}{\partial r^2}\left(r\left(\beta_{12}\left(\frac{1}{r}\frac{\partial \boldsymbol{F}}{\partial r} + \overline{U} \right) + \beta_{22}\left(\frac{\partial^2 \boldsymbol{F}}{\partial r^2} + \overline{U} \right) + \frac{a_{23}}{a_{33}}\varepsilon_z^{\mathbf{0}} \right)\right)$$
$$-\frac{\partial}{\partial r}\left(\beta_{11}\left(\frac{1}{r}\frac{\partial \boldsymbol{F}}{\partial r} + \overline{U} \right) + \beta_{12}\left(\frac{\partial^2 \boldsymbol{F}}{\partial r^2} + \overline{U} \right) + \frac{a_{13}}{a_{33}}\varepsilon_z^{\mathbf{0}} \right) = 0$$

(IV.62)

The potential, $\overline{U}$, defines the body force due to centripetal acceleration as follows,

$$\overline{U} = -\frac{1}{2}\rho\omega^2 r^2 \qquad \text{(IV.63)}$$

where, ρ is the material density and ω is the angular velocity of the pressure vessel. Evaluation of the derivatives and grouping of terms yields a fourth order differential equation,

$$\frac{\partial^4 \boldsymbol{F}}{\partial r^4} + \frac{2}{r}\frac{\partial^3 \boldsymbol{F}}{\partial r^3} - \frac{g^2}{r^2}\frac{\partial^2 \boldsymbol{F}}{\partial r^2} + \frac{g^2}{r^2}\frac{\partial \boldsymbol{F}}{\partial r} = H \qquad \text{(IV.64)}$$

where,

$$H = \frac{1}{\beta_{22}}\rho\omega^2\left(2\beta_{12} + 3\beta_{22} - \beta_{11}\right) \qquad \text{(IV.65)}$$

and

$$g^2 = \frac{\beta_{11}}{\beta_{22}} \qquad \text{(IV.66)}$$

This equation has a homogeneous solution of the form,

$$F_h(r) = c_1 + c_2 r^{1+g} + c_3 r^{1-g} + c_4 r^2 \qquad \text{(IV.67)}$$

and a particular solution of the form,

$$F_p(r) = c_5 r^4 \qquad \text{(IV.68)}$$

Equations IV.50 and IV.51, simplify as follows

$$\sigma_r = \frac{1}{r}\frac{\partial F}{\partial r} + \overline{U}$$

$$\sigma_\theta = \frac{\partial^2 F}{\partial r^2} + \overline{U} \qquad \text{(IV.69 - IV.70)}$$

.The boundary conditions,

$$\sigma_r = P_{\text{int}} \quad \text{at} \quad r = r_{\text{int}}$$

and (IV.71)

$$\sigma_r = P_{ext} \quad \text{at} \quad r = r_{ext}$$

determine the constants in equations IV.67 and IV.68. The resulting expression for radial stress is,

$$\sigma_r = \rho\omega^2 r_{ext}^2 \left(\frac{3+\nu_{\theta r}}{9-g^2}\right)\left(\begin{array}{l}\left(\dfrac{1-c^{g+3}}{1-c^{2g}}\right)\left(\dfrac{r}{r_{ext}}\right)^{g-1} + \\ \left(\dfrac{1-c^{g-3}}{1-c^{2g}}\right)c^{g+3}\left(\dfrac{r_{ext}}{r}\right)^{g+1} - \left(\dfrac{r}{r_{ext}}\right)^2\end{array}\right) +$$
$$\left(\frac{P_{\text{int}} c^{g+1}}{1-c^{2g}}\right)\left(\left(\frac{r}{r_{ext}}\right)^{g-1} - \left(\frac{r_{ext}}{r}\right)^{g+1}\right) +$$
$$\left(\frac{P_{ext}}{1-c^{2g}}\right)\left(c^{2g}\left(\frac{r_{ext}}{r}\right)^{g+1} - \left(\frac{r}{r_{ext}}\right)^{g-1}\right)$$

(IV.72)

and for tangential stress is,

$$\sigma_\theta = \left(\frac{\rho\omega^2 r_{ext}^2}{9-g^2}\right)\left((3+\nu_{\theta r})g\left(\left(\frac{1-c^{g+3}}{1-c^{2g}}\right)\left(\frac{r}{r_{ext}}\right)^{g-1} - \left(\frac{1-c^{g-3}}{1-c^{2g}}\right)c^{g+3}\left(\frac{r_{ext}}{r}\right)^{g+1}\right) - \left(g^2+3\nu_{\theta r}\right)\left(\frac{r}{r_{ext}}\right)^2\right)$$
$$\left(\frac{P_{\text{int}}c^{g+1}g}{1-c^{2g}}\right)\left(\left(\frac{r}{r_{ext}}\right)^{g-1}+\left(\frac{r_{ext}}{r}\right)^{g+1}\right)-$$
$$\left(\frac{P_{ext}g}{1-c^{2g}}\right)\left(\left(\frac{r}{r_{ext}}\right)^{g-1}+c^{2g}\left(\frac{r_{ext}}{r}\right)^{g+1}\right)$$

(IV.73)

where,

$$\nu_{\theta r} = -\frac{\beta_{12}}{\beta_{22}} \qquad \text{(IV.74)} \qquad \text{and} \qquad c = \frac{r_{\text{int}}}{r_{ext}}$$

(IV.75)

Refering back to equation IV.16, and recalling that, due to symmetry, axial stress is expressed as follows,

$$\sigma_z = \frac{\varepsilon_z}{a_{33}} - \frac{1}{a_{33}}\left(a_{13}\sigma_r + a_{23}\sigma_\theta\right) \qquad \text{(IV.76)}$$

Using IV.50, the relations for displacement I.47-I.49 can be rewritten as,

$$u_r = r(\beta_{12}\sigma_r + \beta_{22}\sigma_\theta - \nu_{z\theta}\varepsilon_z^0)$$
$$u_\theta = 0 \qquad \text{(IV.77 -}$$
$$u_z = z\varepsilon_z^0$$

IV.79)

where

$$\nu_{z\theta} = -\frac{a_{23}}{a_{33}} \qquad \text{(IV.80)}$$

Appendix V

Determination of Elastic Constants in Three Dimensions

(after Sun, C.T., Li, S., Three-Dimensional Effective Elastic Constants for Thick Laminates, Journal of Composite Materials, Vol. 22, July 1988, pp. 629-639)

Consider a symmetric laminate comprised of n laminae each of which is governed by the constitutive relation,

$$\sigma_i^{(m)} = D_{ij}^{(m)} \varepsilon_j^{(m)} \qquad m = 1, n \qquad \text{(V.1)}$$

For each lamina, this relation is defined with respect to the cartesian coordinate system of that lamina (i-fibre direction, j-in-plane transverse and k-normal). Note that the $i-j$ plane corresponds to the $z-\theta$ plane in coordinate system of the cylinder although the axes do not coincide unless the wind-angle of the lamina is zero degrees. The k direction corresponds to the r direction in coordinate system of the cylinder.

These lamina stresses and strains can be transformed to the laminate coordinate system, I, J, K, using the rotational stress transformation, $H_{Ij}^{(m)}$ and the rotational strain transformation, $G_{Ij}^{(m)}$.

$$\sigma_I^{(m)} = H_{Ii}^{(m)} \sigma_i^{(m)} \qquad \text{(V.2)}$$

$$\varepsilon_I^{(m)} = G_{Ii}^{(m)} \varepsilon_i^{(m)} \qquad \text{(V.3)}$$

Note that the I, J, K laminate coordinate system corresponds to the z, θ, r coordinate system of the cylinder.

$$\sigma_I^{(m)} = C_{IJ}^{(m)} \varepsilon_J^{(m)} \qquad \text{(V.4)}$$

where

$$C_{IJ}^{(m)} = H_{Ii}^{(m)} D_{ij}^{(m)} \left[G_{Jj}^{(m)} \right]^{-1} \qquad \text{(V.5)}$$

There is an equivalent constitutive relation for the laminate as a whole which may be expressed as,

$$\overline{\sigma}_I = \overline{C}_{IJ} \overline{\varepsilon}_J \qquad \text{(V.6)}$$

and the objective here is to establish a relationship between $C_{IJ}^{(m)}$ and $\overline{C}_{IJ}$.

Now, consider a general laminate consisting of n laminae where the x and y axes lie in the plane of the laminate and the z axis is perpendicular to the plane of the laminate. In keeping with classical laminated plate theory, it can be assumed that,

$$\begin{aligned} \varepsilon_x^{(m)} &= \overline{\varepsilon}_x \\ \varepsilon_y^{(m)} &= \overline{\varepsilon}_y \\ \gamma_{xy}^{(m)} &= \overline{\gamma}_{xy} \end{aligned} \qquad \text{(V.7-9)}$$

In addition, it is assumed that stresses accross the thickness are constant, namely

$$\begin{aligned} \sigma_z^{(m)} &= \overline{\sigma}_z \\ \tau_{yz}^{(m)} &= \overline{\tau}_{yz} \\ \tau_{xz}^{(m)} &= \overline{\tau}_{xz} \end{aligned} \qquad \text{(V.10-12)}$$

Based on these assumptions, Sun and Li derived relations between $C_{IJ}^{(m)}$ and $\overline{C}_{IJ}$ for the case of a general symmetric laminate. They also derived a set of reduced relations for the specific case of a symmetric angle-ply laminate (single material and single wind angle $\pm\alpha$) as follows,

$$\overline{C}_{11} = \frac{1}{h}\Sigma t_m C_{11}^{(m)} \qquad \overline{C}_{23} = C_{23}^{(m)} \qquad \overline{C}_{16} = \frac{1}{h}\Sigma t_m C_{16}^{(m)}$$

$$\overline{C}_{22} = \frac{1}{h}\Sigma t_m C_{22}^{(m)} \qquad \overline{C}_{13} = C_{13}^{(m)} \qquad \overline{C}_{36} = \frac{1}{h}\Sigma t_m C_{36}^{(m)}$$

$$\overline{C}_{33} = C_{33}^{(m)} \qquad \overline{C}_{12} = \frac{1}{h}\Sigma t_m C_{12}^{(m)}$$

(V.13-14) (V.15-17) (V.18-19)

where the lamina thicknesses are t_m.

Appendix VI

Quadratic Failure Criteria

(Tsai, S.W., Composites Design, Fourth Edition, Think Composites, Ohio, 1988)

The quadratic failure criteria for three dimensions is expressed as,

$$F_{ij}\sigma_i\sigma_j + F_i\sigma_i = 1 \quad i,j = 1,2\ldots.6 \qquad \text{(VI.1)}$$

For a three dimensional state of stress, this expands to:

$$\begin{aligned}
&F_{XX}\sigma_X^2 + F_{YY}\sigma_Y^2 + F_{ZZ}\sigma_Z^2 + \\
&F_{SYZ}\tau_{YZ}^2 + F_{SXZ}\tau_{XZ}^2 + F_{SXY}\tau_{XY}^2 + \\
&2F_{XY}\sigma_X\sigma_Y + 2F_{XZ}\sigma_X\sigma_Z + 2F_{YZ}\sigma_Y\sigma_Z + \\
&F_X\sigma_X + F_Y\sigma_Y + F_Z\sigma_Z = 1
\end{aligned}$$

(VI.2)

The terms involving first order shear stresses are not included in this expression because a reversal in the sign of a shear stress should not change calculated strength. For the case of a transversely isotropic material in which the Y-Z plane is the plane of isotropy the following relationships exist,

$$\begin{aligned}
F_{YY} &= F_{ZZ} \\
F_Y &= F_Z \\
F_{XY} &= F_{XZ} \\
F_{SXY} &= F_{SXZ}
\end{aligned} \qquad \text{(VI.3)}$$

which reduce Equation VI.2 to,

$$\begin{aligned}
&F_{XX}\sigma_X^2 + F_{YY}(\sigma_Y^2 + \sigma_Z^2) + \\
&F_{SYZ}\tau_{YZ}^2 + F_{SXY}(\tau_{XZ}^2 + \tau_{XY}^2) + \\
&2F_{XY}\sigma_X(\sigma_Y + \sigma_Z) + 2F_{YZ}\sigma_Y\sigma_Z + \\
&F_X\sigma_X + F_Y(\sigma_Y + \sigma_Z) = 1
\end{aligned} \tag{VI.4}$$

Of the eight strength parameters, five can be determined from the tensile and compressive strengths of the uniaxial composite,

$$\begin{aligned}
F_{XX} &= \frac{1}{XX'} \\
F_{YY} &= \frac{1}{YY'} \\
F_X &= \frac{1}{X} - \frac{1}{X'} \\
F_Y &= \frac{1}{Y} - \frac{1}{Y'} \\
F_{SXY} &= \frac{1}{S_{XY}^2}
\end{aligned} \tag{VI.5}$$

Since the Y-Z plane is a plane of isotropy,

$$F_{SYZ} = \frac{1}{S_{YZ}^2} = 3F_{YY} = \frac{3}{YY'} \tag{VI.6}$$

and

$$F_{YZ} = -\frac{1}{2}F_{YY} \tag{VI.7}$$

The only remaining strength parameter is F_{XY} which is defined as

$$F_{XY} = F^*_{XY}\sqrt{F_{XX}F_{YY}} \tag{VI.8}$$

where F^*_{XY} is the normalized interaction term. Substituting equations VI.7 and VI.8 into VI.6 yields,

$$\begin{aligned}&F_{XX}\sigma_X^2 + F_{YY}(\sigma_Y^2 - \sigma_Y\sigma_Z + \sigma_Z^2 + 3\tau_{YZ}^2) + \\ &F_{SXY}(\tau_{XZ}^2 + \tau_{XY}^2) + 2F^*_{XY}\sqrt{F_{XX}F_{YY}}\,\sigma_X(\sigma_Y + \sigma_Z) + \\ &F_X\sigma_X + F_Y(\sigma_Y + \sigma_Z) = 1\end{aligned} \tag{VI.9}$$

If proportional loading is assumed, then the a "strength ratio", S, such that,

$$\begin{aligned}&F_{XX}S^2\sigma_X^2 + F_{YY}S^2(\sigma_Y^2 - \sigma_Y\sigma_Z + \sigma_Z^2 + 3\tau_{YZ}^2) + \\ &F_{SXY}S^2(\tau_{XZ}^2 + \tau_{XY}^2) + 2F^*_{XY}\sqrt{F_{XX}F_{YY}}S^2\sigma_X(\sigma_Y + \sigma_Z) + \\ &F_XS\sigma_X + F_YS(\sigma_Y + \sigma_Z) = 1\end{aligned} \tag{VI.10}$$

or

$$AS^2 + BS - 1 = 0 \tag{VI.11}$$

where

$$\begin{aligned}A = &F_{XX}\sigma_X^2 + F_{YY}(\sigma_Y^2 - \sigma_Y\sigma_Z + \sigma_Z^2 + 3\tau_{YZ}^2) + \\ &F_{SXY}(\tau_{XZ}^2 + \tau_{XY}^2) + 2F^*_{XY}\sqrt{F_{XX}F_{YY}}\,\sigma_X(\sigma_Y + \sigma_Z)\end{aligned} \tag{VI.12}$$

$$B = F_X\sigma_X + F_Y(\sigma_Y + \sigma_Z)$$

S, can be interpreted as a factor of safety where the failure criteria will be satisfied when S is less than or equal to unity. S is the positve root of the quadratic equation.

$$S = \frac{-B + \sqrt{B^2 + 4AC}}{2A} \tag{VI.13}$$

The negative root has no physical meaning.

Appendix VII

Properties of Unidirectional T300/N5208

(From Tsai, S.W., Composites Design, Fourth Edition, Think Composites, Ohio, 1988)

Elastic modulus in fibre direction:	181 GPa
Elastic modulus in transverse direction:	10.3 GPa
Poisson Ratio in fibre direction:	0.28
Poisson Ratio in transverse/transverse direction:	0.52
Shear Modulus in plane of lamina:	7.17 GPa
Density:	1600 kg/m^3
Ultimate tensile strength in fibre direction:	1500 MPa
Ultimate compressive strength in fibre direction:	1500 MPa
Ultimate tensile strength in transverse direction:	40 MPa
Ultimate compressive strength in transverse direction:	246 MPa
Ultimate in-plane shear strength	68 MPa

Table VII.1 - Properties of T300/N5208

Appendix VIII

Energy Consumption Estimates for Conventional RO and CRO

Unit Capacity (USgpd)	**10,000**	**25,000**	**50,000**	**86,000**	**172,000**
Unit Capacity (m3/day)	**38**	**95**	**189**	**326**	**651**
Recovery Ratio	30%	30%	30%	30%	30%
Cartridge Model	Filmtec 4040	Filmtec 4040	Filmtec 8040	Filmtec 8040	Filmtec 8040
Number of Cartridges[1]	12	28	12	22	42
Operating Pressure[2](psi)	900	900	900	900	900
High Pressure Feed Pump Mechanical Efficiency[3]	90%	90%	90%	90%	90%
High Pressure Feed Pump Volumetric Efficiency[4]	95%	95%	95%	95%	95%
Motor Efficiency[5]	90%	90%	90%	90%	90%
Total Power (kW)[6]	11.78	29.44	58.88	101.27	202.55
Specific Power Consumption (kWh/m3)	**7.47**	**7.47**	**7.47**	**7.47**	**7.47**

Table VIII.1 - Estimated Power Consumption of Conventional RO Plants

1, 2. As determined using FILMTEC Reverse-Osmosis System Analysis Progarm, The Dow Chemical Company, Minneapolis Mn.

3, 4. Personal communication, J. Rienkemeyer, Wheatley Pump and Valve, Tulsa, OK.

5. Personal communication, C. Smitts, Armature Electric, Vancouver

6. Equation 2.15, adjusted for mechanical and volumetric efficiency

Capacity (USgpd)	**10,000**	**25,000**	**50,000**	**86,000**	**172,000**
Capacity (m^3/day)	**38**	**95**	**189**	**326**	**651**
Recovery Ratio	20%	20%	20%	20%	20%
Cart Model(Filmtec)	4040	4040	8040	8040	8040
Number of Cart's[1]	12	28	12	22	42
Number of Pressure Vessels[2]	12	14	12	11	21
Pressure Vessel Outside Dia (in)[3]	5.44	5.44	12.2	12.2	12.2
Pressure Vessel Spacing (in)	0.5	0.5	0.5	0.5	0.5
Outer Shell Thickness[4](in)	1	1	2	2	2
Rotor Diameter(in)	30.39	34.13	65.27	61.28	101.41
Rotor Length[5] (in)	57	97	65	105	106
Operating Pressure[6](psi)	[illegible]	900	900	900	900
Rotor Speed [7](rpm)	4424	3694	2041	2261	1086
Rotor Enclosure Vacuum [8](in Hg)	28.5	28.5	28.5	28.5	28.5
Radial Gap (in)	1	1	1	1	1
Couette Reynolds Number[9]	15430	14472	15291	15901	12637
Moment Coeff [10]	2.09E-03	2.04E-03	1.66E-03	1.68E-03	1.51E-03
Tip Reynolds Number[11]	234461	246990	499017	487202	640775
Moment Coeff [12]	5.25E-03	5.19E-03	4.51E-03	4.53E-03	4.29E-03
Windage Losses (kW)[13]	1.47	2.27	2.82	4.86	3.70
Bearing Losses(kW)[14]	0.16	0.35	0.29	0.53	0.82
Seal Losses (kW)[15]	1.20	2.60	1.85	3.02	2.49
Power To Fresh Water (kW)[16]	5.44	13.59	27.18	46.76	93.52
Feed Pump Power (kW)[17]	0.53	1.32	2.64	4.55	9.09
Vacuum Pump Power (kW)[18]	1	1	2	2	2
Motor Efficiency[19]	90%	90%	90%	90%	90%
Total Power (kW)	10.87	23.47	40.87	68.57	124.02
Specific Power Consumption (kWh/m3)	**6.893**	**5.954**	**5.183**	**5.055**	**4.572**

Table VIII.2 - Projected Power Consumption For CRO

1, 2. As determined using FILMTEC Reverse-Osmosis System Analysis Progarm, The Dow Chemical Company, Minneapolis Mn.

3. Based on dimensions of pressure vessels manufactured by Advanced Structures Corp.

4. Estimated using procedure developed in Chapter 6

5. 3. Based on dimensions of pressure vessels manufactured by Advanced Structures Corp.

6. As determined using FILMTEC Reverse-Osmosis System Analysis Progarm, The Dow Chemical Company, Minneapolis Mn.

7. Based on equation 2.11

8. Vacuum level which was sustained in second prototype

9, 10, 11, 12, 13. See section 2.41

14. Based on data for SKF spherical roller bearings, SKF Catalogue 4000 E

15. Based on friction losses estimates for Chesterton 800 series mechanical seals

16. Based on Equation 2.14

17. Based on a feed pressure of 50 psi and a pump efficiency of 70%

18. Based on power consumption of Corona liquid ring vacuum pumps

19. Personal communication, C. Smitts, Armature Electric, Vancouver